

COSMIC RAY MODULATION IN THE HELIOSPHERE

by

Christopher Paul Baker, B.Sc. (Hons.)
Department of Physics

Submitted in fulfilment of the
requirements for the degree of
Doctor of Philosophy

University of Tasmania
Hobart
May, 1993

This thesis contains no material which has been accepted for the award of any other higher degree or graduate diploma in any tertiary institution. To the best of my knowledge and belief, the thesis contains no material previously published or written by another person, except when due reference is made in the text.

CP Baker

C. P. Baker

ACKNOWLEDGEMENTS

I wish to sincerely thank my supervisors, Dr. John Humble (University of Tasmania) and Dr. Marc Duldig (Australian Antarctic Division). Without their continual guidance, support and encouragement, this thesis would not have been possible.

I am grateful to have been given access to data collected by the network of neutron monitors and muon telescopes operated by the Cosmic Ray Section of the Australian Antarctic Division and the Cosmic Ray Section of the Physics Department, University of Tasmania. I wish to extend my gratitude to the Australian Antarctic Division for the opportunity to visit Mawson for three months during 1991, and for the use of word-processing facilities at the Cosmic Ray Section, on which this thesis was prepared. Thanks also to the Physics Department, University of Tasmania for providing financial support to allow me to work at the University of Arizona for three months during 1990.

I wish to thank Professor J.R. Jokipii for useful discussions on transport theory and numerical solutions to the transport equation, and for the hospitality and financial support I received while working at the University of Arizona. Thanks also to Dr. J.T. Hoeksema for supplying neutral-sheet data used in Chapter 6 and Professor K. Nagashima for supplying the Nagoya GG muon telescope data used in Chapters 6 and 8.

I have been fortunate to have the friendship and support of many post-graduate students and staff working in the Physics Department. Special thanks goes to Damian Hall for making Room 303 so much fun (!) and particularly for the many helpful discussions and contributions to the work in Chapters 7 and 8. Thanks also to Edward King and others who helped me substantially with computer support, and to Judy Whelan (Australian Antarctic Division) who cheerfully performed many tasks on my behalf.

I have had a Research Scientist Cadetship with the Microwave Radar Division, Defence Science and Technology Organization, for the duration of my candidature. The division has, in particular, supported my attendance at a number of conferences during the last four years. For this, I am very grateful.

Finally, I would not have been able to undertake this degree if it were not for my father and mother. They provided me with endless support and encouragement for which I will always be grateful. Thanks Mum and Dad.

ABSTRACT

Models describing the modulation of galactic cosmic rays in the heliosphere have been developed and investigated. These models are numerical solutions of the cosmic ray transport equation under idealized heliospheric conditions. Primarily, the models were used to predict the radial gradient g_r of galactic cosmic rays in the vicinity of the Earth during solar-minimum conditions specified by a flat neutral sheet and no propagating shock disturbances. It was found that g_r was not sensitive to the assumed value of the cosmic ray distribution at the Sun, but was very sensitive to (a) the diffusion coefficients used to specify the rate of diffusion of the cosmic ray distribution near the Sun, and (b) the choice of the integrating algorithm used to determine the distribution from the transport equation. The stability of each integrating algorithm used was also investigated. There have been many measurements of the value of g_r at Earth in the past, mainly derived from data collected by polar-based neutron monitors or detectors on board satellites. From all sources of data and over a wide range of energy (tens of MeV to ~ 100 GeV) the general consensus is that g_r at Earth is less than $5\% \text{ AU}^{-1}$ and probably around $1\text{-}2\% \text{ AU}^{-1}$. The models investigated in this thesis predict a gradient in this range but only if certain diffusion coefficients are specified.

The models were also used to investigate the relative importance of shocks, or propagating solar disturbances, to the total eleven year cycle of cosmic ray modulation for medium energy (1-10 GeV) particles. It was found that such disturbances were unable to produce the observed intensity difference seen from solar minimum to solar maximum. It was concluded that these, and higher energy particles, are modulated significantly by changes in the overall global average heliospheric magnetic field through bulk drift motion. An example of this bulk-drift modulation was investigated by looking at the correlation of neutral-sheet position with isotropic intensity wave variations seen in the cosmic ray data. For this analysis, a generalized model of the neutral sheet was developed.

An independent measurement of g_r was also calculated from data collected by the network of cosmic ray detectors operated by the Hobart cosmic ray group during the years 1975-78 and 1982-85. This group consists of the Cosmic Ray Section of the Australian Antarctic Division and the Cosmic Ray Section of the University of Tasmania (Physics Department). The gradient g_r was determined by applying a north-south anisotropy analysis to the data. The value of g_r obtained was sensitive to the assumed energy spectrum of the north-south anisotropy but was not inconsistent with other experimentally determined values. The gradient was generally less than $5\% \text{ AU}^{-1}$. It was necessary to calculate coupling coefficients and atmospheric correction coefficients for the Mawson muon telescopes in order to use the data from these detectors in the north-south anisotropy analysis.

TABLE OF CONTENTS

| | |
|--|-----|
| Acknowledgements | iii |
| Abstract | iv |
| Chapter 1. Background | |
| 1.1 Introduction | 1 |
| 1.2 Thesis Summary | 2 |
| 1.3 Theory | 4 |
| 1.3a. The Diffusion Tensor and Drift Velocity | 4 |
| 1.3b. The Solar Wind | 6 |
| 1.3c. The Magnetic Field | 7 |
| 1.3d. The Streaming Vector | 7 |
| 1.3e. The Anisotropy Vector | 8 |
| 1.4 Models | 8 |
| 1.5 Observations | 10 |
| Chapter 2. Numerical Methods | |
| 2.1. Introduction | 12 |
| 2.2. Discretizing the parabolic equation | 13 |
| 2.3. Implicit integrating methods | 15 |
| 2.4. Explicit integrating methods | 19 |
| 2.5. Numerical evaluation of V_D | 20 |
| Chapter 3. Stability Analysis | |
| 3.1. Introduction | 21 |
| 3.2. Theory | 21 |
| 3.3. Application to the Transport Equation | 23 |
| 3.3a. Stability for the LOD scheme (interior grid points) | 23 |
| 3.3b Explicit boundary points (LOD scheme) | 25 |
| 3.3c. Mixed space-derivatives | 26 |
| 3.3d. Stability for explicit schemes | 27 |
| 3.3e. Stability for ADI schemes | 28 |
| Chapter 4. Numerical Results | |
| 4.1. Introduction | 29 |
| 4.2. Results for 2 space dimensions | 30 |
| 4.3. Explicit algorithms | 33 |
| 4.4. Inner boundary analysis | 34 |
| 4.4a. Method 1. Power-Law inner-boundary | 34 |
| 4.4b. Method 2. Improved forms for $K_{//}$, K_{\perp} | 35 |

| | |
|--|----|
| 4.4c. Method 3. Zero streaming at inner-boundary | 36 |
| 4.4d. Summary of inner-boundary analysis | 37 |
| 4.5. Shocks | 38 |
| 4.6. 3 Space dimensions | 43 |

Chapter 5. Coupling Coefficients for Neutron Monitors and Muon Telescopes.

| | |
|--|----|
| 5.1. Introduction | 47 |
| 5.2. Formalism | 47 |
| 5.3. Results for SNCOMB and SSCOMB | 51 |
| 5.4. Interpolating coupling coefficients | 53 |
| 5.5. Neutron monitor coupling coefficients for non- solar minimum / maximum periods | 53 |

Chapter 6. Intensity Waves and the Neutral Sheet

| | |
|---|----|
| 6.1. Introduction to the neutral sheet | 56 |
| 6.2. Parameterizing the neutral sheet | 58 |
| 6.2a Calculating f : 2-sector structure | 59 |
| 6.2b Generalized formula for the neutral sheet | 60 |
| 6.3. Determining the neutral sheet from data | 61 |
| 6.4. Intensity waves | 65 |
| 6.4a Intensity wave definition | 65 |
| 6.4b Sampling sphere | 66 |
| 6.5. Intensity waves vs Neutral sheet correlation | 67 |

Chapter 7. Atmospheric Corrections for Muon Data

| | |
|--|----|
| 7.1. Introduction | 69 |
| 7.2. Evaluating the coefficients | 70 |
| 7.3. Effect of correlation in meteorological data | 72 |
| 7.4. Coefficients for Mawson surface muon detectors | 72 |
| 7.4a Meteorological data | 72 |
| 7.4b Non-meteorological related variations in the muon data | 74 |
| 7.4c Detector efficiency | 74 |
| 7.4d Regression analysis - Results | 76 |
| 7.4e Pressure-Height only correction procedure | 80 |
| 7.5. Coefficients for Mawson underground detectors | 85 |

Chapter 8. North-South Anisotropy Analysis

| | |
|---|----|
| 8.1. Introduction | 86 |
| 8.2. Theory | 88 |
| 8.3. ξ_{NS} from observational data for an arbitrary detector | 92 |
| 8.4. Determining R_z : Method 1 | 94 |
| 8.5. Determining R_z : Method 2 | 96 |
| 8.6. T/A sector binning | 97 |

| | |
|--|-----|
| 8.7. Algorithm | 98 |
| 8.8. Results | 101 |
| 8.9. Discussion of results | 108 |
| 8.10. Removing effects of intensity waves | 110 |
| 8.11. Summary of the north-south anisotropy analysis | 112 |
| 8.12. Boundary crossing intensity analysis | 113 |
| Conclusion | 117 |
| References | 120 |
| Appendices | |
| Appendix 1 | |
| Power-law relationship for inner-boundary condition | 125 |
| Appendix 2 | |
| Fourier series for error terms in von Neumann stability analysis | 126 |
| Appendix 3 | |
| Line of best fit through data with annual variation and efficiency decay | 127 |
| Appendix 4 | |
| Coupling coefficients for SNCOMB ($\times 10^4$) | 129 |
| Appendix 5 | |
| Coupling coefficients for SSCOMB ($\times 10^4$) | 131 |
| Appendix 6 | |
| Level-change / spike recognition algorithm | 133 |
| Appendix 7 | |
| North-South anisotropy analysis: Results using method 1 | 135 |
| Appendix 8 | |
| North-South anisotropy analysis: Results using method 2 | 152 |
| Appendix 9 | |
| North-South anisotropy analysis: Contours of χ^2 for results using method 1 | 169 |
| Appendix 10 | |
| Plots of distribution function for the 2-space dimensional heliosphere | 178 |
| Appendix 11 | |
| Publications | 192 |

Chapter 1. Background.

1.1 INTRODUCTION

Galactic cosmic rays are high energy charged particles. It is known that they originate from regions external to our own solar system, however their precise origin is still unknown. They include fully ionized atomic nuclei roughly in the same galactic abundances as their neutral counterparts and electrons. Most (~90%) of the positively charged cosmic rays are protons. Galactic cosmic rays are characterized by their extremely high kinetic energies. The energies of those that reach the surface of Earth range from the order of 10^8 eV to 10^{20} eV (eV = electron volt) per particle. From observations of very high energy cosmic rays it appears that they are essentially isotropically distributed in the galaxy. See Berezhinskii *et al.* 1990 for a comprehensive review of the properties of galactic cosmic rays.

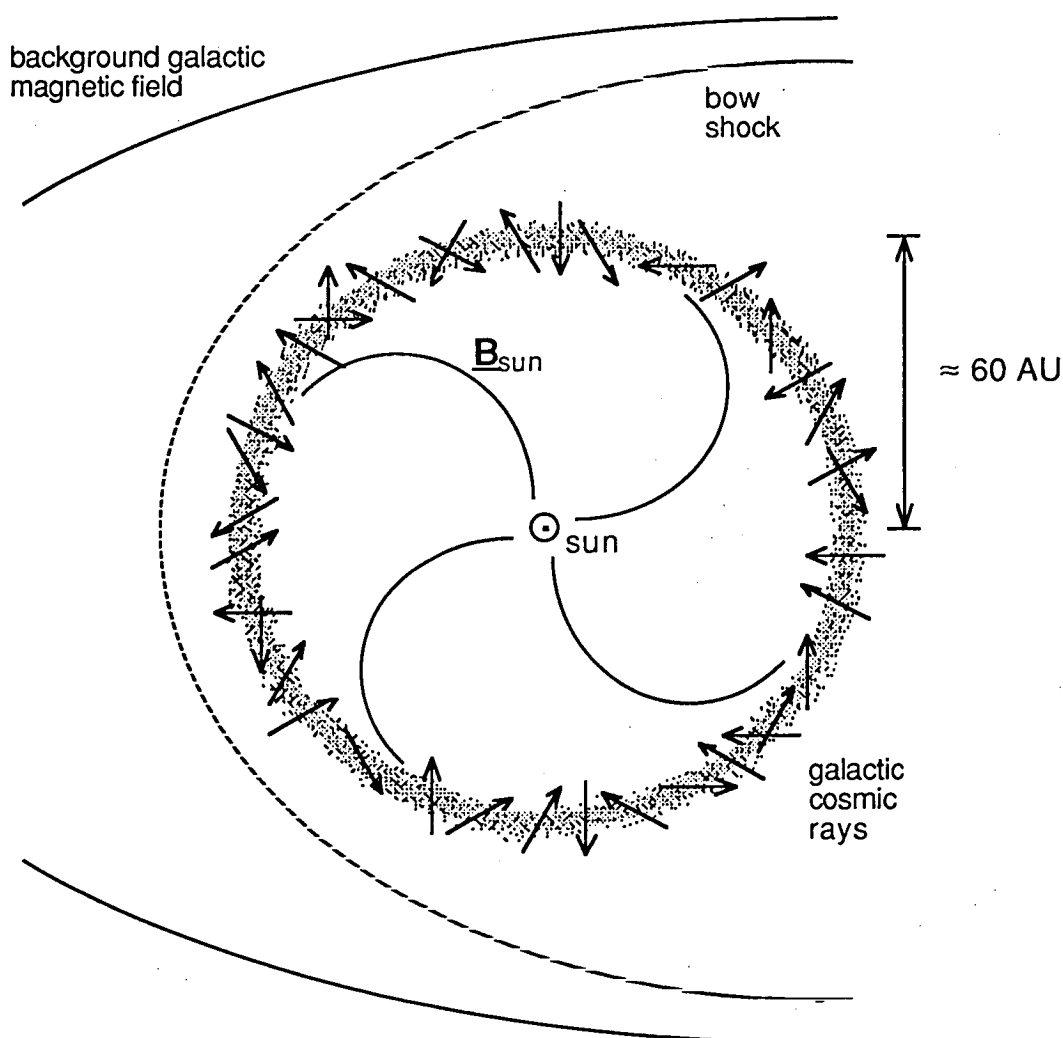


Figure 1.1. The heliosphere is defined as the region where the influence of the Sun's magnetic field dominates the background galactic magnetic field. At the boundary of the heliosphere, it appears that the distribution of galactic cosmic rays is essentially isotropic. A shock is formed where the solar wind goes from a supersonic to subsonic flow, shown here as a fuzzy region roughly 60 AU from the Sun. The actual distance of the boundary of the heliosphere and the shock position from the Sun is not known but most likely varies throughout the solar-cycle.

As cosmic rays enter our solar system, their paths are altered and re-distributed by the solar wind (\underline{V}_{sw}) and magnetic field (\underline{B}). This region, where \underline{V}_{sw} and \underline{B} influence the background galactic field, is termed the *heliosphere* and is shown in Figure 1.1. At the boundary of the heliosphere \underline{V}_{sw} drops to effectively zero and \underline{B} merges with the background galactic magnetic field.

By observing these galactic cosmic rays using both spacecraft and terrestrial based particle detectors, and modelling their interaction with \underline{B} and \underline{V}_{sw} , we can gain both a better understanding of interplanetary fields and solar processes and an appreciation of the properties of these particles in space.

The path of a single cosmic ray particle as it enters the heliosphere is affected by four main processes. These processes are directly related to \underline{V}_{sw} and \underline{B} , which can be written as $(\langle \underline{B} \rangle + \delta \underline{B})$ where $\langle \underline{B} \rangle$ is the large-scale average magnetic field and $\delta \underline{B}$ is the average magnitude of the small-scale random fluctuations in \underline{B} caused by solar disturbances. These disturbances include, for example, flares and coronal mass ejections. The cosmic ray particles undergo large-scale gradient and curvature drift due to $\langle \underline{B} \rangle$. They are scattered in pitch-angle due to the small-scale turbulence in \underline{B} . The amount of scattering is characterized by a *diffusion* timescale which is related to $\delta \underline{B}$. The particles undergo energy changes by the process of Fermi-acceleration and they are convected by the solar wind. The combined effect of these processes describes the total *modulation* of the particles.

Because of the large numbers of galactic cosmic rays in the heliosphere, it is impossible to attempt to keep track of every possible individual particle as it travels through this region. Instead, the galactic cosmic ray intensity at any point in the heliosphere at a given time is described in terms of a distribution function f . This is analogous to describing the motion of a large number of particles in a gas in terms of kinetic theory. The spatial and time dependence of this distribution function is governed by a *transport equation*. This equation relates the evolution of f to the physical parameters which affect the motion of the galactic cosmic rays mentioned above. See Gleeson and Webb (1980), Quenby (1984) and Jokipii (1971) for a detailed derivation of the transport equation and discussion of transport theory in general.

Modelling f is complicated by the fact that both \underline{B} and \underline{V}_{sw} are not only spatially dependent but also time dependent. The large scale solar magnetic field is approximately dipolar near the surface of the Sun. The magnetic field lines are frozen into the solar wind plasma and drawn out into the heliosphere radially by this wind. Over an (on average) eleven year period, in phase with the sunspot cycle, the dipole tilt of \underline{B} on the source surface increases until there is a complete reversal in the direction of the magnetic field at solar maximum. This periodic change in \underline{B} affects the bulk drift velocity of the cosmic ray particles. On a shorter timescale, solar disturbances (discussed for example by Burlaga *et al.* 1985) increase the turbulence in \underline{B} and hence cause more local scattering of the particles. Again analogous to kinetic theory, greater scattering of individual particles corresponds to a decrease in the rate of diffusion of the particle distribution.

1.2 THESIS SUMMARY

The theory of the transport equation and the various physical parameters that define the state of the heliosphere are introduced in the next section. A brief review of the currently developed models and inferences drawn from them is then given in Section 1.4. A brief

review of the parameters inferred from measurements taken by terrestrial and spacecraft detectors is given in Section 1.5.

The main thrust of this thesis is to investigate further the model predictions for the medium energy cosmic ray intensity distribution in the vicinity of the Earth and to compare these predictions with measurements from ground-based neutron monitors and muon detectors. The reviews in Section 1.4 and 1.5 will thus concentrate on observations and model predictions for the cosmic ray intensity distribution in the vicinity of Earth. Note however, when finding this intensity distribution using numerical methods, the intensity distribution must be solved at all points in the heliosphere to obtain the value at Earth. This is a consequence of how the boundary conditions are imposed.

The rest of the thesis can be divided into two parts. The first part comprises Chapters 2 to 4 and contains the modelling theory and results. Chapter 2 describes the numerical procedures used to solve the transport equation under pre-specified heliospheric conditions. Chapter 3 explores the numerical stability (and to an extent, the accuracy) of these procedures as they are implemented on a computer. Chapter 4 contains all the results of the modelling runs. In particular, the main results presented are values for the radial gradient of galactic cosmic rays near Earth, predicted for an axially symmetric heliosphere under various inner-boundary conditions. It will be shown that this gradient is sensitive predominantly to the functional form of the diffusion coefficients near Earth. The role of interplanetary shocks in the eleven-year modulation of cosmic rays is also investigated in this chapter. Difficulties in solving the transport equation in three space dimensions (*non* axially symmetric heliosphere) are also discussed.

The second part of the thesis comprises Chapters 5 to 8 and consists mainly of data analyses. This section culminates in Chapter 8 where analyses and results are presented for the radial gradient of galactic cosmic rays at Earth *measured* by the network of detectors operated by the Hobart cosmic ray groups (Cosmic Ray Section, Physics Department, University of Tasmania, Australia, and Cosmic Ray Section, Auroral and Space Physics, Australian Antarctic Division, Australia) for the periods of 1975-78 and 1982-85. The results presented are generally consistent with predictions made by the modelling runs in Chapter 4 and also independent observations from other researchers. In order to use data from a number of muon-telescopes at Mawson for these analyses, previously undetermined coupling coefficients and atmospheric correction coefficients were calculated. The method by which the coupling coefficients are calculated is presented in Chapter 5. This chapter also serves as a general introduction to coupling coefficients. Such coefficients were also required for the work presented in Chapter 6. Chapter 7 contains the methods of analyses and results for the determination of the atmospheric correction coefficients for a number of Mawson muon detectors. Chapter 6 is, in a way, a stand-alone chapter. It consists of work done to correlate certain isotropic intensity wave modulation phenomena seen in the Mawson muon data to the position of the three-dimensional neutral sheet (see Equation 1.19 and related text). A generalized model of the neutral sheet is developed in the first part of that chapter. The observed correlation shows that the neutral sheet has an effect on the relatively high energy cosmic rays to which muon telescopes are sensitive. The fact that the correlation exists supports a conclusion in Chapter 4 that interplanetary shock waves do not seem to be sufficient to explain the observed eleven-year solar cycle of galactic cosmic rays.

Publications which arose from research undertaken during the course of this degree are listed in Appendix 11.

1.3 THEORY

The cosmic ray distribution function $f = f(\underline{x}, p, t)$ is a five-dimensional scalar function of space $\underline{x} = \underline{x}(r, \theta, \phi)$, momentum p (magnitude only) and time t . The space coordinates are most naturally described on a spherical polar coordinate system, r being the radial distance from the Sun, θ being the polar angle measured from the rotation axis of the Sun, and ϕ being the azimuth coordinate. The usual definition of f is such that there exist $p^2 f(\underline{x}, p, t) d^3\underline{x} dp$ particles with momentum in the range p to $p+dp$ in a spatial region $d^3\underline{x}$ about \underline{x} at time t . With this definition, the differential intensity of particles is

$$j(\underline{x}, p, t) \propto p^2 f(\underline{x}, p, t) \quad (1.1)$$

and the integral intensity is

$$I(\underline{x}, t) \propto \int_0^\infty j(\underline{x}, p, t) dp \quad (1.2)$$

The differential *number density* of particles is given by $U = 4\pi p^2 f$. Using arguments of particle continuity and energy conservation in phase-space, it was first shown by Parker (1965) (see also Jokipii *et al.* 1977, Jokipii and Kopriva 1979 and references therein) that f satisfies the partial differential equation:

$$\frac{\partial f}{\partial t} = \nabla \cdot (\underline{K}^S \cdot \nabla f) - (\underline{V}_D + \underline{V}_{SW}) \cdot \nabla f + \frac{1}{3} (\nabla \cdot \underline{V}_{SW}) p \frac{\partial f}{\partial p} \quad (1.3)$$

This is known as the transport equation and is a parabolic type partial differential equation, being second-order in space coordinates and first-order in time. \underline{K}^S denotes the symmetric part of the diffusion tensor. The diffusion tensor is a 3x3 matrix whose terms include the diffusion coefficients parallel and perpendicular to the magnetic field. These coefficients are functions of the turbulence $\delta \underline{B}$ of the field. \underline{V}_D denotes the drift velocity which describes the total effect of the gradient and curvature drifts of the distribution of particles and is a function of the average field $\langle \underline{B} \rangle$. The transport equation can also be written with the full-diffusion tensor where the anti-symmetric part corresponds to the drift-term (see below). \underline{V}_{SW} denotes the solar wind speed. As a first approximation, the solar wind is radial in direction and has a magnitude around 400 km s⁻¹. The adiabatic energy loss of particles is related to the divergence of the solar-wind.

1.3a. The Diffusion Tensor and Drift Velocity:

In a coordinate system aligned with the local magnetic field (x-axis parallel to \underline{B}) the full diffusion tensor is

$$\underline{K} = \begin{pmatrix} K_{//} & 0 & 0 \\ 0 & K_{\perp} & K^A \\ 0 & -K^A & K_{\perp} \end{pmatrix} \quad (1.4)$$

where $K_{//}$ is the diffusion coefficient for diffusion parallel to the magnetic field and K_{\perp} is the diffusion coefficient for diffusion perpendicular to the magnetic field. K^A is the anti-symmetric coefficient and is related to the drift-velocity:

$$\begin{aligned}\nabla \cdot (\underline{K} \cdot \nabla f) &= \frac{\partial}{\partial x_i} \left(K_{ij} \frac{\partial}{\partial x_j} \right) \\ &= \frac{\partial}{\partial x_i} \left((K_{ij}^S + K_{ij}^A) \frac{\partial}{\partial x_j} \right) \\ &= \nabla \cdot (\underline{K}^S \cdot \nabla f) + \nabla \cdot (\underline{K}^A \cdot \nabla f)\end{aligned}\tag{1.5}$$

$$\text{Now, } \nabla \cdot (\underline{K}^A \cdot \nabla f) = \frac{\partial K_{ij}^A}{\partial x_i} \frac{\partial f}{\partial x_j}\tag{1.6}$$

$$\text{Define } (\underline{V}_D)_j = -\frac{\partial K_{ij}^A}{\partial x_i}\tag{1.7}$$

$$\text{Then, } \nabla \cdot (\underline{K}^A \cdot \nabla f) = -(\underline{V}_D \cdot \nabla f)\tag{1.8}$$

$$\text{With } K^A = \frac{p\nu}{3q|\underline{B}|}$$

$$\underline{V}_D = \frac{p\nu}{3q} \nabla \times \left(\frac{\underline{B}}{\underline{B} \cdot \underline{B}} \right)\tag{1.9}$$

where p, ν and q are respectively the particle's momentum, speed and charge. See Isenberg and Jokipii (1979) for a complete derivation of the form of the drift velocity given in equation (1.9). This paper also gives references to work which treat this drift as the anti-symmetric part of the diffusion tensor.

In the spherical polar coordinate system described in Section 1.1,

$$\begin{aligned}\underline{K} &= \begin{pmatrix} K_{rr} & K_{r\theta} & K_{r\phi} \\ K_{\theta r} & K_{\theta\theta} & K_{\theta\phi} \\ K_{\phi r} & K_{\phi\theta} & K_{\phi\phi} \end{pmatrix} \\ &= \begin{pmatrix} \cos \psi & 0 & \sin \psi \\ 0 & 1 & 0 \\ -\sin \psi & 0 & \cos \psi \end{pmatrix} \begin{pmatrix} K_{//} & 0 & 0 \\ 0 & K_{\perp} & K^A \\ 0 & -K^A & K_{\perp} \end{pmatrix} \begin{pmatrix} \cos \psi & 0 & -\sin \psi \\ 0 & 1 & 0 \\ \sin \psi & 0 & \cos \psi \end{pmatrix}\end{aligned}\tag{1.10}$$

where ψ is the angle between \underline{B} and \underline{r} , given by equation (1.17).

It is generally accepted (eg: Jokipii 1971, Gleeson and Webb 1980, Potgieter 1984) that, for particles with energies around 1 GeV and above, the parallel and perpendicular diffusion coefficients are of one of the forms:

$$K_{\parallel} = K_0 \beta P^{\alpha} \left(\frac{|\underline{B}_e|}{|\underline{B}|} \right)^{\eta} \quad \alpha \in \left(\frac{1}{2}, 2 \right), \quad \eta \in \left(\frac{1}{2}, 1 \right) \quad (1.11a)$$

or alternatively,

$$K_0 \beta P^{\alpha} \left(1 + \left(\frac{r}{r_e} \right)^{\nu} \right) \quad \nu \in (1, 4) \quad (1.11b)$$

$$K_{\perp} \approx \mu K_{\parallel} \quad \mu \in (0.01, 0.1) \quad (1.12)$$

where \underline{B}_e and r_e are respectively the magnetic field and radial position at Earth; β is the ratio of the speed of the particle to the speed of light; and P is the *rigidity* of the particle, a measure of its relativistic momentum per unit charge:

$$P = \frac{pc}{q} \quad (1.13)$$

The diffusion coefficient is the least known parameter of any of those which define the state of the heliosphere. It will be seen (Chapter 4) that the functional form of the parallel and perpendicular diffusion coefficients significantly affects the solutions obtained for f near Earth. Palmer (1982) estimated the parallel mean-free-path of galactic cosmic rays in the vicinity of the Earth to be between 0.08 and 0.3 AU (astronomical units) over a wide energy range up to 5 GeV. This gives an estimate of the value of K_{\parallel} (equation 1.11) to be around $10^{18} \text{ m}^2\text{s}^{-1}$.

1.3b. The Solar Wind:

A first approximation to the solar wind velocity is given by

$$\underline{V}_{sw} = U(r) \hat{r} \quad (1.14)$$

where

$$U(r) = \begin{cases} 4 \times 10^5 \text{ m} \cdot \text{s}^{-1} & r < r_{sh} \\ 1 \times 10^5 \left(\frac{r_{sh}}{r} \right)^2 \text{ m} \cdot \text{s}^{-1} & r \geq r_{sh} \end{cases} \quad (1.15)$$

Here, r_{sh} denotes the radial position of the termination shock in the solar wind (see Jokipii 1986). It is seen from (for example) Nagashima *et al.* 1988 that $|\underline{V}_{sw}|$ varies between around 300 and 700 km s^{-1} with an average value around 400 km s^{-1} in the ecliptic plane. The solar wind increases with increasing heliographic latitude, plateauing at about 500-600 km s^{-1} at around $\pm 60^\circ$ (Newkirk and Fisk 1985, Sheeley *et al.* 1991). It turns out that values of the distribution function derived by solving the transport equation are insensitive to $|\underline{V}_{sw}|$ in the range ~ 350 -600 km s^{-1} for a spherically symmetric wind. A latitude varying

wind was not used in any of the models in this thesis. Most of the models solve the transport equation in solar minimum conditions where the approximation to V_{sw} by equation 1.14 is adequate.

1.3c. The Magnetic Field:

Parker (1958) was the first to predict that the magnetic field forms an Archimedean spiral structure in the heliosphere. See also Gleeson and Webb (1980) and Jokipii and Thomas (1981) for a discussion on the form of the heliospheric magnetic field. The field is frozen into the solar wind plasma and drawn out radially with this wind as the Sun rotates. The so-called Parker spiral field is described by the equation:

$$\underline{B} = \frac{B_0}{r^2} (\underline{\hat{r}} - \Gamma \underline{\hat{\phi}}) (1 - 2S(\zeta)) \quad (1.16)$$

where B_0 is a constant which can be obtained by noting that $|\underline{B}|$ is roughly 5 nT at Earth. Also,

$$\Gamma = \tan \psi = \frac{r \Omega \sin \theta}{U(r)} \quad (1.17)$$

$$S(\zeta) = \begin{cases} 1 & \zeta \geq 0 \\ 0 & \zeta < 0 \end{cases} \quad (1.18)$$

and

$$\zeta = \theta - \frac{\pi}{2} - \alpha \sin \left(\phi - \frac{r\Omega}{U(r)} \right) \quad (1.19)$$

for small α . Equation (1.19) denotes the structure of the *neutral sheet*. α is the *tilt angle*. The neutral sheet is the locus of points in space (a smooth warped sheet structure) which separates regions in space where the radial component of the magnetic field points toward the Sun and regions where the field points away from the Sun. It is fully described in Chapter 6. Jokipii and Kota (1989) add a modification to the standard spiral field which has, predominantly, the effect of changing $|\underline{B}|$ near the poles of the heliosphere. The modification attempts to model randomly orientated fields which may dominate at the poles. This modification, the details of which are described in the above reference, has been used when evaluating the magnitude of the magnetic field for the numerical models which derive f in this thesis.

1.3d. The Streaming Vector:

The *streaming* of cosmic rays \underline{S} (as opposed to the intensity) is a measure of the *flow* of cosmic rays in a particular direction. Hence it is a vector quantity. The streaming is generally defined such that the net flow of particles crossing a surface element $d\underline{A}$, at position \underline{x} and time t with momentum in the range p to $p+dp$ is $d\underline{A} \cdot \underline{S}(\underline{x}, p, t) dp$. With this definition, Gleeson and Webb (1980) (for example) show that the streaming vector can be written in terms of the number density ($U=4\pi p^2 f$) as

$$\underline{S} = C \underline{V}_{sw} U - \underline{K} \cdot \nabla U \quad (1.20)$$

where C is a coefficient describing the so-called Compton-Getting effect (Compton and Getting 1935) and is given by

$$\begin{aligned} C &= 1 - \frac{1}{3U} \frac{\partial}{\partial p}(pU) \\ &= -\frac{1}{3} \frac{\partial \ln f}{\partial \ln p} \end{aligned} \quad (1.21)$$

and \underline{K} is the *full* diffusion tensor. In terms of the distribution function,

$$\underline{S} = 4\pi p^2 \left(-\underline{K} \cdot \nabla f - \frac{\underline{V}_{sw}}{3} \frac{\partial f}{\partial \ln p} \right) \quad (1.22)$$

1.3e. The Anisotropy Vector:

The anisotropy vector ξ is a measure of the fractional departure of the intensity of cosmic rays from isotropy. Again, see Gleeson and Webb (1980) for a full derivation and justification of the form of ξ . If the intensity distribution is almost isotropic, then ξ is adequately given by

$$\xi = \frac{3\underline{S}}{4\pi v p^2 f} \quad (1.23)$$

This vector will be important in deriving the correct theoretical expression for the north-south anisotropy in Chapter 8.

1.4 MODELS

As no analytical solution exists for the general transport equation, numerical techniques are employed to solve for f under pre-specified (and generally idealized) heliospheric conditions. Stable numerical codes used in solving multidimensional partial differential equations are generally very computationally intensive. Solutions given by Kota and Jokipii (1991a, 1991b) are the only examples of three-space dimensional time-dependent solutions for f . Other authors have solved f in one or two space dimensions, or time-independent three space dimensions (eg: Kota and Jokipii 1983, Perko and Fisk 1983, Potgieter and Moraal 1985, Kadokura and Nishida 1986).

There have been many reviews written on the current progress of the ability of increasingly complex models to simulate observational data. For example, see McKibben (1987), Forman (1987), Jokipii (1989), Simpson (1989) or Fluckiger (1991). The general consensus is that there are two principal model types, which assign the major modulation features of the 11 year cycle of galactic cosmic ray intensity to different causes. The first model type assigns the primary cause of the 11 year modulation to a superposition of the

effects of propagating disturbances in the solar wind / heliospheric magnetic field and the second model assigns the primary cause of this, and other modulation effects, to variations in gradient and curvature drifts experienced by the cosmic rays in the heliospheric magnetic field. Some models are being developed which incorporate both effects in a time-dependent manner in order to ascertain the major cause of the various observed modulation effects. Ultimately, computer resources place limits on the complexity of models able to be solved. Proponents of the first type of model suggest that the 11 year cycle of integral galactic cosmic ray intensity can be accurately simulated by a one-dimensional spherically symmetric model of the heliosphere including enhanced regions of magnetic scattering either co-rotating with the Sun, as in corotating interaction regions (CIR's), or propagating radially from the Sun, caused by coronal mass ejections and shock waves produced by solar flares (eg: Perko and Fisk 1983, Perko and Burlaga 1987). These regions increase in frequency or spatial extent from solar minimum to solar maximum and have the effect of inhibiting the cosmic rays from entering the inner heliosphere. Perko and Burlaga (1992) suggest that the 11 year cycle is caused by strong particle diffusion inside long lived merged interaction regions (combined CIR's). They suggest that their one-dimensional model is sufficient to explain the 11 year cosmic ray cycle and that drift effects are secondary and most noticeable around solar minimum, when modulation is minimal. See also Burlaga *et al.* (1985). Note that the above authors are modelling the *integral* cosmic ray intensity above about 70 MeV - the energy range of particles detected by telescopes on board spacecraft (eg: Voyager 1 and 2, Pioneer 10 and 11). Thomas and Gall (1982) simulated the effects of CIR's and found that these greatly perturbed the drift pattern anticipated for simple fields. They concluded that the expected streaming produced from drift effects no longer applied in the presence of these modulating regions. Recently, Burlaga *et al.* (1991) presented observational evidence which support the idea that drifts may be important in areas of the heliosphere away from merged interaction regions.

On the other hand, proponents of the second type of model suggest that the major modulation features are drift-dominated. For example, Kota and Jokipii (1991b) suggested from their highly complex three-space dimensional model that regions of stronger magnetic field (eg: CIR's) resulted in rapid *local* decreases of the cosmic ray flux, but that fluctuations in the diffusion tensor (caused by these regions) only weakly affected the global modulation - which was drift dominated. Other proponents of the drift model include, for example, Potgieter *et al.* (1987, 1989) and Smith (1990).

Although a two-space dimensional model with drift and perpendicular diffusion is the minimum level of complexity required to explain such effects as latitudinal gradients and the asymmetry in the temporal cosmic ray intensity profile between successive solar cycles of opposite magnetic polarity, the question is whether they are necessary to explain the global modulation pattern. It is most probably the case that the various modulation processes vary in their relative importance at different energies. Diffusion / scattering probably dominates at low energies and large scale drift probably dominates at higher energies. To suggest that the integral intensity is governed predominantly by one process is most likely too simplistic an approach. Indeed, at least two processes of equal importance are required to ensure a steady state solution other than the two extreme solutions: $f=0$, or f =galactic-distribution everywhere in the heliosphere. What would resolve many discrepancies would be spacecraft observations of differential intensity throughout the heliosphere. However, the practical problems involved in building a detector for spacecraft use which completely shields particles of energies up to tens of GeV are insurmountable at present.

The solutions for the distribution function given in the above references are generally for particle energies below about 5 GeV, and the value of f in the vicinity of the Earth (at 1 AU from the Sun) has not been well-specified. Kota for example remarked that results from a three-space dimensional model (Kota 1990) were inaccurate at radii less than 2-3 AU and thus could not be directly compared with observed radial gradients at Earth. Other results, for example Kadokura and Nishida (1986) and Potgieter et al. (1989), also predict a radial gradient at the position of Earth much larger than is likely from terrestrial based observation. They conclude that this is due to inappropriate diffusion coefficients and inner boundary conditions. It will be seen in the solutions presented in Chapter 4 that the radial gradient of the integral cosmic ray intensity remains low throughout the heliosphere. This remains true even at radial distances of less than 1 AU from the Sun, as long as a floating (rather than fixed) inner boundary condition and certain diffusion coefficients are used. In contrast with comments made by Kota (1990), the accuracy of the determined distribution function and radial gradient at 1 AU does not suffer greatly from using a sparse grid.

1.5 OBSERVATIONS

Early spacecraft observations of the radial gradient of cosmic rays were restricted to regions between the orbits of Venus and Mars. According to O'Gallagher (1972), by 1972 there had been 22 spacecraft measurements of g_r . These measurements were mainly for particle energies much lower than can be observed by ground-based detectors, however it is interesting to note that results for g_r in the MeV region ranged from $-350\% \text{ AU}^{-1}$ to $+500\% \text{ AU}^{-1}$ and most commonly a null-result with large errors was found.

Problems which prevented a reliable result being obtained from spacecraft observations in the early period (1960-70's) included unreliable detector systems, inadequate methods for removing solar particle contamination and transient modulation and, perhaps most importantly, obtaining a comparable reference monitor to distinguish spatial variations from temporal variations. As an example of the latter, Neher and Anderson (1964) used an ionization chamber on board Mariner 2 and detected particles with energy above a threshold of $\sim 10 \text{ MeV}$ as the spacecraft travelled from Earth to Venus. Note that this is one of very few spacecraft that have made direct measurements of galactic cosmic rays on the Sun-ward side of the Earth. They used neutron monitors at Deep River and Mt. Washington as a temporal baseline. From observing that the count-rate on board Mariner 2 remained constant for the journey while at the same time Earth-based detectors observed an increase in count-rate (due to solar-cycle variations), Neher and Anderson concluded that g_r must be $12 \pm 4\% \text{ AU}^{-1}$ at 1 AU in the detected energy range. As a comparison, O'Gallagher and Simpson (1967) obtained a value for g_r of $9.6 \pm 0.9\% \text{ AU}^{-1}$ from measurements taken on board Mariner 4 on its journey to the orbit of Mars. These measurements were taken in solar minimum conditions and they estimated that the mean energy observed was 6 GeV - comparable with neutron monitor energies.

Several recent papers report on observations of temporal and spatial variations in the integral cosmic ray intensity and gradients measured using spacecraft data (eg: Lopate and Simpson 1991, Webber and Lockwood 1991, McDonald *et al.* 1992). Spacecraft are now distributed throughout the heliosphere to near 60 AU. At present however, there are still only a handful of such detectors and they are all (with the exception of Ulysses)

concentrated near the heliographic equator (see Parthasarathy and King 1991). One of the drawbacks of spacecraft measurements is that the observations are generally for particles with energies above a small threshold. There is no way of determining differential information, for example, what the average value of g_r is for particles in the energy range 1-10 GeV or 10-100 GeV etc.. In fact, ground-based particle detectors are currently the only method for determining the intensity distribution of galactic cosmic rays near the Earth for particles above ~ 10 GeV (see McKibben, 1987).

From spacecraft measurements, it is known that there exists a positive radial gradient of cosmic rays near the heliographic equator. That is, there are fewer galactic cosmic ray particles on the Sun-ward side of the Earth than beyond 1 AU. Fillius (1989) gives an excellent review of spacecraft observations of the radial gradient. IMP 8, Pioneer 10 & 11, Voyager 1 & 2 have all made observations of g_r . The instruments on board detect particles with energies above some threshold (about 70 MeV) and so data obtained are for an integral spectrum with mean energy around 2 GeV. The general consensus from these spacecraft observations is that the gradient is remarkably spatially constant out to about 30 AU and has a value of about 2-3 % AU⁻¹. Webber and Lockwood (1991) for example report that the radial gradient changes from 1.5 to 3% AU⁻¹ for negative polarity states of the heliospheric magnetic field and is temporally constant at 3% AU⁻¹ for positive polarity states. Note however that these spacecraft have not made detailed measurements of g_r for heliocentric radii less than 1-2 AU.

Values of g_r measured by ground-based telescopes using a north-south anisotropy analysis are presented in Chapter 8.

Chapter 2. Numerical Methods.

2.1. INTRODUCTION

In this chapter the numerical methods employed to solve the transport equation under pre-specified heliospheric conditions are discussed. These methods are commonly employed, in one form or another, by those who attempt to solve multidimensional partial differential equations.

The galactic cosmic ray intensity everywhere in the heliosphere is theoretically completely determined via the solution to the transport equation, given two things. Firstly, that the *state* of the heliosphere is completely specified. This means that the sun's magnetic field, the solar wind and the diffusion coefficients are pre-determinable at every point in the heliosphere. Secondly, that the boundary conditions in all variables are also completely specified. It will be seen in Chapter 4 that an inability to accurately specify these boundary conditions, especially the inner-boundary condition in the radius coordinate, inevitably leads to an inaccurate determination of the intensity distribution.

As is the case with most theoretical systems which aim to model phenomena in nature, solutions to the transport equation inevitably lack the accuracy required to completely explain all the phenomena detected by cosmic-ray monitors. Nature is generally too complicated to be completely and accurately specified. We are, in practice, also constrained by computer memory and speed. This means that the transport equation is solved in a simplified and idealistic heliosphere. Because an *analytic* solution to the transport equation has been found only under highly idealized conditions (for example, a spherically symmetric heliosphere), we are constrained to a *numerical* solution. The heliosphere is discretized into an n-dimensional grid - one dimension for each variable in the equation. The solution is found at each point on the grid. It is assumed that the solution is smooth and continuous between grid points. If this is the case, then interpolation routines can be used to determine the intensity distribution of the cosmic rays between grid points.

If the state of the heliosphere is time-dependent, then the full transport equation must be integrated in time from some pre-specified initial condition to a time of interest. An example of this is the case where it is of interest to determine the change in the galactic cosmic ray intensity distribution at Earth as a shock wave, emanating from the Sun, passes. In this case, the initial condition may be the steady-state solution ($\partial f / \partial t = 0$) and the transport equation is integrated in time from, for example, when the shock-wave first leaves the Sun until it is well past the Earth (say 5 AU).

If the steady-state solution is of interest, then either (a) the right-hand side of the transport equation (1.3) is solved, ie: $\partial f / \partial t$ is set to zero, or (b) the transport equation is integrated from some pre-specified initial condition under a steady-state heliosphere until $\partial f / \partial t$ becomes sufficiently small - ideally zero. The question of "how small is sufficiently small" is subjective and somewhat dependent on the specific details of the problem. A steady-state heliosphere is one where the sun's magnetic field, solar wind, and the diffusion coefficients are time-independent. This would be reflected in the time-independence of the coefficients of the derivatives of the distribution function in the transport equation. Under these conditions, an integration of the transport equation in time should converge - so long as the

integrating procedure is computationally stable. In practice, (b) above is chosen as the preferred path to the steady-state solution. It is computationally more straight-forward, except under one specific case. That is when the coefficient of $\partial f/\partial p$ is never zero in the heliosphere. In that case, it is easier to integrate with respect to momentum p , starting from the initial condition that the distribution function everywhere in the heliosphere is equal to the galactic value at the outer-boundary for a sufficiently high rigidity. If the coefficient of $\partial f/\partial p$ is zero then the equation to solve is elliptic and not parabolic. This would happen if the solar wind were spherically symmetric and had an inverse square dependence on radius as is the case normally associated with the conditions beyond a solar-wind termination shock. The solution methods given below are not applicable to this case. Difficulties with solutions to the elliptic equation are discussed below.

2.2. DISCRETIZING THE PARABOLIC EQUATION

Consider the problem of solving the full transport equation ($\partial f/\partial t \neq 0$). The equation is written as a difference equation on a finite grid. Initial and boundary conditions are specified for f at time $t = 0$. f is then solved for all points on the grid for $t = \Delta t$, a finite time interval. The distribution function is then solved at all points for incrementing timesteps of Δt using the solution at the previous timestep as the initial condition for the current timestep. If \underline{B} , \underline{V}_{sw} and \underline{K} are time-independent, then this iteration continues until the solution becomes sufficiently steady-state. The boundary conditions used in solving the transport equation are as follows. Firstly, the outer boundary of the heliosphere ($r = r_{max}$) is assumed to be spherically symmetric and a source of galactic cosmic rays with a pre-assumed spectrum. For other radius values along the polar axis ($\theta = 0, \pi$), smoothness and symmetry across this axis implies $\partial f/\partial \theta = 0$. If the azimuthal coordinate is included, then $f(\phi=0) = f(\phi=2\pi)$ is the boundary condition. It is assumed that $\partial^2 f/\partial p^2$ at each momentum boundary ($p=p_{min}$, $p=p_{max}$) is also zero. This condition is equivalent to requiring that the boundary value is a linear extrapolation of the values on the closest two grid points. If p_{max} is sufficiently large, then the upper-boundary condition for f in the momentum coordinate could be specified by requiring that no modulation occurs anywhere in the heliosphere at this momentum value. The values used for the upper-boundary of momentum in the model-runs of Chapter 4 corresponded to a particle rigidity of 10 GV. This is too low a value to assume no modulation. A number of different inner-boundary conditions ($r = r_{min}$) were tested and each will be discussed in Chapter 4. Some boundary conditions used by other authors include $f(r = r_{min}) = 0$ or $(\partial f/\partial r)_{r=r_{min}} = 0$ (see Chapter 4).

Specific notation is now introduced to describe the numerical methods employed to solve the transport equation. Let the discretized version of the transport equation (given by 1.3) be written as

$$\frac{\delta f}{\delta t} = \sum_{\alpha} \mathcal{L}_{\alpha} f \quad (2.1)$$

where the \mathcal{L}_{α} 's are difference operators acting on f , a separate operator for each coordinate. The discretized version of the idealized axially-symmetric transport equation is written as

$$\frac{\delta f}{\delta t} = (\mathcal{L}_r + \mathcal{L}_\theta + \mathcal{L}_p)f \quad (2.2)$$

where, for example, the difference operator corresponding to the radius coordinate is

$$\mathcal{L}_r = A_{rr} \frac{\delta^2}{\delta r^2} + A_r \frac{\delta}{\delta r} \quad (2.3)$$

A_r and A_{rr} are position dependent, time independent coefficients. $\delta/\delta r$ and $\delta^2/\delta r^2$ are the difference operators corresponding to first and second derivatives with respect to r .

To explain the numerical concepts behind the integrating routines applied to the transport equation, it is appropriate to firstly consider the case of a simple one-dimensional partial differential equation. The discretized notation for the equation

$$\frac{\partial f}{\partial t} = \frac{\partial^2 f}{\partial x^2} \quad (2.4)$$

evaluated at (t, x) would be written as

$$\left. \frac{\delta f}{\delta t} \right|_{t,x} = \mathcal{L}_x f_{t,x} \quad \text{where} \quad \mathcal{L}_x = \frac{\delta^2}{\delta x^2} \quad (2.5)$$

On a one dimensional grid where $x = i\Delta x$, $i=0\dots I$,

$$\frac{f_{t+\Delta t,i} - f_{t,i}}{\Delta t} = \frac{f_{t,i+1} - 2f_{t,i} + f_{t,i-1}}{(\Delta x)^2} \quad (2.6)$$

is the central-difference form of $\mathcal{L}_x f$ at time t . This difference equation is an approximation to the continuous differential equation and is derived by considering the Taylor series expansion of f about the point x . Such expansions and their accuracy are discussed in Chapter 3.

As can be seen, if f is known at all points i at time t , then it is a trivial task to derive f at all points i for time $t+\Delta t$ through equation 2.6. In practice, if this is being done on a computer, then depending on the relative sizes of Δt and Δx , after not too many iterations (generally far fewer than is required to fully solve the equation), computer round-off errors can accumulate and the solution can become more and more inaccurate and eventually diverge to infinity. If this occurs, then the difference approximation to the partial differential equation is said to be unstable. The question of stability is addressed in Chapter 3. It will be shown that instead of equation (2.5), the difference approximation

$$\left. \frac{\delta f}{\delta t} \right|_{t,x} = \lambda \cdot \mathcal{L}_x f_{t+\Delta t,x} + (1-\lambda) \cdot \mathcal{L}_x f_{t,x} \quad (2.7)$$

where $\lambda \in [0.5, 1]$, is stable for any choice of Δt or Δx . The first term on the right hand side of this equation denotes the difference operator acting on the value of f at the *next* timestep. In full,

$$\begin{aligned} \frac{f_{t+\Delta t, i} - f_{t, i}}{\Delta t} = & \lambda \cdot \left(\frac{f_{t+\Delta t, i+1} - 2f_{t+\Delta t, i} + f_{t+\Delta t, i-1}}{(\Delta x)^2} \right) \\ & + (1-\lambda) \cdot \left(\frac{f_{t, i+1} - 2f_{t, i} + f_{t, i-1}}{(\Delta x)^2} \right) \end{aligned} \quad (2.8)$$

This is known as an implicit difference formula since the value of f at $t+\Delta t$ is written as a function of other values of f at the next timestep. Equation (2.8) as it stands is a single equation in three unknowns, namely $f_{t+\Delta t, i+1}$, $f_{t+\Delta t, i}$ and $f_{t+\Delta t, i-1}$. The full set of equations given by (2.8) for each $i=1 \dots I-1$ form a complete set if the boundary values $f_{t+\Delta t, i=0}$ and $f_{t+\Delta t, i=I}$ are pre-specified.

Specific difference equations and numerical solutions for the transport equation are now addressed. Unless otherwise stated, it may be assumed (and is proven in Chapter 3) that the difference approximations given here are computationally stable. The different algorithms are demonstrated on the axially-symmetric ($f = f(r, \theta, p, t)$) transport equation. Such implicit integrating routines for parabolic partial differential equations are described, for example, in Chapter 4 of Lapidus and Pinder (1982). The Alternating-Direction-Implicit (ADI) and Locally-One-Dimensional (LOD) routines are applied to equation (2.2). The philosophy behind these routines is that they attempt to integrate the multi-dimensional problem through a series of steps - each step being a one-dimensional integration in time. Implicit routines such as these are generally required to ensure computational stability (as demonstrated in Chapter 3). The fully explicit integrating algorithm and its limitations are discussed later in this chapter.

2.3. IMPLICIT INTEGRATING METHODS

Following Lapidus and Pinder (1982), the steps which take f from time t to time $t+\Delta t$ using the ADI method can be written as:

$$\frac{f_{t+\frac{\Delta t}{3}} - f_t}{\Delta t} = \frac{1}{2} \left(\mathcal{L}_r f_{t+\frac{\Delta t}{3}} + \mathcal{L}_r f_t \right) + \mathcal{L}_\theta f_t + \mathcal{L}_p f_t \quad (2.9A)$$

$$\frac{f_{t+\frac{2\Delta t}{3}} - f_{t+\frac{\Delta t}{3}}}{\Delta t} = \frac{1}{2} \left(\mathcal{L}_r f_{t+\frac{\Delta t}{3}} + \mathcal{L}_r f_{t+\frac{2\Delta t}{3}} \right) + \frac{1}{2} \left(\mathcal{L}_\theta f_{t+\frac{2\Delta t}{3}} + \mathcal{L}_\theta f_{t+\frac{\Delta t}{3}} \right) + \mathcal{L}_p f_{t+\frac{\Delta t}{3}} \quad (2.9B)$$

$$\begin{aligned} \frac{f_{t+\Delta t} - f_{t+\frac{2\Delta t}{3}}}{\Delta t} = & \frac{1}{2} \left(\mathcal{L}_r f_{t+\frac{\Delta t}{3}} + \mathcal{L}_r f_{t+\frac{2\Delta t}{3}} \right) + \frac{1}{2} \left(\mathcal{L}_\theta f_{t+\frac{2\Delta t}{3}} + \mathcal{L}_\theta f_{t+\frac{\Delta t}{3}} \right) \\ & + \frac{1}{2} \left(\mathcal{L}_p f_{t+\Delta t} + \mathcal{L}_p f_{t+\frac{2\Delta t}{3}} \right) \end{aligned} \quad (2.9C)$$

Equation (2.9C) is the so-called *combined* ADI form and takes f from t to $t+\Delta t$ directly. However, the intermediate values $f_{t+\Delta t/3}$ and $f_{t+2\Delta t/3}$ must be fully solved in order to use this equation. In practice, two other steps are used in place of (2.9B) and (2.9C) and are derived by subtracting (2.9A) and (2.9B) from (2.9C). They are

$$\frac{f_{t+\frac{2\Delta t}{3}} - f_{t+\frac{\Delta t}{3}}}{\Delta t} = \frac{1}{2} \left(\mathcal{L}_\theta f_{t+\frac{2\Delta t}{3}} - \mathcal{L}_\theta f_t \right) \quad (2.9B^*)$$

$$\frac{f_{t+\Delta t} - f_{t+\frac{2\Delta t}{3}}}{\Delta t} = \frac{1}{2} \left(\mathcal{L}_p f_{t+\Delta t} - \mathcal{L}_p f_t \right) \quad (2.9C^*)$$

The steps which take f from time t to time $t+\Delta t$ using the LOD method are:

$$\frac{f_{t+\frac{\Delta t}{3}} - f_t}{\Delta t} = \lambda \cdot \mathcal{L}_r f_{t+\frac{\Delta t}{3}} + (1-\lambda) \cdot \mathcal{L}_r f_t \quad (2.10A)$$

$$\frac{f_{t+\frac{2\Delta t}{3}} - f_{t+\frac{\Delta t}{3}}}{\Delta t} = \lambda \cdot \mathcal{L}_\theta f_{t+\frac{2\Delta t}{3}} + (1-\lambda) \cdot \mathcal{L}_\theta f_{t+\frac{\Delta t}{3}} \quad (2.10B)$$

$$\frac{f_{t+\Delta t} - f_{t+\frac{2\Delta t}{3}}}{\Delta t} = \lambda \cdot \mathcal{L}_p f_{t+\Delta t} + (1-\lambda) \cdot \mathcal{L}_p f_{t+\frac{2\Delta t}{3}} \quad (2.10C)$$

λ is a parameter. To ensure stability, $\lambda \in [0.5, 1]$. The combined LOD formula is then

$$\begin{aligned} \frac{f_{t+\Delta t} - f_t}{\Delta t} &= \lambda \cdot \left(\mathcal{L}_r f_{t+\frac{\Delta t}{3}} + \mathcal{L}_\theta f_{t+\frac{2\Delta t}{3}} + \mathcal{L}_p f_{t+\Delta t} \right) \\ &\quad + (1-\lambda) \cdot \left(\mathcal{L}_r f_t + \mathcal{L}_\theta f_{t+\frac{\Delta t}{3}} + \mathcal{L}_p f_{t+\frac{2\Delta t}{3}} \right) \end{aligned} \quad (2.11)$$

The actual method of using these algorithms is now explained. Consider the discretized grid for the axially symmetric heliosphere. Let

$$\begin{aligned} r &= i(\Delta r) + r_{\min}, & i &= 0 \dots I \\ \theta &= j(\Delta \theta), & j &= 0 \dots J \\ p &= k(\Delta p) + p_{\min}, & k &= 0 \dots K \end{aligned} \quad (2.12)$$

such that $f(t, r, \theta, p) = f_{t, i, j, k}$. Consider each ADI or LOD step in turn. For each j and each k the system of equations given by (2.9A) or (2.10A) for $i=0 \dots I$ is solved. This gives $f_{t+\Delta t/3}$ at every grid point (i, j, k) . For each i and each k the system of equations given by (2.9B*) or (2.10B) for $j=0 \dots J$ is solved. This gives $f_{t+2\Delta t/3}$ at every (i, j, k) . For each i and each j the system of equations given by (2.9C*) or (2.10C) for $k=0 \dots K$ is solved giving $f_{t+\Delta t}$ at every (i, j, k) . The whole procedure is repeated for the next timestep using the new result at the current timestep as the initial condition. Note that the boundary values

for the current timestep must be specified before each integration step. Note also that if the boundary values are time-dependent, then allowance for this fact must be made at the intermediate values $f_{t+\Delta t/3}$ and $f_{t+2\Delta t/3}$. The boundary values are able to be specified by applying the partial differential equation to the known boundary values at the current and next timestep. This case is discussed in Gourlay and Mitchell (1972). Fortunately, it is not expected (at least on timescales short compared with the solar cycle) that the boundary values for the transport equation are time dependent and so allowance for this possibility is not required.

As an example of each step, consider equation (2.10A) for $\lambda = 1$ in full detail. Assume, for example, that

$$\mathcal{L}_r = A_r \frac{\delta}{\delta r} + A_{rr} \frac{\delta^2}{\delta r^2} \quad (2.13)$$

corresponding to

$$\frac{\partial f}{\partial t} = A_r \frac{\partial f}{\partial r} + A_{rr} \frac{\partial^2 f}{\partial r^2} + \dots \quad (2.14)$$

Assuming also that the coefficients A_r and A_{rr} are functions of (r, θ, p) but not time, then this LOD step, in full, is given by

$$\begin{aligned} \frac{f_{t+\frac{\Delta t}{3},i,j,k} - f_{t,i,j,k}}{\Delta t} &= \frac{(A_{rr})_{i,j,k}}{(\Delta r)^2} \cdot \left[f_{t+\frac{\Delta t}{3},i+1,j,k} - 2f_{t+\frac{\Delta t}{3},i,j,k} + f_{t+\frac{\Delta t}{3},i-1,j,k} \right] \\ &\quad + \frac{(A_r)_{i,j,k}}{(2\Delta r)} \cdot \left[f_{t+\frac{\Delta t}{3},i+1,j,k} - f_{t+\frac{\Delta t}{3},i-1,j,k} \right] \end{aligned} \quad (2.15)$$

for $i=0..I$. Other difference formulae may be used to represent the discrete version of the first and second partial derivatives. The advantage of using the central-difference formulae in (2.15) is that this system of equations (for all i) can be written as

$$a_i \left(f_{t+\frac{\Delta t}{3},i-1,j,k} \right) + b_i \left(f_{t+\frac{\Delta t}{3},i,j,k} \right) + c_i \left(f_{t+\frac{\Delta t}{3},i+1,j,k} \right) = d_i \quad i = 1 \dots I-1 \quad (2.16)$$

where

$$a_i = (\Delta t) \cdot \left(-\frac{(A_{rr})_{i,j,k}}{(\Delta r)^2} + \frac{(A_r)_{i,j,k}}{(2\Delta r)} \right)$$

$$b_i = \left(1 + \frac{2(\Delta t) \cdot (A_{rr})_{i,j,k}}{(\Delta r)^2} \right)$$

$$c_i = (\Delta t) \cdot \left(-\frac{(A_{rr})_{i,j,k}}{(\Delta r)^2} - \frac{(A_r)_{i,j,k}}{(2\Delta r)} \right) \quad (2.17)$$

$$d_i = f_{t,i,j,k}$$

whereby it is seen that equation (2.16) exactly describes the tri-diagonal matrix system:

$$\underline{T} \cdot \underline{f} = \underline{d} \quad (2.18)$$

where

$$\underline{T} = \begin{pmatrix} b_1 & c_1 & & & \\ a_2 & b_2 & c_2 & & \\ & a_3 & b_3 & c_3 & \\ & & \ddots & \ddots & \\ & & & a_{I-3} & b_{I-3} & c_{I-3} \\ & & & & a_{I-2} & b_{I-2} & c_{I-2} \\ & & & & & a_{I-1} & b_{I-1} \end{pmatrix} \quad (2.19)$$

$$\underline{f} = \begin{pmatrix} f_{t+\frac{\Delta t}{3},1,j,k} \\ f_{t+\frac{\Delta t}{3},2,j,k} \\ \vdots \\ \vdots \\ f_{t+\frac{\Delta t}{3},I-2,j,k} \\ f_{t+\frac{\Delta t}{3},I-1,j,k} \end{pmatrix} \quad (2.20)$$

$$\underline{d} = \begin{pmatrix} d_1 - a_1 f_{t+\frac{\Delta t}{3},0,j,k} \\ d_2 \\ \vdots \\ \vdots \\ d_{I-2} \\ d_{I-1} - c_{I-1} f_{t+\frac{\Delta t}{3},I,j,k} \end{pmatrix} \quad (2.21)$$

Lapidus and Pinder (1982, Chapter 4) or Press *et al.* (1986, Chapter 2) give routines which solve the tri-diagonal system easily. In essence, the solution consists of two steps:

$$\begin{aligned}\underline{\underline{T_L}} \cdot \underline{\underline{s}} &= \underline{\underline{d}} \\ \underline{\underline{T_U}} \cdot \underline{\underline{f}} &= \underline{\underline{s}}\end{aligned}\tag{2.22}$$

where

$$\underline{\underline{T}} = \underline{\underline{T_L}} \cdot \underline{\underline{T_U}}\tag{2.23}$$

is the LU decomposition of the matrix. T_L and T_U are lower and upper-triangular matrices respectively.

2.4. EXPLICIT INTEGRATING METHOD

Explicit finite difference algorithms run much faster per integration timestep on a computer than implicit schemes. The nested systems of equations required to be solved for the implicit schemes are replaced in the explicit scheme by a single one-line statement taking f from t to $t+\Delta t$ at each grid point (i,j,k) :

$$\frac{f_{t+\Delta t} - f_t}{\Delta t} = (\mathcal{L}_r + \mathcal{L}_\theta + \mathcal{L}_p) f_t\tag{2.24}$$

such that the difference operators act only on the value of f at time t . This is equivalent to the combined LOD algorithm where $\lambda=0$ (to order Δt accuracy). As mentioned previously however, explicit algorithms are only computationally stable for a subset of values of $(\Delta t) \leq \tau_{max}$ (for a given set of grid element sizes $\Delta r, \Delta \theta, \Delta p$). For the case of the axially symmetric transport equation, it will be shown in Chapter 4 that even though each integration step is faster to compute for the explicit algorithm, constraints on (Δt) to ensure computational stability are such that it is far quicker computationally to fully-integrate the transport equation (to steady-state for example) using an implicit scheme.

At this point, mention should be made as to why the elliptic equation $\partial f / \partial t = 0$ is not solved directly if the final result required is the steady-state solution. It is because (apart from the case where the coefficient of $\partial f / \partial p$ is non-zero everywhere and the equation can be integrated with respect to the momentum coordinate) the equation requires explicit boundary conditions and no initial conditions. The partial differential equation must be solved at every point in the heliosphere $f_{i,j,k}$, $i=0\dots I$, $j=0\dots J$, $k=0\dots K$, at the one time. Even though the matrix system would be sparse, it would nevertheless *not* be upper or lower triangular. Hence, given that each coordinate may have anywhere between 10 and 100+ grid points (depending on the the accuracy of the solution required), the system of equations would be too large to be computationally solvable in practice.

2.5. NUMERICAL EVALUATION OF \underline{V}_D

The components of the drift velocity \underline{V}_D in three dimensional space are given by:

$$(\underline{V}_D)_r = \left(\frac{pv}{3q} \right) \cdot \left(\frac{1}{r \sin \theta} \right) \cdot \frac{\partial}{\partial \theta} (\sin \theta A_\phi) \quad (2.25)$$

$$(\underline{V}_D)_\theta = \left(\frac{pv}{3q} \right) \cdot \left[\left(\frac{1}{r \sin \theta} \right) \cdot \frac{\partial}{\partial \phi} (A_r) - \frac{1}{r} \frac{\partial}{\partial r} (r A_\phi) \right] \quad (2.26)$$

$$(\underline{V}_D)_\phi = \left(\frac{pv}{3q} \right) \cdot \left[-\frac{1}{r} \left(\frac{\partial A_r}{\partial \theta} \right) \right] \quad (2.27)$$

where \underline{A} is expressed in terms of the sun's magnetic field as

$$\underline{A} = \left(\frac{\underline{B}}{\underline{B} \cdot \underline{B}} \right) = \frac{r^2}{B_0 (1 + \Gamma^2)} (\hat{r} - \Gamma \hat{\phi}) \cdot (1 - 2 S(\zeta)) \quad (2.28)$$

Γ and ζ are given by equations (1.17) and (1.19). It is seen that the analytical evaluation of the components of \underline{V}_D therefore contain a delta-function (since \underline{A} contains a step-function). The full analytical expression for the drift velocity, including delta-function, is shown in, for example, Jokipii and Thomas (1981). The delta-function arises solely from the fact that the magnetic field is modelled as a step function at the neutral sheet. In practice, there is a finite distance over which the field reverses, corresponding to the small but finite width of the neutral sheet. It is for this reason that \underline{V}_D is more appropriately evaluated through numerically differentiating the components of \underline{A} . The step-size for the numerical derivative should be representative of the distance over which the field reverses in practice. For example,

$$(\underline{V}_D)_\phi(r, \theta, \phi) = \left(\frac{-pv}{3qr} \right) \cdot \left[\frac{A_r(r, \theta + d\theta, \phi) - A_r(r, \theta - d\theta, \phi)}{2 d\theta} \right] \quad (2.29)$$

where $d\theta \ll \Delta\theta$, the grid step-size used in the numerical integration of the transport equation. Given that the expression for \underline{A} is analytic, we are free to evaluate it anywhere - not just on the grid points of the discretized heliosphere.

It will be seen that derivatives of some of the components of the diffusion tensor will be required in order to evaluate the coefficients of the discretized transport equation. Such derivatives are most easily obtained again via the numerical approach above.

Chapter 3. Stability Analysis.

3.1. INTRODUCTION

When implementing the algorithms described in the previous chapter for solving the transport equation, practical problems associated with the discrete representation of real numbers and partial derivatives on a computer are introduced. In this chapter, these practical limitations are explored and their relevance to the model solutions in Chapter 4 are discussed.

The model partial differential equation (PDE) is described by a difference equation on a finite grid. It is hoped that the numerical solution to the difference equation converges and also that it converges to the "true" solution represented by the PDE. A particular solution to a finite difference equation that converges is said to be *stable*. One that converges to the true solution is said to be *consistent*. A finite difference solution to a PDE is therefore successful if it is consistent. Note that an unsuccessful solution may be stable but not consistent, or of course neither consistent nor stable.

The approximation to a partial differential equation by a finite difference equation invariably has a *truncation* error associated with it which is generally proportional to the grid-spacing over which the finite differencing is taking place. The finite difference equation is consistent with the model PDE if all the truncation errors associated with the difference equation approach zero as the gridsize goes to zero.

An integrating technique used to numerically solve the finite difference equation is stable if round-off errors associated with the computations (eg: round-off errors in the computer) do not grow as the computation proceeds. A useful method to test stability is known as von Neumann analysis. This method was first introduced by O'Brien *et al.* (1950). Applications of the analysis for various integrating schemes can also be found in Lapidus and Pinder (1982).

The following section first addresses the question of consistency for the finite difference representations used for the transport equation. A summary of the theory of von Neumann analysis is then presented. This method is then applied in subsequent sections to the various finite difference representations and integrating techniques used in the solution to the transport equation presented in Chapter 2.

3.2. THEORY

Consider the one-space dimensional function $U(t,x)$ on a uniform space-grid $x = ik$, $k=(\Delta x)$, $i=0,1,2, \dots, I$, with time $t=rh$, $h=(\Delta t)$, $r=0,1,2, \dots, R$. Let $U_{r,i}$ denote $U(rh,ik) = U(t,x)$. The Taylor-series expansion of U about $x+\Delta x$ and $x-\Delta x$ is:-

$$U_{i+1} = U_i + k U^x|_i + \frac{k^2}{2!} U^{xx}|_i + \frac{k^3}{3!} U^{xxx}|_i + \frac{k^4}{4!} U^{xxxx}|_i + \dots \quad (3.1)$$

$$U_{i-1} = U_i - k U^x|_i + \frac{k^2}{2!} U^{xx}|_i - \frac{k^3}{3!} U^{xxx}|_i + \frac{k^4}{4!} U^{xxxx}|_i + \dots \quad (3.2)$$

where $U^x|_i$ is $\frac{\partial U(t,x)}{\partial x}$ evaluated at $x = ik$, $U^{xx}|_i$ is $\frac{\partial^2 U(t,x)}{\partial x^2}$ evaluated at $x = ik$ and so on. The subscript r is not explicitly shown in the above equations because the expansion is for a fixed time t . The well-known finite-difference forms (to order k^2) for the first and second derivatives of U are found, with truncation error, from the difference and sum of the equations 3.1 and 3.2:-

$$U^x|_i = \frac{U_{i+1} - U_{i-1}}{2k} - \frac{k^2}{12} U^{xxx}|_{\xi_1} - \frac{k^2}{12} U^{xxx}|_{\xi_3} \quad (3.3)$$

$$U^{xx}|_i = \frac{U_{i+1} - 2U_i + U_{i-1}}{k^2} - \frac{k^2}{24} U^{xxxx}|_{\xi_2} - \frac{k^2}{24} U^{xxxx}|_{\xi_4} \quad (3.4)$$

where ξ_1, ξ_2 are in the range $(x, x+\Delta x)$ and ξ_3, ξ_4 are in the range $(x-\Delta x, x)$ (eg: see Arfken 1985). These difference forms are the ones used to represent the transport equation as a finite-difference equation. Note that in both (3.3) and (3.4) the error is proportional to k^2 , so as the grid spacing k approaches zero the finite difference approximation approaches the true derivative (ie: truncation error goes to zero). Such finite-difference representations are therefore consistent. Note however that if the truncation error is changed by $k\Phi$, where Φ is an arbitrary function of x , then the approximation is still consistent. Hence there are infinitely many consistent finite difference approximations to a partial derivative. The *accuracy* of a particular approximation is determined by the size of the total truncation error. In many cases it is difficult or even impossible to quantitatively determine the magnitude of the truncation error.

Consider now the von Neumann method of determining the stability of a finite-difference scheme. Note that all the solutions given in Chapter 2 to the transport equation are found by numerically integrating with respect to time. It is of interest to determine whether small errors introduced at some stage in the computing procedure by some round-off mechanism will propagate through the computation getting larger at each stage, or whether such errors will die out as the computation proceeds in time.

If the PDE is *linear* then any initial error will propagate according to the finite difference scheme. In other words, consider the partial differential equation $U^t = U^{xx}$. Let the corresponding difference equation be $\delta U / \delta t = \delta^2 U / \delta x^2$. If there is an error $E(t, x)$ associated with the solution to this finite difference equation then it can be shown (eg: O'Brien *et al.* 1950) that $\delta E / \delta t = \delta^2 E / \delta x^2$.

Von Neumann analysis relies on the fact that the error $E(t, x)$ in a finite difference scheme can be represented by

$$E(t, x) = e^{\gamma t} e^{j\beta x} \quad (3.5)$$

Here γ may be complex and a function of β , and $j=\sqrt{-1}$. Note that the discussion here is still restricted to one-space dimensional functions. Generalization to n-space dimensions is discussed later. In general, the true error in a finite difference scheme at (t,x) may be more complicated than the form given in (3.5). However complicated it may be though, it can be harmonically decomposed (via Fourier analysis) into terms each of the form given in (3.5). See Appendix 2 for further discussion. Since the PDE's of concern are linear, each term in the harmonic decomposition can be treated separately. The stability analysis is done on one representative term only. Since information on the values of β , ie: the spectrum of the error, may in practice be unattainable, only those integrating techniques whose stability criteria is independent of the choice of β should be used. In such cases, if it can be shown that one term in the Fourier series does not grow in time through the computational procedure, then no term will grow and the integrating technique will be stable. Note however that stability may be a function of grid spacing in the space or time direction.

Using the same grid notation as above, the error $E(t,x)$ can be written as

$$E(t,x) = e^{\gamma rh} e^{j\beta ki} \quad (3.6)$$

The *initial* error at time $t=0$ is simply $e^{j\beta ki}$. The integrating technique will be stable if

$$|e^{\gamma}| = |e^{\gamma rh}| \leq 1.0 \quad (3.7)$$

Then for all time t , the error E will be equal to or smaller than the initial error. Note that it is more convenient to test

$$|\xi| = |e^{\gamma h}| \leq 1.0 \quad (3.8)$$

It follows that if equation (3.8) holds then so does equation (3.7) because r is a positive integer. Following O'Brien *et al.* (1950) or Lapidus and Pinder (1982), ξ is found by substituting $E(t,x)$ given by equation (3.6) into the difference equation under consideration. If ξ satisfies equation (3.8) then the corresponding difference equation is stable. This procedure is applicable to testing whether errors introduced at any stage in the computation (other than $t=0$) will or will not grow. Because the equations under consideration are linear, a coordinate transformation $t'=(t-\alpha)$ can be made, where α corresponds to the time when the error is introduced. In this new t' frame, the stability analysis proceeds identically as above and the same criterion, namely $\xi \leq 1.0$ is required for stability. $|\xi|$ is often called the *amplification factor* for the difference scheme.

3.3. APPLICATION TO THE TRANSPORT EQUATION

3.3a. Stability for the LOD scheme (interior grid points):

Consider the LOD integrating scheme given in equation (2.11). Each step in the scheme is, as the name implies, one-dimensional and of the form:-

$$U^t = A(x) \cdot U^{xx} + B(x) \cdot U^x \quad (3.9)$$

where x is either the radius-transformed coordinate z (see equation 4.1), the polar-angle coordinate θ or the momentum coordinate p . U corresponds to the distribution function. Away from the boundaries of the space-grid, the corresponding fully-implicit difference equation used for a single LOD step was:-

$$\frac{U_{r+1,i} - U_{r,i}}{h} = A_i \frac{U_{r+1,i+1} - 2U_{r+1,i} + U_{r+1,i-1}}{k^2} + B_i \frac{U_{r+1,i+1} - U_{r+1,i-1}}{2k} \quad (3.10)$$

where $A_i = A(ik) = A(x)$ etc... Substituting $E(t,x)$ for $U(t,x)$ and dividing through by $e^{\gamma r h} e^{j\beta i k}$ gives

$$\xi - 1 = \rho_1 (\xi e^{j\beta k} - 2\xi + \xi e^{-j\beta k}) + \rho_2 (\xi e^{j\beta k} - \xi e^{-j\beta k}) \quad (3.11)$$

where

$$\rho_1 = A_i \frac{h}{k^2} \quad \text{and} \quad \rho_2 = B_i \frac{h}{2k} \quad (3.12)$$

Solving for ξ gives

$$\xi = \frac{1}{1 + 4\rho_1 \sin^2\left(\frac{\beta k}{2}\right) - 2j\rho_2 \sin(\beta k)} \quad (3.13)$$

The condition $|\xi| \leq 1.0$ for ξ given by this equation is satisfied when

$$8\rho_1 \sin^2\left(\frac{\beta k}{2}\right) + \left[4\rho_1 \sin^2\left(\frac{\beta k}{2}\right)\right]^2 + [2\rho_2 \sin(\beta k)]^2 \geq 0.0 \quad (3.14)$$

Since the last two terms of equation (3.14) are always positive and h , the gridsize in the time coordinate, is positive then equation (3.14) is satisfied when $A_i \geq 0$. Note that (3.14) may also hold for $A_i < 0$ over various domains of β , k , and h . These domains may in practice be impossible to completely specify. Hence to ensure the stability of the finite difference scheme given in equation (3.10) over all domains of β , k , and h , the coefficient $A(x)$ of the second derivative of the function is required to be *positive* over the region of x through which the integration is performed.

The full LOD integration scheme given by equation (2.11) consists of three integration steps, each one of the form given in equation (3.9). If each step is computationally stable, then the combined scheme (to step from t to $t+\Delta t$) will also be stable. This follows from the fact that the combined total amplification factor for a multi-stage integration scheme is the *product* of the amplification factors for each of the separate stages (see Lapidus and Pinder, 1982). One notable consequence of this fact is that if one of the stages is unstable then the combined three-stage integration procedure is not precluded from being stable. It is only required that the total amplification factor be less than or equal to one.

3.3b Explicit boundary points (LOD scheme):

Consider the difference equation for the partial differential equation given in (3.9) at the boundary of the space grid where the boundary value is specified at the *current* time step. That is, the boundary value is *explicitly*, rather than *implicitly*, specified. For completeness, the stability of both cases (explicit lower and upper boundary) is examined.

The difference scheme for an explicit lower boundary value is

$$\frac{U_{r+1,1} - U_{r,1}}{h} = A_1 \frac{U_{r+1,2} - 2U_{r+1,1} + U_{r,0}}{k^2} + B_1 \frac{U_{r+1,2} - U_{r,0}}{2k} \quad (3.15)$$

Again define ρ_1 and ρ_2 by equation (3.12). Substituting $E(t,x)$ for $U(t,x)$ and dividing through by $e^{r h} e^{j \beta k}$, where in this case $i=1$, gives

$$\xi - 1 = \rho_1 (\xi \cdot e^{j \beta k} - 2\xi + e^{-j \beta k}) + \rho_2 (\xi \cdot e^{j \beta k} - e^{-j \beta k}) \quad (3.16)$$

Solving for ξ gives

$$\xi = \frac{[1 + (\rho_1 - \rho_2) \cos \beta k] - j [(\rho_1 - \rho_2) \sin \beta k]}{[1 + 2\rho_1 - (\rho_1 + \rho_2) \cos \beta k] - j [(\rho_1 + \rho_2) \sin \beta k]} \quad (3.17)$$

and therefore

$$|\xi| = \sqrt{\frac{[1 + (\rho_1 - \rho_2) \cos \beta k]^2 + [(\rho_1 - \rho_2) \sin \beta k]^2}{[1 + 2\rho_1 - (\rho_1 + \rho_2) \cos \beta k]^2 + [(\rho_1 + \rho_2) \sin \beta k]^2}} \quad (3.18)$$

Since all terms under the square-root sign are positive, the condition $|\xi| \leq 1.0$ for this expression is satisfied when the numerator is less than the denominator. Expanding out the terms, this occurs when

$$\rho_1^2 + \rho_1 + \rho_1 \rho_2 \geq 0.0 \quad (3.19)$$

or in terms of the grid spacings and coefficient functions, when

$$2hA_i^2 + 2k^2A_i + hkA_iB_i \geq 0.0 \quad \text{for } i=1. \quad (3.20)$$

The difference scheme for an explicit upper boundary value is

$$\frac{U_{r+1,I-1} - U_{r,I-1}}{h} = A_{I-1} \frac{U_{r,I} - 2U_{r+1,I-1} + U_{r+1,I-2}}{k^2} + B_{I-1} \frac{U_{r,I} - U_{r+1,I-2}}{2k} \quad (3.21)$$

The corresponding amplification factor is determined via

$$\xi = \frac{[1 + (\rho_1 + \rho_2) \cos \beta k] + j[(\rho_1 + \rho_2) \sin \beta k]}{[1 + 2\rho_1 - (\rho_1 - \rho_2) \cos \beta k] + j[(\rho_1 - \rho_2) \sin \beta k]} \quad (3.22)$$

Again, the condition $|\xi| \leq 1.0$ is satisfied when

$$\rho_1^2 + \rho_1 - \rho_1 \rho_2 \geq 0.0 \quad (3.23)$$

or

$$2hA_i^2 + 2k^2A_i - hkA_iB_i \geq 0.0 \quad (3.24)$$

for $i=I-1$. Note that the stability criteria expressed in terms of h , k , A and B in (3.20) and (3.24) are slightly different. In both cases, the stability of the integrating scheme is not unconditionally satisfied.

3.3c. Mixed space-derivatives:

The case of the stability for the r -implicit step in the solution to the three-space dimensional (rigidity independent) transport equation is now considered (see Section 4.6). This step differs from the other LOD steps described above because the r - ϕ mixed derivative was evaluated at the *current* timestep (explicitly) rather than the *next* timestep (implicitly). For this step, the PDE has the form

$$U^t = A(x, y) \cdot U^{xx} + B(x, y) \cdot U^x + C(x, y) \cdot U^{xy} \quad (3.25)$$

where x would correspond to the z -transformed radius variable and y would correspond to the azimuth variable ϕ . Define the y -spaced grid via $y=mw$, $m=0, 1, \dots, M$, $w=(\Delta y)$. Since U in equation (3.25) is locally two-space dimensional, a two-space dimensional error function can be associated with the corresponding difference equation:

$$E(t, x, y) = E(rh, ik, mw) = e^{\gamma rh} e^{j\beta_1 ik} e^{j\beta_2 mw} \quad (3.26)$$

As for the one-dimensional case, this represents only one component of a Fourier series of error functions of the same form and again each component is treated separately. The difference equation corresponding to (3.25), with the last term explicit, is given by

$$\begin{aligned} \frac{U_{r+1,i,m} - U_{r,i,m}}{h} &= A_{i,m} \frac{U_{r+1,i+1,m} - 2U_{r+1,i,m} + U_{r+1,i-1,m}}{k^2} \\ &+ B_{i,m} \frac{U_{r+1,i+1,m} - U_{r+1,i-1,m}}{2k} + C_{i,m} \frac{U_{r,i+1,m+1} - U_{r,i-1,m+1} - U_{r,i+1,m-1} + U_{r,i-1,m-1}}{4kw} \end{aligned} \quad (3.27)$$

Substituting the error term in (3.26) into this difference equation gives

$$\begin{aligned}\xi - 1 &= \rho_1 \xi (e^{j\beta_1 k} - 2 + e^{-j\beta_1 k}) + \rho_2 \xi (e^{j\beta_1 k} - e^{-j\beta_1 k}) \\ &+ \rho_3 (e^{j\beta_1 k} e^{j\beta_2 w} - e^{j\beta_1 k} e^{-j\beta_2 w} - e^{-j\beta_1 k} e^{j\beta_2 w} + e^{-j\beta_1 k} e^{-j\beta_2 w})\end{aligned}\quad (3.28)$$

where

$$\rho_1 = A_{i,m} \frac{h}{k^2}, \quad \rho_2 = B_{i,m} \frac{h}{2k} \quad \text{and} \quad \rho_3 = C_{i,m} \frac{h}{4kw} \quad (3.29)$$

Solving for the amplification factor in (3.28) gives

$$\xi = \frac{1 - 4\rho_3 \sin(\beta_1 k) \sin(\beta_2 w)}{1 + 4\rho_1 \sin^2\left(\frac{\beta_1 k}{2}\right) - 2j\rho_2 \sin(\beta_1 k)} \quad (3.30)$$

and therefore

$$|\xi| = \frac{|1 - 4\rho_3 \sin(\beta_1 k) \sin(\beta_2 w)|}{\sqrt{\left(1 + 4\rho_1 \sin^2\left(\frac{\beta_1 k}{2}\right)\right)^2 + [2\rho_2 \sin(\beta_1 k)]^2}} \quad (3.31)$$

Unfortunately, this is one case where the stability criterion $|\xi| \leq 1$ depends on the spectrum (range of β) of the error. Because in practice there is no straight-forward way of determining β_1 and β_2 there is no guarantee that the integrating procedure given by (3.27) will be stable.

3.3d. Stability for explicit schemes:

Implicit differencing schemes (as discussed in Chapter 2) often have unconditional stability criteria. It seems that explicit schemes always have *conditional* stability criteria. To ensure the stability of an explicit difference scheme for a parabolic-type PDE generally requires tight constraints on the grid steps in the space and time dimensions. Here the constraints on the grid steps for the *explicit* difference equation representing the two-space dimensional transport equation (given by equation 4.5) are examined. The equation has the form

$$U^t = A(x, y, z)U^{xx} + B(x, y, z)U^x + C(x, y, z)U^{yy} + D(x, y, z)U^y + G(x, y, z)U^z \quad (3.32)$$

where, applied to the transport equation, x corresponds to the radius coordinate, y the heliographic polar-angle and z the momentum. With grid-indices defined through $t=r(\Delta t)$, $x=i(\Delta x)$, $y=m(\Delta y)$ and $z=n(\Delta z)$, the explicit difference equation representing (3.32) at interior grid points in the space-grid is

$$\begin{aligned}
U_{r+1,i,m,n} &= U_{r,i,m,n} \\
&+ \rho_1(U_{r,i+1,m,n} - 2U_{r,i,m,n} + U_{r,i-1,m,n}) + \rho_2(U_{r,i+1,m,n} - U_{r,i-1,m,n}) \\
&+ \rho_3(U_{r,i,m+1,n} - 2U_{r,i,m,n} + U_{r,i,m-1,n}) + \rho_4(U_{r,i,m+1,n} - U_{r,i,m-1,n}) \\
&+ \rho_5(U_{r,i,m,n+1} - U_{r,i,m,n-1})
\end{aligned} \tag{3.33}$$

where

$$\rho_1 = \frac{(\Delta t)A_{imn}}{(\Delta x)^2}, \rho_2 = \frac{(\Delta t)B_{imn}}{2(\Delta x)}, \rho_3 = \frac{(\Delta t)C_{imn}}{(\Delta y)^2}, \rho_4 = \frac{(\Delta t)D_{imn}}{2(\Delta y)}, \rho_5 = \frac{(\Delta t)G_{imn}}{2(\Delta z)} \tag{3.34}$$

and (for example) $A_{imn} = A(i\Delta x, m\Delta y, n\Delta z) = A(x, y, z)$ etc... Since this integrating procedure has three space dimensions associated with it, the corresponding error function is three-space dimensional and of the form

$$E(t, x, y, z) = E(r\Delta t, i\Delta x, m\Delta y, n\Delta z) = E_{r,i,m,n} = e^{\gamma r h} e^{jX_1 i} e^{jX_2 m} e^{jX_3 n} \tag{3.35}$$

where

$$X_1 = \beta_1(\Delta x), X_2 = \beta_2(\Delta y) \text{ and } X_3 = \beta_3(\Delta z) \tag{3.36}$$

The β 's here define the spectrum of the error as in equation (3.6) or (3.26). Substituting the error term into (3.33) and solving for the amplification factor gives

$$|\xi|^2 = \left[1 - 4\rho_1 \sin^2\left(\frac{X_1}{2}\right) - 4\rho_3 \sin^2\left(\frac{X_2}{2}\right) \right]^2 + 4[\rho_2 \sin(X_1) + \rho_4 \sin(X_2) + \rho_5 \sin(X_3)]^2 \tag{3.37}$$

The stability criterion $|\xi| \leq 1$ gives a complicated condition between the various ρ 's and β 's. If the β 's in the actual error could be evaluated at any particular stage in the computation then this equation would give a condition relating the grid step in the time direction to the grid steps in the space direction and the other coefficients A, B, C, D, G . In fact, the inequality specifies a *maximum* step in the time-direction that can be taken to ensure the stability of the integrating procedure. Since the β 's are un-computable in practice, some assumptions are required to obtain an estimate of this maximum time step required to ensure stability. This is undertaken in Chapter 4 for the application of the transport equation.

3.3e. Stability for ADI schemes:

Not all alternating-direction-implicit schemes are unconditionally stable. It is often the case that each step in an ADI scheme has an amplification factor whose modulus is greater than +1. In many cases however, the modulus of the product of the amplification factors of each step is less than +1 ensuring unconditional stability. The ADI scheme given by equations 2.9A, 2.9B* and 2.9C* has been shown elsewhere to be unconditionally stable (eg: section 4.10 of Lapidus and Pinder 1982).

Chapter 4. Numerical Results.

4.1. INTRODUCTION

The results of the computer modelling, applying the theory of Chapters 1, 2 and 3, are presented in this chapter. Most of the results shown are for an axially symmetric heliosphere (two space dimensions). The work concentrates on predicting the value of the radial gradient g_r of galactic cosmic rays at a heliographic radius of 1 AU and co-latitude of 90° (the average position of Earth) under various inner-boundary conditions, using the two different implicit algorithms discussed in Chapter 2. The possible use of explicit algorithms for this model is also investigated. Also presented are results for the two space dimensional model when radially propagating shocks are introduced to simulate the 11-year solar cycle of galactic cosmic ray modulation.

Note that because the value of f is determined on a finite grid, the value of g_r has to be determined numerically using this grid. The differential gradient $g_r = 1/f \partial f / \partial r$ has been determined in this chapter using a central-difference approximation:

$$g_r(i,j,k) = \frac{1}{f_{i,j,k}} \cdot \frac{(f_{i+1,j,k} - f_{i-1,j,k})}{(r_{i+1} - r_{i-1})}$$

The integral value of the radial gradient between two rigidity values was calculated using the same central difference approximation, except using integral intensity I (given by equations 1.1 and 1.2) instead of f . The values of the radial gradient quoted in this chapter are integral gradients for particles with rigidity between 0.5 and 10 GV, corresponding to the rigidity range over which the transport equation was solved.

All the models in this section are restricted to solving the distribution function for cosmic rays of rest-mass equal to one proton, as the majority of galactic cosmic rays *are* protons. The magnetic state of the heliosphere in all the runs was *toward* in the northern hemisphere ($A < 0$, see Section 6.1) as was the case for years 1958-1970 and 1980-1991. This is the state predicted by modulation models to have a higher radial gradient than the opposite ($A > 0$) polarity state (eg: Kota and Jokipii 1983 or Potgieter *et al.* 1989). Independent observations however show no discernible difference for the radial gradient at Earth in each polarity state - although there may be an 11 year solar cycle variation of the gradient (see Bieber and Pomerantz 1986 for example). Because the theories predict a radial gradient higher than that inferred from observations in both magnetic states of the heliosphere, the discrepancy between theory and observation is less for the positive polarity state. This is why the simulations undertaken have concentrated on the negative polarity state. As will be seen, the models investigated in this chapter generally predict a gradient which is too high compared with observation. They are restricted to a flat neutral sheet (see Chapter 6) and hence model the heliosphere in solar minimum conditions.

The modulation work presented here is by no means a definitive set of results for the modulation of galactic cosmic rays in the heliosphere. There are many more parameter investigations that can be undertaken. These include, for example, investigating (a) the effects of modifying the position of the heliosphere boundary and the solar-wind

termination shock - even making them time-dependent in phase with solar activity; (b) the effect of a two dimensional solar wind and the corotating interaction regions set up as a consequence (see Kota and Jokipii, 1991b); (c) changing the functional form of the diffusion tensor, including higher-order effects in the transport equation - for example the helicity effects investigated by Bieber and Burger (1990); and (d) solving the transport equation for a wider range of energy values. There is also the study of the modulation of the anomalous component of cosmic rays (see for example McKibben 1987) which is not addressed in this thesis. As each integration of the transport equation is computer intensive, even with modern computer facilities, one cannot investigate all of parameter-space because of limited time and computer resources. The essence of this thesis, and hence the results presented in this chapter, is to show some of the things which affect predictions of the radial gradient of cosmic rays at 1 AU and compare the predictions with the observed gradient determined from the data analysis undertaken in the second half of the thesis.

4.2. RESULTS FOR 2 SPACE DIMENSIONS

The results for the case when $f = f(r, \theta, p, t)$ are examined in this section. This is the case when the heliosphere is considered to be axially-symmetric, ie: terms in the transport equation involving derivatives with respect to the azimuth coordinate are zero. Since $\partial/\partial\phi \rightarrow 0$, the neutral sheet is flat ($\alpha=0$ in equation 1.19). This approximates the conditions of the heliosphere at solar minimum. In practice it is highly unlikely that the neutral sheet is flat at any time. It is assumed that the behaviour of the galactic cosmic ray distribution under conditions where the neutral sheet is only slightly tilted (say, $\alpha \leq 10^\circ$) is similar to the behaviour when the neutral sheet is flat. At any one time and place, the neutral sheet itself may have a tilt which is dependent on the radial coordinate (as depicted in Williams and Potgieter 1991). This is a consequence of the fact that the value of the neutral sheet tilt is solar-cycle dependent and it takes a finite time for conditions at the Sun to propagate outward at the solar wind speed to the boundary of the heliosphere. Modelling f becomes very complicated under these conditions. It may be asked: why look at the azimuthally symmetric case if it is unrepresentative of the heliosphere? The answer lies in the complexity of the fully 3-space dimensional transport equation. It will be seen that the solution to the general case $f = f(r, \theta, \phi, p, t)$ would have taken far too long to be practically computable on the computing resources available at the University of Tasmania. The simplified transport equation is useful in its predictions for a heliosphere around solar minimum and it is also useful when comparing the effect on the solution for f under differing heliospheric states and differing boundary conditions.

The 2-space dimensional transport equation is given by expanding equation 1.3 in the radius coordinate, polar angle coordinate and momentum coordinate (r, θ, p) . It is convenient (following J.R. Jokipii, private communication) to make a transformation in the radius coordinate to a new variable z such that

$$r = \epsilon \tan z \quad (4.1)$$

The transport equation is then solved on a grid (z, θ, p) with constant grid spacing Δz . In this way, the grid points in the radius coordinate become more dense as $r \rightarrow 0$. This allows for higher spatial resolution near the Sun where most of the parameters are changing fastest. In that case,

$$A_r \frac{\partial f}{\partial r} + A_{rr} \frac{\partial^2 f}{\partial r^2} = A_z \frac{\partial f}{\partial z} + A_{zz} \frac{\partial^2 f}{\partial z^2} \quad (4.2)$$

$$A_{zz} = \left(\frac{\cos^2 z}{\epsilon} \right)^2 A_{rr} \quad (4.3)$$

$$A_z = \left(\frac{\cos^2 z}{\epsilon} \right) A_r + \left(\frac{\cos^2 z}{\epsilon} \right) \left(\frac{-\sin(2z)}{\epsilon} \right) A_{rr} \quad (4.4)$$

and the 2-space dimensional transport equation is given by:

$$\frac{\partial f}{\partial t} = (\mathcal{L}_z + \mathcal{L}_\theta + \mathcal{L}_p) f \quad (4.5)$$

where

$$\mathcal{L}_z = A_z \frac{\partial}{\partial z} + A_{zz} \frac{\partial^2}{\partial z^2} \quad (4.6a)$$

$$\mathcal{L}_\theta = A_\theta \frac{\partial}{\partial \theta} + A_{\theta\theta} \frac{\partial^2}{\partial \theta^2} \quad (4.6b)$$

$$\mathcal{L}_p = A_p \frac{\partial}{\partial \ln p} = p A_p \frac{\partial}{\partial p} \quad (4.6c)$$

are the differential operators, and the coefficients are given by

$$A_z = A_z(z, \theta, p) = \left[\frac{2K_{rr}}{r} + \frac{\partial K_{rr}}{\partial r} - U(r) - (\underline{V}_D)_r \right] \cdot \left(\frac{\cos^2 z}{\epsilon} \right) + K_{rr} \left(\frac{-\sin 2z}{\epsilon} \right) \cdot \left(\frac{\cos^2 z}{\epsilon} \right)$$

$$A_\theta = A_\theta(z, \theta, p) = \left[\frac{\cos \theta}{r^2 \sin \theta} K_{\theta\theta} + \frac{1}{r^2} \frac{\partial K_{\theta\theta}}{\partial \theta} - \frac{1}{r} (\underline{V}_D)_\theta \right]$$

$$A_{zz} = A_{zz}(z, \theta, p) = K_{rr} \cdot \left(\frac{\cos^2 z}{\epsilon} \right)^2$$

$$A_{\theta\theta} = A_{\theta\theta}(z, \theta, p) = \frac{K_{\theta\theta}}{r^2}$$

$$A_p = A_p(z) = \frac{1}{3} \left(\frac{2U(r)}{r} + \frac{\partial U(r)}{\partial r} \right) \quad (4.7)$$

Here we assume the diffusion tensor (see Section 1.3a), the solar wind speed (see Section 1.3b) and the heliospheric magnetic field (see Section 1.3c) are all time independent. The transport equation has been solved using the two different integrating algorithms discussed in Chapter 2, namely ADI and LOD. The boundary conditions used were as specified in Section 2.2. In particular, two inner boundary conditions in the radius coordinate were used. The first was a zero inner boundary ($f(t, r=r_{\min}, \theta, p) = 0 \forall t, \theta, p$) and the second was a 'floating' inner-boundary ($\partial^2 f / \partial r^2 = 0$ at $r=r_{\min} \forall t, \theta, p$) corresponding to the inner boundary being a linear extrapolation of the nearest grid points. The outer boundary value for the distribution in the radius coordinate corresponds to the assumed galactic distribution of cosmic rays at the boundary of the heliosphere. It was assumed that this distribution was isotropic in space, with a spectrum given by $f(t, r=r_{\max}, \theta, p) \propto p^{-1} E^{-3.6} \forall t, \theta, p$ where E is the energy of the particle (this follows Kota and Jokipii 1983). The range of coordinates are: $r \in (0.2, 90)$ AU (LOD algorithm), $r \in (0.3, 93)$ AU (ADI algorithm), $\theta \in (0, \pi)$, momentum such that in terms of rigidity (P), $P \in (0.5, 10)$ GV. Cases were solved with and without a solar-wind termination shock set at 60 AU (see equation 1.15). The magnetic field constant was determined such that the magnitude of the field at Earth was 5 nT. The diffusion coefficients used were those given by equations (1.11a) and (1.12) with $\alpha=0.5$, $\eta=1.0$ and $\mu=0.05$. These coefficients are consistent with those used by the majority of the other researchers noted in Section 1.4. The model predicts that the heliosphere would reach steady-state in around 2×10^7 seconds (~ 8 months) for this energy range. It was found that the accuracy of the result depended on the value of (Δt) used for the integration - the smaller the better. However, measurably greater accuracy was not achieved by using a value of (Δt) less than approximately 2×10^4 seconds. The main justification for solving the transport equation in this case was to determine the value of the radial gradient g_r at Earth for the various cases. A table of values of g_r at 1 AU and $\theta=90^\circ$ is presented in Table 4.1. Plots of each run are shown in Appendix 10. Each figure in this appendix is a plot of the value of f vs r for $\theta=90^\circ$ for a range of rigidity values from 0.5 to 10 GV.

| RUN | Inner-boundary condition | Algorithm | Termination shock | g_r at Earth (% AU ⁻¹) |
|-----|--------------------------|-----------|-------------------|--------------------------------------|
| 1 | zero | LOD | no | 19.3 |
| 2 | zero | ADI | no | 16.2 |
| 3 | zero | ADI | yes | 15.8 |
| 4 | floated | LOD | no | 17.4 |
| 5 | floated | LOD | yes | 17.1 |
| 6 | floated | ADI | yes | 8.0 |

Table 4.1. Values of the integral radial gradient (0.5 - 10 GV) of galactic cosmic rays at Earth computed from the solution to the 2-space dimensional transport equation under various assumptions. Plots of the results are shown in Appendix 10.

The relative contribution to the observed modulation of the differential intensity of galactic cosmic rays at Earth, with rigidities above 10 GV, is substantially less than within this energy range. Higher energy particles are less affected by the solar wind and irregularities in the interplanetary magnetic field. Also, the energy spectrum of galactic cosmic rays is such that for an increase of energy by a factor of 10, the differential intensity decreases by almost a factor of 10^5 . Runs were attempted for much higher energies (~ 100 GeV), however, it was found that stability and accuracy problems became more significant as

energy increased. These problems could not be alleviated in the time allocated for this project.

It is clear from Table 4.1 that the runs produced values of g_r far higher than expected from observational evidence (see Section 1.5 and Chapter 8). Section 4.4 explores possible reasons for this. Firstly, the possibility of using *explicit* integrating algorithms for evaluating the 2-space dimensional transport equation is explored.

4.3. EXPLICIT ALGORITHMS.

Recall from Chapter 2 and Chapter 3 that explicit algorithms are computationally stable for only a subset of integrating timesteps Δt . Equation (3.37) is expanded on the right hand side. Because no direct knowledge of the X_i values are attainable, assumptions need to be made in order to obtain an estimate of the maximum value of Δt able to be used in order for the explicit algorithm to be stable. These assumptions include

$$\sin^2\left(\frac{X_1}{2}\right) \approx \sin^2\left(\frac{X_2}{2}\right) \quad (4.8)$$

so that

$$\rho_1 \sin^2\left(\frac{X_1}{2}\right) \geq 2\rho_1\rho_3 \sin^2\left(\frac{X_1}{2}\right) \sin^2\left(\frac{X_2}{2}\right) + 2\rho_1^2 \sin^4\left(\frac{X_1}{2}\right) \quad (4.9)$$

is satisfied when

$$\rho_1 \geq 2\rho_1\rho_3 + 2\rho_1^2 \quad (4.10)$$

Under these and similar assumptions, the condition for stability for the 2-space dimensional transport equation case reduces to

$$\rho_1 + \rho_3 \geq 4\rho_1\rho_3 + 2(\rho_1^2 + \rho_2^2 + \rho_3^2 + \rho_4^2 + \rho_5^2) + |\rho_2\rho_4| + |\rho_2\rho_5| + |\rho_4\rho_5| \quad (4.11)$$

This gives a condition relating Δt to the coefficients of the partial differential equation. The ρ values are given by equation (3.34).

Restricting $r \in (0.2, 90)$ AU, $\theta \in (0, \pi)$ and P (rigidity) $\in (0.5, 10)$ GV, this condition was applied to every grid point in the discretized heliosphere. For \underline{B} , \underline{V}_{SW} and \underline{K} specified as in Section 1.3, the inequality given by equation 4.11 is equivalent to

$$\Delta t \leq 13.98 \text{ seconds} \quad (4.12)$$

Recall that the implicit routines described in Section 4.2 required t_{\max} of the order 2×10^7 seconds for the integration to be sufficiently steady-state for this energy range. For $\Delta t \sim 14$ seconds, this requires $\sim 1.4 \times 10^6$ integration steps. Implementing the explicit algorithm

(given by 3.33) on a MicroVax 3500 computer (the fastest available in the Physics Department at the time) it was discovered that the computer could perform one integration step roughly every 4 CPU seconds. One integration step takes the distribution function f from t to $t+\Delta t$ through equation 3.33 for every grid point in the discretized heliosphere. Hence the total machine time required to integrate to steady state is approximately 1400 CPU hours. This far exceeds the time required with the implicit routines where timesteps of around 2×10^4 seconds were used. It is interesting to note that the explicit algorithm was implemented with $\Delta t = 13.98$ seconds and was still converging after approximately 1 hour CPU time (~ 900 integration steps). In contrast, a value $\Delta t = 28$ was used and the results started diverging rapidly after only ~ 200 timesteps. It is therefore considered that Δt given by equation 4.12 is an accurate maximum timestep allowable for a stable explicit algorithm and the explicit integrating technique was not practical in this case.

4.4. INNER BOUNDARY ANALYSIS

The ADI/LOD results given in Section 4.2 predict a value of the radial gradient g_r at Earth too high compared with predictions inferred from observation data (see Chapter 8). Various methods were investigated in order to determine the cause of this discrepancy. The investigations centred around trying to find a better inner-boundary condition or a better functional form of the diffusion tensor near Earth. "Better" in this sense refers to results which give closer agreement between theory and observation.

4.4a. Method 1. Power-Law inner-boundary.

Assume that, in the energy window of interest, the energy spectrum of the galactic cosmic rays at the inner boundary follows a power-law spectrum. Two specific assumptions are made. Firstly, that the spectral index of the power spectrum is constant with energy over the energy window of concern. Secondly, that there exists an energy above which no modulation occurs and therefore the value of the differential intensity at that energy at the inner boundary is the same as the intensity at the outer boundary. Denote this energy by E_{\max} . The differential intensity with respect to momentum is given by equation 1.1. The galactic spectrum, with respect to energy E , is given by

$$j_G(E) = j_0 E^{-\gamma_0} \quad (4.13)$$

where j_0 and γ_0 are constants. In the energy range of concern, $\gamma_0 = 2.65$ (eg: Berezhinskii *et al.* 1990). Let the inner boundary spectrum be given by

$$j_I(E) = j_1 E^{-\gamma_1} \quad (4.14)$$

where j_1 and γ_1 are constants. Let

$$\frac{j_I(E)}{j_G(E)} = x(E) \quad (4.15)$$

Then it can be shown (see Appendix 1) that

$$x(E) = \left(\frac{E}{E_{\max}} \right)^{\gamma_0 - \gamma_1} \quad (4.16)$$

The inner boundary value of the differential intensity (and hence the distribution function f) is thus completely specified by the choice of the pair (γ_1, E_{\max}) . Run 7 (Appendix 10) shows the result of using the LOD algorithm with a solar-wind termination shock and values of $(\gamma_1, E_{\max}) = (2.4, 200 \text{ GeV})$. The calculated radial gradient at Earth is 15.9% AU⁻¹. Other values of (γ_1, E_{\max}) were tried but none gave a value of g_r at Earth greatly different from this value. As can be seen by the plot in Appendix 10, the value of f at the inner boundary seems not to have a discernable bearing on g_r at 1 AU. This was also the case with other (γ_1, E_{\max}) pairs.

Jokipii and Thomas (1981), Kota and Jokipii (1983), Potgieter and Moraal (1985) and Kadokura and Nishida (1986), for example, report that they expect the relationship between $\ln(f)$ and $\ln(E)$ to flatten from a straight line (power law spectrum) as energy is decreased and eventually change sign (from negative to positive slope as energy decreases). The energy at which the slope goes to zero is given as around 1 GeV. The results here *support* the prediction by the authors that $\partial \ln(f) / \partial \ln(E)$ is *not* constant down to about 1 GeV. If it *was* constant, it is expected that Run 7, and similar runs, should have predicted a lower gradient. The change in the spectrum may indeed be a consequence of, or a requirement for, a low gradient at the inner boundary.

4.4b. Method 2. Improved forms for K_{\parallel} , K_{\perp} .

Kadokura and Nishida (1986) commented that the *"increase in radial gradient at the inner boundary is primarily due to the mean free path being proportional to B^{-1} so that as the inner boundary is approached, the diffusion coefficients increased as r^2 "*. Motivated by this comment, the two dimensional models were run using a variety of different radially dependent forms for the diffusion coefficient to see if such a form could be found which gave a significantly smaller value of g_r than the previous models. Results presented in Table 4.2 are for diffusion coefficients specified by

$$K_{\parallel} = K_0 \beta P \left(1 + \left(\frac{r}{r_e} \right)^2 \right)$$

$$K_{\perp} = \frac{K_0}{50} \beta P \left(\frac{|B_e|}{3|B|} \right) \quad (\text{SET A})$$

and also for values of K_{\parallel} and K_{\perp} specified in Section 4.2 but where values for $r < 5 \text{ AU}$ were substituted for values at $r = 5 \text{ AU}$ (SET B). Plots of each run are shown in Appendix 10 (Runs 8-11). The forms of the coefficients described by SET A were chosen because they gave a much lower rate of change in the coefficients as a function of radius than those used in Section 4.2. They produced the lowest gradient g_r (using the ADI algorithm) of all the runs investigated. They are also similar to the coefficients used by Potgieter and Moraal (1985). The reason for the discrepancy in the results between the two different integrating algorithms is discussed in Section 4.4d.

| RUN | Diffusion coefficients* | Algorithm | Termination shock | g_r at Earth (% AU ⁻¹) |
|-----|-------------------------|-----------|-------------------|--------------------------------------|
| 8 | SET A | LOD | yes | 23.4 |
| 9 | SET A | ADI | yes | 2.03 |
| 10 | SET B | LOD | yes | 27.1 |
| 11 | SET B | ADI | yes | 3.7 |

Table 4.2 Values of the integral radial gradient (0.5 - 10 GV) of galactic cosmic rays at Earth computed from the solution to the 2-space dimensional transport equation under various assumptions. Plots of the results are shown in Appendix 10. * See main text above for explanation.

Note that in these runs and in the runs of Section 4.2, changing ϵ (equation 4.1) by upwards of a factor of 5 had a negligible effect on the values of g_r determined. For ϵ much larger than about 100, there were insufficient grid points in the outer-heliosphere to ensure an accurate solution for the distribution function. A number of runs were repeated to specifically look at the effect of the finite size of the grid near the Sun. The steady-state solution at 4 AU was used as a boundary condition to solve the transport equation to steady state within the radius range $r \in (0.3, 4)$ AU only. This allowed for a much large number of grid points within this radius range. The value of the radial gradient at 1 AU did not significantly change from the values presented above, even, for example, in the case of Run 2 where it would seem from the plot (shown in Appendix 10) that the large finite grid spacing around 1 AU could detrimentally affect the solution. Note also that the position of the inner boundary was changed between 0.2 and 0.8 AU without noticeably affecting the solution.

4.4c. Method 3. Zero streaming at inner-boundary.

Motivated by the physical argument that the Sun would *not* be a dominant sink for galactic cosmic rays, it was decided that a reasonable inner-boundary condition was that the radial component of the streaming vector went to zero as the radius coordinate approached the inner-boundary:

$$(\underline{S} \cdot \underline{r})_{r=r_{\min}} = 0 \quad (4.17)$$

where the streaming function \underline{S} is given by equation 1.22. This component is given by

$$\underline{S}_r = -4\pi p^2 \left(K_{rr} \frac{\partial f}{\partial r} + \frac{K_{r\theta}}{r} \frac{\partial f}{\partial \theta} + \frac{U(r)}{3} \frac{\partial f}{\partial \ln p} \right) \quad (4.18)$$

and so the condition of equation (4.17) is equivalent to

$$K_{rr} \frac{\partial f}{\partial r} \Big|_{r=r_{\min}} + \frac{K_{r\theta}}{r} \frac{\partial f}{\partial \theta} \Big|_{r=r_{\min}} + \frac{U(r)}{3} \frac{\partial f}{\partial \ln p} \Big|_{r=r_{\min}} = 0 \quad (4.19)$$

in the 2-space dimensional case. Note that $K_{r\theta}$ is related to the asymmetric part of the diffusion tensor via

$$K_{r\theta} = -K^A \sin \psi \quad (4.20)$$

where K^A is given by

$$K^A = \frac{pv}{3qB} \quad (4.21)$$

which is consistent with the value of the drift-velocity given by equation 1.9. In implementing this inner-boundary condition in the tri-diagonal matrix solution (see Section 2.3) for the radius implicit step,

$$\begin{aligned} d_2 &\rightarrow d_2 + a_2 \left(\frac{X+Y}{Z} \right) \\ c_2 &\rightarrow c_2 + a_2 \\ b_2 &\rightarrow b_2 \\ a_2 &\rightarrow 0 \end{aligned} \quad (4.22)$$

where $X = \left(\frac{K_{r\theta}}{r} \frac{\delta f}{\delta \theta} \right)_{2,j,k}$

$$Y = \left(\frac{U(r)}{3} \frac{\delta f}{\delta \ln p} \right)_{2,j,k}$$

$$Z = \left(K_{rr} \frac{dz}{dr} \cdot \frac{1}{2(\Delta z)} \right)_{2,j,k} \quad (4.23)$$

Using this inner boundary condition, the LOD algorithm produced a value of g_r at Earth of 15.8 % AU⁻¹ and the ADI algorithm produced 8.2 % AU⁻¹. The results are shown in Appendix 10 as Run 12 and 13 respectively. A solar-wind termination shock was included and the diffusion coefficients used were the same as for Runs 1-6. As for Run 7, the value of the distribution function at the inner boundary does not seem to affect the value of g_r at 1 AU.

4.4d. Summary of inner-boundary analysis.

It is apparent from Runs 1-13 that (a) the ADI method produces a lower value of the radial gradient of galactic cosmic rays at Earth compared with the LOD method; (b) the choice of inner boundary condition in the radius coordinate has a secondary effect on g_r at 1 AU for a given algorithm; and (c) the presence of a solar-wind termination shock at 60 AU has negligible effect on g_r at 1 AU. Only the results from Runs 9 and 11 predict a low enough

gradient to be consistent with observational data. Note that g_r seems to be relatively constant over the energy range considered for a particular run, especially for Run 9. It is therefore proposed that the trends would be true for energies above 10 GeV and so be applicable to muon data as well as neutron monitor data. It is proposed that the diffusion coefficients used in Run 9 are more appropriate than others which give a value of g_r too high to be consistent with observational data.

It is proposed that LOD is an inappropriate algorithm to use for the solution of the 2-space dimensional transport equation as is demonstrated by the high gradients predicted in *all* the runs using this algorithm. The difference between the two algorithms was investigated but the only conclusion that could be drawn to explain the discrepancy between their predictions of g_r at Earth was that LOD is intrinsically a *less accurate* algorithm than ADI. An analysis of the truncation error of each of the discretized forms of the partial differential equation shows that, for each integrating step, LOD has an error of order $(\Delta t) + (\Delta x)^2$ whereas ADI has an error of order $(\Delta t)^2 + (\Delta x)^2$. In each case, Δx refers to the grid step in the implicit space coordinate and Δt refers to the integration time step (see Lapidus and Pinder 1982, Chapter 4). The ADI algorithm contains higher order truncations error terms than LOD and is thus expected to be more accurate. Indeed, Gourlay and Mitchell (1972) find, in a paper comparing the structure of ADI and LOD difference methods, that high accuracy LOD schemes for more than two operators do not exist.

4.5. SHOCKS

As well as the four physical processes of drift, diffusion, convection and adiabatic energy loss, interplanetary shocks caused by coronal mass ejections and flare related events are also thought to impede cosmic rays from entering the inner heliosphere. As discussed in Section 1.4, there has been considerable debate regarding the relative importance of each of the modulation effects to the total modulation of galactic cosmic rays in the heliosphere. In particular, there is disagreement as to whether the 11/22 year cycle of observed intensity is predominantly due to the changing solar magnetic fields structure altering the drift component of the cosmic rays, or due to a succession of Forbush decrease type events which increase in frequency toward solar maximum. Radially propagating shocks have been included in the time-dependent two-space dimensional transport equation, by introducing transient regions of enhanced magnetic field turbulence, in an attempt to ascertain the importance of these shocks in the total modulation of particles reaching Earth. The ultimate motivation for this study was to understand the long-term modulation of galactic cosmic rays as seen by neutron monitors and muon telescopes. Hence the model simulations will be restricted to primary particles of energy ≥ 1 GeV.

Again, the model was restricted to a flat neutral sheet. The integrating method, diffusion coefficients used and inner boundary condition were the same as in Run 9 of Section 4.4b as those conditions gave the lowest radial gradient in the steady-state solution. The initial condition was the steady-state solution itself. The rigidity bounds, solar wind speed, polarity state etc. were all equivalent to Run 9. To include the effect of transient shocks, the work of Perko and Fisk (1983) and Perko and Burlaga (1987) was followed. The shocks were considered as spherically symmetric regions of enhanced magnetic scattering propagating at 600 km s^{-1} radially outward from the Sun. The effect of the presence of

these regions was to cause a reduction in the magnitude of K_0 (the diffusion constant) behind the shock up to a fixed maximum decrease.

$$K_0 \rightarrow K_0 \left(1 - \alpha \sin^2 \left[\frac{\pi(r_{sh} - r)}{2\lambda} \right] \right) \quad \text{for } r \in (r_{sh} - 2\lambda, r_{sh}) \quad (4.24)$$

where r_{sh} is the radial position of the shock, λ is the position of maximum decrease and α determines the magnitude of the decrease. The frequency of shock creation at the Sun is given by

$$\# \text{ shocks } (t) = n_1 + (n_2 - n_1) \sin^2 \left(\frac{\pi t}{\tau} \right) \quad (4.25)$$

where n_1 is the number of shocks per year at solar minimum ($t=0$ years), n_2 is the number per year at solar maximum ($t=5.5$ years) and $\tau = 11$ years. For the results presented in this section, values of $n_1=3$, $n_2=26$ and $\lambda = 1$ AU were chosen. This was consistent with work by the authors mentioned above.

Results presented by Sanderson *et al.* (1991) report that the radial diffusion coefficient can change by up to a factor of 77 for a 1 GeV proton during the passage of a Forbush decrease type event. Motivated by this, two runs were undertaken, the first with $\alpha = 0.9$ and the second with $\alpha = 0.99$. At the end of each integrating loop, each active shock had its position updated according to its propagating speed (600 km s^{-1}) and the time interval of integration. Equation 4.25 was then used to determine whether a new shock (emanating from r_{min}) was required, based on the frequency of shock production at any one time. Then the effect of *each* shock on K_0 was calculated (as a function of radius) noting that the effect of overlapping shocks (if that scenario arose) was to multiply together each individual effect, given by equation 4.24. All the coefficients, which are ultimately functions of K_0 , were re-calculated for the next integration step. Obviously if a shock reaches the outer-boundary of the heliosphere then it is discarded from further calculations.

Figure 4.1 shows the effect on the observed integral intensity (proportional to $\int p^2 f dp$) of one of the shocks passing Earth for both α values. Figures 4.2 and 4.3 show the steady-state (solid line) and shock modulated intensity (dashed line) for $\alpha = 0.9$ and $\alpha = 0.99$ respectively. The steady state solution represents solar minimum conditions. The shock-modulated solution represents solar maximum, neglecting the effect of an increase in the waviness of the neutral sheet from solar minimum to solar maximum. Along the flat neutral sheet, the difference in the integral intensity between the two situations is $\leq 5\%$. The intensity becomes depressed by up to 20% at non-equatorial heliographic latitudes. There was no significant change in the rigidity spectrum after shock modulation. The shocks used here were spherically symmetric. There is an obvious integral decrease of cosmic ray intensity as shown by Figure 4.1. However, it was observed that there was an *increase* in the intensity of the very highest energy particles as the shock passes. This was attributed to the fact that the number density of the particles in generalized space-momentum phase space must remain constant if there is no source or sink of particles. Since in this case spherical symmetry was imposed, there was nowhere for the particles to redistribute in space. Hence to preserve phase-space density, the number of particles with the highest energy increased.

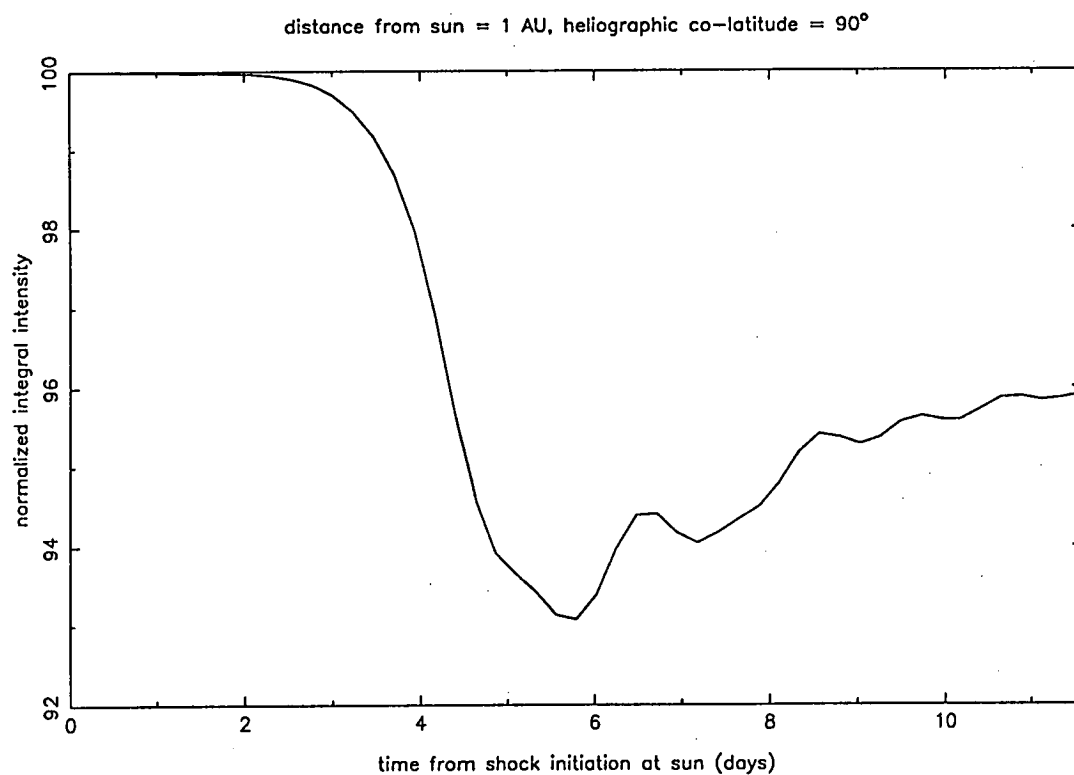
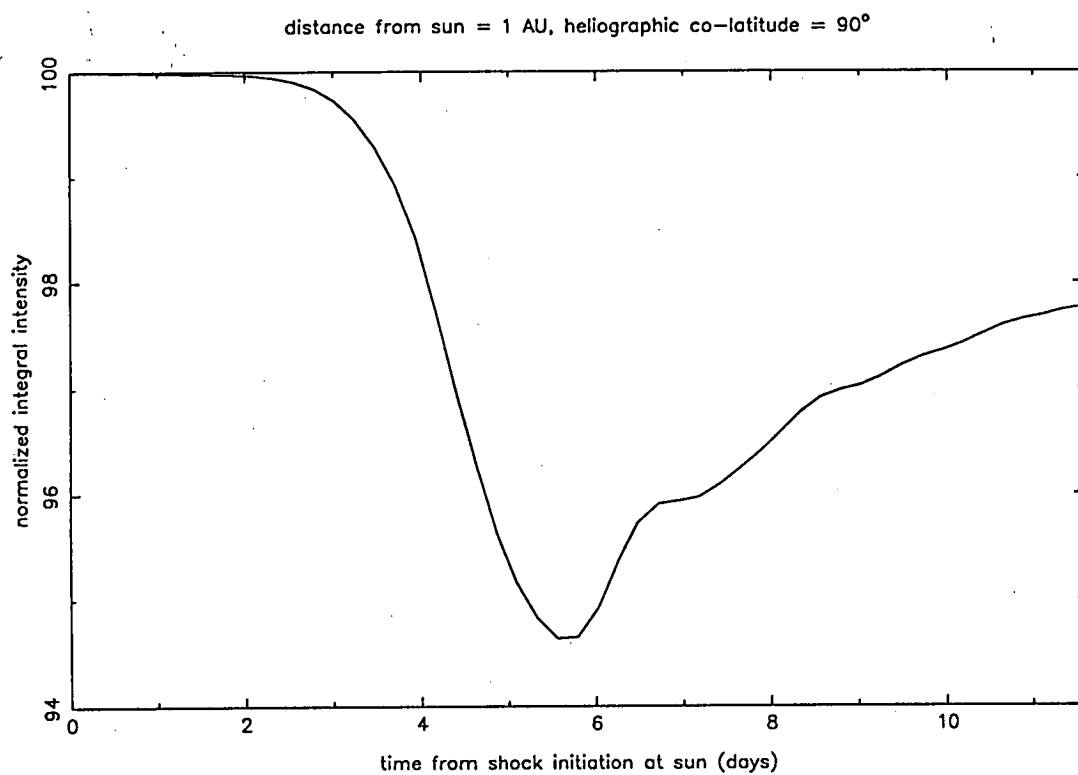


Figure 4.1. The top plot shows the effect on the integral intensity of cosmic rays between 0.5 and 10 GV rigidity of a radially propagating transient shock passing Earth. The strength of the shock is as given in equation 4.24 with $\alpha=0.9$. The bottom plot shows the effect for $\alpha=0.99$.

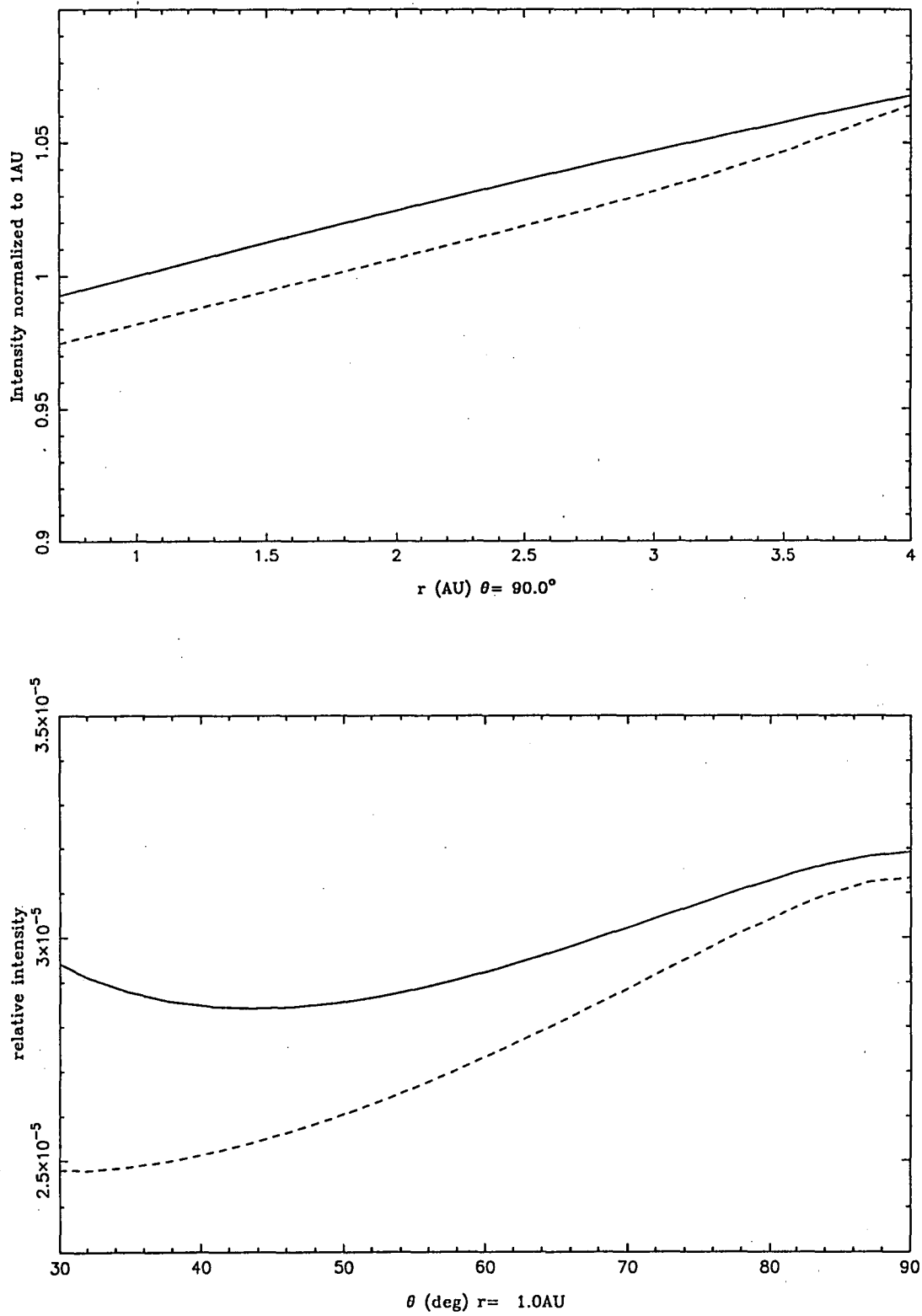


Figure 4.2. The solid line is the steady-state integral intensity of cosmic rays and the dashed line is the intensity after shock modulation (5.5 years). $\alpha=0.9$ in this case.

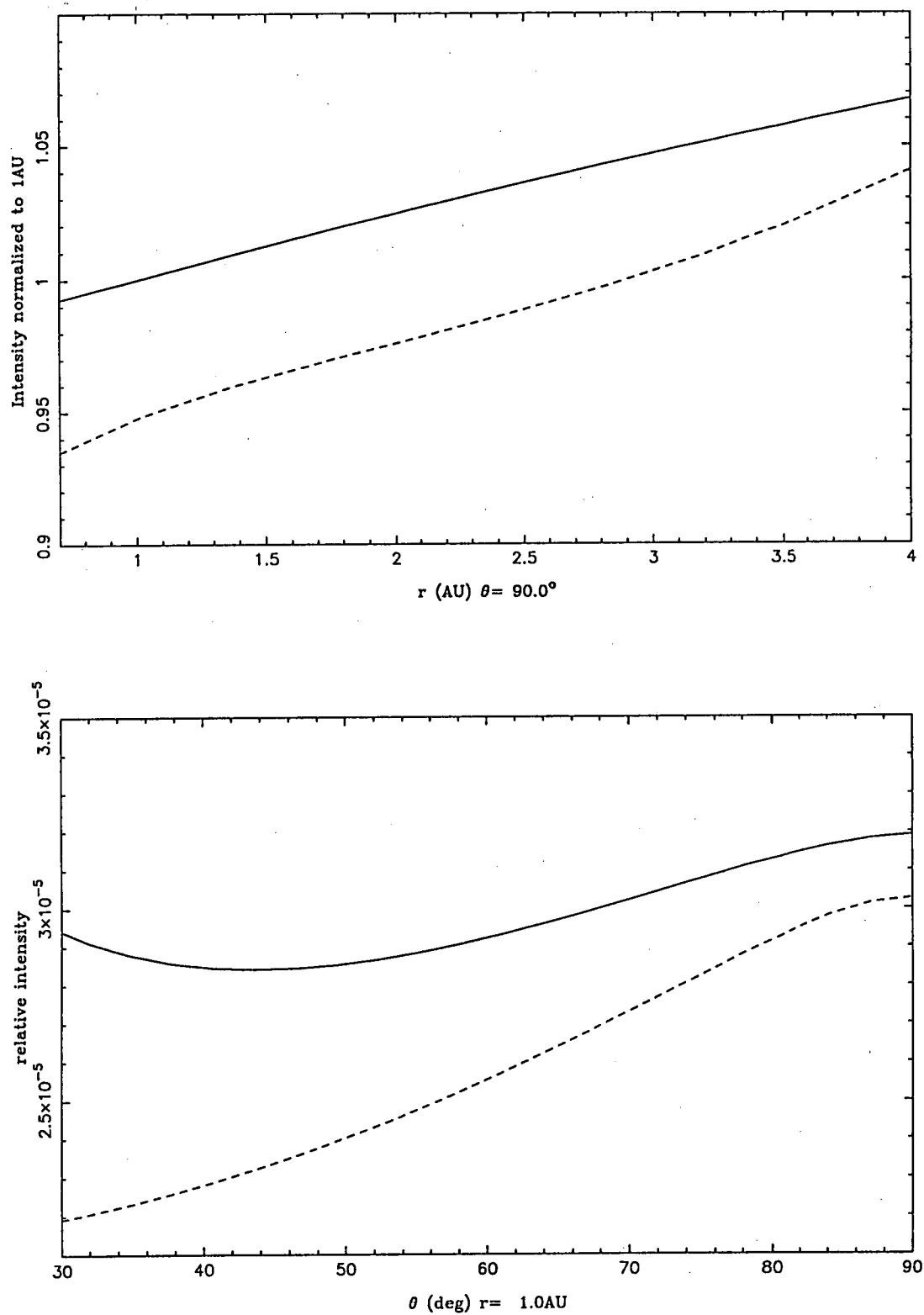


Figure 4.3. The solid line is the steady-state integral intensity of cosmic rays and the dashed line is the intensity after shock modulation (5.5 years). $\alpha=0.99$ in this case.

Waves in the integral intensity with period approximately one day are present during the recovery phase of the decrease, as shown in Figure 4.1. These waves are more obvious for the case when $\alpha = 0.99$. They appear to be similar to the enhanced diurnal variations reported (for example) by Duldig and Humble (1990). According to J.E. Humble and M.L. Duldig (private communication), it is common to see such enhancements in cosmic ray data during the recovery phase of a Forbush decrease. An area of future research could be to test whether enhanced diurnal variations are some resonance effect which occurs when the diffusion coefficients are perturbed from their steady-state value. Alternatively, the waves could simply be due to some kind of damped numerical instability.

Summing the integral intensity of particles in a 1 AU region about Earth, it was found that the intensity after shock-modulation was depressed by approximately 8% ($\alpha=0.9$) and 14.5 % ($\alpha=0.99$). Data from high-latitude neutron monitors show intensity changes of around 20% during 11-year solar cycles. These instruments are sampling the galactic cosmic rays last modulated within a region of approximately 1 AU from Earth. The fact that the simulation results presented here fail to produce the observed intensity decrease from solar minimum to solar maximum suggests that a further modulation process is required in the model. This claim is only valid if the frequency, spatial extent and strength of the shocks used have been correctly estimated, or over-estimated. It is suggested that the frequency and extent of the shocks used are an over-estimate of the real situation for two reasons. Firstly, neutron monitor data do not show observable Forbush decreases as frequently as 26 per year at solar maximum. Secondly, the recovery time for these decreases is observed in the data to be, on average, about one week. The recovery time in Figure 4.1 is much greater than this, suggesting that the radial extent of the shocks in the models presented here is too large. Note however that the large recovery time may be, in part, due to the inadequacy of the two-dimensional model to allow for filling, in the azimuthal direction, of the intensity depression.

From Figure 4.1, the percentage decrease of integral intensity due to the passage of the shock agrees well with observed Forbush decreases. This suggests that the strength of the shocks is well modelled. Finally, it is not expected that flares and coronal mass ejections, originating from generally localized regions on the Sun, would produce interplanetary shocks that would be spherically symmetric, even if such regions merge together and co-rotate in the outer heliosphere. It is concluded that the observed 11-year modulation of cosmic rays above 1 GeV cannot be explained purely by a succession of interplanetary shocks which increase in frequency toward solar maximum. The 11 year cycle of these cosmic rays is most likely due to the combination of the above effect and also the increase in waviness of the neutral sheet and presence of steady-state corotating interaction regions (Kota and Jokipii 1991b) where each effect contributes significantly.

4.6. 3-SPACE DIMENSIONS

In the 2-space dimensional model, the adiabatic energy loss term (the term involving the derivative with respect to momentum) becomes less significant than the others as momentum increases. It is certainly not the dominant coefficient for energies around 10 GeV and higher. If this term can be effectively left out of the model without practically altering the solution for f at a given energy, then the loss of the momentum variable allows the inclusion of the extra space dimension (azimuth coordinate ϕ) without the complexity of

the integrating algorithm increasing by an order of magnitude. Physically, it turns out that without this energy-loss term, there is no mechanism to prevent the heliosphere from eventually "filling up" (ie: reaching the galactic particle density) at any energy. This means that the value for f at any given energy becomes the same as the boundary value for all points within the heliosphere. A 3-space dimensional (momentum-independent) transport equation was integrated in order to test whether this is demonstrated by the model. The equation for the transport equation in this case is

$$\frac{\partial f}{\partial t} = \nabla \cdot (\underline{K}^S \cdot \nabla f) - (\underline{U} + \underline{V}_D) \cdot \nabla f \quad (4.26)$$

where $f = f(t, r, \theta, \phi)$ and

$$\nabla f = \left(\frac{\partial f}{\partial r}, \frac{1}{r} \frac{\partial f}{\partial \theta}, \frac{1}{r \sin \theta} \frac{\partial f}{\partial \phi} \right) \quad (4.27)$$

$$\underline{U} = (U(r), 0, 0) \quad (4.28)$$

and $U(r)$, the magnetic field, 3-dimensional diffusion tensor and drift velocity are as given in Section 1.3. In particular, the drift velocity is calculated numerically via the method presented in Section 2.5. Altogether,

$$\frac{\partial f}{\partial t} = A_r \frac{\partial f}{\partial r} + A_{rr} \frac{\partial^2 f}{\partial r^2} + A_\theta \frac{\partial f}{\partial \theta} + A_{\theta\theta} \frac{\partial^2 f}{\partial \theta^2} + A_\phi \frac{\partial f}{\partial \phi} + A_{\phi\phi} \frac{\partial^2 f}{\partial \phi^2} + A_{r\phi} \frac{\partial^2 f}{\partial r \partial \phi} \quad (4.29)$$

where

$$A_r = A_r(r, \theta, \phi) = \left[\frac{2K_{rr}}{r} + \frac{\partial K_{rr}}{\partial r} - U(r) - (\underline{V}_D)_r \right] \quad (4.30a)$$

$$A_\theta = A_\theta(r, \theta, \phi) = \left[\frac{\cos \theta}{r^2 \sin \theta} K_{\theta\theta} + \frac{1}{r^2} \frac{\partial K_{\theta\theta}}{\partial \theta} - \frac{1}{r} (\underline{V}_D)_\theta \right] \quad (4.30b)$$

$$A_\phi = A_\phi(r, \theta, \phi) = \left[\frac{1}{r^2 \sin \theta} K_{r\phi} + \frac{1}{r \sin \theta} \frac{\partial K_{r\phi}}{\partial r} - \frac{1}{r \sin \theta} (\underline{V}_D)_\phi \right] \quad (4.30c)$$

$$A_{rr} = A_{rr}(r, \theta, \phi) = K_{rr} \quad (4.30d)$$

$$A_{\theta\theta} = A_{\theta\theta}(r, \theta, \phi) = \frac{K_{\theta\theta}}{r^2} \quad (4.30e)$$

$$A_{\phi\phi} = A_{\phi\phi}(r, \theta, \phi) = \frac{K_{\phi\phi}}{r^2 \sin^2 \theta} \quad (4.30f)$$

$$A_{r\phi} = A_{r\phi}(r, \theta, \phi) = \frac{2K_{r\phi}}{r \sin \theta} \quad (4.30g)$$

Because of the mixed-derivative term $\partial^2 f / \partial r \partial \phi$, a standard ADI (or LOD) algorithm would not produce a straight-forward series of tri-diagonal matrix equations to solve. The required matrix equations (non-triangular) turn out to be too computationally intensive to

allow for a fully implicit algorithm to solve for this term. Instead, as in Kota and Jokipii (1983) a modified implicit algorithm is used to solve (4.29), where the $\partial^2 f / \partial r \partial \phi$ term is always explicit but shared in the first two integration steps - the final step being fully implicit. The steps are given by:

$$\frac{f_{t+\frac{\Delta t}{3}} - f_t}{\Delta t} = \lambda \cdot \left(A_r \frac{\delta f_{t+\frac{\Delta t}{3}}}{\delta r} + A_{rr} \frac{\delta^2 f_{t+\frac{\Delta t}{3}}}{\delta r^2} \right) + (1-\lambda) \cdot \left(A_r \frac{\delta f_t}{\delta r} + A_{rr} \frac{\delta^2 f_t}{\delta r^2} \right) + \frac{A_r \phi}{2} \frac{\delta^2 f_t}{\delta r \delta \phi} \quad (4.31a)$$

$$\begin{aligned} \frac{f_{t+\frac{2\Delta t}{3}} - f_{t+\frac{\Delta t}{3}}}{\Delta t} &= \lambda \cdot \left(A_\phi \frac{\delta f_{t+\frac{2\Delta t}{3}}}{\delta \phi} + A_{\phi\phi} \frac{\delta^2 f_{t+\frac{2\Delta t}{3}}}{\delta \phi^2} \right) + (1-\lambda) \cdot \left(A_\phi \frac{\delta f_{t+\frac{\Delta t}{3}}}{\delta \phi} + A_{\phi\phi} \frac{\delta^2 f_{t+\frac{\Delta t}{3}}}{\delta \phi^2} \right) \\ &\quad + \frac{A_r \phi}{2} \frac{\delta^2 f_{t+\frac{\Delta t}{3}}}{\delta r \delta \phi} \end{aligned} \quad (4.31b)$$

$$\frac{f_{t+\Delta t} - f_{t+\frac{2\Delta t}{3}}}{\Delta t} = \lambda \cdot \left(A_\theta \frac{\delta f_{t+\Delta t}}{\delta \theta} + A_{\theta\theta} \frac{\delta^2 f_{t+\Delta t}}{\delta \theta^2} \right) + (1-\lambda) \cdot \left(A_\theta \frac{\delta f_{t+\frac{2\Delta t}{3}}}{\delta \theta} + A_{\theta\theta} \frac{\delta^2 f_{t+\frac{2\Delta t}{3}}}{\delta \theta^2} \right) \quad (4.31c)$$

The stability of this scheme was discussed in Section 3.3c.

It was found that the program converged for timesteps of $\Delta t \leq 2$ seconds (for energies up to 10 GeV), however, as discussed in Section 4.3, this timestep is far too small to allow practical computation of $f(r, \theta, \phi)$. For $\Delta t > 2$ seconds the program diverged. The initial instability occurred at or near the boundary of θ ($\theta=0, \pi$) and then propagated along lines of constant θ . The instability is most likely due to the explicit cross-derivative term. As discussed in Section 3.3c, von Neumann stability analysis could not determine that the above algorithm was unconditionally stable.

The program was re-run for a 2-space dimensional (momentum independent) heliosphere, $f = f(t, r, \theta)$. Because of the lack of the cross-derivative, the ADI/LOD algorithms used to evaluate f were unconditionally stable. For these runs, the boundary of the heliosphere was set to 10 AU to decrease computational time. It was found that the heliosphere did indeed fill up so that $f(r, \theta) = f(r=r_{\max})$ everywhere within the heliosphere after a characteristic length of time which was energy-dependent. As a rule of thumb,

$$(\text{RIGIDITY}) \times (\text{TIME TO FILL HELIOSPHERE}) \approx 3 \times 10^7 \text{ GV}\cdot\text{sec.}$$

The conclusion here is that the adiabatic energy loss term is definitely required, even for high energies. Note however that as momentum (or rigidity) increases, the heliosphere fills closer to the boundary value - seen in the plots of f vs r in Section 4.2 - a reflection of the lessening effect of this term in the balanced steady-state condition.

Note that if $\partial f / \partial t = 0$ (steady-state solution), the transport equation (1.3) can be re-arranged as:

$$\frac{\partial f}{\partial \ln p} = -\frac{3}{(\nabla \cdot \underline{V}_{SW})} \left[\nabla \cdot (\underline{K}^S \cdot \nabla f) - (\underline{V}_{SW} + \underline{V}_D) \cdot \nabla f \right] \quad (4.32)$$

which can be integrated with respect to $\ln p$ instead of time, so long as the divergence in the solar wind remains non-zero. This procedure was undertaken by Kota and Jokipii (1983). This equation was integrated for the case of $f = f(p, r, \theta)$ and no solar-wind termination shock. The initial condition was that the value of the distribution function for a sufficiently high momentum (> 10 GV) was equal to the value at the heliospheric outer-boundary for all points within the heliosphere. Equation (4.32) was then integrated from this high momentum value to the minimum momentum considered. It was found that the value of g_r at the position of Earth was equivalent to that derived by the time-dependent algorithms discussed in Section 4.2.

This method was attempted for the case $f = f(p, r, \theta, \phi)$ however, for the reasons discussed above in this section, the algorithms turned out to be unstable for the momentum-integrating step sizes required.

Chapter 5. Coupling Coefficients for Neutron Monitors and Muon Telescopes.

5.1. INTRODUCTION

The paths of primary cosmic rays incident upon the Earth's magnetic field deviate within the field according to their incident direction and rigidity. As they enter the Earth's atmosphere they interact with atmospheric nuclei to produce secondary cosmic rays. The nucleon and muon component are of interest as they are the secondary particles detected by neutron monitors and muon telescopes respectively - data from these detectors are used in the north-south anisotropy analysis described in Chapter 8. The number and energy range of the secondary particles detected depends on the geographic location, size and pointing direction of the detector. It also depends on the amount of atmosphere and other absorbing material (eg: rock) between the creation site of the secondary particles and the detector. The relationship between the primary cosmic ray distribution and the observed secondary distribution can be quantified in terms of *coupling coefficients* (and atmospheric corrections - see Chapter 7). Such coefficients have been calculated for most muon telescopes in existence before 1976 by Fujimoto *et al.* (1984). For neutron monitor coupling coefficients, see Yasue *et al.* (1982). Baker (1988) has also calculated coefficients for some high-zenith angle telescopes at Mawson. However, coefficients for the Mawson surface muon telescopes SNCOMB and SSCOMB (described in Section 5.3) have not previously been calculated. Some of these coefficients are used in Chapter 8.

This chapter summarises the formalism proposed by Nagashima (1971) to describe the functional form of the coupling coefficients for the muon component of secondary cosmic rays and their relationship to the distribution of primary cosmic rays in space. Results for SNCOMB and SSCOMB are then presented. The theory of coupling coefficients for neutron monitors is described in Yasue *et al.* (1982) and is not repeated here as neutron monitor coupling coefficients were not derived. Subsidiary procedures for *interpolating* neutron monitor coupling coefficients for periods between solar minimum and solar maximum are however discussed, along with the procedure adopted for interpolating the coefficients for 'non-standard' spectral indices (used in Chapter 8).

5.2. FORMALISM

Following Nagashima (1971), let $J(P, \chi, \Lambda)$ be the flux per second per steradian of primary cosmic rays with rigidity P , moving in a direction defined by polar angle χ and azimuth angle Λ relative to some coordinate system. The assumption is made that this distribution is almost isotropic, so that any variation of J with (χ, Λ) is small:

$$J(P, \chi, \Lambda) = J(P) + \delta J(P, \chi, \Lambda) \quad (5.1)$$

The assumption is also made that the anisotropy is axis-symmetric. This may not be true for a general anisotropy, but one can decompose such an anisotropy into a series of axis-symmetric anisotropies and then apply the theory to each component. The coordinate system is defined so that the symmetry axis coincides with $\chi = 0$. The anisotropy can then be written as

$$\frac{\delta J(P, \chi, \Lambda)}{J(P, \chi, \Lambda)} = F(\chi) \cdot G(P) \quad (5.2)$$

where the assumption of separable variables is implicit. $G(P)$ is called the *differential rigidity spectrum of the anisotropy* and $F(\chi)$ is called the *space distribution of the anisotropy*. For the north-south anisotropy discussed in Chapter 8 and other anisotropies for which the coupling coefficients calculated by Fujimoto *et al.* (1984) are applied, it is assumed that $G(P)$ can be written as a power-law spectrum:

$$G(P) = \begin{cases} (P/10)^\gamma & P \leq P_U \\ 0 & P > P_U \end{cases} \quad (P \text{ measured in GV}) \quad (5.3)$$

γ is the spectral index and P_U is the upper limiting rigidity beyond which the anisotropy vanishes. Coupling coefficients are calculated as functions of (γ, P_U) pairs. Note that this spectrum is idealized. We do not expect $G(P)$ to suddenly vanish above $P = P_U$. In practice, P_U is thought of as the average rigidity in the range where $G(P)$ ceases to be significant.

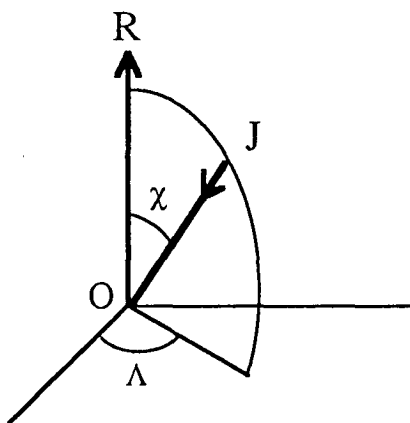


Figure 5.1. The reference axis of the anisotropy is defined by OR. The incident particle direction JO is given by polar angle χ and azimuth angle Λ .

In Nagashima's formalism, $F(\chi)$ is written in terms of a series of Legendre polynomials:

$$F(\chi) = \sum_{n=0}^{\infty} F_n(\chi) = \sum_{n=0}^{\infty} \sum_{m=0}^n f_n^m(\chi) \quad (5.4)$$

where

$$f_n^m(\chi) = \eta_n \cdot P_n^m(\cos \theta_R) \cdot P_n^m(\cos \theta_J) \cdot \cos m(\alpha_J - \alpha_R) \quad (5.5)$$

and

η_n = magnitude of component n of the space distribution,
 (α_R, θ_R) = right-ascension and co-declination of symmetry axis OR
 (α_J, θ_J) = right-ascension and co-declination of incident direction JO.
 (see Figure 5.1)

and

$$P_n^m(x) = \begin{cases} P_{n,m}(x) & m = 0 \\ \sqrt{\frac{2(n-m)!}{(n+m)!}} P_{n,m}(x) & m \neq 0 \end{cases} \quad (5.6)$$

are semi-normalized spherical functions related to the ordinary Legendre functions $P_{n,m}$. $f_n^m(\chi)$ is the m^{th} projected harmonic component of the n^{th} space distribution $F_n(\chi)$. This n^{th} space distribution produces $(n+1)$ such associated projected components, all of which are independent. The projected component $f_n^m(\chi)$ produces a time variation in intensity $D_n^m(t)$ as observed by a terrestrial-based detector which is stationary with respect to the ground and which therefore scans the sky as the Earth rotates about its axis. The total variation observed by this detector is the sum of all the harmonic components of the axis-symmetric anisotropy:

$$D(t) = \sum_{n=0}^{\infty} \sum_{m=0}^n D_n^m(t) \quad (5.7)$$

The relationship between $D_n^m(t)$ and $f_n^m(\chi)$ is expressed through coupling coefficients c_n^m and s_n^m . Let

$$D_n^m(t) = A_n^m \cos \frac{2\pi m}{24} t + B_n^m \sin \frac{2\pi m}{24} t \quad (5.8)$$

where t is solar time measured in hours. The coupling coefficients are defined through

$$\begin{aligned} A_n^m &= c_n^m x_n^m + s_n^m y_n^m \\ B_n^m &= -s_n^m x_n^m + c_n^m y_n^m \end{aligned} \quad (5.9)$$

where

$$\begin{aligned}
x_n^m &= \eta_n \cdot P_n^m(\cos \theta_R) \cdot \cos \frac{2\pi m}{24} t_R \\
y_n^m &= \eta_n \cdot P_n^m(\cos \theta_R) \cdot \sin \frac{2\pi m}{24} t_R
\end{aligned} \tag{5.10}$$

t_R is the local time representation of the reference axis:

$$t_R = \frac{24}{2\pi} (\alpha_R - \alpha_S + \pi) \tag{5.11}$$

where α_R is the right-ascension of the reference axis and α_S is the right-ascension of the Sun. With the above definitions, it can be shown (eg: Baker 1988) that the coupling coefficients for muon telescopes have the form:

$$\begin{aligned}
c_n^m &= \frac{1}{I} \int_{P_c}^{\infty} \int_{\Omega} Y \cdot A \cdot G(P) \cdot P_n^m(\cos \theta_{or}) \cdot \cos m(\psi_{or} - \psi_{st}) \cdot d\omega dP \\
s_n^m &= \frac{1}{I} \int_{P_c}^{\infty} \int_{\Omega} Y \cdot A \cdot G(P) \cdot P_n^m(\cos \theta_{or}) \cdot \sin m(\psi_{or} - \psi_{st}) \cdot d\omega dP
\end{aligned} \tag{5.12}$$

where

$$I = \int_{P_c}^{\infty} \int_{\Omega} Y \cdot A \cdot d\omega dP \tag{5.13}$$

and

$Y = Y(P, d(\theta), x(\theta, \psi))$ is the *response function*, in units of particles $s^{-1}m^{-2}str^{-1}$, which gives the number of muons, produced by primary particles of rigidity P , arriving at the telescope along the direction defined by (θ, ψ) ;

θ, ψ are the zenith angle and azimuth angle of arrival (in local coordinates) of an incident particle;

d is the atmospheric depth along the incident direction (θ, ψ) ;

x is the rock depth along the incident direction (θ, ψ) ;

$A = A(\theta, \psi)$ is the geometrical factor which gives the relative overlap of the two outer trays constituting the muon telescope in the direction (θ, ψ) , in m^2str ;

$\theta_{or} = \theta_{or}(P, \lambda_{st}, \psi_{st}, \theta, \psi)$ is the geographic co-latitude defining the asymptotic direction of approach of primary particles with rigidity P which produce muons arriving at the telescope with a local direction defined by (θ, ψ) ;

$\psi_{or} = \psi_{or}(P, \lambda_{st}, \psi_{st}, \theta, \psi)$ is the corresponding geographic longitude of the asymptotic direction;

λ_{st}, ψ_{st} are the geographic latitude and longitude of the telescope site;

Ω is the solid angle subtended by the two outer trays of the muon telescope;

$d\omega$ is the element of solid angle ($= \sin(\theta) d\theta d\psi$);

P_c is the cut-off rigidity below which $Y \equiv 0$.

Note that the coupling coefficients are a function of (γ, P_u) which define the rigidity spectrum of the anisotropy. Fujimoto *et al.* (1984) and Yasue *et al.* (1982) tabulate c_n^m

and s_n^m for values of $\gamma = -2.0, -1.5, -1.0, -0.5, 0.0, 0.5$ and $P_\mu = 30, 50, 100, 200, 500$ and 1000 GV.

5.3. RESULTS FOR SNCOMB and SSCOMB

Vrana (1976) fully describes the configuration of the Mawson high zenith angle surface muon telescopes SNCOMB and SSCOMB. The telescopes consist of three vertical walls of Gieger tubes. However, the coupling coefficients are only a function of the two outer trays, depicted in Figure 5.2:

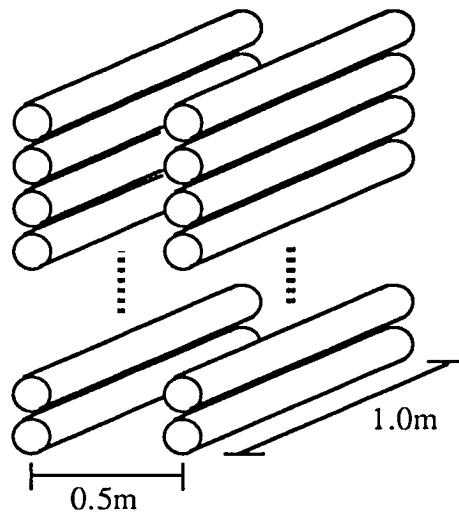


Figure 5.2. Schematic of the arrangement of the Gieger-tubes (diameter 4cm) constituting the two outer walls of the muon telescopes SNCOMB and SSCOMB. The tubes are aligned east/west so that the telescope points north/south.

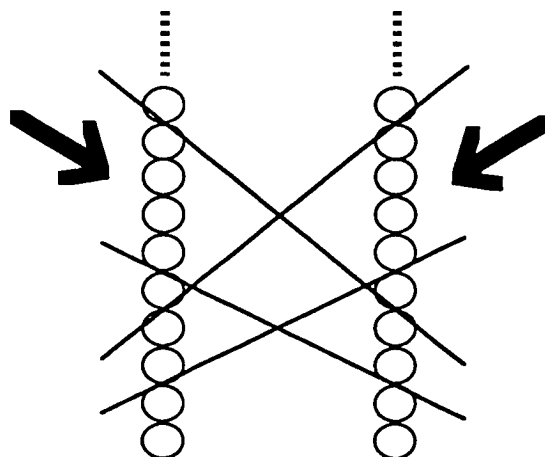


Figure 5.3. Side view of the outer walls of the muon telescope depicted in Figure 5.2 showing the allowed directions of incidence (both north and south). Coincidence between the walls occurs only if the difference in height of the tube triggered in one wall compared to the other is as depicted.

The tubes are hard-wired so that a coincidence is recorded *only* if the path of the secondary particle is within the solid angle shown in Figure 5.3. No other hard-wired arrangements giving different incident acceptance solid angles were present.

In order to calculate the coupling coefficients c_n^m and s_n^m for this configuration using the method given by Baker (1988), it is necessary to treat each telescope as the sum of two configurations, namely, those shown in Figure 5.4a and Figure 5.4b:

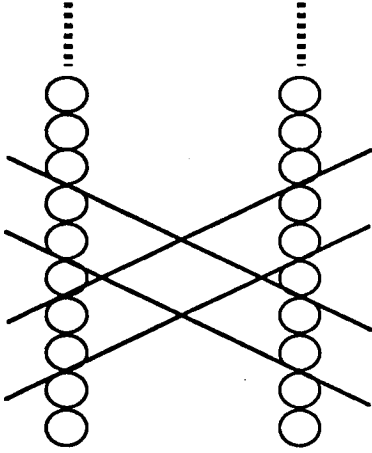


Figure 5.4a

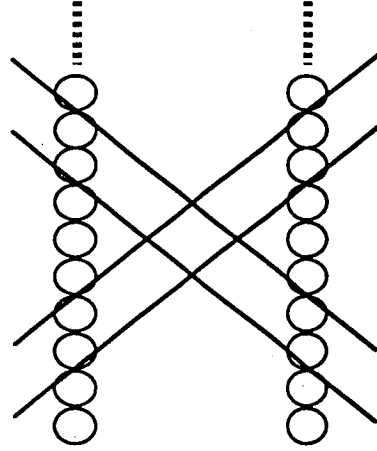


Figure 5.4b

These diagrams show the high-zenith wiring configuration (a) and low-zenith configuration (b) which combine to allow the coincidence solid angle for telescopes SNCOMB and SSCOMB shown in Figure 5.3.

Each pair of tubes in one wall is hard-wired with a pair of tubes '3-up' in the other wall in the case of the arrangement shown in Figure 5.4a, or '5-up' in the case of Figure 5.4b, for both the north and south incident directions. SNCOMB and SSCOMB coupling coefficients (for the arrangement depicted in Figure 5.3) can be calculated from

$$c_n^m = \frac{c_{n,a}^m I_a + c_{n,b}^m I_b}{(I_a + I_b)}$$

$$s_n^m = \frac{s_{n,a}^m I_a + s_{n,b}^m I_b}{(I_a + I_b)} \quad (5.14)$$

where c_n^m , s_n^m , and I_a are the coupling coefficients and total-intensity for the telescope configuration depicted in Figure 5.4a. c_n^m , s_n^m and I_b are the coupling coefficients and total intensity for the telescope configuration depicted in Figure 5.4b. SNCOMB and SSCOMB coupling coefficients calculated using this method are tabulated in Appendix 4 and Appendix 5 respectively.

5.4. INTERPOLATING COUPLING COEFFICIENTS

As mentioned previously, the coupling coefficients are functions of (γ, P_U) , the parameters describing the spectral index of the anisotropy. In theory, the coefficients could be calculated for any value of γ or P_U . However, for computational convenience they are tabulated for a discrete set of each parameter, where the range of each is within the expectation value for heliospheric anisotropies. In order to calculate c_n^m and s_n^m for values of γ and P_U , other than those tabulated in Appendices 4 and 5 or found in Fujimoto *et al.* (1984) and Yasue *et al.* (1982) (for muon telescopes and neutron monitors respectively), a polynomial interpolation procedure was used. Examples of the fitted polynomials to c_I^0 (required for the north-south anisotropy analysis of Chapter 8) as a function of γ for a fixed P_U for the Mt. Wellington neutron monitor MTWIQS and the Mawson muon telescope SNCOMB are shown in Figure 5.5. The various P_U 's used correspond to the values for which coupling coefficients had been tabulated in the above references. As can be seen, the functional dependence of c_I^0 with γ is very smooth over the range $\gamma \in (-2.0, 0.5)$. The sign difference between the neutron monitor and muon telescope coefficients reflects the fact that the two detectors are viewing different regions of space. The cosmic rays detected by the neutron monitors are generally of lower energy and thus their paths are more curved by the Earth's magnetic field. Interpolated values for $\gamma \in (0.0, 0.5)$ were found to be accurate to within 5% of those calculated directly using equation 5.12 for any of the telescopes. Extrapolated values ($\gamma > 0.5$) are expected to be less accurate, although values up to $\gamma = 0.7$ were thought to be acceptable.

5.5. NEUTRON MONITOR COUPLING COEFFICIENTS for NON-SOLAR MINIMUM / MAXIMUM PERIODS.

Yasue *et al.* (1982) list separate coefficients for neutron monitors during solar minimum and solar maximum conditions. The values of the coefficients change significantly from solar minimum to solar maximum. This is mainly due to the primary proton energy spectrum changing significantly in the energy range for which neutron monitors are sensitive. The change in the primary spectrum in the energy range for which muon telescopes are sensitive is much less significant, mainly due to the fact that higher energy particles are less modulated by solar activity. Hence muon telescope coupling coefficients are assumed to be constant over the solar cycle. It was decided to use an interpolating procedure to obtain accurate neutron monitor coefficients c_I^0 (used in Chapter 8) in the years between solar minimum and solar maximum. That is,

$$c_I^0 = \frac{w_1 c_{I,solar\ min.}^0 + w_2 c_{I,solar\ max.}^0}{(w_1 + w_2)} \quad (5.15)$$

where $(w_1, w_2) = (1, 0)$ at solar minimum and $(0, 1)$ at solar maximum. Assuming that solar minimum occurred around 1975-6 and solar maximum around 1982, the weights (w_1, w_2) used for other years for which the north-south anisotropy analysis (Chapter 8) was undertaken are given in Table 5.1.

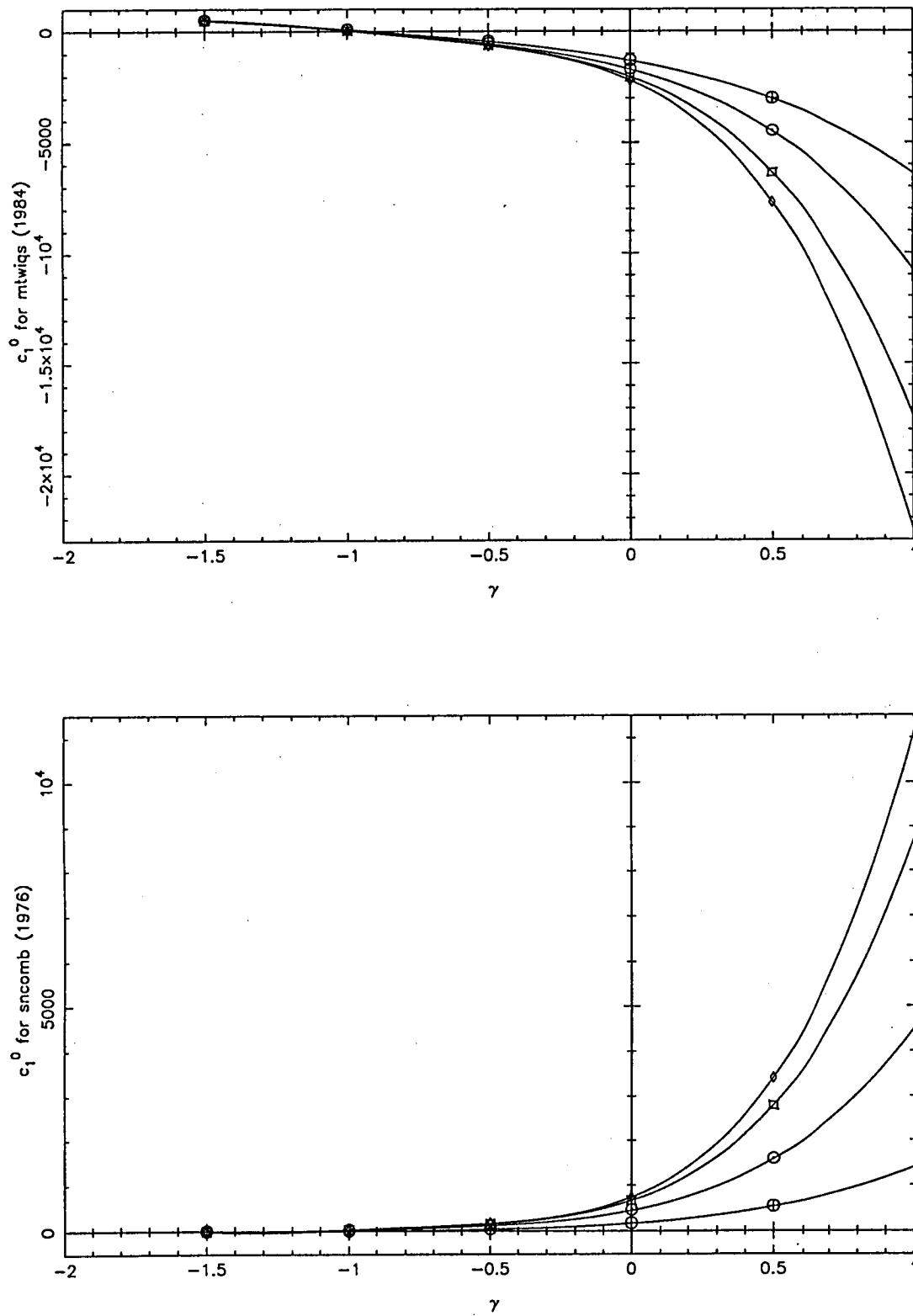


Figure 5.5. Examples of polynomial fits to coupling coefficient c_1^0 for neutron monitor MTWIQS (Mt. Wellington, Tasmania) and muon telescope SNCOMB (Mawson, Antarctica) as a function of spectral index γ . In the top plot, the traces are for $P_U = 100, 200, 500$ and 1000 GV from top to bottom respectively. In the bottom plot, the traces are for $P_U = 100, 200, 500$ and 1000 GV from bottom to top respectively.

| year | w_1 | w_2 |
|------|-------|-------|
| 1975 | 1 | 0 |
| 1976 | 1 | 0 |
| 1977 | 0.9 | 0.1 |
| 1978 | 0.8 | 0.2 |
| 1982 | 0 | 1 |
| 1983 | 0.3 | 0.7 |
| 1984 | 0.4 | 0.6 |
| 1985 | 0.7 | 0.3 |

Table 5.1. Weights used in determining neutron monitor coupling coefficients for times other than strictly solar minimum/maximum conditions. See equation 5.15.

The weights in Table 5.1 were chosen qualitatively by observing the relative cosmic ray intensity as seen by the Mt. Wellington neutron monitor over solar cycle 21 and surrounding years. This intensity, shown in Figure 5.6, was used as a measure of absolute solar activity over the cycle.

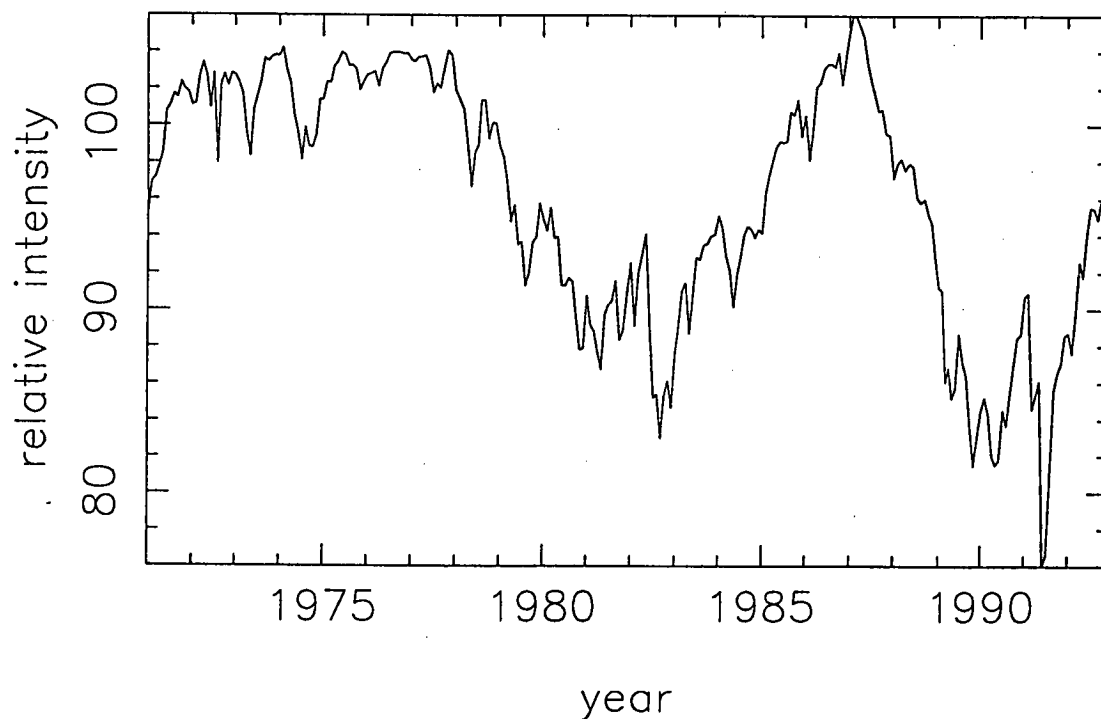


Figure 5.6. Count rate of the Mt. Wellington neutron monitor.

Chapter 6. Intensity Waves and the Neutral Sheet.

6.1. INTRODUCTION TO THE NEUTRAL SHEET

In this chapter, the concept of the neutral sheet is formally introduced. A formula describing a neutral sheet of arbitrary shape is then derived. This formulation is used to derive the actual three-dimensional shape of the neutral sheet from measurements of the latitudinal displacement of the sheet from Earth (as a function of time). The neutral sheet position is then correlated with observed "Intensity Waves" to demonstrate the presence of an asymmetry in the intensity of cosmic rays across the neutral sheet for certain periods in 1982 and 1984. This analysis demonstrates that small but measurable modulation occurs for cosmic rays with energies well above 1 GeV and that the neutral sheet is a significant large scale structure which affects the modulation of high energy cosmic rays.

The Sun has associated with it a magnetic field. This magnetic field is dragged out into the heliosphere by the plasma (solar wind) being ejected from the Sun. For a detailed description of the solar wind and a review of the hydrodynamic equations governing its outflow (developed by E.N. Parker), see Brandt 1970. The solar wind flow is virtually radial at low and mid-latitudes. At the time of solar-minimum the Sun's magnetic field at its surface looks dipolar (like the field of a bar-magnet). The dipole axis is aligned with the rotation axis of the Sun. Further out in the heliosphere, the region around the heliographic equator defines a discontinuity in the radial component of the field. This is illustrated in Figure 6.1. This discontinuity is called the *neutral sheet* or *current sheet*. Such a sheet segments the heliosphere into so-called *sectors*. For the case when the Sun's magnetic field corresponds to that shown in Figure 6.1, the region above the neutral sheet defines an *away* sector because the direction of the radial component of the heliospheric magnetic field is away from the Sun. The region below the neutral sheet is a *towards* sector. This polarity existed during (for example) 1970-1980 and is referred to as "*A positive*" (as opposed to *A negative*).

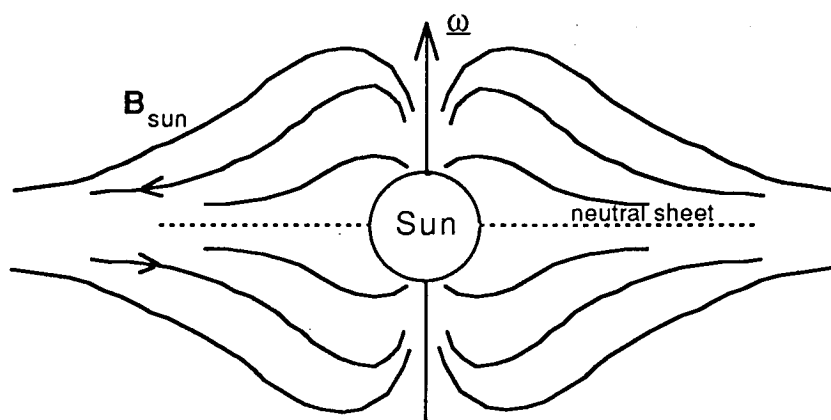


Figure 6.1. The Sun's dipolar field is dragged outward into the heliosphere by the radially flowing solar wind. Along the heliographic equator there is a discontinuity in the radial component of the heliospheric magnetic field. This is called the neutral sheet.

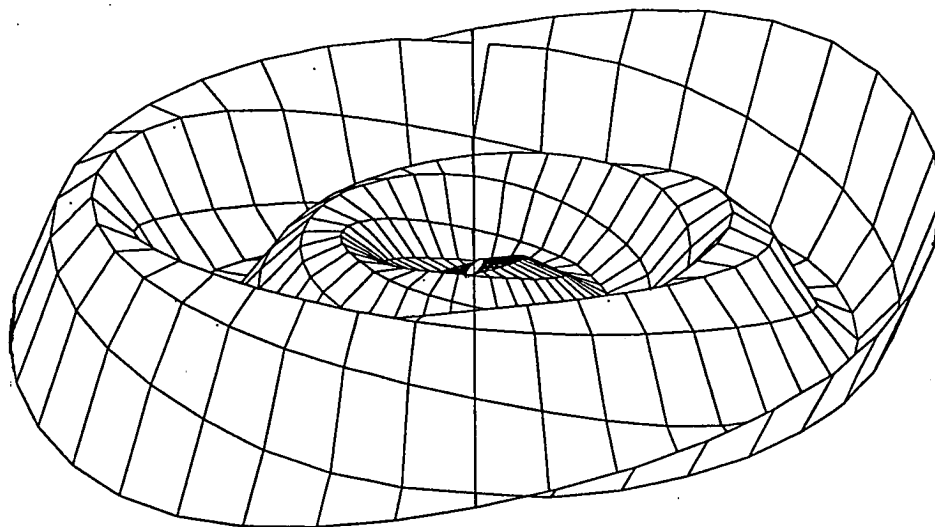


Figure 6.2a. A contour diagram of a 2-sector neutral sheet for a tilt-angle of 15 degrees. The Sun is located at the centre of the diagram and the neutral sheet extends to a heliographic radius of 12 AU.

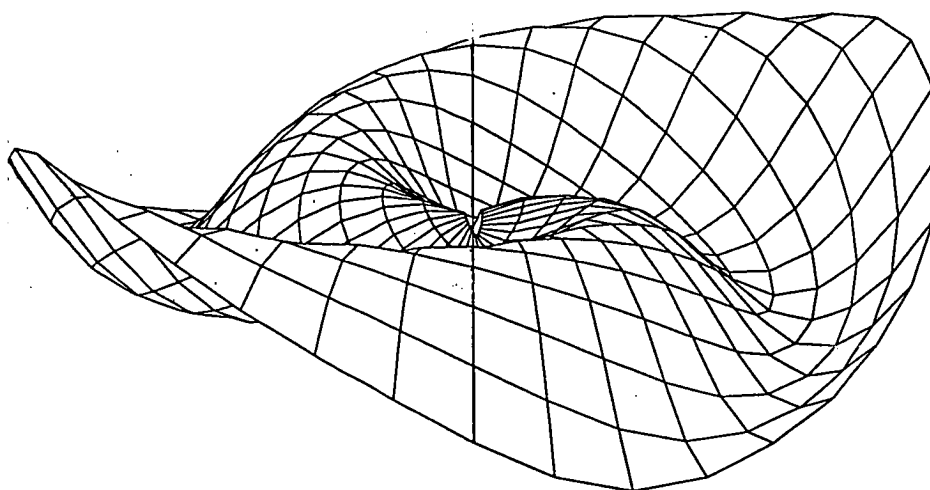


Figure 6.2b. A contour diagram of a 4-sector neutral sheet for a tilt-angle of 15 degrees. The Sun is located at the centre of the diagram and the neutral sheet extends to a heliographic radius of 6 AU.

Except for times around field-reversal (see Section 1.1), the Sun's magnetic field near its surface is approximated by a dipole field whose inclination α to the rotation axis of the Sun is zero at solar-minimum and increases steadily towards solar maximum (Behannon *et al.* 1989, Smith 1990). When α is non-zero the combined effect of the radial outflow of the solar wind and the rotation of the Sun produce a neutral sheet which is wavy. Figure 6.2a shows what the neutral sheet looks like for a tilt-angle $\alpha = 15^\circ$. From this figure it is clear that if α is greater than the heliographic latitude of the position of the Earth, then the Earth will pass from a *towards* to an *away* sector and back again as the Sun rotates every 27 days. This is the case of a so-called two sector structure. In practice, the Sun's magnetic field is not purely dipolar. For more complicated cases the Earth may pass through two towards and two away sectors every solar rotation as shown in Figure 6.2b. In this case the interplanetary field at Earth would be said to have a four-sector structure. In other cases the size of successive sectors may vary in space and time. It is important in the study of cosmic ray modulation to identify these sector regions because gyro-orbits and drift velocities have opposite directions in the differing regions. The neutral sheet therefore seems to be an important large-scale structure which affects the modulation of the cosmic rays.

Hoeksema *et al.* (1982, 1983) describe a method of inferring the neutral sheet position through observations of the photospheric magnetic field structure made at the Stanford Solar Observatory. They give positions of the neutral sheet as a function of heliographic latitude and longitude. It can be seen from their plots that the neutral sheet roughly follows a two-sector or four-sector structure except perhaps around solar maximum when the field is reversing.

6.2. PARAMETERIZING THE NEUTRAL SHEET

Let $f(\theta, \phi)$ describe the neutral sheet on the source surface. Here θ is the heliographic latitude and ϕ is the heliographic longitude of a point on the neutral sheet. The aim is to find a suitable generalized formula for $f(\theta, \phi)$. The source surface is taken by Hoeksema *et al.* (1982, 1983) to be $2.25 R_s$ (R_s is the radius of the Sun). Let ω denote the rotational frequency of the Sun. Let \underline{V} be the solar wind speed and assume that this is purely radial so that $\underline{V} = V\hat{r}$. Define a cartesian coordinate system centred at the Sun with the z-axis aligned with the rotation axis of the Sun and the x-axis defined by $\phi = 0$ as illustrated in Figure 6.3.

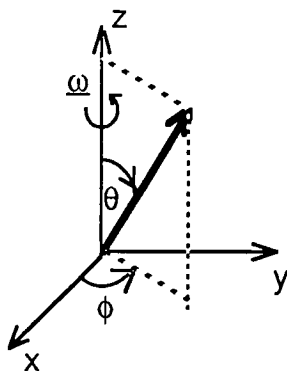


Figure 6.3. The orientation of the coordinate system used in developing the equations for the neutral sheet. The Sun is at the origin. θ is the heliographic co-latitude or polar-angle and ϕ is the heliographic longitude or azimuth angle.

$$\begin{aligned}
\hat{\omega} &= \hat{z} \\
|\hat{\omega}| &= \Omega \\
z &= r \cos \theta \\
y &= r \sin \theta \sin \phi \\
x &= r \sin \theta \cos \phi
\end{aligned} \tag{6.1}$$

It is assumed in this derivation that the solar wind carries out the magnetic field radially. This is not strictly true, especially near the Sun (see Weber and Davis Jr. 1967), however any inaccuracies introduced because of this assumption are insignificant. If $\Omega = 0$ (ie: the Sun is not rotating) then the neutral sheet satisfies

$$f(\theta, \phi) = 0 \tag{6.2}$$

for any $r \geq 2.25 R_s$. However, $\Omega \neq 0$. In the frame of reference of the rotating Sun, the solar wind is carried out a distance dr in time dt where $dr = Vdt$. In this time the heliographic coordinate system has rotated through an angle $d\phi = \Omega dt$. Hence

$$\frac{d\phi}{dr} = \frac{\Omega}{V} \tag{6.3}$$

$$\text{or} \quad \phi = \frac{(r - 2.25 R_s) \Omega}{V} \tag{6.4}$$

In other words, in the time that the solar wind transports the surface magnetic field a distance r , the rotating frame of reference of the Sun has rotated through an angle ϕ given by (6.4). Since r of the order around 1 AU or greater is the region of concern, R_s in (6.4) is negligible. Therefore, in the rotating frame of reference, the neutral sheet now satisfies the equation

$$f(\theta, \phi + \frac{r\Omega}{V}) = 0 \tag{6.5}$$

for $r \gg R_s$. Consider an observer who is stationary with respect to distant stars, viewing the rotational period of the Sun as τ , where $\tau = 2\pi/\Omega$. In this frame of reference, the azimuth of a fixed point in the reference frame of the rotating Sun varies as $\Omega t = 2\pi t/\tau$. The neutral sheet then satisfies the equation

$$f(\theta, \phi + \frac{r\Omega}{V} - \Omega t) = 0 \tag{6.6}$$

6.2a Calculating f : 2-sector structure.

A 2-sector neutral sheet arises from a simple tilted dipole model of the Sun's magnetic field. For this field configuration, the neutral sheet on the source surface is just the locus of points lying perpendicular to, and symmetric with, the dipole. If the tilt-angle α is zero, the neutral sheet coincides with the plane defined by the solar equator. With the coordinate system defined by Figure 6.3, the locus of points defining the neutral sheet on the source surface, as shown in Figure 6.4, satisfies the equation

$$z = (\tan \alpha) y \tag{6.7}$$

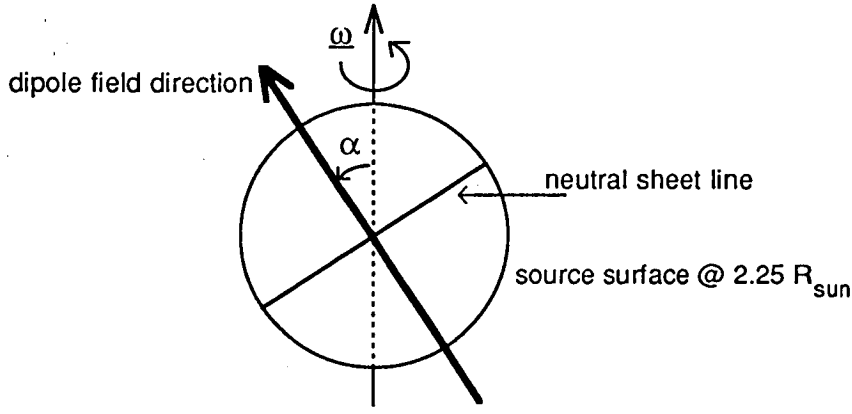


Figure 6.4. The dipole magnetic field is tilted an angle α to the rotation axis of the Sun. The neutral sheet is circular on the source-surface.

Substituting values for z and y described in (6.1) gives

$$r \cos \theta = (\tan \alpha) r \sin \theta \sin \phi \quad (6.8)$$

Therefore

$$\theta = \frac{\pi}{2} - \tan^{-1} (\tan \alpha \sin \phi) \quad (6.9)$$

or

$$f(\theta, \phi) = \theta - \frac{\pi}{2} + \tan^{-1} (\tan \alpha \sin \phi) = 0 \quad (6.10)$$

which gives the formula for the neutral sheet on the source surface. For $r \geq 2.25R_s$,

$$\theta = \frac{\pi}{2} - \tan^{-1} \left(\tan \alpha \sin \left(\phi + \frac{r\Omega}{V} \right) \right) \quad (6.11)$$

by equation (6.5) and in the fixed frame (stationary with respect to distant stars),

$$\theta(t) = \frac{\pi}{2} - \tan^{-1} \left(\tan \alpha \sin \left(\phi + \frac{r\Omega}{V} - \Omega t \right) \right) \quad (6.12)$$

by equation (6.6).

6.2b Generalized formula for the neutral sheet.

For small α , $\tan \alpha \approx \alpha$. Note that $(\pi/2 - \theta) \in [-\alpha, \alpha]$, so for small α , $\tan(\pi/2 - \theta) \approx \pi/2 - \theta$. Hence for small α , the equation for the neutral sheet becomes

$$\theta = \frac{\pi}{2} - \alpha \sin \left(\phi + \frac{r\Omega}{V} - \Omega t \right) \quad (6.13)$$

Consider a four-sector neutral sheet. The latitude of the neutral sheet in heliographic coordinates $\lambda = \pi/2 - \theta$ reaches $+\alpha$ twice per revolution $\phi \rightarrow \phi + 2\pi$. Hence a four-sector neutral sheet satisfies the equation

$$\theta = \frac{\pi}{2} - \alpha \sin\left(2\phi + \frac{r\Omega}{V} - 2\Omega t\right) \quad (6.14)$$

for small α . Generalizing, an n -sector neutral sheet would satisfy

$$\theta = \frac{\pi}{2} - \alpha \sin\left(\frac{n}{2}\phi + \frac{r\Omega}{V} - \frac{n}{2}\Omega t\right) \quad (6.15)$$

again for small α . In practice, the neutral sheet tilt angle may not be small enough to justify the above approximations. Also the neutral sheet may not be a pure 2 sector or 4 sector shape - in the sense that the average shape may be 2 or 4 sector but there may be small fluctuations in the shape on a local scale. Just as an arbitrary function can be represented as a Fourier series of sine and cosine functions, it is proposed that a neutral sheet with arbitrary shape can be represented as a sum of a 2 sector, 4 sector, 6 sector, etc... neutral sheet, each being represented by a formula given by (6.15). That is, for a general neutral sheet shape,

$$\theta(t) = \frac{\pi}{2} - \sum_{i=1}^n \left[\alpha_{2i-1} \sin\left(i\left[\phi - \Omega t\right] + \frac{r\Omega}{V}\right) + \alpha_{2i} \cos\left(i\left[\phi - \Omega t\right] + \frac{r\Omega}{V}\right) \right] \quad (6.16)$$

The neutral sheet is specified by the values of the coefficients α_i . From the above discussion, this formula should have the correct ϕ dependence. The α_i values are no longer constrained to be small, since any inaccuracies in the approximation which lead to the forms of the neutral sheet given by equations (6.13) to (6.15) will be accounted for by higher order terms in equation (6.16).

6.3. DETERMINING THE NEUTRAL SHEET FROM DATA

This section describes the method used to determine the actual shape of the neutral sheet in terms of the model given by equation (6.16). J.T. Hoeksema (private communication) has supplied neutral sheet data obtained from observations at the Stanford Solar observatory. The data give the latitudinal displacement of the neutral sheet from Earth (at the same heliographic radius and azimuth angle) as a function of time. Specifically, one data point per day was provided. Let (r_e, θ_e, ϕ_e) denote the position of Earth and $(r_{ns}, \theta_{ns}, \phi_{ns})$ denote the position of the neutral sheet in heliographic coordinates. Call the neutral sheet data $D(t)$. Then

$$D(t) = \theta_{ns}(t) - \theta_e(t)$$

$$\text{where } r_{ns} = r_e, \text{ and } \phi_{ns} = \phi_e \quad (6.17)$$

$\theta_{ns}(t)$ is specified by the model (equation 6.16) and $\theta_e(t)$ is given by

$$\theta_e(t) = \frac{\pi}{2} - \tan^{-1}(\tan \xi \cos \phi_c(t)) \quad (6.18)$$

where
$$\phi_e(t) = \frac{2\pi t}{\tau_e} + \phi_0 \quad (6.19)$$

(following the same argument for the equation of a circle offset from the rotation axis of the Sun given by equation 6.9). In equation (6.18) $\xi \approx 7.5^\circ$. In (6.19) $\tau_e = 365.25$ days, the rotational period of Earth about the Sun and $\phi_0 \approx 76^\circ$. Both ξ and ϕ_0 vary very slightly from year to year. An accurate value of both for any particular year can be found in the *Astronomical Almanac*. The value of ϕ_0 was determined from the longitude of the ascending node of the solar equator on the ecliptic.

The coefficients α_i in equation (6.16) were found from fitting the linear model

$$\begin{aligned} \frac{\pi}{2} - D(t) - \theta_e(t) &= \frac{\pi}{2} - \theta_{ns}(t) \\ &= \sum_{i=1}^n \left[\alpha_{2i-1} \sin\left(i\left[\phi_e - \Omega t\right] + \frac{r_e \Omega}{V}\right) + \alpha_{2i} \cos\left(i\left[\phi_e - \Omega t\right] + \frac{r_e \Omega}{V}\right) \right] + \alpha_{2n+1}t + \alpha_{2n+2} \end{aligned} \quad (6.20)$$

over a sufficient number of days, using the generalized least-squares routine described in Chapter 14 of Press *et al.* (1986). The last two terms on the right hand side of equation (6.20) allow for a linear offset of the latitude of symmetry of the neutral sheet from the solar equator. Figure 6.5 shows a comparison between the supplied neutral sheet data and the fitted model using $n=6$ when the neutral sheet had a roughly 2-sector structure during 1982. Figure 6.6 shows the same fit for $n=10$. Figure 6.7 shows a 2-sector fit in 1984 for $n=6$ and Figure 6.8 shows the same fit for $n=10$. As can be seen by comparing these figures, there is no gain in accuracy in using $n>6$. Because the neutral sheet structure changes as a function of time, any one model fit is only accurate for a finite length of time. This length of time is a function of the order of the fit (ie: value of n used) and a function of how fast the neutral sheet itself is changing shape, for example transiting from a 2-sector to a 4-sector structure. As a rough guide, the fit is generally accurate for about 80 to 100 days using $n=6$.

Hoeksema derived the neutral sheet data by using Zeeman observations of the line of sight component of the photospheric magnetic field (details in Hoeksema *et al.* 1982) and assuming a 4.5 day lag in the field from the source surface to Earth. Obviously the time-lag depends on the solar wind speed V which varies between roughly 300 and 700 km s⁻¹. Cramp (1991) noticed that the times of sector field crossing predicted by the above model and the actual time of crossing observed by various sources including satellite data (J.E. Humble, *private communication*) varied by up to 2 days in some instances. Cramp also found instances where the Earth was known to have passed from one sector to another and back again over the period of one day, but the model predicted that the neutral sheet, although coming close, did not actually cross the helio-latitude of the Earth. Such observations place limits on the accuracy of the above model which are estimated to be about ± 1 day in the time coordinate and ± 0.2 radians along the latitude coordinate.

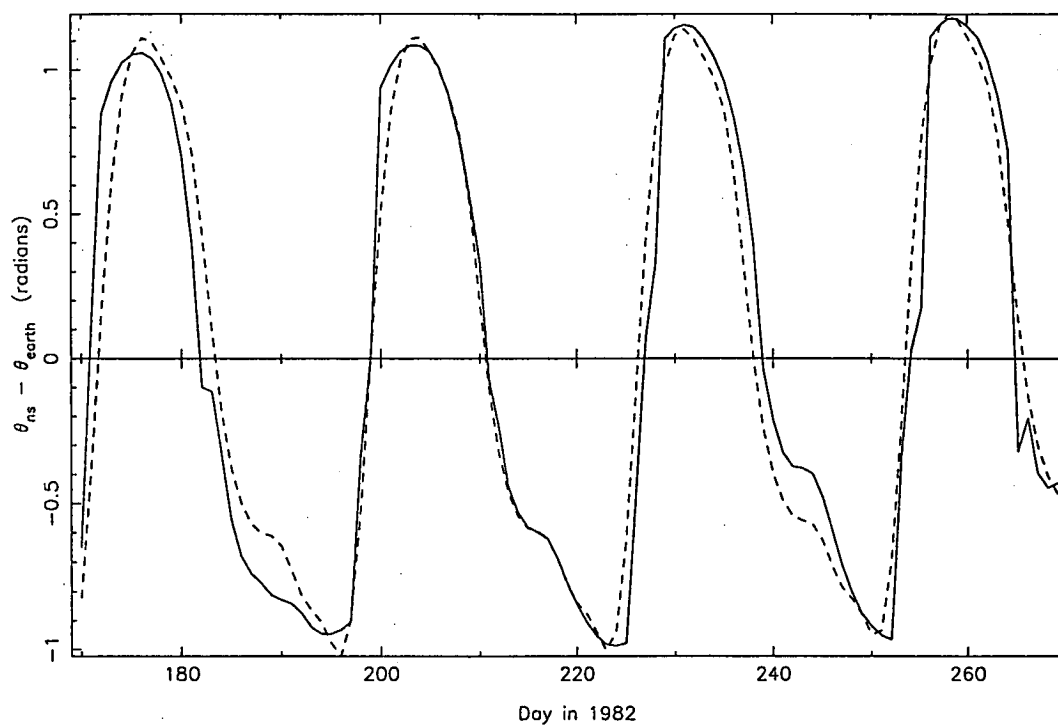


Figure 6.5. Latitudinal displacement of the neutral sheet from Earth during days 170 to 270 of 1982. The neutral sheet has a 2-sector structure. The solid line is the data supplied by Hoeksema (*private communication*) and the dashed line is the model fit using $n=6$.

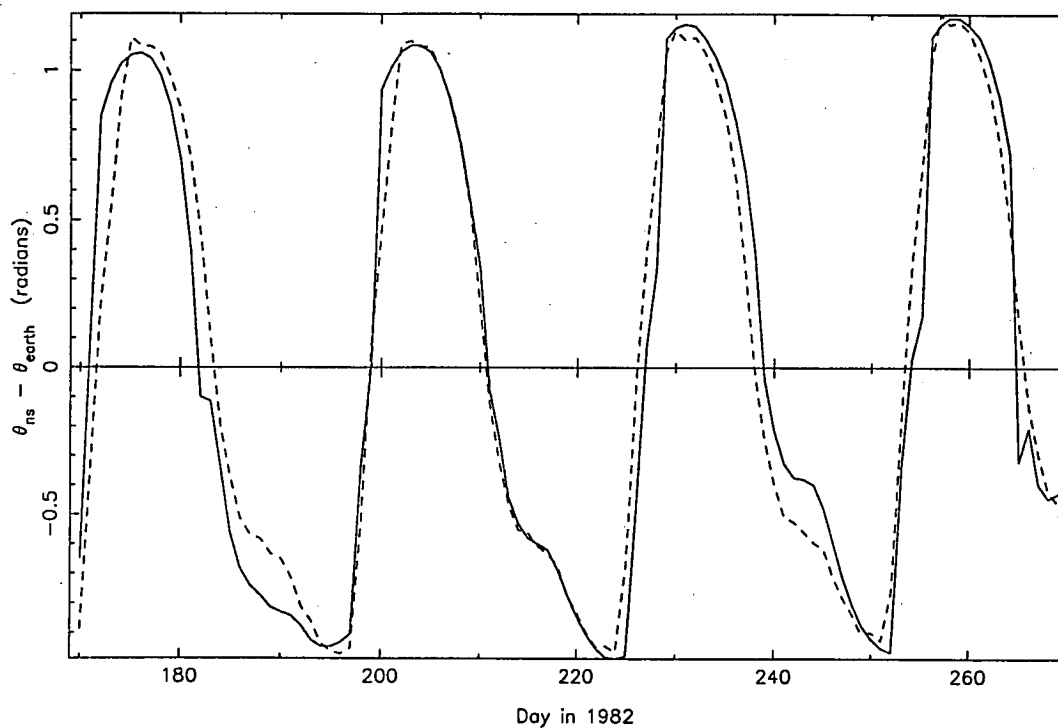


Figure 6.6. Latitudinal displacement of the neutral sheet from Earth during days 170 to 270 of 1982. The neutral sheet has a 2-sector structure. The solid line is the data supplied by Hoeksema (*private communication*) and the dashed line is the model fit using $n=10$.

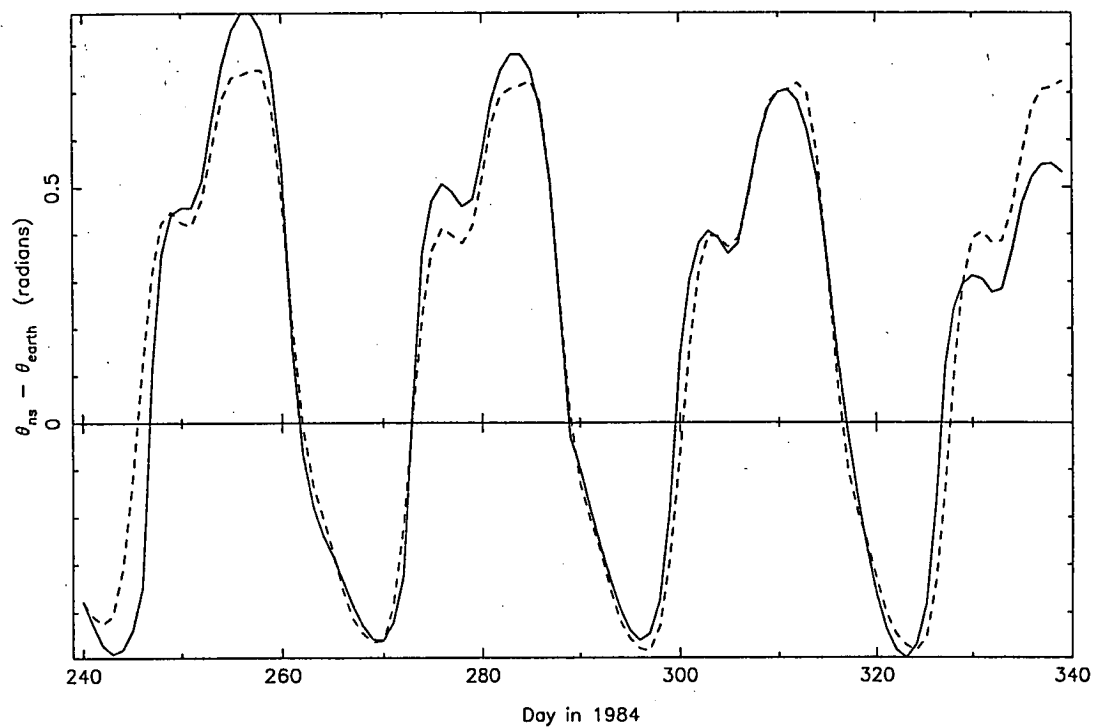


Figure 6.7. Latitudinal displacement of the neutral sheet from Earth during days 240 to 340 of 1984. The neutral sheet has a 2-sector structure. The solid line is the data supplied by Hoeksema (*private communication*) and the dashed line is the model fit using $n=6$.

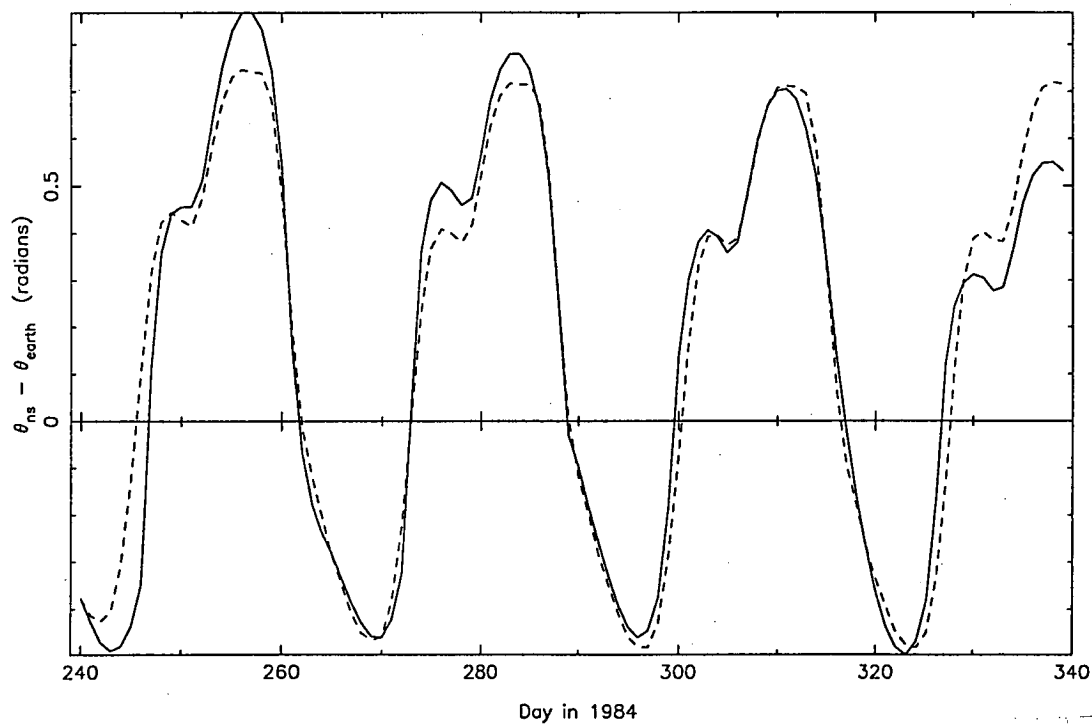


Figure 6.8 Latitudinal displacement of the neutral sheet from Earth during days 240 to 340 of 1984. The neutral sheet has a 2-sector structure. The solid line is the data supplied by Hoeksema (*private communication*) and the dashed line is the model fit using $n=10$.

6.4. INTENSITY WAVES

So-called *isotropic intensity waves* have been observed in cosmic ray data from Mawson and other observatories between 1982 and 1986. For a description of the telescope systems operating during this period, see Duldig (1990). There is evidence in the data for the existence of these waves for post 1986 periods, however the amplitude of the waves has never been as large as it was in 1982 and 1984. The rest of this chapter concentrates on the intensity waves detected at Mawson during those two years. The waves are characterized by a 13.5 or 27 day approximately sinusoidal variation in the count-rate of cosmic ray detectors. The term *isotropic* is used because such a variation, when it is present, appears in data collected by other detectors around the world and the phase of the variation is the same at each detector. Moreover, it appears that there is no energy dependence of the variation in the energy range of the order 10 to 150 GeV. A detailed description of the intensity wave phenomenon has been given by Duldig *et al.* 1985 and Jacklyn *et al.* 1987 and a summary is reproduced below. It has been proposed (Duldig 1987) that the observed waves in the cosmic ray data could be interpreted as being due to sampling the cosmic ray particles from regimes of the heliosphere above and below the neutral sheet and that the neutral sheet, at times when the waves are present in the data, acts as a boundary between two regimes of the heliosphere with unequal cosmic ray density. This proposal is investigated here by calculating the relative volume of a *sampling sphere*, centred at Earth, above and below the neutral sheet during times when the intensity waves were present in the data. This sampling sphere represents the volume of space, around Earth, within which galactic cosmic ray particles are last modulated before being detected by terrestrial-based cosmic ray detectors.

6.4a Intensity wave definition.

The intensity waves are derived from the Mawson underground data (denoted by UG) by removing two other varying components. Isotropic phenomena, such as Forbush decreases, having an E^{-1} type energy (E) spectrum are removed from the data by applying the relevant scaling factor to neutron monitor data (denoted by NM) from the same site. Similarly the North-South anisotropy component is removed using a scaling factor applied to the Nagoya (denoted by GG) data. These scaling factors are related to the corresponding coupling coefficients (see Chapter 5) of the detectors involved. The resulting residual variation is thus defined as

$$W = \left(\frac{\Delta I}{I_o} \right)_{UG} - c_1 \cdot \left(\frac{\Delta I}{I_o} \right)_{NM} - c_2 \cdot \left(\frac{\Delta I}{I_o} \right)_{GG} \quad (6.21)$$

The reference level I_o for each detector corresponds to an arbitrary reference day which must be the same for all three detectors. Normalization of the wave W about zero is thus achieved by selecting a suitable reference day. See Jacklyn *et al.* (1987) for a discussion on the derivation of the appropriate scaling constants c_1 and c_2 appearing in equation (6.21).

6.4b Sampling sphere.

The notion of a *sampling sphere* is used to estimate the relative volume of interplanetary space from which cosmic rays are sampled by terrestrial-based detectors. Let the sampling sphere be that volume of interplanetary space within a sphere radius of R_{ss} centred at Earth. R_{ss} should be of the same order of magnitude as the gyro-radius of the primary cosmic rays which are sampled. This is required so that the sampling sphere includes the relevant volume of space over which the observed modulation is occurring.

The neutral sheet separates the northern hemisphere interplanetary magnetic field from the southern field. The proportion of the sampling sphere above the neutral sheet is a first order estimate of the proportion of observed cosmic rays arriving from above the neutral sheet. Figure 6.9 is a graphical representation of a sampling sphere of radius 1 AU. Let the index k be defined through

$$k = 2 \cdot \left(\frac{V_U}{V_T} - \frac{1}{2} \right) \quad (6.22)$$

where V_U is the volume of the sampling sphere above the neutral sheet and V_T is the total volume of the sphere. The range of k is $[-1, +1]$. If $k = -1$ then the sampling sphere is totally below the neutral sheet, ie: is totally in the southern IMF. If $k = +1$ the sphere is totally in the northern IMF and if $k = 0$ the sampling sphere is equally divided above and below the neutral sheet. To evaluate k at any time it is essential to know the position of the neutral sheet. This was done using equation (6.20) and the method given in Section 6.3 above.

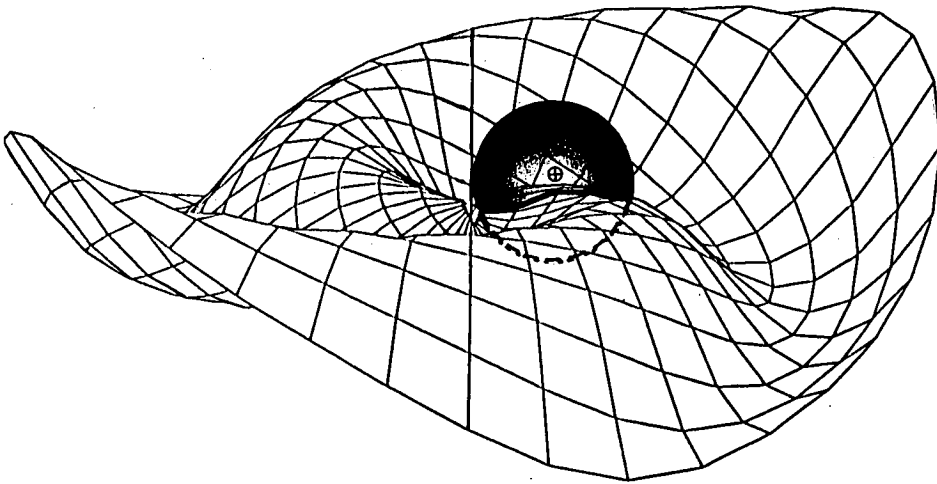


Figure 6.9 A sampling sphere of radius 1AU centred on Earth. The sphere is superimposed over a pure 4-sector neutral sheet extending to 6AU. The shaded area is the volume of the sphere above the neutral sheet. In this case, $k > 0$.

6.5. INTENSITY WAVES vs NEUTRAL SHEET CORRELATION

The variation of k (actually, $-k$) is plotted in Figures 6.10 and 6.11 along with the intensity wave variation W for the times in 1982 and 1984 when the waves were observed in the data. For both cases a solar-wind speed V_{sw} of 400 km s^{-1} in the neutral sheet model and a sampling sphere radius of 1AU were used. The neutral sheet model is insensitive to changes in the solar wind speed. Varying V_{sw} from 300 to 600 km s^{-1} had a negligible effect on the phase and amplitude variation of k . Changing R_{ss} had the effect of changing the amplitude variation in k . A small value of R_{ss} results in a large maximum amplitude of k , up to ± 1 for large tilt-angles of the neutral sheet. The larger R_{ss} the smaller is the maximum amplitude of k . However, the phase variation of k is relatively unaffected by changes in R_{ss} .

In Figure 6.10, the fit had a linear correlation coefficient of 0.7661. In Figure 6.11, the correlation coefficient was 0.5279. In both cases, over the duration of the fit, these coefficients give a probability of less than 0.001% that the correlation occurred by chance (see Section 13.7 of Press *et al.* 1986).

The positive correlation between the intensity variations and $-k$ shows that when $k > 0$ the muon flux is lower. This indicates that in the presence of these intensity waves there were more galactic cosmic rays in the southern hemisphere, at least at the energies to which the telescopes were sensitive.

Such a difference in the density of cosmic rays between the two hemispheres could arise in several ways. It may be that, for example, more solar modulation was present in the northern hemisphere as a result of differential solar activity between the hemispheres when the waves were present. Solar activity, as measured using sunspot number and area data, were compared between hemispheres but no correlation could be found between differential solar activity and intensity wave amplitude over the short time periods when the waves were observed. Other researchers have found evidence for an asymmetry in the cosmic ray density over longer time periods ($\gg 1$ year). Swinson *et al.* (1990a, 1990b, 1991) considered the distribution in the number of days the Earth was in a Towards or Away sector and compared this with solar activity as measured by sunspot numbers. They inferred from their observations that an asymmetric level of activity on the Sun causes a displacement of the neutral sheet north or south of the heliographic equator. A latitudinally symmetric density distribution with respect to the neutral sheet is then observed as an asymmetric distribution from the ecliptic. Chen *et al.* (1991) on the other hand interpreted changes in the phase and amplitude of the diurnal anisotropy (over many years) as indicating a true uni-directional latitudinal gradient across the neutral sheet, caused by asymmetric solar activity.

The results reported in this chapter support the hypothesis that the neutral sheet is a significant large-scale boundary structure, even for high energy ($\sim 100 \text{ GeV}$) particles. The switching mechanisms for the appearance of these relatively short term waves have not been addressed here. Indeed, such mechanisms have yet to be conclusively determined.

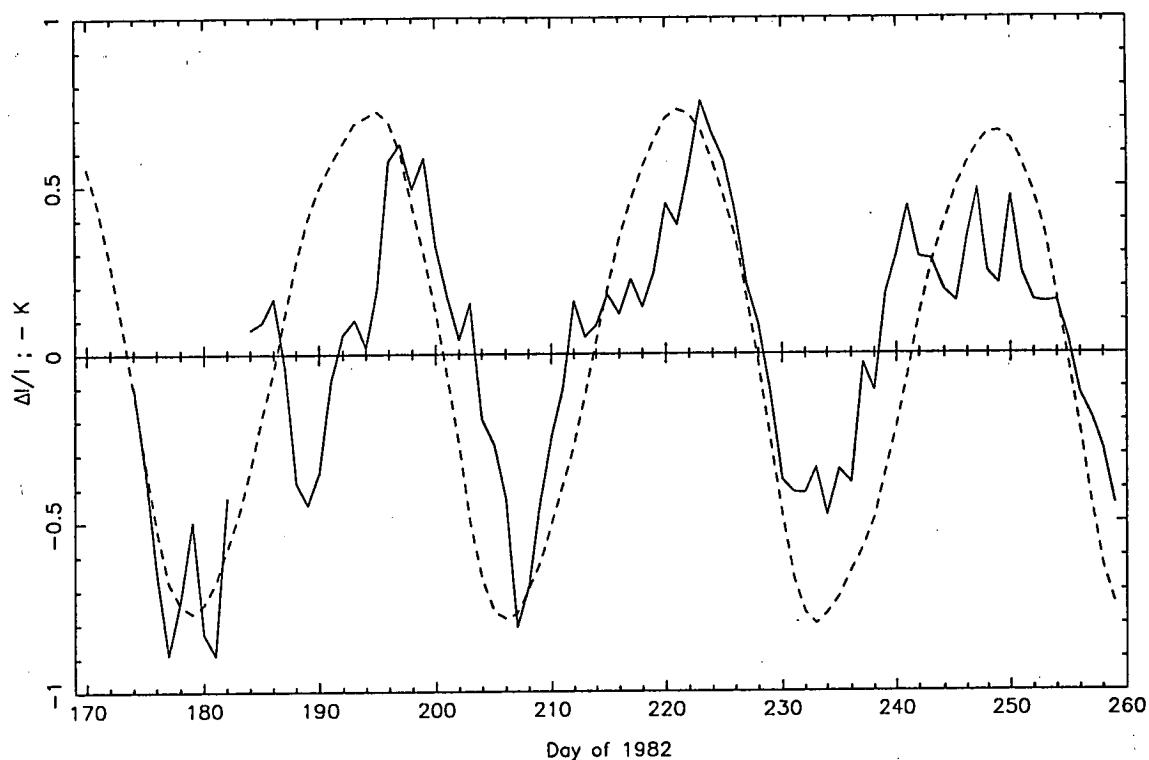


Figure 6.10. Intensity wave variation W (%) (solid line) and sampling sphere index $(-k)$ (dashed line) between days 170 and 260 in 1982. Note that the period of the variation is roughly 27 days which corresponds to the neutral sheet having a 2-sector structure at this time (see Figure 6.5).

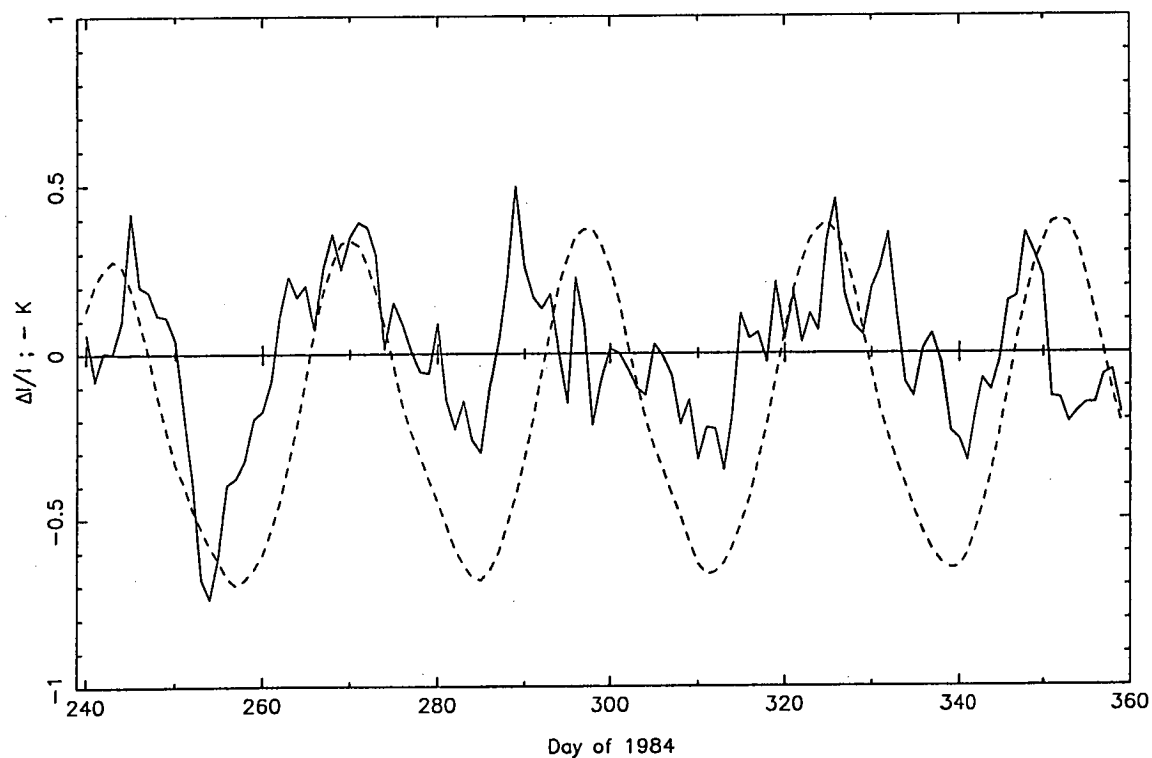


Figure 6.11. Intensity wave variation W (%) (solid line) and sampling sphere index $(-k)$ (dashed line) between days 240 and 360 in 1984. Note that the period of the variation is roughly 27 days which corresponds to the neutral sheet having a 2-sector structure at this time (see Figure 6.7).

Chapter 7. Atmospheric Corrections for Muon Data.

7.1. INTRODUCTION

Changes in atmospheric structure influence the count-rate I of a muon detector in three major ways. These need to be accounted for in order to use the data for analysis of the galactic cosmic ray anisotropy. The atmospheric effects are summarized below. The method for correcting the data is then given, along with the application of this method for the Mawson surface muon detectors SNCOMB and SSCOMB (see Chapter 5 on Coupling Coefficients for specifications of these detectors). The atmospheric-corrected data are used in the north-south anisotropy analysis described in Chapter 8.

As primary cosmic ray particles enter the atmosphere, they interact with atmospheric nuclei to produce, amongst other products, pions. The pions, having a very short lifetime, subsequently decay to the muons that are detected by muon telescopes. An increase in sea-level pressure P represents an increase in the absorbing material between the location where the muon is created and where it is detected. Therefore the muon has a higher probability of being absorbed. As P increases, I decreases and as P decreases, I increases. This is known as the *pressure effect*. The pion production level, expressed as a total column density, is roughly constant (~ 125 mb). The height H (in km say) of this production level varies seasonally. The amplitude of this seasonal variation is also latitude dependent. If the pions are produced higher in the atmosphere then they decay to muons higher in the atmosphere and hence, because the muons have further to travel before being detected, more will decay to positrons. Positrons have short ranges in air and will subsequently be absorbed before reaching the detector. As H increases, I decreases and as H decreases, I increases. This is known as the *height (or negative temperature) effect*. The density of air near the pion production level is inversely proportional to the temperature T there. If the air density is low then the pion has a lower probability of being absorbed before decaying to a muon. As T increases, I increases and as T decreases, I decreases. This is known as the *(positive) temperature effect*.

The atmospheric effect on the muon intensity can be described by the 4-fold regression equation

$$\frac{(I - I_o)}{I_o} = \beta_P(P - P_o) + \beta_H(H - H_o) + \beta_T(T - T_o) \quad (7.1a)$$

where P_o , H_o , T_o are reference values for the pressure, height and temperature described above, I_o is the value to which the intensity would be corrected if all the variations in I were due to these three atmospheric effects only, $\{\beta_P, \beta_H, \beta_T\}$ are the atmospheric correction coefficients and should be a constant for a particular telescope (see Sandstrom 1965). More accurately,

$$\frac{\Delta I}{I_o} = \int_{P_o}^P \delta\beta_P(p)dp + \int_{H_o}^H \delta\beta_H(h)dh + \int_{T_o}^T \delta\beta_T(t)dt \quad (7.1b)$$

where $\delta\beta_i$ ($i=P,H,T$) are differential correction coefficients which are functions of P, H and T . The total effect on the count rate of the muon detector is found by integrating these differential functions over the range of fluctuations in the atmospheric parameters from their reference values. In practice, there are almost always insufficient meteorological data to determine these functions, and the integral form given by equation (7.1a) is sufficient given the accuracy of the fluctuations in the data *known* to have been caused by atmospheric effects only.

Primarily, the reason for determining the effect of variations in the atmosphere on the count rate of muon detectors is to remove such effects from the data in order to determine the free-space variations in intensity. Secondly, if the observations of atmospheric conditions are accurate enough, comparisons between such observations and theoretical models can be undertaken to test the validity of models describing the interactions in the secondary-particle cascade through the atmosphere. The coefficients are functions of such variables as the proton and pion absorption length, ionization loss rates and the equation of state of the atmosphere. Theoretically predicted atmospheric correction coefficients have been studied by a number of authors including Dorman (1974) and Maeda (1960). The coefficients for a particular telescope are expected to depend on the telescope's zenith angle of viewing, and also on the average energy of the particles being detected (see also Lyons, 1981). There is probably a small effect of latitude on the coefficients due to the temperature structure of the atmosphere changing slightly over the Earth. However, for a particular telescope with fixed viewing direction, the coefficients should not be a function of time. This statement is correct only to first-order accuracy. The coefficients may indeed have a small solar-cycle dependence although it appears that this dependence is smaller than the accuracy to which the coefficients themselves can be determined. It is therefore assumed in this chapter that the correction coefficients are constant in time for a given telescope.

Having determined a set of correction coefficients for a particular telescope, the intensity of that telescope corrected for atmospheric effects becomes

$$I_{corrected}(t) = \frac{I(t)}{[1 + \beta_P(P(t) - P_o) + \beta_H(H(t) - H_o) + \beta_T(T(t) - T_o)]} \quad (7.2)$$

This is a simple re-arrangement of equation (7.1a) with $I_{corrected}$ replacing I_o . It seems that the values obtained for β_P , β_H and β_T are essentially insensitive to the choice of (P_o , H_o , T_o) as long as these reference values are within the ranges of the respective data.

7.2. EVALUATING THE COEFFICIENTS

Re-arranged, equation (7.1a) becomes

$$I_i = I_o + I_o\beta_P(\Delta P)_i + I_o\beta_H(\Delta H)_i + I_o\beta_T(\Delta T)_i \quad (7.3)$$

where $\Delta P = (P - P_o)$, $\Delta H = (H - H_o)$, $\Delta T = (T - T_o)$ and the subscript i represents the i^{th} data point. Notice therefore that in order to determine the correction coefficients,

meteorological data for H and T (and station-level pressure P) corresponding to the recorded intensity are needed. For n data-points, where $n > 3$, equation (7.3) is written as a matrix:

$$\underline{y} = A\underline{x} \quad (7.4)$$

where

$$\underline{y} = \begin{pmatrix} I_1 \\ I_2 \\ \vdots \\ I_n \end{pmatrix}, \quad A = \begin{pmatrix} 1 & \Delta P_1 & \Delta H_1 & \Delta T_1 \\ 1 & \Delta P_2 & \Delta H_2 & \Delta T_2 \\ \vdots & \vdots & \vdots & \vdots \\ 1 & \Delta P_n & \Delta H_n & \Delta T_n \end{pmatrix}, \quad \underline{x} = \begin{pmatrix} I_o \\ I_o\beta_P \\ I_o\beta_H \\ I_o\beta_T \end{pmatrix} \quad (7.5)$$

The coefficients (and the reference intensity) are found from the least-squares solution to equation (7.4). The "best" least-squares estimate of \underline{x} is

$$\hat{\underline{x}} = (A^T A)^{-1} A^T \underline{y} \quad (7.6)$$

with error

$$\sigma_{x_i}^2 = (A^T A)^{-1}_{ii} \sigma_y^2 \quad (7.7)$$

where σ_y^2 is the variance of the set of $\{y_i\}$. An unbiased estimate of σ_y can be found using

$$\sigma_y^2 = \frac{R}{(n - p - 1)} \quad (7.8)$$

$$\text{and } R = e_i e_i \quad \text{with } e_i = y_i - A_{ij} x_j \quad (7.9)$$

In equation (7.8), p is the number of independent variables (4 in the case of equation 7.4), R is called the residual sum of squares. The total correlation coefficient r is given by

$$r^2 = 1 - \frac{R}{T} \quad \text{where } T = y_i y_i \quad (7.10)$$

T is usually called the total sum of squares. r is useful since it is a single number which gives a measure of the goodness of fit. $r = 1$ is a perfect fit, $r = 0$ implies there is no correlation between the parameters and the data and $r = -1$ implies perfect *anti*-correlation.

Note that the error given in equation (7.7) for the correction coefficients is only the *formal error* in the sense that the measurement errors on \underline{y} do not necessarily follow a normal distribution. Only when the measurement errors follow a normal distribution does it make sense to say that (for example) there is a 68% confidence limit on the coefficients, correct to $\pm 1\sigma$, of the values given by equation (7.6). See Chapter 14 of Press *et al.* (1986) for further discussion on this point. Even though errors of the muon intensity I approximately follow a normal distribution (the Poisson distribution for large count-rates closely approximates a normal distribution), *other* variations in the data not due to atmospheric

effects or counting statistics (eg: solar modulation effects) will influence the determination of the coefficients. Some of these effects are discussed in the subsequent sections.

7.3. EFFECT OF CORRELATION IN METEOROLOGICAL DATA

If two or more of the atmospheric parameters P, H, T are not completely independent and if they have associated with their values a *random* measurement error, then the atmospheric correction coefficients determined from the least-squares fit will be biased. Denoting the measurement errors by $\sigma_P, \sigma_H, \sigma_T$ and assuming that there is no cross-correlation between them, and also that there is no correlation between these errors and either A or \underline{y} , then the effect of this bias can be removed by replacing $(A^T A)^{-1}$ by $(A^T A - nS)^{-1}$ in the solution for \underline{x} given by (7.6), where

$$nS = n \cdot \begin{pmatrix} 0 & & & \\ & \sigma_P^2 & & \\ & & \sigma_H^2 & \\ & & & \sigma_T^2 \end{pmatrix} \quad (7.11)$$

$$\text{ie:} \quad \hat{\underline{x}}_{unbiased} = (A^T A - nS)^{-1} A^T \underline{y} \quad (7.12)$$

See Trefall and Nordo (1959) for the theory behind this correction process. It can be shown (see Seber 1977) that if n is large and S small, the formal error for $\hat{\underline{x}}_{unbiased}$ is still given by equation (7.7).

7.4. COEFFICIENTS FOR MAWSON SURFACE MUON DETECTORS

7.4a. Meteorological data.

Surface pressure P was measured by a barometer/transducer at the detector site. Height and temperature data were measured using radiosondes on weather-balloons flown once-daily at Mawson by meteorologists working for the Australian Bureau of Meteorology. The radiosonde measurements include (among other things) the height (meters) and temperature ($^{\circ}\text{C}$) of pressure levels ranging from 1000 to 50 mb. H used in the regression analysis was the height of the 125mb level. At Mawson, this height varies from approximately 13.3 km in late July to 14.5 km in late December. T used in the regression analysis was the mean temperature in the interval 80 to 200 mb. This temperature varies between roughly -80°C (late July) and approximately -40°C (late December). Due to the polar location of Mawson, the seasonal variation of these parameters is very large compared with equatorial or mid-latitude sites. The diurnal variation is also relatively small in comparison with both lower latitude sites and with the seasonal variation because solar diurnal heating of the atmosphere is not significant at high latitudes.

Because H and T data may vary significantly over a period of one day, it is valid only to regress these data with the detector count-rate measured at the same time as the balloon flight. During the 1970's and early 1980's, detectors at Mawson only recorded hourly count-rates. It was assumed that the H and T data were valid for a period of one hour

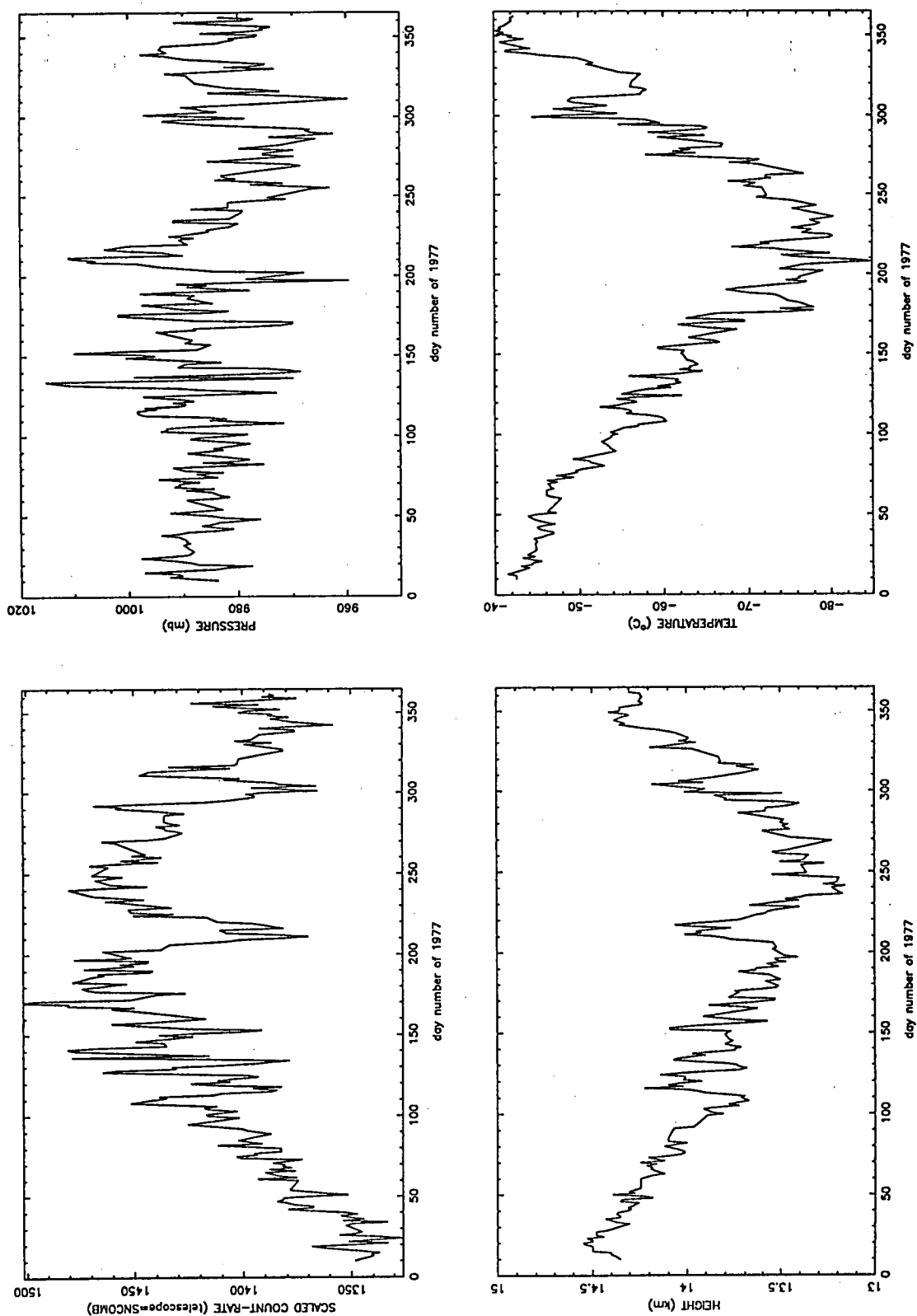


Figure 7.1. Raw data used in the regression analysis for the muon telescope SNCOMB for 1977. The scaled count-rate for this detector is uncorrected. The pressure has been measured by an auto-barograph at the detector site. Height is that of the 125mb level, temperature is the average between the 80 and 200mb levels.

before and one hour after the radiosonde measurement. This measurement was regressed with the average hourly count rate of the muon telescopes over these two hours. Figure 7.1 shows the pressure, height and temperature data along with the count-rate for the surface north-pointing muon detector at Mawson for 1977.

7.4b. Non-meteorological related variations in the muon data.

Transient variations in detector count-rate which are not due to atmospheric effects should be removed to prevent possible bias in the regression analysis. It is of course impossible to remove all these variations without identifying them in the first place. Before finding the appropriate atmospheric correction coefficients, it is not clear what variations are due to atmospheric effects alone. Major transient variations in the data which are known (by some means) not to be atmospheric related are removed, and it is assumed that the remaining variations in the data (which are not of atmospheric origin) are not correlated with P , H and T so that no bias is introduced into the regression analysis. The solar diurnal variation is not present in the data if the average of the hourly count rate for the two hours bracketing the radiosonde measurement are used. This is because, at Mawson, radiosonde measurements are taken at the same time each day. The muon detectors are observing cosmic rays at the same phase of the diurnal variation each day - assuming that over the period of regression the change in phase of the diurnal variation is less than the statistical scatter of the data. Forbush decreases are removed using data from a neutron monitor at the same site as the muon telescope. The neutron monitor count rate is only affected by changes in P (when considering atmospheric effects). The pressure coefficient for a neutron monitor can be accurately found by looking at the change in count rate during a short period where there is a large pressure change. For Mawson, this could be the period during the passage of a blizzard. The pressure-corrected neutron monitor count rate will show the periods when Forbush decreases were present. The pressure-corrected Mawson neutron monitor count rate was scanned and days when a Forbush decrease was observed were flagged. These days were excluded from the regression analysis for determining the muon atmospheric correction coefficients. A Forbush decrease detected by a muon telescope will always be detected by a neutron monitor at the same site because the spectrum of the decrease is such that the intensity of lower-energy particles is depressed more than the intensity of higher energy particles. There is a risk of removing excess muon data in the regression analysis using this method since a muon telescope may not *necessarily* see a Forbush decrease if a neutron monitor does (i.e. if the upper cut-off rigidity for the event is lower than the threshold rigidity for the muon telescope but higher than the threshold for the neutron monitor). This problem cannot be avoided and it is better to remove more muon data from the regression analysis than not enough if there is a chance that some remaining data still contain Forbush decreases. Finally, periods in the muon data which had level shifts and data spikes - due to detector and/or power supply malfunction - were identified by visual inspection of the uncorrected data. A spike-recognition algorithm (see Appendix 6) was also applied to the data with limited success. These periods were removed from the regression analysis.

7.4c. Detector efficiency.

Before 1982 the muon telescopes in use at Mawson employed Geiger tubes. These tubes decrease in efficiency such that, in the absence of any anisotropy in the primary cosmic rays, the count rate of the detectors decreases exponentially. The time constant is

sufficiently slow that over the period of a couple of years this decrease is linear. Such an efficiency trend needs to be removed from the data before the regression analysis is undertaken. There are problems in simply comparing the average hourly count rate at the start of a year and at the end of the same year, and fitting a straight line in order to remove the efficiency trend. If the meteorological conditions are not exactly the same at the two times then any differences will show up as intensity variations which will affect the straight-line fit. It is more accurate to fit a straight line through a complete year's data - or in fact two or three year's combined data to best fit the "average" linear efficiency trend. Note that in order to accurately determine the β_H and β_T coefficients, data for at least one complete year should be used in the regression analysis. H and T vary approximately sinusoidally with a period of one year. Also over short timespans, H and T data do not generally vary enough to produce an effect in the intensity of the detector which is greater than the statistical accuracy of the data. Unfortunately, doing the regression analysis over a long period such as a year introduces other problems including the fact that real solar-cycle variations may be significant. In an attempt to alleviate this, the regression analysis was done for years around solar minimum.

It turns out for the Mawson (surface) muon telescopes around the 1975 solar minimum, that the magnitude of the seasonal variation in the data due to H and T variations was roughly of the same order as the magnitude of the average decrease in intensity due to the Geiger tube efficiency deterioration. This posed problems when trying to identify and remove the linear efficiency trend because the sinusoidal seasonal variation biased the fit to a straight line of the data (see Appendix 3).

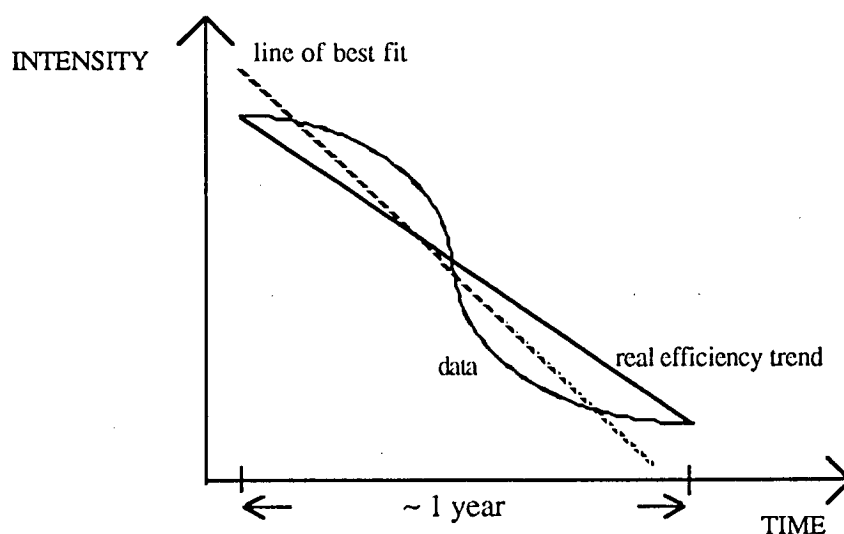


Figure 7.2. For data which sinusoidally varies over a year and which has a superimposed (linear) efficiency decay, the line of best fit through the data (dashed line above) does NOT equal the declining efficiency trend.

This problem was alleviated by fitting a sine wave of arbitrary phase PLUS a straight line to the data, the sine wave representing the best-fit to a seasonal variation. The efficiency trend was then identified by the straight line part of the fit only. This linear trend was removed from the data by rotating around its average. For reasons described above, the straight line plus sine wave fit was performed over three consecutive years of data combined (near solar minimum).

7.4d. Regression analysis - Results.

Some authors, on reporting values obtained for atmospheric correction coefficients for a particular muon telescope, do not explicitly state that they calculated I_o as a fit-parameter (eg: Fenton et al. 1961, Lyons 1981). Instead of using equation (7.4), the regression analysis could just as easily be done using

$$\underline{y} = \begin{pmatrix} \frac{I - I_o}{I_o} \\ | \\ | \\ \downarrow \end{pmatrix}, \quad \underline{x} = \begin{pmatrix} \beta_P \\ \beta_H \\ \beta_T \end{pmatrix} \quad \text{and} \quad A = \begin{pmatrix} \Delta P & \Delta H & \Delta T \\ | & & \\ | & & \\ \downarrow & & \end{pmatrix} \quad (7.13)$$

for a pre-specified value of I_o (say the average intensity over the span of data). It was found that the coefficients obtained from such a fit are very sensitive to the value of I_o used - even if the choice of I_o was restricted to the range of I in the data span. Therefore I_o was one of the parameters to be determined by the regression analysis. Figure 7.3 shows an example of the sensitivity of the fitting procedure to the choice of I_o .

Correction coefficients for the Mawson surface telescopes (both north and south pointing) for 1975, 76, 77 and 1984 were calculated. Results are tabulated in Table 7.1. It was found that, even though the pressure coefficient was consistent between telescopes and from year to year, the height and temperature coefficients varied significantly, the error on the height coefficient in particular being quite large. Note that both the north and south pointing telescopes should have the same coefficients (they are both looking through the same amount of atmosphere) and these coefficients are expected to be constant over the period 1975-77. The temperature coefficient determined was always negative, in contradiction with the theoretically expected value.

| Year | Detector | β_P (% mb ⁻¹) | β_H (% km ⁻¹) | β_T (% °C ⁻¹) |
|------|----------|---------------------------------|---------------------------------|---------------------------------|
| 1975 | sncomb | -0.10 ± 0.01 | -3.0 ± 0.8 | -0.15 ± 0.03 |
| 1975 | sscomb | -0.10 ± 0.01 | -3.6 ± 0.7 | -0.13 ± 0.02 |
| 1976 | sncomb | -0.11 ± 0.01 | -3.4 ± 0.5 | -0.13 ± 0.02 |
| 1976 | sscomb | -0.11 ± 0.01 | -2.5 ± 0.5 | -0.15 ± 0.02 |
| 1977 | sncomb | -0.07 ± 0.01 | -2.9 ± 0.7 | -0.08 ± 0.02 |
| 1977 | sscomb | -0.08 ± 0.01 | -2.3 ± 0.6 | -0.12 ± 0.02 |
| 1984 | sncomb | -0.12 ± 0.01 | -1.9 ± 0.6 | -0.13 ± 0.02 |
| 1984 | sscomb | -0.12 ± 0.01 | -2.2 ± 0.6 | -0.13 ± 0.02 |

Table 7.1. Correction coefficients for the Mawson surface muon detectors obtained using the full 4-fold regression analysis. Note that β_T is negative, in contradiction with theoretically expected values.

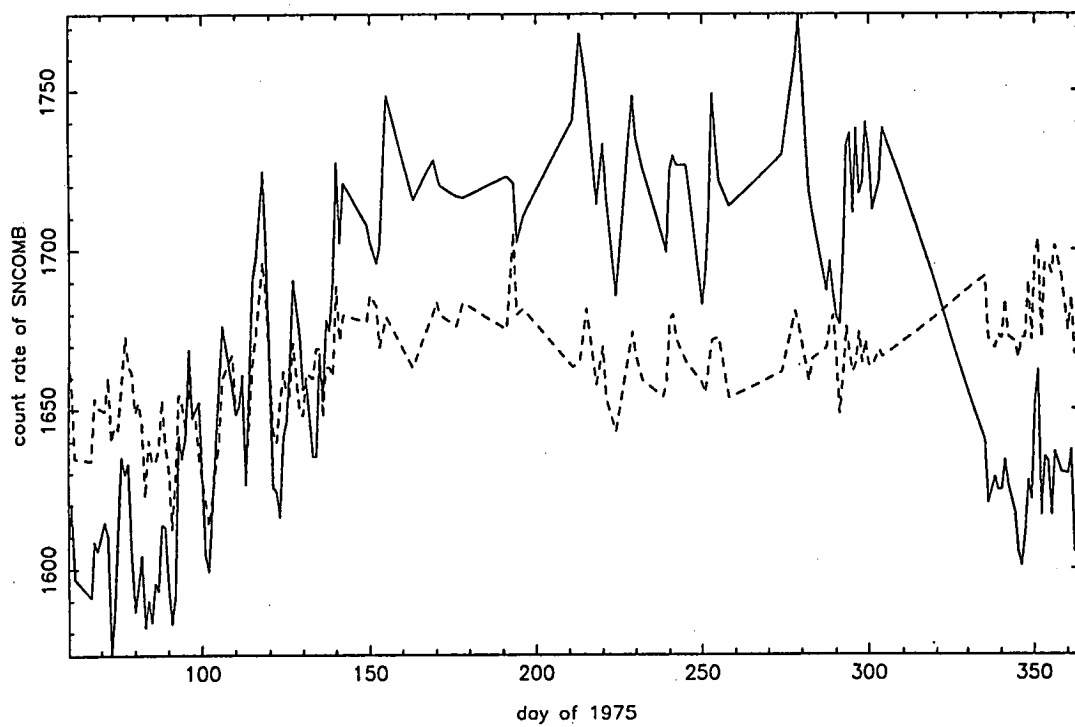
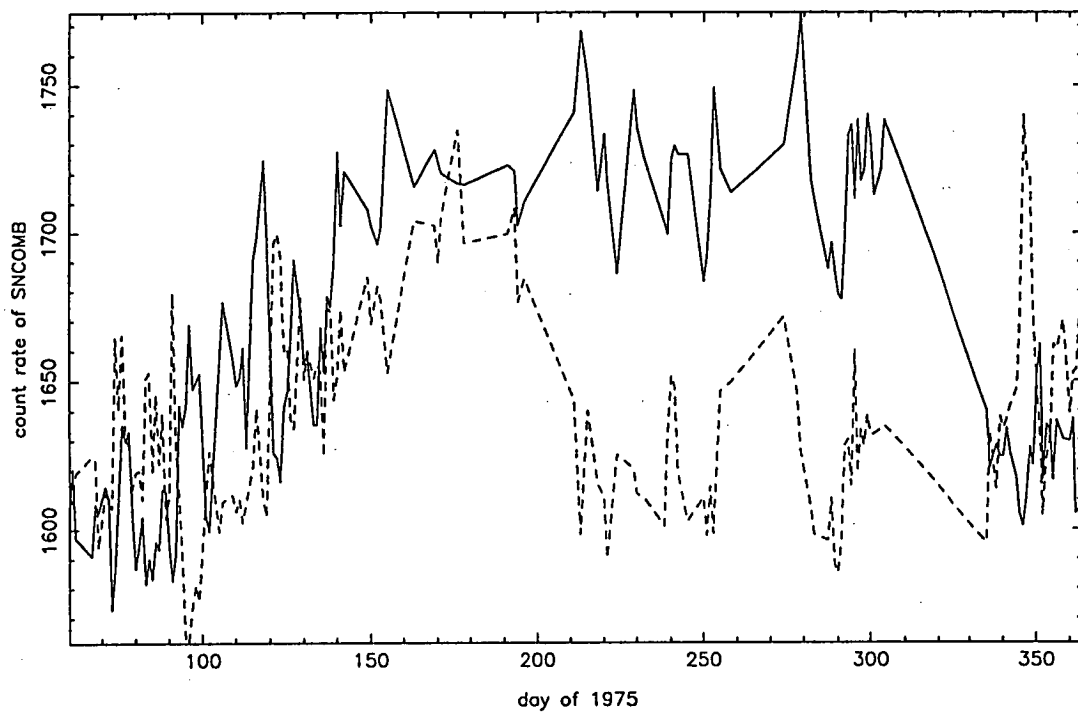


Figure 7.3. Uncorrected (solid line) and corrected (dashed line) count rate of SNCOMB. The top plot used $I_o = 1595$ in the analysis (via 7.13), the bottom used $I_o = 1663$, approximately the average count-rate of the span. Note that the uncorrected data had the linear-trend removed.

It should be noted that the errors given in Tables 7.1 and 7.2 are components of the error *vector* given by (7.7). The fact that the errors for β_H and to a lesser extent for β_T are rather large reflect the fact that there is a large range of values of the pair (β_H, β_T) which give an equally adequate fit to the model in the regression analysis. In fact, it was found that if the correction coefficients determined from (7.6) were changed by an amount $\pm\sigma_{\beta_i}$ and then applied to the data, the corresponding corrected data did not change by more than about 1%. In some cases, the correction coefficients could be altered by up to 3σ without noticeably affecting the result of correcting the data. Figure 7.4 gives an example of the relative insensitivity of the corrected data to the correction coefficients. Because of this relative insensitivity, the correction coefficients determined from one year's data generally adequately corrected another year's data, even though the coefficients from year to year may not have been consistent.

From experience, it does seem that β_H can increase while β_T decreases, and vice-versa, with little effect on the quality of the fit. This is due to the high degree of correlation between the height and temperature aerological data. As discussed earlier, it is usual to use the bias-matrix procedure to correct for this correlation (equation 7.12).

The meteorological data for H and T at Mawson are partially correlated - both varying sinusoidally and in phase with a period of 1 year. To prevent any bias in the correction coefficients a bias matrix nS was included, where $\sigma_P = 0.2$ mb, $\sigma_H = 50$ m and $\sigma_T = 2.2^\circ\text{C}$. These figures were based on Lyons' (1981) estimate of the data errors in radiosonde measurements, determined from various sources and locations (eg: Trefall and Nordo, 1959). The results analogous to Table 7.1 are shown in Table 7.2.

| Year | Detector | β_P (% mb ⁻¹) | β_H (% km ⁻¹) | β_T (% °C ⁻¹) |
|------|----------|---------------------------------|---------------------------------|---------------------------------|
| 1975 | sncomb | -0.13 ± 0.01 | 0.55 ± 1.4 | -0.27 ± 0.05 |
| 1975 | sscomb | -0.12 ± 0.01 | -1.1 ± 1.3 | -0.21 ± 0.04 |
| 1976 | sncomb | -0.12 ± 0.01 | -1.6 ± 0.7 | -0.19 ± 0.02 |
| 1976 | sscomb | -0.13 ± 0.01 | -0.1 ± 0.7 | -0.23 ± 0.02 |
| 1977 | sncomb | -0.07 ± 0.01 | -2.7 ± 0.8 | -0.09 ± 0.02 |
| 1977 | sscomb | -0.08 ± 0.01 | -1.7 ± 0.7 | -0.14 ± 0.02 |
| 1984 | sncomb | -0.13 ± 0.01 | -0.4 ± 0.8 | -0.18 ± 0.03 |
| 1984 | sscomb | -0.13 ± 0.01 | -0.7 ± 0.7 | -0.18 ± 0.02 |

Table 7.2. Correction coefficients for the Mawson surface muon detectors obtained using the full 4-fold regression analysis AND using a bias matrix where $\sigma_P = 0.2$ mb, $\sigma_H = 50$ m and $\sigma_T = 2.2^\circ\text{C}$.

Notice from Table 7.2 that the values for β_H and β_T were even *more* scattered than in Table 7.1. Some of the values for the height coefficient were less than the error estimate. The values used in the bias-matrix may have been inappropriate for the Mawson aerological data. In an attempt to find a "best" bias matrix (equation 7.11), coefficients β_P , β_H and β_T were calculated over 1975-1977 for a *range* of (σ_H, σ_T) values.

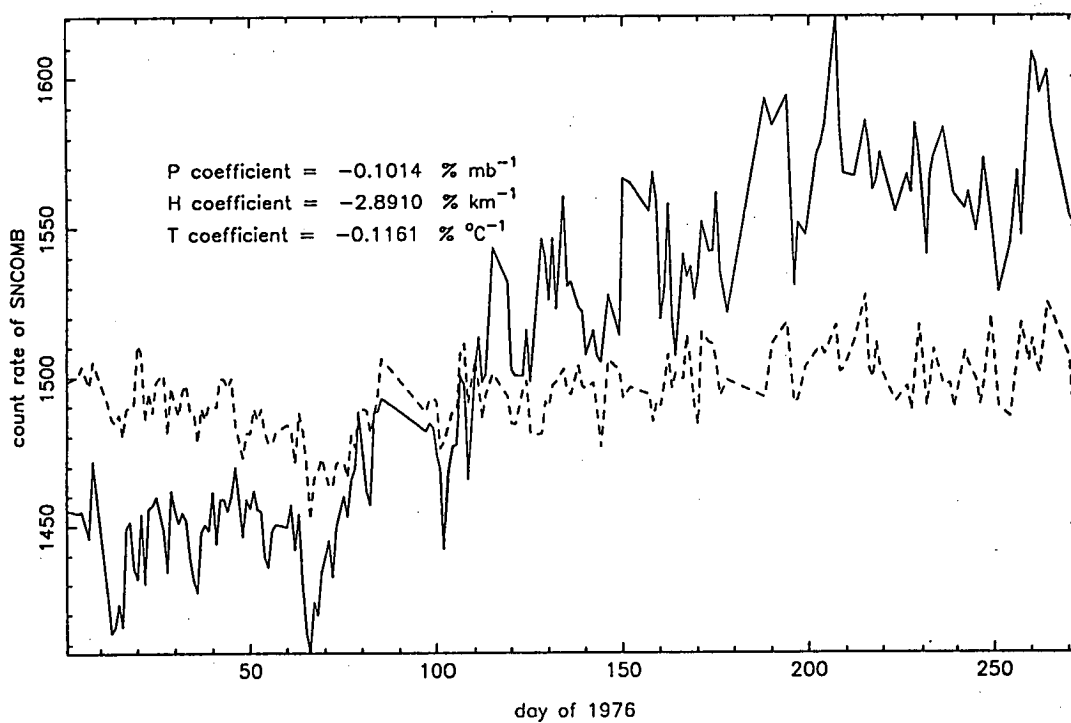
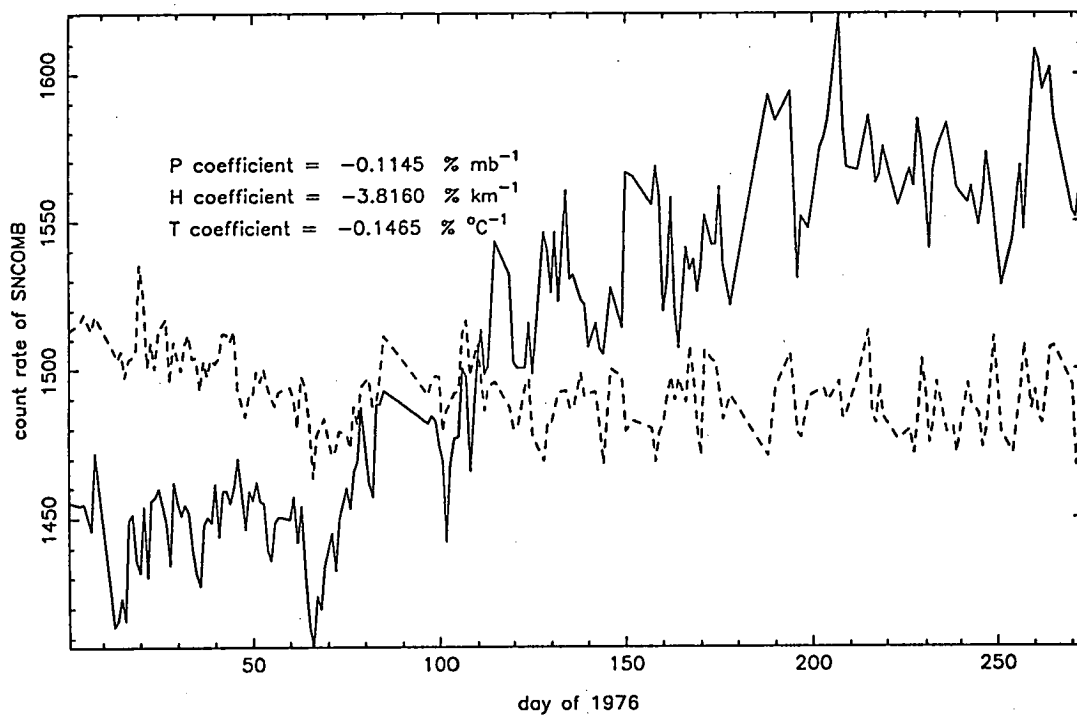


Figure 7.4. Uncorrected (solid line) and corrected (dashed line) count rate of SNCOMB. The top plot used correction coefficients $\underline{\beta} - \underline{\sigma}$, the bottom plot used $\underline{\beta} + \underline{\sigma}$, where $\underline{\beta}$ is the correction coefficient vector solution given by (7.6) and $\underline{\sigma}$ is the error vector given by (7.7). The uncorrected data had the linear-trend removed.

For each different combination of bias-matrix elements, three values were calculated, namely:

$$\begin{aligned}
 A &= \sum_{\text{year} \neq 1975} (\beta_{P,1975} - \beta_{P,\text{year}})^2 \\
 B &= \sum_{\text{year} \neq 1975} (\beta_{H,1975} - \beta_{H,\text{year}})^2 \\
 C &= \sum_{\text{year} \neq 1975} (\beta_{T,1975} - \beta_{T,\text{year}})^2
 \end{aligned} \tag{7.14}$$

The assumption is that when A, B and C are a minimum then the coefficients are the most consistent from year to year and hence most likely to be the "correct" ones. σ_H was varied between 0 and 60m in steps of 5m, σ_T was varied from 0 to 3°C in steps of 0.5°C (also including 2.2°C). Coefficients and hence A, B and C were calculated for both surface muon detectors at Mawson. For SNCOMB, the value A was insensitive to changes in (σ_H, σ_T) . B had a local minimum usually when $\sigma_T = 2.2^\circ\text{C}$ for a given σ_H , the global minimum being at $\sigma_H = 0.0$. C had a minimum usually when $\sigma_T = 0$ for a given σ_H , the global minimum being at $\sigma_H = 20\text{m}$. For SSCOMB, trends for C were as above. B had a local minimum for $\sigma_T = 1.0^\circ\text{C}$ generally, with the global minimum at $(\sigma_H, \sigma_T) = (0.0, 1.0)$. It is therefore apparent that there was no value (or range of values) of (σ_H, σ_T) which clearly gave a more consistent set of coefficients between the three years. Using any of the values of (σ_H, σ_T) which gave a local minimum in A, B or C gave no "better" results for $(\beta_P, \beta_H, \beta_T)$ than in Table 7.1, in the sense of being more consistent or having smaller errors.

It proved to be very difficult to determine consistent correction coefficients (for β_H and β_T) from year to year and between telescopes. It is believed that the reason for this was the high degree of correlation between the H and T aerological data, *and* the assumptions of no correlation between errors in H, T and values in A and χ breaking down (hence the bias-matrix method was inappropriate).

7.4e. Pressure-Height only correction procedure.

Visually inspecting the intensity (I) variations and the corresponding H and T variations over 1 year for Mawson surface muon telescopes (eg: Figure 7.1) shows that there is an obvious anti-correlation between I and H (as would be expected for β_H negative). Since there is a correlation between H and T , there is also anti-correlation between I and T . For a positive β_T , a positive correlation between I and T would be expected (in the absence of H variations). Hence for the Mawson muon telescopes, the positive temperature effect must be small compared with the negative height effect. To alleviate problems of H variations biasing β_T and T variations biasing β_H , it was decided to correlate I variations with P and H only, and neglect any effect of T variations on I . The new regression equation becomes

$$I = I_o + I_o \beta_P(\Delta P) + I_o \beta_H(\Delta H) \tag{7.14}$$

Another way of looking at this is that this new β_H is a *total* height coefficient which describes I variations produced by $H + T$ variations (somewhat justified when considering that H and T are partially correlated).

To more accurately determine β_P , it was decided to correlate the intensity variation with pressure variation over a couple of hours only - at times of high pressure variability, e.g. the passage of a blizzard. Over this length of time, H variations (and indeed any variations in the data due to solar modulation and Geiger tube efficiency changes) are negligible. The Mawson cosmic ray observatory is equipped with a static pressure head. The pressure records are known to be unaffected (to first order) by high winds and blizzard conditions (M L Duldig, private communication). Using

$$\frac{\Delta I}{I_o} = \beta_P \Delta P \quad (7.15)$$

and therefore

$$I = I_o + I_o \beta_P \Delta P \quad (7.16)$$

β_P was determined from the slope of a linear regression of data with pressure variations. Averaging over a number of runs, each run consisting of data from less than or equal to two consecutive days, the average pressure coefficient (for both SNCOMB and SSCOMB) was found to be

$$\beta_P = -0.09 \pm 0.01 \% \text{ mb}^{-1} \quad (7.17)$$

Using this pressure coefficient, the muon data were pressure corrected over 1975, 1976 and 1977 and the efficiency trend was removed. The residual intensity variation was regressed with H variations only to determine I_o and β_H for each of the three years and the results were averaged to find a "constant" β_H which would adequately correct all three year's data for each of the surface telescopes equally well. The average height coefficient over these three years (for both SNCOMB and SSCOMB) was found to be

$$\beta_H = -6.0 \pm 0.8 \% \text{ km}^{-1} \quad (7.18)$$

See Figure 7.5 for an example of corrected data using this method over 1975-77. Figure 7.6 shows the difference in the corrected data if instead of using the *average* β_H given by equation 7.18, the height coefficient determined for each of the three years separately was used. Height coefficients determined for the separate years were -6.97, -5.25 and -5.83 % km^{-1} for 1975, 1976 and 1977 respectively. As can be seen, the two methods give very similar results. This indicates that the "average" β_H given by equation 7.18 is adequate.

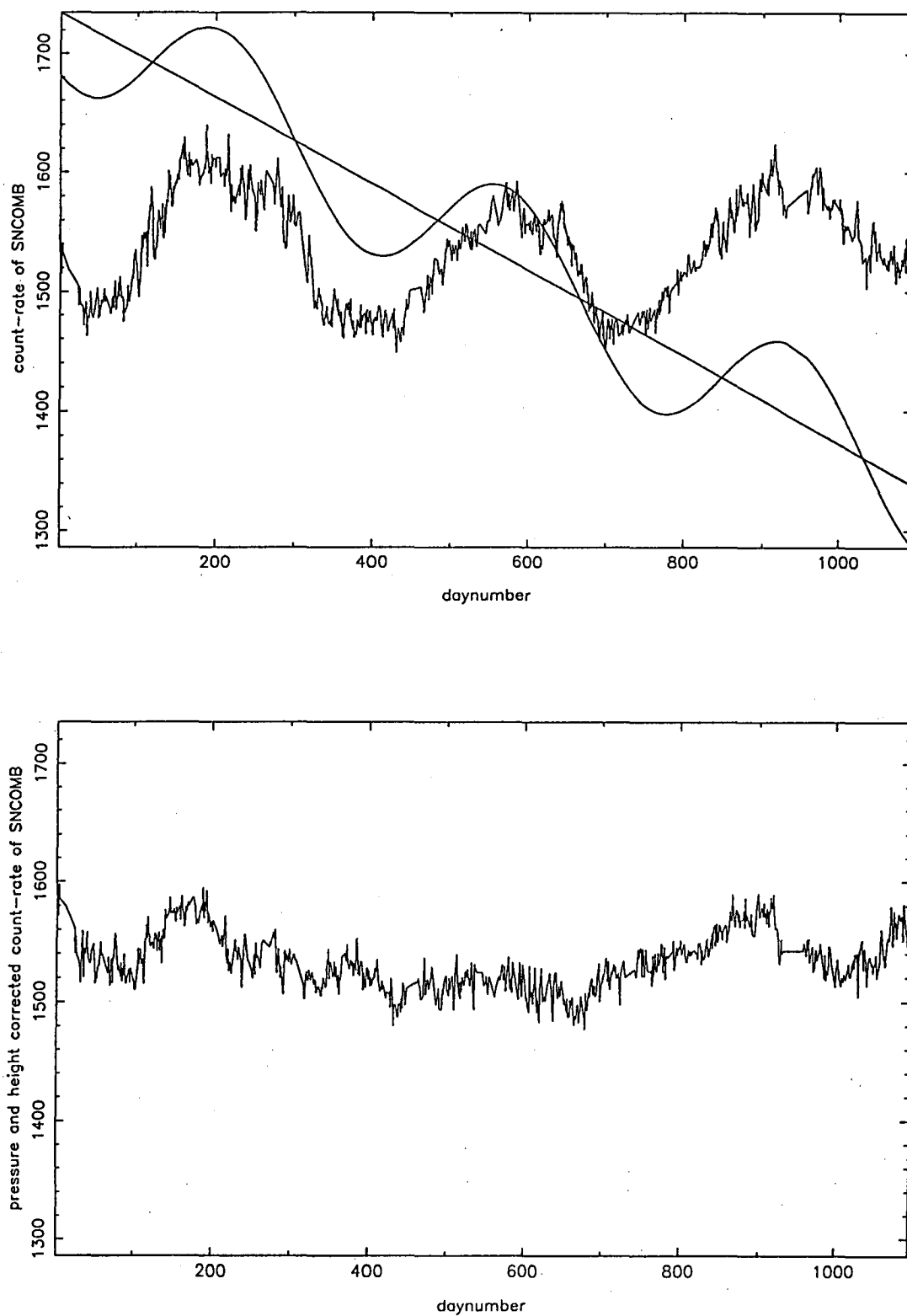


Figure 7.5. The top plot is the count rate of SNCOMB over 1975-77 corrected for pressure variations only. Daynumber is from 1 Jan 1975. The sine-wave fit and the linear efficiency trend have also been shown. The data have been rotated around this linear trend to remove the detector efficiency decay. The bottom plot is the same data with the average height correction coefficient ($\beta_H = -6.0 \% \text{ km}^{-1}$) applied over the whole data span.

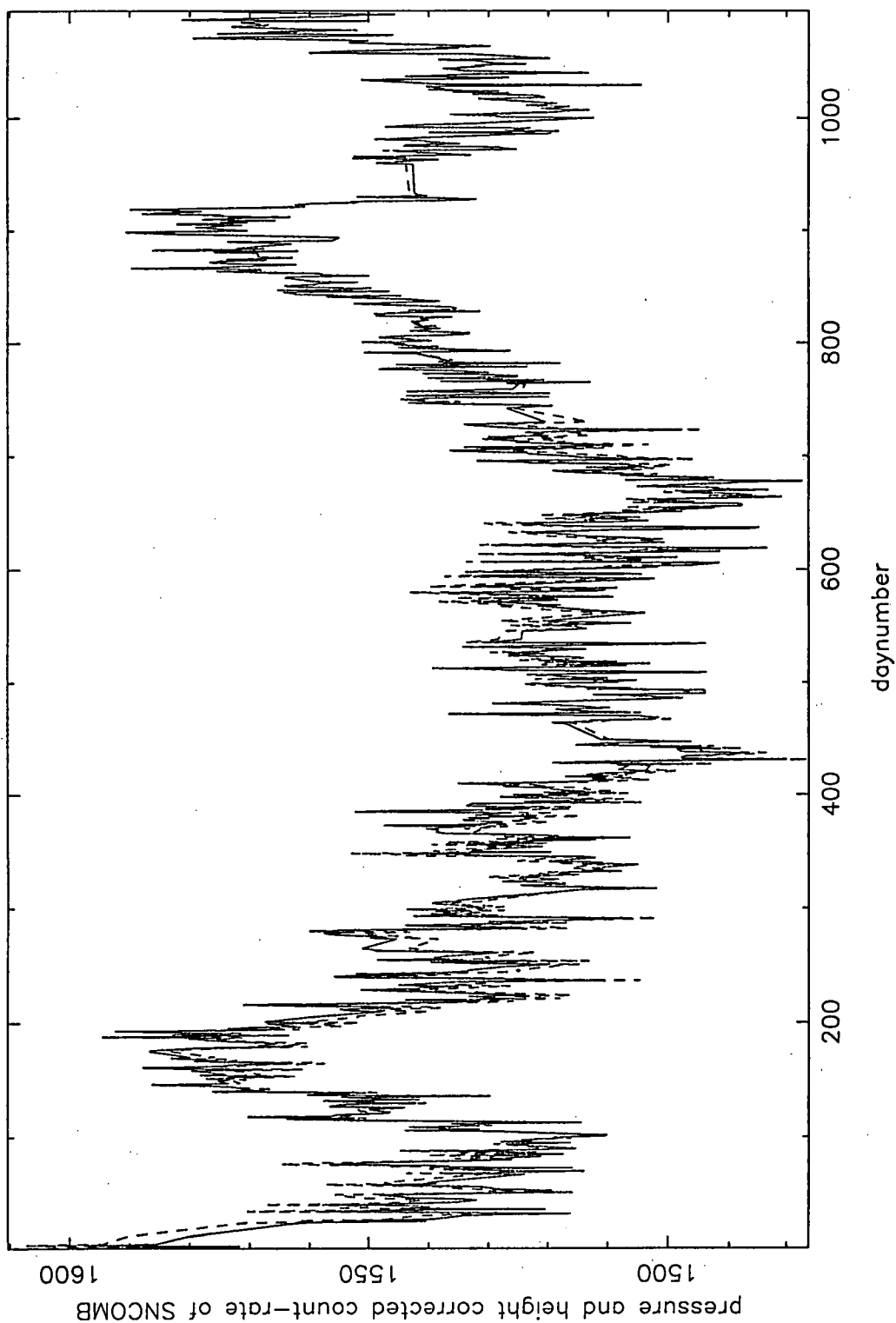


Figure 7.6. The solid line is the same data as in the bottom plot of Figure 7.5. The dashed line is corrected intensity of the same data except that the height coefficients used were those determined from the analysis for each separate year (-6.97 , -5.25 , -5.83 $\% \text{ km}^{-1}$ for 1975, 1976, 1977 respectively).

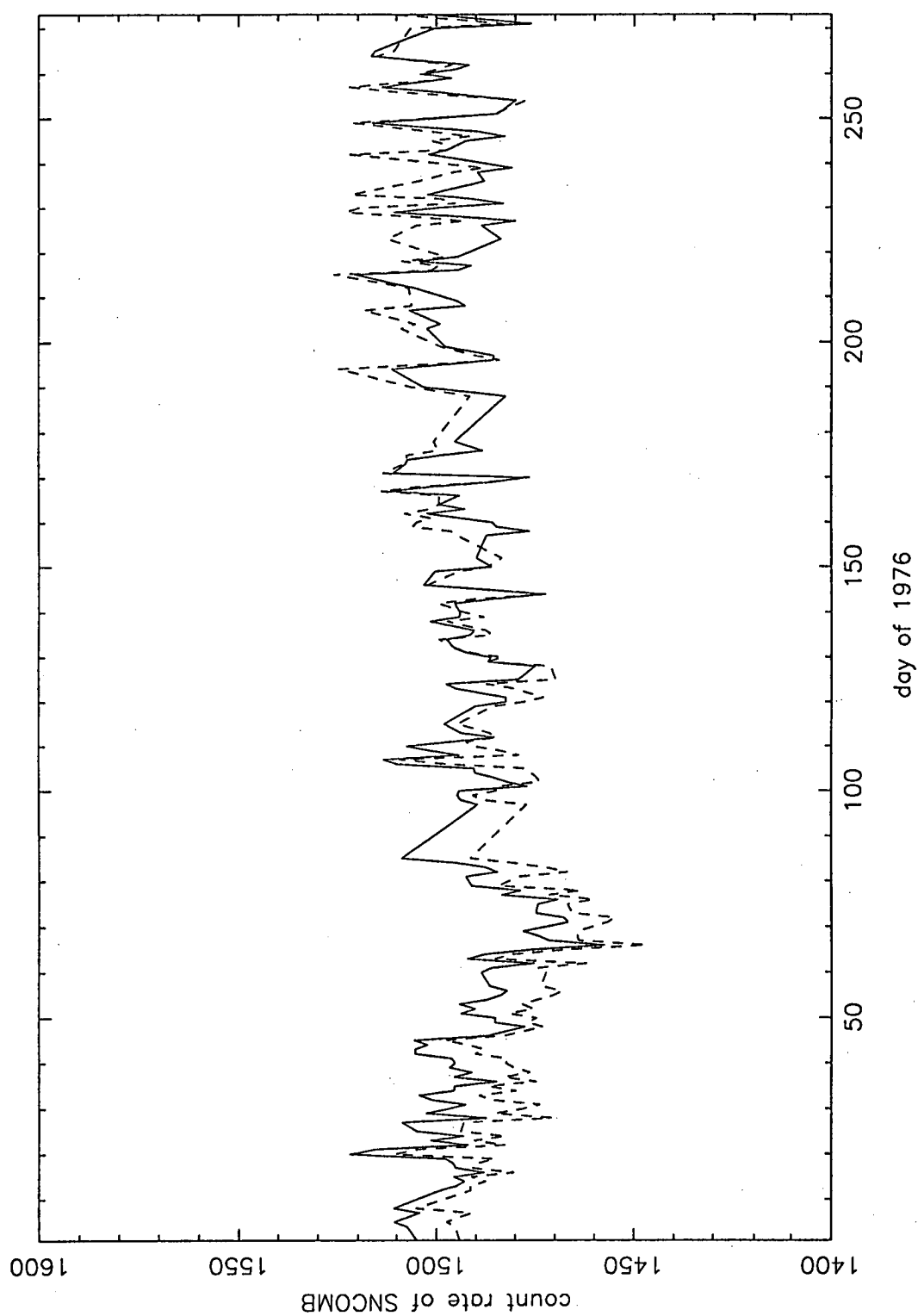


Figure 7.7. The solid line is the count rate of SNCOMB, corrected using coefficients determined from a full 4-fold regression analysis (see Table 7.1). The dashed line is the same data corrected using $(\beta_P, \beta_H, \beta_T) = (-0.09 \% \text{ mb}^{-1}, -6.0 \% \text{ km}^{-1}, 0.0)$.

On using (β_P, β_H) determined from the "average" method to correct a span of data for atmospheric effects, it was found that the corrected intensity may vary by up to ~2% from the corresponding corrected intensity determined using a full 4-fold regression analysis over the same span of data. See Figure 7.7 for an example. The reason for this is probably that the full 4-fold analysis not only correlates intensity variations caused by atmospheric effects with H and T but also correlates other (real) fluctuations in the data which have not been removed. By determining an "average" consistent β_P and β_H over a number of years around solar minimum, it is believed that the application of these coefficients to any data span will have removed atmospheric effects alone.

7.5. COEFFICIENTS FOR MAWSON UNDERGROUND DETECTORS

Atmospheric correction coefficients for the underground muon detectors (UNCOMB, USCOMB) at Mawson were determined using the method given above. Due to their low count rates, the counting statistics were not as good for these telescopes as for the surface detectors. The average value for the pressure and height coefficients were determined for both detectors to be

$$\beta_P = -0.06 \pm 0.02 \% \text{ mb}^{-1} \quad (7.19)$$

and

$$\beta_H = -0.73 \pm 0.20 \% \text{ km}^{-1} \quad (7.20)$$

It is expected that these coefficients would be lower than the corresponding coefficients for the surface telescopes. The underground telescopes have a median energy of response higher than the surface detectors. Higher energy particles would have a smaller absorption cross-section and hence would be less affected by changes in the amount of absorbing material between creation and detection points (hence a lower pressure coefficient). Changes in H would have less of an effect on higher energy particles because of their shorter Lorentz contracted flight time from the production point to the detector (hence a lower height coefficient).

Note that the coefficients for both surface and underground telescopes given in this chapter are consistent with theoretically expected and experimental values determined by other authors (eg: Fenton *et al.* 1961, Sandstrom 1965, Dorman 1987).

Chapter 8. North-South Anisotropy Analysis.

8.1. INTRODUCTION

We are interested in comparing the predictions of the model for the intensity distribution of particles at 1 AU to that observed by ground-based particle detectors (neutron monitors and muon telescopes) and spacecraft borne instruments. North-south anisotropy analysis is one of only a handful of methods whereby direct comparisons can be made between the model and ground-based observations. In particular, it gives a method whereby the radial gradient g_r of galactic cosmic rays at 1 AU in the Sun's equatorial plane can be determined from neutron monitor and muon telescope data.

The Nagoya GG telescope (eg: Yasue 1980) is the only muon telescope which has been used extensively to measure the north-south anisotropy. Obviously, for maximum sensitivity, it is advantageous to compare the count-rate of a detector viewing directly north and another viewing directly south. In the past, the neutron monitors at Thule (Greenland) and McMurdo (Antarctica) have been used. (eg: Bieber and Pomerantz 1986). In this chapter, values of the north-south anisotropy and the radial gradient at 1 AU determined from data collected by the network of neutron monitors and muon detectors operated by the University of Tasmania and the Australian Antarctic Division are presented. This is the first attempt at deriving g_r using these detectors. Firstly however, the theoretical description of the north-south anisotropy is given. Two methods for obtaining g_r from observations of this anisotropy are presented.

| REFERENCE | YEARS | ENERGY | g_r (% AU ⁻¹) at Earth. |
|-----------------------------|---------|---------|--|
| Yasue (1980) | 1969-73 | 5 GeV | 5 |
| | | 10 GeV | 3 |
| | | 100 GeV | 0.6 |
| Bercovitch (1969) | 1964-5 | 5 GeV | 1.6 |
| | | 10 GeV | 0.8 |
| Bercovitch (1971) | 1967-8 | 5 GeV | 9 |
| | | 10 GeV | 5 |
| Duggal and Pomerantz (1977) | 1964-75 | 10 GeV | 2 |
| Bieber and Pomerantz (1986) | 1961-83 | ~10 GeV | 1 to 3* |

TABLE 8.1. Values of the radial gradient g_r at the position of Earth for the given energy.
(* values range from 1 to 3% during a solar cycle).

Bercovitch (1969, 1971) was the first to use a type of north-south anisotropy analysis in order to determine g_r from neutron monitor data. Essentially, the radial gradient of galactic cosmic rays in space is manifested as a latitudinal anisotropy at Earth - the north-south

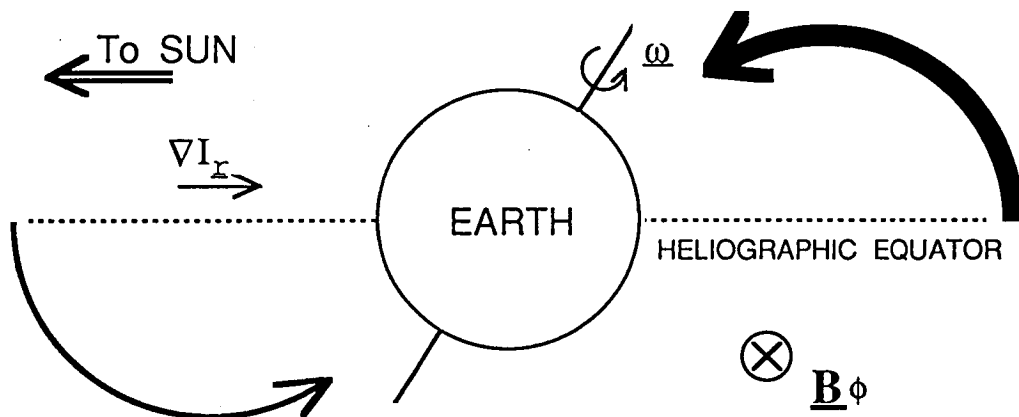


FIGURE 8.1. Typical gyro-paths of particles in a 'TOWARD' field configuration are schematically shown. Note that the gyro-radii of galactic cosmic ray particles are much larger than the scale of the Earth. The azimuthal component of the Sun's magnetic field is directed into the page. The radial component is toward the Sun. The radial gradient of cosmic rays along the heliographic equator causes more particles to be observed in the northern hemisphere due to particle gyration around the azimuthal component of the solar field.

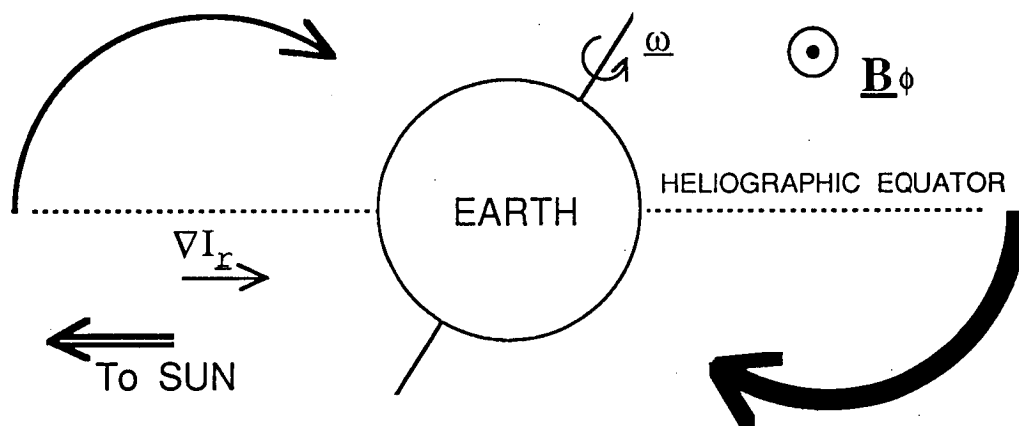


FIGURE 8.2. Typical gyro-paths of particles in an 'AWAY' field configuration are schematically shown. Note that the gyro-radii of galactic cosmic ray particles are much larger than the scale of the Earth. The azimuthal component of the Sun's magnetic field is directed out of the page. The radial component is away from the Sun. The radial gradient of cosmic rays along the heliographic equator causes more particles to be observed in the southern hemisphere due to particle gyration around the azimuthal component of the solar field.

anisotropy - caused by particles gyrating around local interplanetary magnetic field lines. Figures 8.1 and 8.2 show the typical gyro-paths of these particles in a 'toward' and 'away' field configuration. The two configurations are separated in space by the neutral sheet (see Chapter 6) and the Earth passes from one configuration to the other as the Sun revolves about its axis. By observing the difference between the count-rates of two terrestrial detectors observing at differing asymptotic latitudes, or the difference between the count-rate of a single detector in different field-states, the radial gradient g_r at 1 AU can be calculated. Table 1 summarizes some measurements of the radial gradient from observational data using this method.

Bercovitch (1971) and Duggal and Pomerantz (1977) assumed a P^{-1} type spectrum (P =rigidity) for their analyses. The result of Duggal and Pomerantz is dependent on the value of the diffusion constant which they used in their analysis. Yasue was the only one of these investigators to incorporate muon telescope data. He derived a spectrum of $P^{-0.7}$ for the radial gradient.

Others have done similar analyses to derive the upper-limiting rigidity of the north-south anisotropy and its variation over 27 days and 11 years. Swinson (1969, 1971) was the first to use this analysis to derive the related sidereal daily variation of galactic cosmic rays. Because the Earth's rotation axis and the Sun's rotation axis are not aligned, a constant north-south anisotropy (perpendicular to the heliographic equator) is manifested as a temporally constant north-south asymmetry in the flux of cosmic rays along the Earth's rotation axis and a sidereal daily variation. See Figure 8.4. Figure 8.3 schematically shows the relationship between the Sun's and Earth's rotation axis, the solar equatorial plane or heliographic equator, the ecliptic plane and the celestial equator.

Swinson (1971) estimated a rigidity upper bound for the north-south anisotropy of between 50 and 100 GV based on O'Gallagher and Simpson's (1967) proposal that $g_r \propto P^{-1}$. He also noted that this upper bound may be a reflection of the finite size of the magnetic sectors rather than an energy upper limit to the positive radial gradient. For comparison, Yasue (1980) determined the upper bound to be in the order of 200 GV. Errors on this result were +150 and -50 GV.

Pomerantz *et al.* (1982) and Swinson & Yasue (1991a,b) have demonstrated 27 day and 11 year waves in the north-south anisotropy and attribute this mainly to corresponding changes in the local interplanetary magnetic field.

8.2. THEORY

In terms of transport theory (see Chapter 1), the anisotropy vector is given by

$$\xi = \frac{3\underline{S}}{4\pi\nu p^2 f} \quad (8.1)$$

where \underline{S} is the vector which describes the streaming of cosmic rays. In heliographic coordinates, the north-south anisotropy is

$$\xi_{NS} = \xi_{\theta} \Big|_{\theta=\pi/2, r=1AU} \quad (8.2)$$

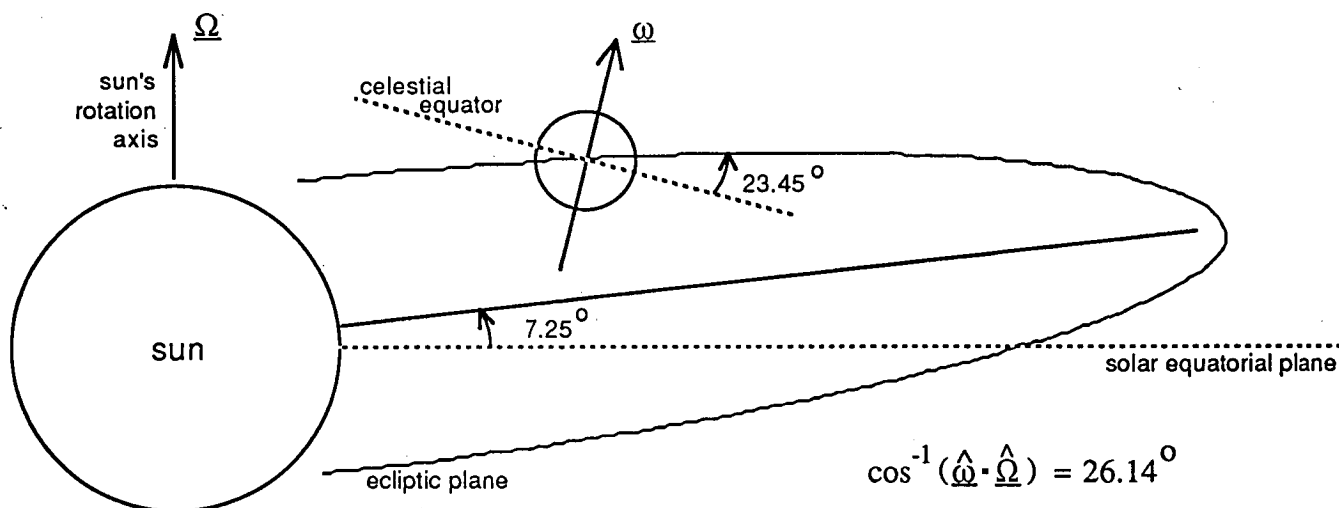


FIGURE 8.3. Schematic view of the orbit of the Earth around the Sun and the planes that define the heliographic coordinate system. The angle between the Earth's rotation axis and the Sun's rotation axis is measured to be $\theta_R = 26.14^\circ$.

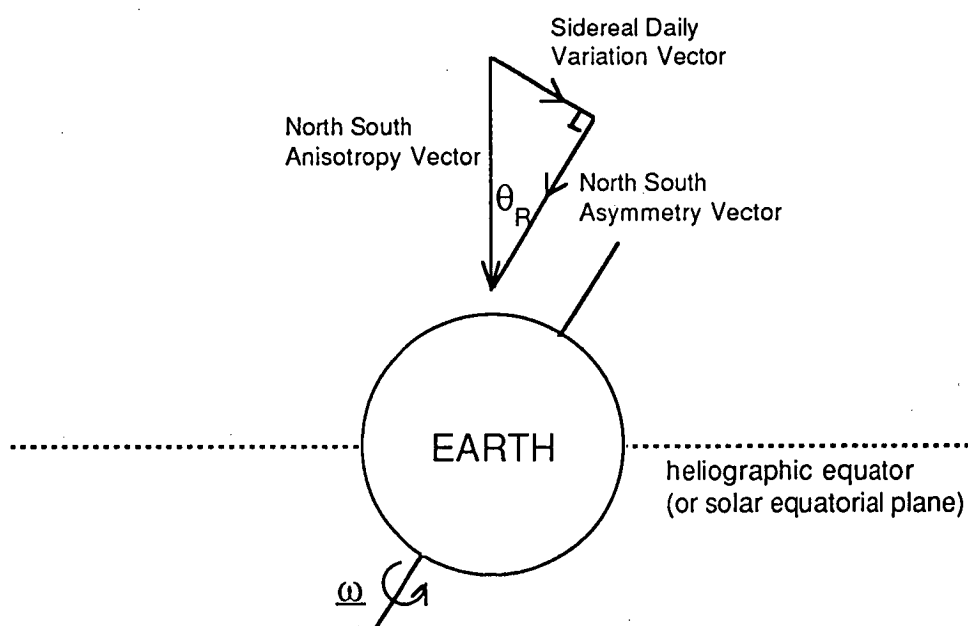


FIGURE 8.4. Relative orientation of the north-south anisotropy vector, north-south asymmetry vector and the sidereal daily variation vector. $\theta_R = 26.14^\circ$ as in Figure 8.3.

That is, the north-south anisotropy vector is the component of the general anisotropy vector along the polar angle θ at the Earth. In terms of the cosmic ray density function U , the streaming vector is given by (see Forman and Gleeson 1975):

$$\underline{S} = C \underline{V} U - K \left(\frac{\partial U}{\partial \underline{r}} \right)_{//} - \frac{K}{1 + (\omega\tau)^2} \left(\frac{\partial U}{\partial \underline{r}} \right)_{\perp} - \frac{\omega\tau K}{1 + (\omega\tau)^2} \left(\frac{\partial U}{\partial \underline{r}} \times \frac{\underline{B}}{|\underline{B}|} \right) \quad (8.3)$$

Therefore,

$$\begin{aligned} S_{\theta} &= - \frac{\omega\tau K}{1 + (\omega\tau)^2} \left(\frac{\partial U}{\partial \underline{r}} \times \hat{\underline{B}} \right) \\ &= - \frac{\omega\tau K}{1 + (\omega\tau)^2} U g_r \sin \psi \end{aligned} \quad (8.4)$$

$$\text{where } g_r = \frac{1}{U} \frac{\partial U}{\partial \underline{r}} \quad \text{and} \quad \hat{\underline{B}} \cdot \hat{\underline{r}} = \cos \psi \quad (8.5)$$

In going from equation 8.3 to 8.4, the perpendicular component has been neglected. Bieber and Pomerantz (1986) suggested that this component is generally much smaller than the asymmetric term. With this assumption,

$$\begin{aligned} \xi_{\theta} &= \frac{3S_{\theta}}{vU} = \frac{3K}{v} \cdot \frac{-(\omega\tau)}{1 + (\omega\tau)^2} g_r \sin \psi \\ &= \frac{-\lambda (\omega\tau)}{1 + (\omega\tau)^2} g_r \sin \psi \end{aligned} \quad (8.6)$$

where λ is the scattering mean-free-path. The gyro-frequency ω , the gyro-radius r_g , the collision time τ and the scattering mean free path are related by

$$(\omega\tau) = \frac{\lambda}{r_g} \quad (8.7)$$

Therefore,

$$\begin{aligned} \xi_{\theta} &= \frac{\left(\frac{-\lambda}{\omega\tau} \right)}{1 + \frac{1}{(\omega\tau)^2}} g_r \sin \psi \\ &= \frac{-r_g g_r \sin \psi}{1 + \left(\frac{r_g}{\lambda} \right)^2} \end{aligned} \quad (8.8)$$

Assuming $\frac{r_g}{\lambda} \ll 1$, then

$$\xi_{\theta} = -r_g g_r \sin \psi \quad (8.9)$$

This result assumes that the components (asymmetric, perpendicular and parallel) of the general diffusion *tensor* are given by

$$K^A = \omega \tau K_{\perp} \text{ (asymmetric component)} \quad (8.10)$$

$$K_{\perp} = \frac{K_{//}}{1 + (\omega \tau)^2} \quad \text{(perpendicular component)} \quad (8.11)$$

$$K_{//} = \frac{1}{3} v^2 \tau \quad \text{(parallel component)} \quad (8.12)$$

(eg: Forman and Gleeson 1975). In terms of the cosmic ray distribution function f ,

$$\begin{aligned} \xi_{\theta} &= \frac{3S_{\theta}}{4\pi v p^2 f} \\ &= \frac{3}{4\pi v p^2 f} (-4\pi p^2) \left[\underline{K} \cdot \nabla f - \frac{v}{3} \frac{\partial f}{\partial \ln p} \right]_{\theta} \quad \text{(see equation 1.22)} \\ &= - \frac{3}{v f} \begin{pmatrix} K_{\theta r} & K_{\theta \theta} & K_{\theta \phi} \end{pmatrix} \cdot \begin{pmatrix} \frac{\partial f}{\partial r} \\ \frac{1}{r} \frac{\partial f}{\partial \theta} \\ 0 \end{pmatrix} \\ &= - \frac{3}{v f} \left(K_{\theta r} \frac{\partial f}{\partial r} + \frac{K_{\theta \theta}}{r} \frac{\partial f}{\partial \theta} \right) \\ &= - \frac{3}{v} \left(K_{\theta r} g_r + \frac{K_{\theta \theta}}{r} g_{\theta} \right) \end{aligned} \quad (8.13)$$

where the gradient operators are defined by

$$g_r = \frac{1}{f} \frac{\partial f}{\partial r} \quad \text{and} \quad g_{\theta} = \frac{1}{f} \frac{\partial f}{\partial \theta} \quad (8.14)$$

and \underline{K} is the full diffusion tensor.

Now, $K_{\theta\theta} = K_{\perp}$

$$K_{\theta r} = K^A \sin \psi$$

$$K^A = \frac{p\nu}{3qB} \quad (8.15)$$

(see Chapter 1). Hence,

$$\xi_{\theta} = \frac{-3}{\nu} \left(\frac{p\nu}{3qB} g_r \sin \psi + \frac{K_{\perp}}{r} g_{\theta} \right) \quad (8.16)$$

From this theoretical expression it can be seen that the north-south anisotropy can be explained by the existence of a radial gradient (first term) and perpendicular diffusion driven by a latitudinal gradient (second term). Again, neglecting the second term (as for equation 8.4), the north-south anisotropy can be written in terms of the radial gradient as

$$\xi_{NS} = \xi_{\theta} \Big|_{\theta=\pi/2, r=1AU} = \frac{-p}{qB} g_r \sin \psi = -r_g g_r \sin \psi \quad (8.17)$$

which coincides with the expression derived at equation (8.9). It is clear from this equation that a direct measurement of ξ_{NS} using terrestrial based particle detectors gives a measure of g_r as a function of energy.

8.3. ξ_{NS} FROM OBSERVATIONAL DATA FOR AN ARBITRARY DETECTOR.

The formalism given in Chapter 5 is used throughout this section. In the case of the north-south anisotropy, $F(\chi)$ can be approximated by $\eta \cos \chi$ where the symmetry axis is perpendicular to the heliographic equator. Consider Figure 8.5. \underline{R} is a vector along the symmetry axis of the anisotropy with magnitude η . As the Earth rotates, this north-south anisotropy will give rise to a constant increase/decrease (depending on the sign of η) in the count rate of a particle detector due to that component of \underline{R} along the Earth's rotation axis (R_z), along with a sidereal daily variation of intensity due to the components of \underline{R} perpendicular to the rotation axis ($R_x + R_y$). That is,

$$\begin{aligned} R_x &= \eta \sin \theta_R \cos \alpha_R \\ R_y &= \eta \sin \theta_R \sin \alpha_R \\ R_z &= \eta \cos \theta_R \end{aligned} \quad (8.18)$$

where

$$\alpha_R = \frac{2\pi}{24} t_{(\text{hours})} \quad (8.19)$$

The magnitude of the anisotropy is

$$|\xi_{NS}| = \eta \cdot G(P) \quad (8.20)$$

The *observed* variation \underline{D} of count-rate in a particle detector due to the space variation \underline{R} is related through the coupling coefficients c_I^0 , c_I^1 and s_I^1 via:

$$\begin{pmatrix} D_x \\ D_y \\ D_z \end{pmatrix} = \begin{pmatrix} c_1^1 & s_1^1 & 0 \\ -s_1^1 & c_1^1 & 0 \\ 0 & 0 & c_1^0 \end{pmatrix} \cdot \begin{pmatrix} R_x \\ R_y \\ R_z \end{pmatrix} \quad (8.21)$$

(see Chapter 5, equations 5.8 to 5.10, with $n=0,1$).

Having determined $|\underline{R}| = \eta$, the magnitude of the north-south anisotropy is found via equation 8.20 and the magnitude of the radial gradient of cosmic rays in the vicinity of the Earth can be determined via equation 8.17 for a given energy.

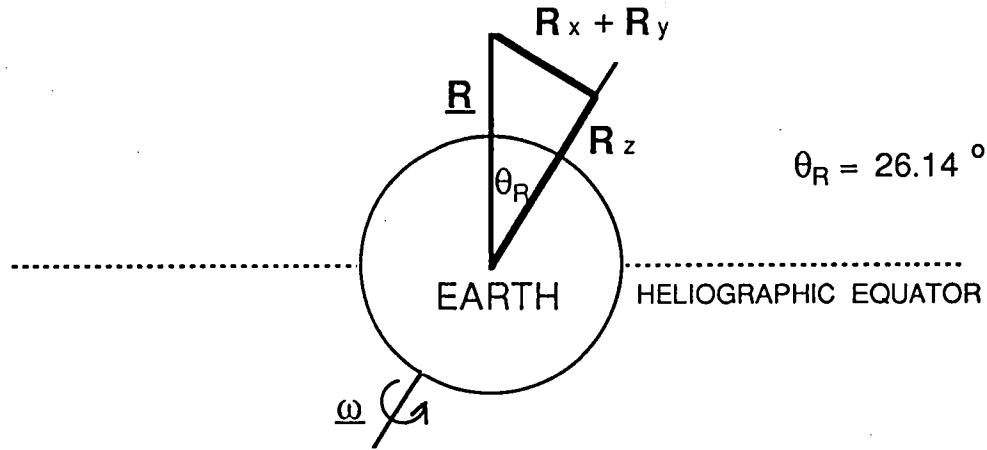


FIGURE 8.5. Components of the vector \underline{R} which is aligned with the symmetry-axis of the north-south anisotropy.

From Figure 8.5 and equation 8.21 it is seen that

$$\eta = \frac{R_z}{\cos \theta_R} = \frac{D_z}{c_1^0 \cos \theta_R}, \quad \theta_R = 26.14^\circ \quad (8.22)$$

Hence, for a chosen set of (γ, P_U) which uniquely determine the coefficient c_I^0 for a given particle detector, a determination of R_z is sufficient to uniquely specify η . This is convenient because daily averages of count-rate recorded by particle detectors can be used. The $R_x + R_y$ terms average to zero over one complete (sidereal) day. Then, assuming R_z is known,

$$\eta = \frac{R_z \times 100}{\cos \theta_R} \% \quad (8.23)$$

$$|\xi|_{NS} = \eta \left(\frac{P}{10} \right)^\gamma \% , \quad P \leq P_U \quad (8.24)$$

and

$$g_r = \frac{|\xi|_{NS}}{r_g \sin \psi} \% \text{ AU}^{-1} \quad (\text{given } r_g \text{ in AU}) \quad (8.25a)$$

Assuming the interplanetary magnetic field strength at Earth is 5nT then (using 8.45)

$$g_r \approx 35.4 \times \left(\frac{P(\text{GV})}{10} \right)^{\gamma-1} \cdot R_z \times 100 \% \text{ AU}^{-1} \quad \text{at 1 AU} \quad (8.25b)$$

Two methods of determining R_z are now given.

8.4. DETERMINING R_z : METHOD 1.

Let I_i be the total intensity (daily average count rate) of particle-detector i . Let J_i be the total intensity of the same detector neglecting that component of the count rate due to the north-south anisotropy. Let $D_{z,i}$ be the (fractional) change of daily-averaged intensity due to the north-south anisotropy. Then, following equation 5.2,

$$D_{z,i} = \frac{\Delta I}{I} = \frac{I_i - J_i}{J_i} \quad (8.26)$$

and

$$\begin{aligned} I_i &= J_i (1 + D_{z,i}) \\ &= J_i (1 \pm c_{I,i}^0 R_z) \end{aligned} \quad (8.27)$$

Note from Figures 8.1 and 8.2 that the north-south anisotropy changes sign, but not magnitude, when moving from a 'toward' magnetic field sector to an 'away' sector. Hence the reason for the \pm sign in the above formula. Use '+' for *away* sectors and '-' for *toward* sectors. Comparing two separate detectors denoted by indices i and j , define a normalization factor between them $A_{i,j}$ such that

$$J_i = A_{i,j} J_j \quad (A_{i,i} = 1, A_{j,i} = A_{i,j}^{-1}) \quad (8.28)$$

Averaging data over an equal number of *toward* and *away* days,

$$\langle I_i \rangle = \langle J_i \rangle \quad (\text{hence } A_{i,j} = \langle I_i \rangle / \langle I_j \rangle) \quad (8.29)$$

Combining equation 8.28 with 8.27 for two separate detectors,

$$I_i - A_{i,j} I_j = J_i (1 \pm c_{l,i}^0 R_z) - A_{i,j} J_j (1 \pm c_{l,j}^0 R_z) \quad (8.30)$$

$$\therefore I_i - A_{i,j} I_j = \pm J_i (c_{l,i}^0 - c_{l,j}^0) R_z \quad (8.31)$$

where, again, the \pm sign depends on whether the Earth is in an away or towards sector field. In this form R_z is a fraction. R_z can be calculated from equation 8.31 by regressing the intensity data with the coupling coefficients over a number of pairs of detectors (i, j). The energy dependence of the anisotropy may be found simultaneously by varying the coupling coefficients (which are a function of the energy spectrum of the anisotropy) and finding the 'best-fit' regression over the parameters γ and P_U .

Consider two detectors denoted by indices 1 and 2. Rearranging equation 8.31,

$$\left(\frac{I_1}{J_1} - \frac{I_2}{J_2} \right) = \pm (c_{1,1}^0 - c_{1,2}^0) R_z \quad (8.32)$$

$$\text{Let } y = \left(\frac{I_1}{J_1} - \frac{I_2}{J_2} \right), \quad x = \pm (c_{1,1}^0 - c_{1,2}^0)$$

Then,

$$y = R_z x \quad (8.33)$$

There is a unique data point (x, y) for each independent pair of detectors. Assume all the errors in this regression are due to the y variable and denote the error by Δy . This error is due to random measurement errors and statistical fluctuations in the count rate of the detectors. There is a random and somewhat indeterminable error in the x variable (due to the uncertainty in the coupling coefficients) but this is neglected for now. Associated with each data point, define a weight w via:

$$w = \frac{1}{\left(\frac{\Delta y}{y} \right)^2} \quad (8.34)$$

The reason for defining the weight term in this way is that the model under regression is constrained to pass through the point $(x, y) = (0, 0)$. Points far from the origin with large errors influence the fit similarly to points close to the origin with small errors. On summing over all independent pairs of detectors ($i=1..n$),

$$R_z = \frac{\sum_i w_i x_i y_i}{\sum_i w_i x_i x_i} \quad (8.35)$$

with associated 'error'

$$(\Delta R_z)^2 \approx \frac{1}{(n-1)} \frac{\sum_i w_i d_i d_i}{\sum_i w_i x_i x_i} \quad (8.36)$$

where

$$d_i = (y_i - R_z x_i) \quad (8.37)$$

Δy is obtained via a standard propagation of errors:

$$(\Delta y)^2 = \left(\frac{\partial y}{\partial I_{T1}} \Delta I_{T1} \right)^2 + \left(\frac{\partial y}{\partial I_{T2}} \Delta I_{T2} \right)^2 + \left(\frac{\partial y}{\partial I_{A1}} \Delta I_{A1} \right)^2 + \left(\frac{\partial y}{\partial I_{A2}} \Delta I_{A2} \right)^2 \quad (8.38)$$

where I_{T1} is the intensity of detector 1 and I_{T2} the intensity of detector 2 in towards sectors for a given pairing. I_{A1} and I_{A2} are the corresponding intensities in away sectors. The errors ΔI are the standard errors in the *mean* count-rate (due to statistical fluctuations in the data).

8.5. DETERMINING R_z : METHOD 2.

For a given detector, denote the average daily intensity recorded in a towards sector by I_T and in an away sector by I_A . Then from equation 8.27,

$$I_T = J(1 - c_I^0 R_z) \quad (8.39)$$

$$I_A = J(1 + c_I^0 R_z) \quad (8.40)$$

$$\therefore R_z = \frac{-1(I_T - I_A)}{c_I^0(I_T + I_A)} \quad (8.41)$$

which can be calculated for each of the available detectors independently. The error on R_z determined from this formula is

$$(\Delta R_z)^2 = \left(\frac{\partial R_z}{\partial I_T} \Delta I_T \right)^2 + \left(\frac{\partial R_z}{\partial I_A} \Delta I_A \right)^2 \quad (8.42)$$

Hence, given a pair $(R_z, \Delta R_z)$ and an associated weight

$$w = \frac{1}{(\Delta R_z)^2}$$

for each available detector, an average or mean value of R_z can be found via

$$\overline{R_z} = \frac{\sum w_i R_{z,i}}{\sum w_i} \quad (8.43)$$

with associated variance

$$\sigma^2_{\overline{R_z}} = \frac{1}{\sum w_i} \quad (8.44)$$

8.6. T/A SECTOR BINNING.

From the preceding section, it is seen that interplanetary field data are required for each day in order to determine whether the Earth is in a towards or an away sector. The field data set used in this analysis was the standard set used by the Hobart cosmic-ray groups. The set has been compiled from various sources by D.B. Swinson (University of New Mexico) and J.E. Humble (University of Tasmania). The sources include data from whatever spacecraft measurements are available and deductions, published in Solar Geophysical Data, from polar magnetograms. The data set consists of a single estimate for each day. If the Earth is in a toward sector the day is labelled 'T'. If the Earth is in an away sector the day is labelled 'A'. If it is unclear whether the Earth is in a single sector because the field is mixed, the day is labelled 'X'. Days for which there are no data are labelled 'N'. Sector boundary crossings (ie: the Earth crossing the neutral sheet) can be identified as changes in the field direction from one day to the next. Note however that if a number of 'N' or 'X' days appear between a 'T' and 'A' day, for example, then it is impossible to locate the temporal position of the boundary crossing (to within one day).

The north-south anisotropy arises from particle gyration about the local interplanetary magnetic field and only gives a smooth latitudinal gradient if all of the particles which are incident on the Earth have gyro-orbits within a single sector. If the sector boundary is too close, then some particles will have been incident on the Earth from an opposite sector (a greater proportion are affected at higher energies) and will not be gyrating in the correct sense to produce a monotonic gradient as shown in Figures 8.1 and 8.2. We must be sure therefore that the sector boundary is not so close as to significantly influence the analysis. Since the gyroradius is proportional to rigidity the Earth needs to be further from a sector boundary in order for the anisotropy to exist at higher energies. The gyroradius of a particle r_g , its rigidity P , and the magnetic field strength B are related by

$$r_g \text{ (in AU)} \approx \frac{1}{45} \frac{P \text{ (in GV)}}{B \text{ (in nT)}} \quad (8.45)$$

For a 5γ (or 5 nT) field (which is an average value near 1AU), a 50 GV particle has a gyroradius of roughly 0.2 AU. Since the Sun rotates with a period of approximately 27 solar days, this gyroradius corresponds to approximately 1 day's rotation in the azimuth coordinate. Hence to be sure that a 50 GV particle has been last modulated within a single sector, the Earth needs to be at least 1 day from a sector boundary crossing.

Correspondingly, there would need to be a 0.2 radian latitudinal displacement of the Earth from the neutral sheet. These distances would double for a 100 GV particle.

Because of this, a routine was written to screen the T/A data and only accept those days for which it is certain that the Earth is further than some fixed number of days, denoted by n , from a boundary crossing, where $n=1$ for particles with rigidity ≤ 50 GV, $n=2$ for particles with rigidity ≤ 100 GV etc. For $n=1$ as an example, a string of days such as

...TTTTXTTTAAAAATTTTXXTNXXTNTTTAAAA...

would be replaced by

...TTT***T##AAA##TTT*****T##AAA...

where * denotes a rejected day, # denotes a boundary crossing.

Because the neutral sheet is a surface in three-dimensions, it is possible that the Earth is close to a boundary in heliographic latitude (maybe < 0.2 AU) but a large azimuthal distance from a boundary crossing. See Figure 8.6 (bottom plot around day 78) for an example. T/A days are denoted along the x-axis and the plot is the latitudinal displacement of the neutral sheet from Earth. These data are fully described in Chapter 6. It was thought that the parameterized neutral sheet (see Sections 6.2 and 6.3) could be used to flag days when the Earth is close to the neutral sheet but many days from a boundary crossing, however it was decided that the data were too unreliable on the time scale of a day or so, as shown by Figure 8.6 (top plot). The sector crossings as denoted by a change from T to A or A to T should coincide exactly with $(\theta_c - \theta_{ns}) = 0$. As seen from Figure 8.6, the data can be a day or two displaced from such crossings. The main reason for this is that the neutral sheet data are derived from observations of the photospheric source surface of the Sun and a *constant* propagation speed for the solar wind of 400 km s^{-1} is assumed. The solar wind in practice varies in the range $\sim 300 \text{ km s}^{-1}$ to $\sim 700 \text{ km s}^{-1}$. Features observed at the source surface therefore, may reach Earth a day either side of the predicted arrival time. Note that this sensitivity is in contrast to the insensitivity of the solar wind speed in the correlation analysis described in Section 6.5. In summary, only the rejection criteria of being more than n days from a boundary crossing was used to screen the magnetic field data.

8.7. ALGORITHM.

The following steps describe the algorithm adopted to calculate R_z from neutron monitor and muon telescope data.

- 1) Choose a year of data for the analysis. R_z is calculated from a complete year's data in order that there be enough T and A days to obtain a statistically significant result. Choose the rigidity spectrum of the anisotropy by specifying (γ, P_U) which uniquely define the coupling coefficients for each detector.

- 2) Read in the data and the corresponding coupling coefficients (which are a function of year for neutron monitors as described in Chapter 5) for all available detectors for that year.

- 3) Group the days of the year into towards (T), away (A) or rejected days based on the criteria described in the previous section.

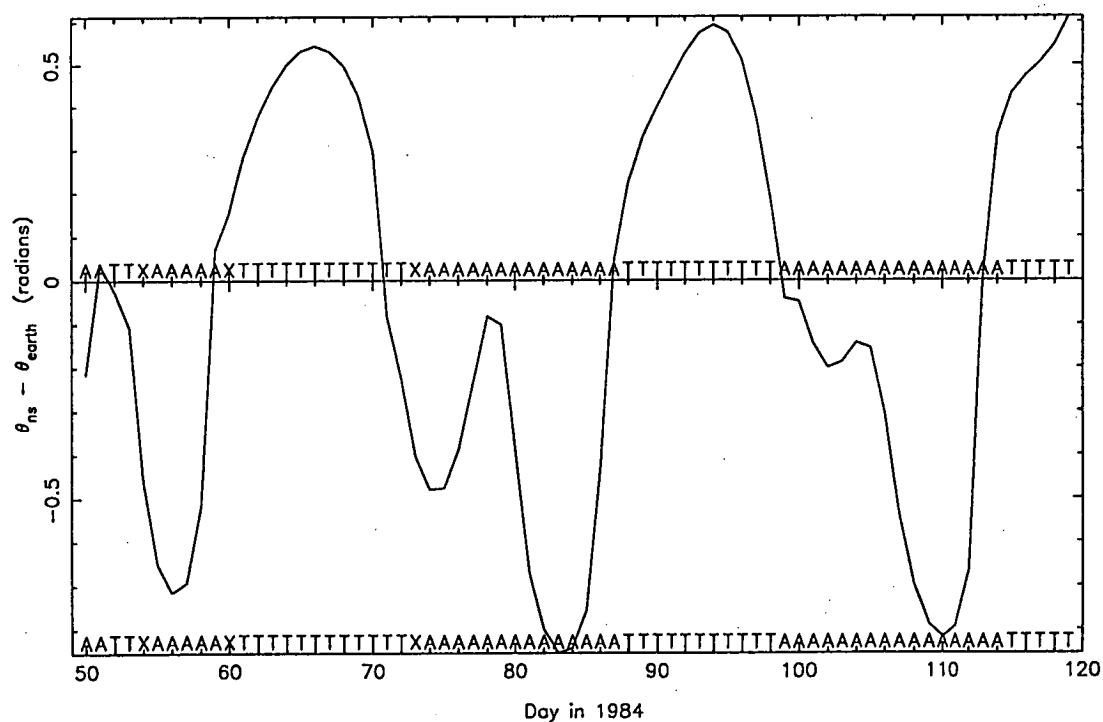
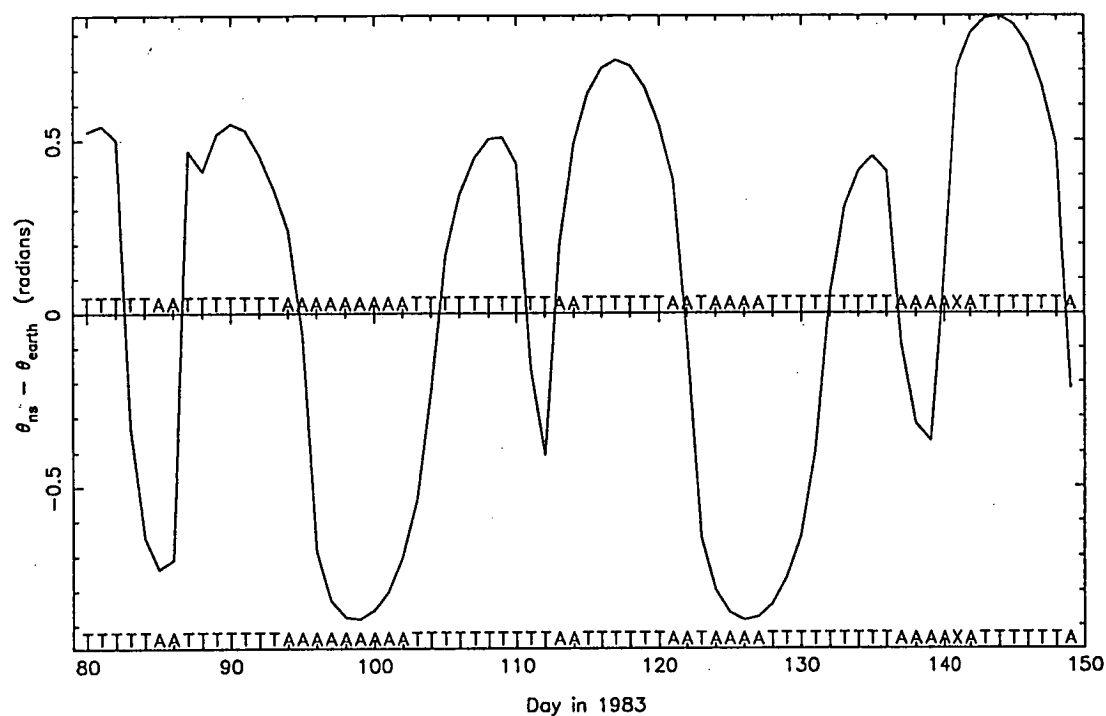


FIGURE 8.6. Plots showing the latitudinal displacement of the neutral sheet from Earth for sample days in 1983 and 1984. The top plot demonstrates an example of discrepancy around boundary crossing times between the neutral sheet data and the T/A sector data used in the north-south anisotropy analysis. The bottom plot is an example of the neutral sheet coming close to Earth but the Earth being many days from a boundary crossing.

| Telescope type | Location | Mnemonic | β_P (% mb^{-1}) | β_H (% km^{-1}) | Available years |
|----------------------------|--------------------|-------------------------------|------------------------------------|------------------------------------|-----------------------------------|
| neutron monitor | Mt. Wellington | mtwiqs | -0.985 | - | 1975,76, 77,78,82, 83,84,85 |
| neutron monitor | Mawson | nmcomb | -0.739 | - | 1975,76, 77,78,82, 83,84,85 |
| neutron monitor | Brisbane | briiqs | -0.739 | - | 1977,78, 82,83,84, 85 |
| neutron monitor | Darwin | dariqs | -0.739 | - | 1978,82, 83,84,85 |
| neutron monitor | Hobart | hobiqs (hobnn before 1978) | -0.739 | - | 1976,77, 78,82,83, 84,85 |
| surface muon telescope | Mawson | sncomb | -0.1 | -6.0 | 1975,76, 77,78,82, 83,84 |
| surface muon telescope | Mawson | sscomb | -0.1 | -6.0 | 1975,76, 77,78,82, 83,84 |
| underground muon telescope | Mawson | uncomb | -0.06 | -0.73 | 1983,85 |
| underground muon telescope | Mawson | uscomb | -0.06 | -0.73 | 1984,85 |
| underground muon telescope | Cambridge (Hobart) | cammu | -0.0487 | 0.0 | 1975,76 |
| underground muon telescope | Cambridge (Hobart) | cam4n | -0.0487 | 0.0 | 1975,76 |
| underground muon telescope | Mawson | p6 | -0.06 | -0.73 | 1984 |

TABLE 8.2. List of available detectors operated by the Hobart cosmic-ray groups between 1975-78 and 1982-85. All available detectors for each year were used in the north-south anisotropy analysis. The Hobart neutron monitor was an IGY detector before 1978 and an IQSY detector after 1978, hence the mnemonic name change.

4) For each detector, correct the data for atmospheric effects. For neutron monitors this is a standard pressure correction. For muon telescopes this is pressure *and* height correction using the algorithm described in Chapter 7. Note that the height data as measured by Mawson radiosondes consist of one measurement per day. For the purpose of correcting the data from the muon telescopes at Mawson, a linear interpolation was applied to the height measurements in order to obtain a value for the height data for each hour of the day. The height correction was performed on the count rate for each hour using this interpolated data. The count rate was then averaged to give a daily averaged count rate for each day.

5) For each detector, flag data spikes and days where Forbush decreases are observed. This was done visually for each detector and for each year of the analysis. A spike and level-change recognition algorithm was developed for the purpose of automatically flagging level shifts and transient spikes in the data. Appendix 6 describes this algorithm. It was found that this algorithm, although the most successful of such algorithms for automatically detecting level-changes, was unsuitable for discriminating days on which there was a shallow Forbush decrease. Considerable effort would be required to develop an algorithm to automatically decide the point at which the count-rate has fully recovered after a Forbush decrease. It was decided that it would be quicker and more accurate to simply *visually* flag such data.

6) Find mutually acceptable days for each detector *pairing* if using 'method 1' (described in Section 8.4) to determine R_z or, if using 'method 2', find days whereby the data are not rejected on the basis of any of (a) a mixed or undetermined field day, (b) Forbush decrease or data spike, (c) null data.

7) Remove any long-term linear trend due to 11-year modulation effects or detector efficiency decay. This was performed by fitting a straight line through the whole year's data and rotating about any linear slope (see Section 7.4c).

8) Bin the data into T or A days and take appropriate averages for each bin. Use 'method 1' (equations 8.26 - 8.38) or 'method 2' (equations 8.39 - 8.44) to calculate R_z as a function of (γ, P_U) . Vary the spectrum and repeat steps 1-8 to determine the 'best-fit' value of R_z .

Table 8.2 lists the available detectors operated by the Hobart cosmic-ray groups between the years 1975-78 and 1982-85. All available detectors for each year were used in the north-south anisotropy analysis. When using method 1, the detectors were paired in such a way that no pair of detectors was a combination of other pairs. For example, if there were four detectors, labelled A, B, C and D, then they could be paired (A,B), (A,C) and (A,D). A pairing (B,C) would not be used as it would be considered a combination of the pairs (A,B) and (A,C). In this sense, the detector *pairs* are said to be independent. The use of 'independent' in this context does not mean that independent *data* were used for each pair. Clearly in the above example, all pairs use data from detector A.

8.8. RESULTS.

Figure 8.7 shows a sample fit for R_z for 1985 using method 1 with $(\gamma, P_U) = (0.5, 200 \text{ GV})$. The detectors corresponding to the marked data points are shown in Table 8.4. The fitted slope was $(1.02 \pm 0.14) \times 10^{-3}$ which corresponds to a radial gradient (for 10 GV particles) of $(3.6 \pm 0.5) \% \text{ AU}^{-1}$. Appendix 7 contains the full results of g_r for 1975-78 and 1982-85 using method 1. Results are presented as graphs of g_r vs

P_U index for γ ranging from 0.7 to -0.5 for a rigidity of 10 GV. Equation 8.25b can be used to determine g_r from these plots for other rigidity values. Values of P_U in GV for the corresponding P_U index are given in Table 8.3. Full results of g_r for various (γ, P_U) pairs derived using method 2 are given in Appendix 8. Appendix 9 contains contour diagrams of χ^2 (goodness of fit) over (γ, P_U) of the results using method 1. Appendix 7 and 8 results are summarized in Figures 8.8, 8.9 (method 1) and 8.10, 8.11 (method 2). These figures are plots of g_r vs *year* for a fixed (γ, P_U) pair.

| P_U index | P_U (GV) | γ index | γ |
|-------------|------------|----------------|----------|
| 1 | 30 | 1 | 0.7 |
| 2 | 50 | 2 | 0.6 |
| 3 | 100 | 3 | 0.5 |
| 4 | 200 | 4 | 0.3 |
| 5 | 500 | 5 | 0.2 |
| 6 | 1000 | 6 | 0.1 |
| | | 7 | 0.0 |
| | | 8 | -0.5 |
| | | 9 | -1.0 |
| | | 10 | -1.5 |

Table 8.3. List of actual values of γ, P_U corresponding to the indices used in figures in Appendices 7 to 9.

| data point | detector pair |
|------------|----------------|
| A1 / T1 | mtwiqs, uscomb |
| A2 / T2 | nmcomb, uscomb |
| A3 / T3 | briiqs, uscomb |
| A4 / T4 | dariqs, uscomb |
| A5 / T5 | hobiqs, uscomb |
| A6 / T6 | uncomb, uscomb |

Table 8.4. Detector pair corresponding to each data point labelled A1-A6 and T1-T6 in Figure 8.7 (ie: all available detectors for 1985).

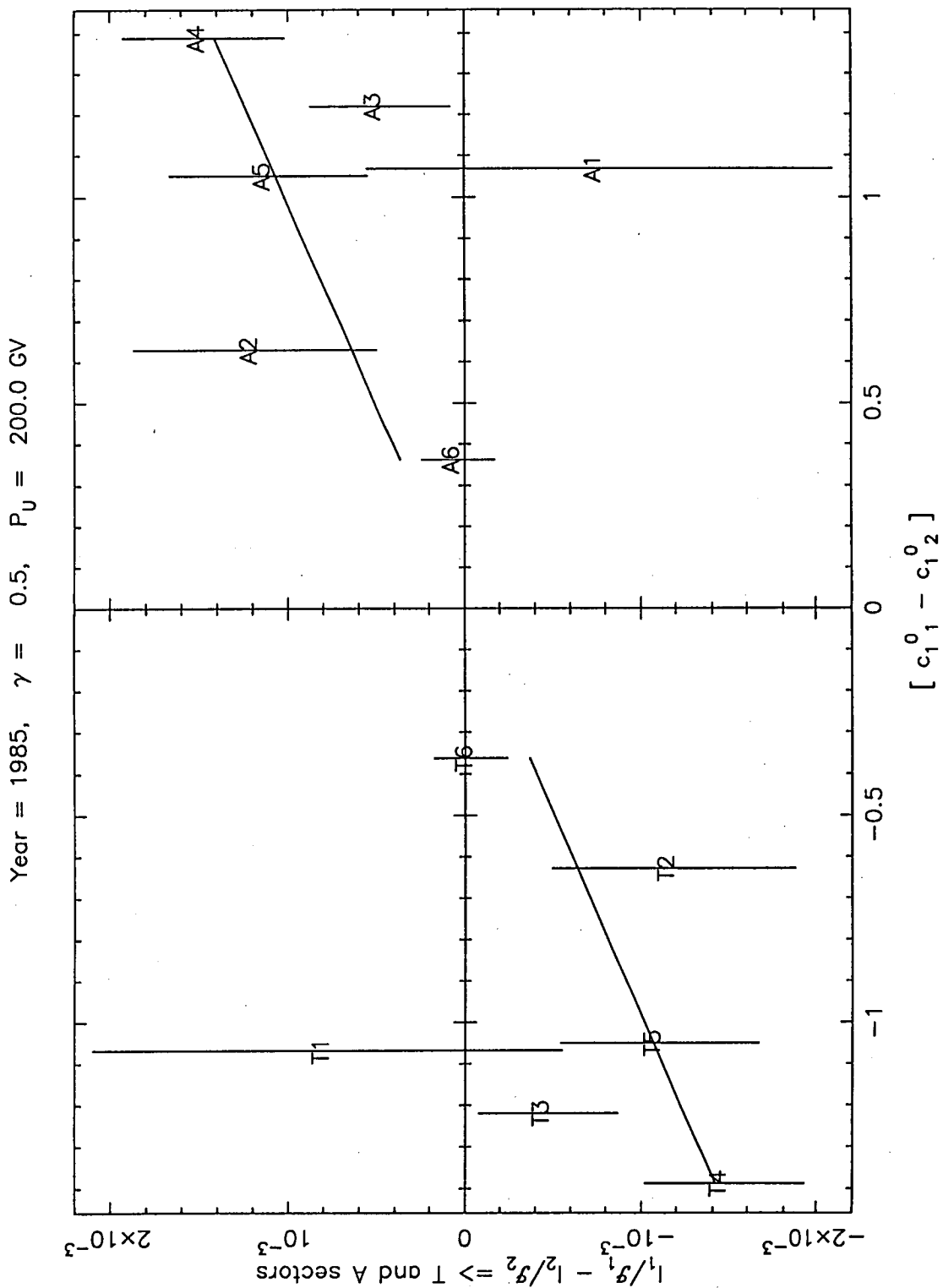


FIGURE 8.7. Fit for R_z (slope) using method 1. Six independent pairs of detectors were used. See Table 8.2 for a list of those detectors available in 1985 and Table 8.4 for a list of the detector pair corresponding to each of the data points. Data from toward days are labelled with a T and data from away days with an A. Error bars are those determined from equation 8.38.

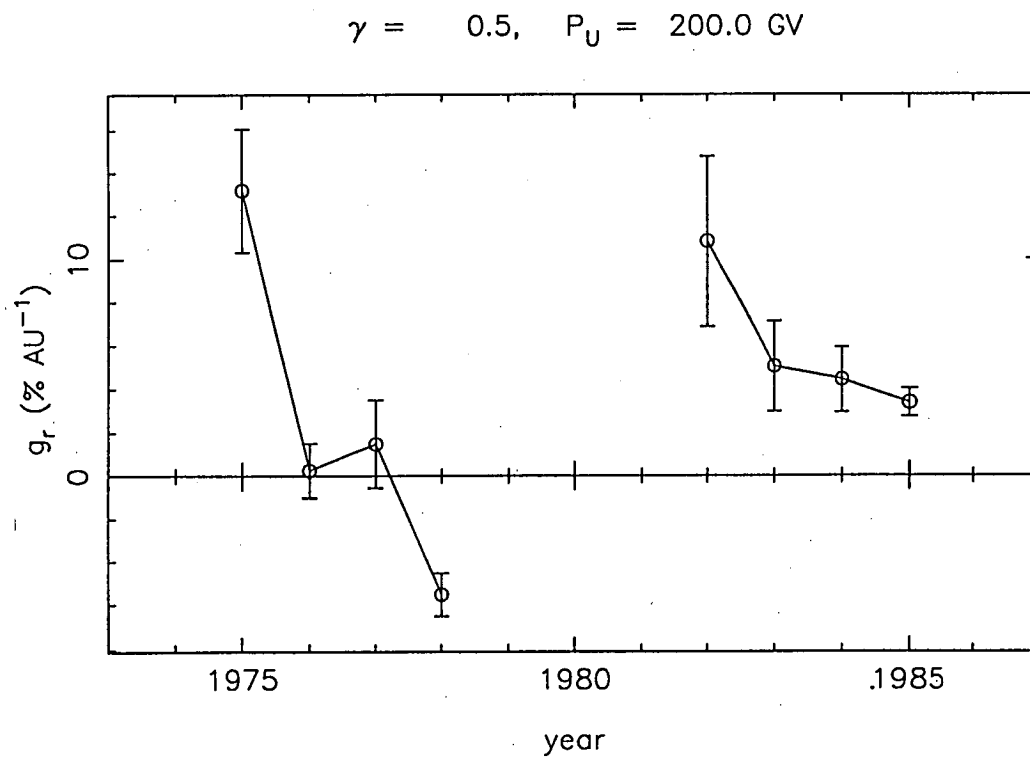
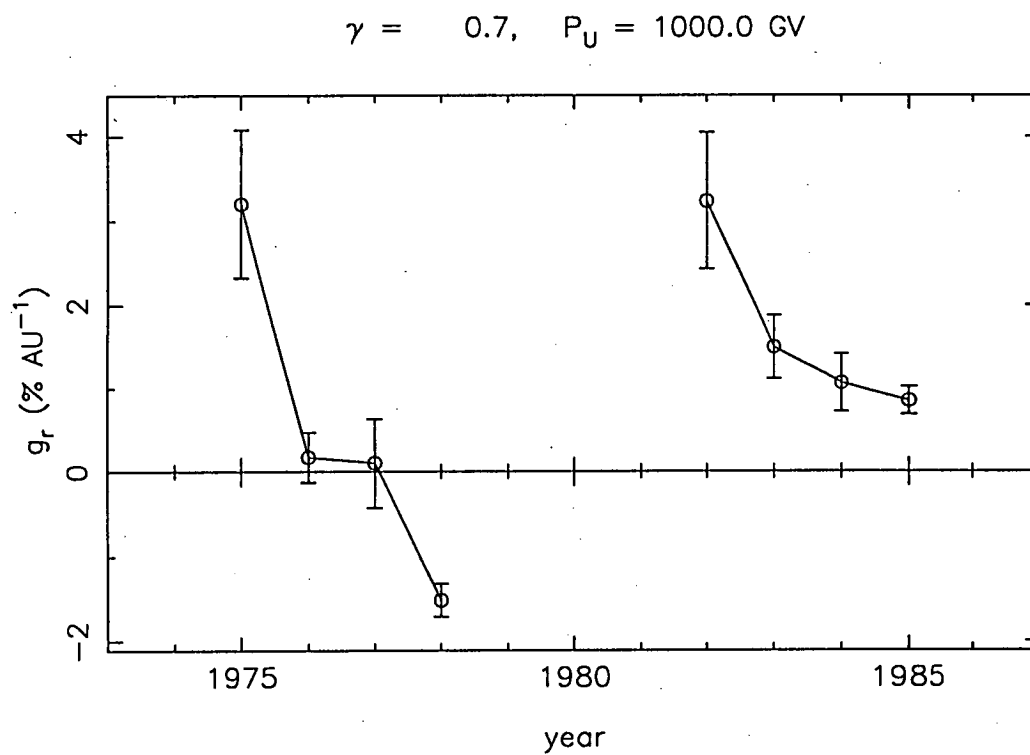


FIGURE 8.8. Plots of radial gradient vs year for a fixed γ, P_U using method 1. Error bars are those determined by equation 8.36. The gradient is for 10 GV rigidity particles. Equation 8.25b can be used to determine the gradient for other rigidities.

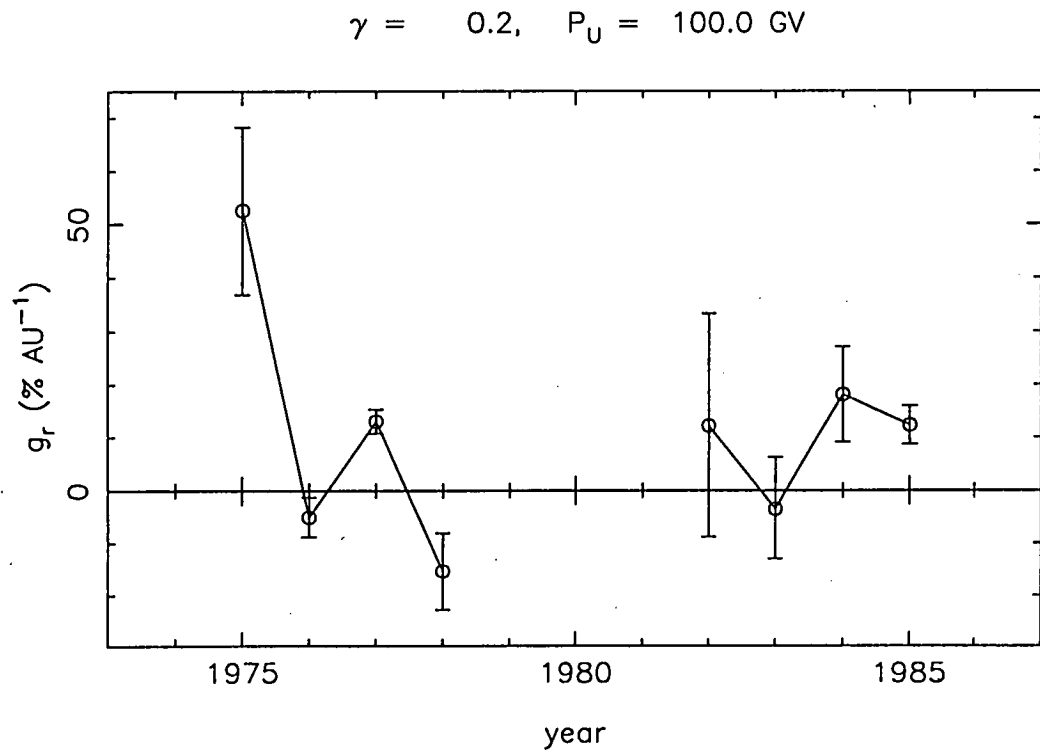
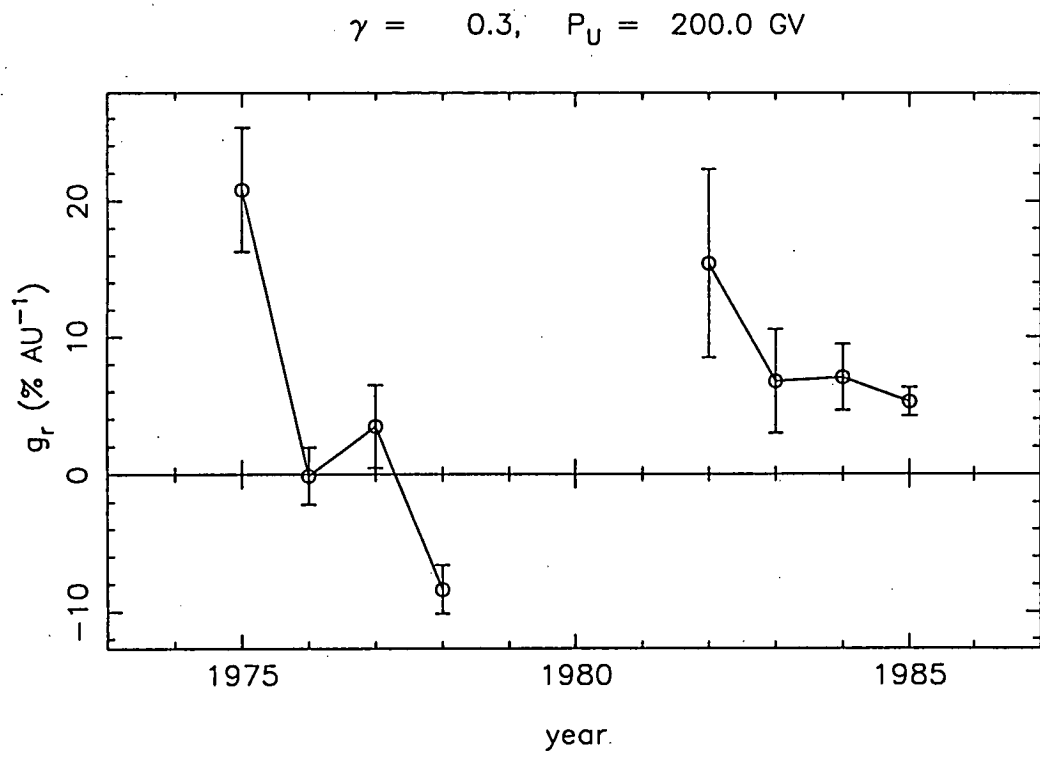


FIGURE 8.9. As for Figure 8.8 but for different γ, P_U values.

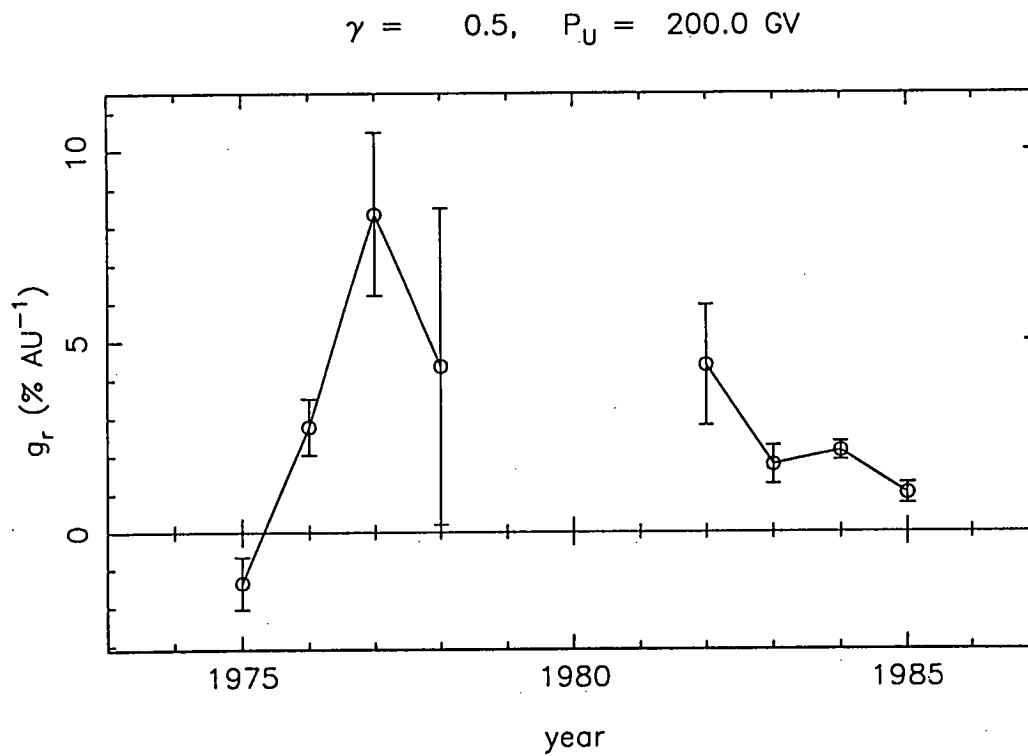
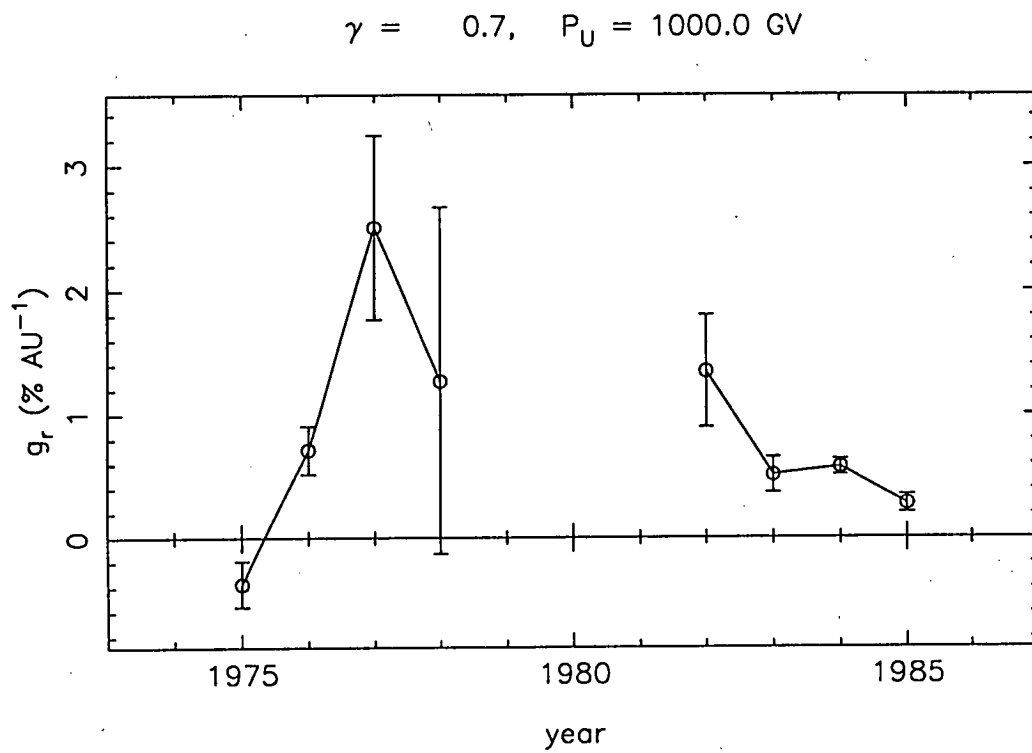


FIGURE 8.10. Plots of radial gradient vs year for a fixed γ, P_U using method 2. Error bars are those determined by equation 8.36. The gradient is for 10 GV rigidity particles. Equation 8.25b can be used to determine the gradient for other rigidities.

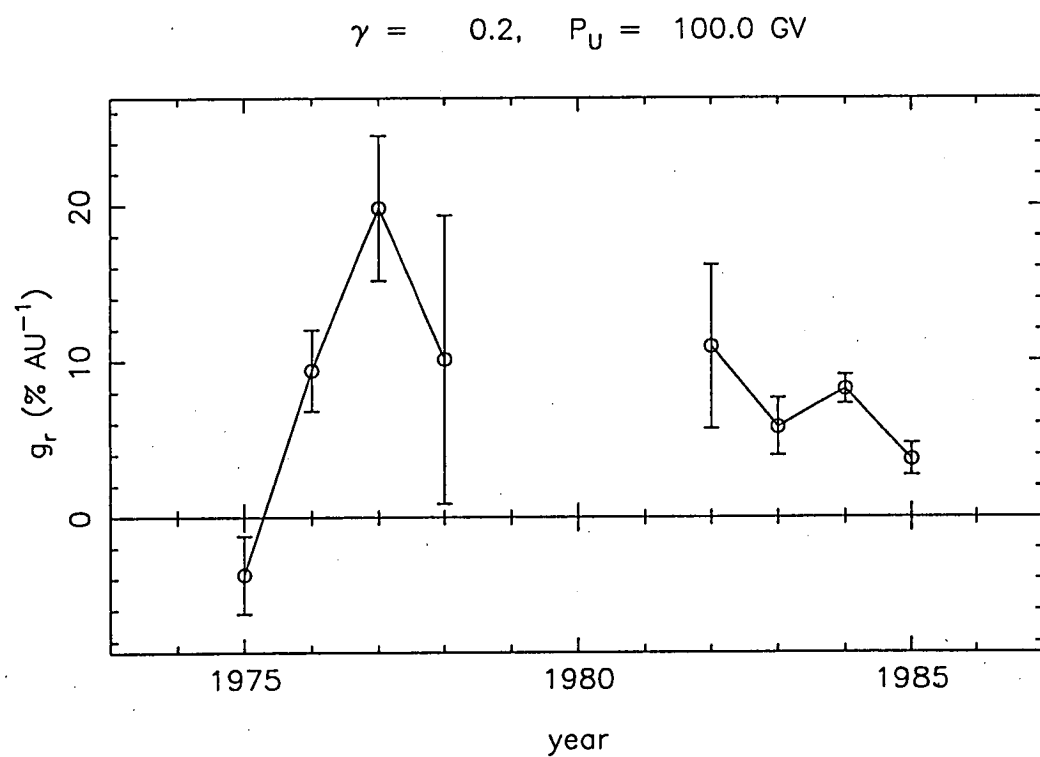
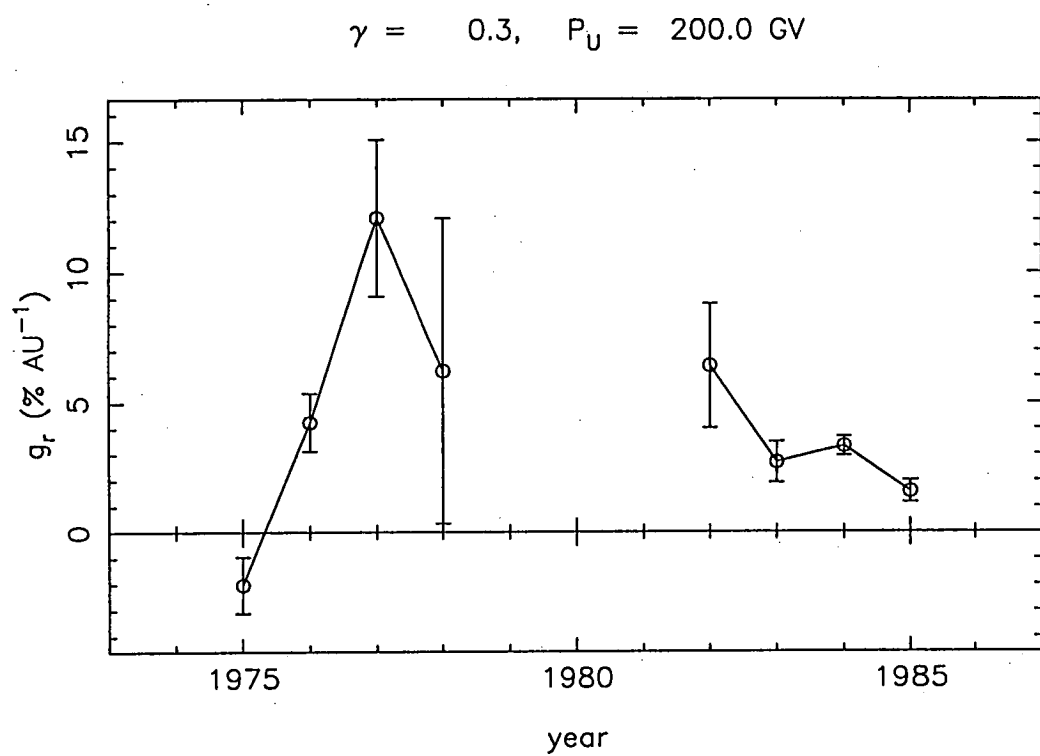


FIGURE 8.11. As for Figure 8.10 but for different γ, P_U values.

8.9. DISCUSSION OF RESULTS.

Consider first the graphs of g_r vs (γ, P_U) in Appendices 7 and 8. For positive γ the graphs look very similar between γ values for a fixed year. There are a couple of notable trends evident. As γ increases, g_r decreases for a fixed P_U index value. The errors also tend to become smaller. As P_U increases (for a fixed γ), g_r generally decreases above $P_U \approx 100$ GV. If g_r is indeed small (say $<1\%$ AU^{-1}) in the energy window in which these detectors are sensitive, then either γ and P_U are large in magnitude (eg: $\gamma, P_U = 0.7, 1000$ GV), or P_U is small (say around 50 GV) and the statistics are not good enough to determine a unique γ and indeed a significant value of g_r .

Consider these possibilities in turn. Above a rigidity of about 200 GV, it is less clear whether the diffusion picture of the transport equation is still appropriate (Jokipii 1971, Kota 1991). If the scattering mean-free-path of the cosmic rays becomes comparable with the scale length of a sector, for example, the theory presented here which relates g_r to the intensity differences between opposing sectors may not be totally valid. It therefore seems inappropriate to increase P_U in order to satisfy any pre-conceived notion that g_r is (say) below 1% AU^{-1} in this energy range. J.E. Humble (private communication) has suggested that a value of g_r of around 3% AU^{-1} at 1 AU (consistent with the result by Yasue 1980) seems too large on the basis that the total intensity change from solar minimum to solar maximum is only about 5% for surface muon telescopes and 15-20% for neutron monitors. It was thought in the past that at solar minimum the galactic cosmic rays were observed essentially unmodulated by the Sun. The reason for this was that the neutron monitor intensity comes back to a remarkably similar level at each successive solar minimum. However, there is nothing concrete to suggest that there is no modulation of particles even up to 200 GV at solar minimum - especially now that the present estimate of the radius of the outer boundary is much larger than was previously supposed. The fact that muon telescopes and neutron monitors achieve the same intensity level for successive solar minimums may only be indicative of the fact that the Sun returns to the same minimum level of activity each cycle. The results shown in this chapter would indicate that if P_U is around 200 GV, then g_r is indeed larger than would have previously been supposed.

It is important to note that the values of (γ, P_U) chosen (and the corresponding value of g_r) should *only* be thought of as being appropriate to the energy window that is being observed by the neutron monitors and muon detectors. It is dangerous to extrapolate using this spectrum to outside this energy range. This applies in particular to lower energy values. At about 1 AU from the Sun, the galactic cosmic ray spectral index below about 1 GeV decreases with energy and eventually changes sign (see Section 4.4a). Fitting the spectrum calculated for the north-south anisotropy by this analysis to particles with energy below about 1 GeV is not justified. It is entirely plausible that the values of (γ, P_U) which best fit the north-south anisotropy are energy dependent over a wide energy range. The model spectrum given by equation 5.3 assumes that γ and P_U are energy independent. It is assumed that this is true over a small enough energy window. Inadequacies and inaccuracies of the results in this chapter may be indicative of the fact that this is not true over the energy range in which neutron monitors and muon detectors are sensitive.

If P_U is around 50 GV, then the statistics of the results are not good enough to give a significant value of g_r . All that can be said in this circumstance is that g_r is bounded above

and below by reasonably large values (refer to the Figures in Appendix 7 and 8). The large error values on g_r for P_U around 50 GV are indicative of the fact that the median energy of the neutron monitors is around 17 GeV but is anywhere between 50 and 100 GeV for the surface muon telescopes and 150 to 200 GeV for the underground muon telescopes used in this analysis. The higher the median energy of response for a particular detector, the lower that detector's response is to an anisotropy with a low upper cutoff rigidity. It is interesting to note that Ahluwalia and Riker (1987) and D.L. Hall (University of Tasmania, private communication) independently calculated the upper limiting rigidity of the diurnal anisotropy for the years between 1965 and 1980 to be between 50 and 100 GV (solar-cycle dependent). Considering that the diurnal variation is just another component of the full anisotropy vector ξ , it is not unreasonable to expect that P_U for each effect is similar.

Consider now the contour graphs shown in Appendix 9. The contours are generally open-ended for high P_U . The levels are also flat over a large range of P_U values - especially considering that the P_U index is (almost) logarithmic. These shapes are not unlike the contour diagrams given in Yasue (1980). Note that many of the χ^2 values are from fits where the error is greater than the value itself. In this circumstance, the contours are insignificant. It is for this reason, along with the fact that the contour levels are flat over the range of (γ, P_U) which most likely is the true spectrum, that it was decided that a "best-fit" (γ, P_U) could *not* be determined on the basis of a minimum contour value.

Consider now Figures 8.8 to 8.11 inclusive. These graphs give g_r as a function of year over the 10 year period 1975 to 1985 (excluding those years around solar maximum) for a fixed spectrum. It is unreasonable to expect that the spectral index is constant over a solar cycle. At least it would be expected that P_U would increase for the north-south anisotropy as the neutral sheet tilt gets larger. The reason for this would be that the size of the sectors, and therefore the furthest distance from the boundary within a sector, would increase with tilt angle. Hence the modulation of higher energy particles would be greater in a single sector and therefore the north-south anisotropy would be increased, relative to solar minimum, at the higher energies. Regardless of the actual (γ, P_U) values shown in these graphs, the *trend* of g_r over these years is similar. This is true because changing the spectrum mainly has the effect of scaling the value of g_r through the coupling coefficient c_I^0 .

Consider the 1980's results. The general trend is that g_r decreases between 1982 and 1985. Within errors, Method 2 results are similar to Method 1 results. It is reasonable to expect that g_r decreases as the level of solar activity subsides.

Consider the 1970's results, which are somewhat inconsistent between Method 1 and Method 2, especially for 1975 and 1978. Results from 1975 may not be good because the neutral sheet is expected to be only slightly tilted around solar minimum and so the detectors were not predominantly sampling from a single sector most of the time. In this case, it is expected that the observed intensity difference $(I_T - I_A)$ will be small and comparable to other random statistical fluctuations in the data. It was also the case that the errors on the detector count rates within single sectors in the 1970's were larger than in the 1980's. This is partly due to some of the detector systems in the earlier years being smaller and therefore having smaller count rates. In the case of Method 2, for some years the errors ΔI_T and ΔI_A were larger than the difference $(I_T - I_A)$ except for one or two detectors

which dominate the weighted average given by equation 8.43. It is envisaged under these circumstances that Method 1 would be less reliable than Method 2. This is because Method 1 relies on a *differencing* technique between two detectors. A large inaccuracy in only one detector will make the difference inaccurate. There will be no significant result unless there are good statistics from both detectors of the pair. As well, if the c_1^0 values have significant errors, the difference of two such coefficients will have an additive effect on the errors. Because such errors (which are unknown) have not been included, it is presumed that the error bars given for Method 1 are an underestimate of the true uncertainty of the results. Consider specifically the 1978 result. This result was determined from analysing a complete year's data. Duggal and Pomerantz (1979) in fact discovered isotropic intensity waves with a 27 day period and a spectrum equivalent to that of Forbush decreases in the data collected by the McMurdo and Thule neutron monitors during 1978. The waves started on September 23rd and persisted until the end of the year. They deduced that this phenomenon was not due to the north-south anisotropy but they could not decide on a definitive explanation of the event. The waves were however deduced to have a different energy spectrum and hence were indicative of a different modulating mechanism compared with the isotropic intensity waves discussed in Chapter 6. Such waves, if they are *not* due to the north-south anisotropy, yet are correlated to the sector structure, would corrupt the analysis and hence should be removed. The north-south anisotropy analysis was repeated for 1978 using only the data preceding 23rd September. Table 8.5 list some results. It is interesting to note that along with an increased accuracy, the new results give a larger value for R_z and hence predict a larger radial gradient.

| γ | P_U (GV) | R_z (using all days in 1978) | R_z (using days preceding 23rd Sept.) |
|----------|---------------|-----------------------------------|--|
| 0.7 | 1000 | $(3.6 \pm 4.0) \times 10^{-4}$ | $(9.5 \pm 4.2) \times 10^{-4}$ |
| 0.5 | 200 | $(1.2 \pm 1.1) \times 10^{-3}$ | $(3.1 \pm 1.2) \times 10^{-3}$ |
| 0.3 | 200 | $(1.8 \pm 1.7) \times 10^{-3}$ | $(4.5 \pm 1.7) \times 10^{-3}$ |
| 0.2 | 100 | $(2.9 \pm 2.6) \times 10^{-3}$ | $(7.2 \pm 2.7) \times 10^{-3}$ |

Table 8.5. R_z calculations for 1978 for a sample range of spectra. Results are calculated using Method 2.

Method 1 results, within error limits, did not change. Some results still remained negative. This fact alone is enough to suggest that Method 1 results are somewhat inaccurate and that the errors shown (for example in Figures 8.8 and 8.9) are an underestimate of the true errors.

8.10. REMOVING EFFECTS OF INTENSITY WAVES.

For part of 1982 and 1984 at least, there existed other isotropic intensity waves in the data. These waves were discussed in Chapter 6. The waves are thought to have a flat spectrum over the range of energies for which neutron monitors and muon detectors are sensitive. Again, these should be removed to prevent these data corrupting the north-south anisotropy analysis. It should be emphasised that these waves were only present for parts of these years and their presence did *not* corrupt the majority of the data. By how much their presence corrupted the rest of the data is now addressed.

Because in the 1980's ($qA < 0$) the intensity waves and the north-south anisotropy were in phase in the southern hemisphere, not removing the intensity waves would make R_z appear to be larger than it actually was. Finding a constant best-fit spectrum for ξ_{NS} between detectors may be impossible if the intensity waves have not been removed. This is because the intensity waves are thought to have a spectrum given by $(\gamma, P_U) \approx (0.0, 200 \text{ GV})$ which is likely to be different from the spectrum for ξ_{NS} .

Two main problems make the removal of the intensity waves from the data difficult. The intensity wave analysis of Chapter 6 showed that these waves are transient and temporally variable in magnitude. It therefore becomes no longer viable to work out I_T and I_A as an average over a complete year. This raises problems with statistical significance of the data. Secondly, and perhaps more importantly, the intensity waves described in Chapter 6 were calculated by removing the competing north-south anisotropy derived by the Nagoya GG muon telescope. The situation is such that the north-south anisotropy is not being *independently* derived from the data by simply removing the intensity waves.

It was decided to test if both the north-south anisotropy and the intensity wave amplitude could be simultaneously derived from the data during those times when the intensity waves were present. The appropriate formula relating the observed intensity variation to the combined isotropic waves and north-south anisotropy in free space is now derived.

Consider first the case where the spatial variation is isotropic only (leading to only the intensity wave variation seen in the observed data). Using Nagashima's formalism as given in Chapter 5, the space variation of cosmic rays due to the isotropic intensity waves is

$$\left(\frac{\Delta J}{J}\right)^W = F^W(\chi) \cdot G^W(P) \quad (8.46)$$

where

$$F^W(\chi) = \eta_0 \text{ (constant)} \quad (8.47)$$

ie: the only non-zero term in the space distribution is the first term (zeroth-harmonic). The observed variation for the zeroth-harmonic is (from equation 5.8)

$$D(t) = D_0^0(t) = A_0^0 \quad (8.48)$$

$$\text{where } A_0^0 = c_0^0 x_0^0 \quad (8.49)$$

$$\text{and } x_0^0 = \eta_0 \quad (8.50)$$

The c_0^0 coefficient is for the spectrum of the intensity waves. Hence,

$$D_0^0(t) = \eta_0 c_0^0 \quad (8.51)$$

is the observed time variation due to the space anisotropy η_0 . Combining this with the north-south anisotropy term ($n=1, m=0$ in Nagashima's formalism), the full variation including both effects is given by

$$D(t) = c_1^0(\gamma^{NS}, P_U^{NS}) \cdot R_Z + c_0^0(\gamma^W, P_U^W) \cdot \eta_0 \quad (8.52)$$

The superscripts "NS" and "W" reflect the fact that these two effects may have different spectra. Note that the space anisotropy due to the intensity waves is given by

$$\left(\frac{\Delta J}{J}\right)^W = \eta_0 \cdot \left(\frac{P}{10}\right)^{\gamma^W} \quad P < P_U^W \quad (8.53)$$

and that in the framework of this formalism, the "W" value as presented in Chapter 6 as a measure of the magnitude of the intensity waves observed by an individual detector is given by

$$W = D_0^0(t) = c_0^0 \eta_0 \quad (8.54)$$

A two-parameter least-squares fit (for R_z and η_0) was performed on the available data using equation 8.52 and a spectrum of $(\gamma^W, P_U^W) = (0.0, 200 \text{ GV})$ for the intensity waves during periods when the waves were observed. These periods were less than 3 months in total in any year. Unfortunately, the accuracy of the data (and the available coupling coefficients) were such that the errors on the values derived for both R_z and η_0 were always larger than the results themselves. The standard least-squares method may also have been somewhat inappropriate because the intensity waves and north-south anisotropy were in phase. The biasing problem discussed in Chapter 7, which arose when trying to simultaneously derive the height and temperature atmospheric correction coefficient, may have been prevalent here. The two-parameter least-squares method was thus unsuccessful and therefore, due to the accuracy of the data, R_z and η_0 could *not* be simultaneously derived.

Jacklyn *et al.* (1987) proposed that the intensity waves were about three times the amplitude of the north-south anisotropy when observed to be present in 1982. After consideration of the duration and amplitude of these waves, it was predicted that the values of R_z , and hence g_r , given in Figures 8.8 to 8.11 are about 50% too large. Values of g_r for 1983 and 1984, where the intensity waves were smaller, would be overestimates by no more than 50%.

8.11. SUMMARY OF THE NORTH-SOUTH ANISOTROPY ANALYSIS

From the discussion in Section 8.9 it seems that Method 2 results were more accurate than Method 1 results. Considering the effect of the isotropic intensity waves the figures in Section 8.9 and Appendices 7 and 8 suggest a radial gradient for 10 GV rigidity particles less than 5% AU^{-1} for a spectrum consistent with that determined by Yasue (1980).

The 1980's results were certainly more accurate and more consistent, both from year to year and between methods, than the 1970's results. 1977 seems to be the odd year out of

the 8 years analysed. The plots in Appendices 7 and 8 for 1977 do not follow the trends of other years. The discrepancy for 1977 between the two methods could not be explained. The discrepancy for 1975, in contrast, may be due solely to the inaccuracies in determining g_r at times when the neutral sheet is reasonably flat. At such times, particles are incident on Earth from both field sectors simultaneously.

Throughout the analysis, the accuracy of the data seemed to be a problem. Analysing the data over too short a timespan would not give enough data points for a statistically significant result. Choosing too long a timespan introduces other damaging effects to the analysis such as possible changes in the rigidity spectrum of the anisotropy over the solar cycle. Other inaccuracies were introduced through, for example, unforeseen days where the neutral sheet came close to Earth causing mixed-field contamination. Also, as mentioned in Section 8.9, the errors associated with the coupling coefficients were not accounted for, although given that they are estimated to be accurate to within 10% (Baker 1988), these errors are not expected to have profound implications on the results.

The chosen power-law spectrum for the north-south anisotropy (shown in equation 8.24) may be inadequate over the energy range for which *both* surface / underground muon telescopes *and* neutron monitors are sensitive. A different functional form for the energy spectrum may be appropriate (eg: an exponential function of rigidity), however, if the anisotropy is to be fitted to a different spectral form, then the corresponding coupling coefficients would have to be recalculated. Note that the coefficients tabulated in Yasue *et al.* (1982) and Fujimoto *et al.* (1984) assume a power-law spectrum.

Since the contours shown in Appendix 9 and those displayed in Yasue (1980) are somewhat open-ended in the spectral-index (γ) parameter, a possible future analysis could be to re-evaluate g_r for $\gamma \geq 1$. Again, this would require new determinations of the relevant coupling coefficients. Note that a significant result for $\gamma \geq 1$ would be controversial since this would imply that the radial gradient of galactic cosmic rays is larger at higher energies at 1 AU.

The sources of inaccuracy mentioned above are all areas where improvements to the data analysis can be made in the future.

8.12. BOUNDARY CROSSING INTENSITY ANALYSIS.

As an aside to the north-south anisotropy analysis, and a further test of the validity of modulation models, the hypothesis that the intensity of galactic cosmic rays around days of sector boundary crossings is greater than away from sector boundaries was tested. Consider for example the iso-intensity contours shown in Kota and Jokipii (1983). Their 3-space dimensional model predicts that there should be a greater number of particles closer to the neutral sheet than further away from it - for the same heliographic radius coordinate and latitude. According to this picture, the Earth will pass through a minimum in cosmic ray intensity when furthest from a boundary crossing. Badruddin *et al.* (1985) used a superposed epoch analysis of cosmic ray neutron monitor data to determine the relative intensity of cosmic rays near the neutral sheet. They found, on average, a local maximum of cosmic rays at the neutral sheet and also evidence to support a displacement of the sheet from the ecliptic plane due to asymmetric solar activity (see Section 6.5). Results presented

by Duggal and Pomerantz (1977) also support a local maximum of cosmic rays at the neutral sheet.

The average daily count rate of a detector given by

$$J_{av} = 0.5 (\langle I_T \rangle + \langle I_A \rangle) \quad (8.55)$$

where $\langle I_T \rangle$ is the average daily count rate on days when the Earth is in a towards sector (averaged over a year) and $\langle I_A \rangle$ is the corresponding average count rate in away sectors, should be a reflection of the intensity of particles away from a boundary crossing. The north-south anisotropy, being of opposite sign in the two sectors, is automatically removed when using the above average. This value was determined over a full year for the detectors listed in Table 8.2 and compared with the corresponding average count rate for that year for days where the Earth was crossing the neutral sheet - denoted by J_x . Note that the question of whether there is a larger *streaming* of cosmic rays along the neutral sheet than away from the sheet is not being tested here. Such an effect would produce a larger diurnal variation near sector-boundary crossings. This was tested by Cramp (1991) and a small dependence on the magnitude of the diurnal variation with proximity to the neutral sheet was found. Because daily-average count rates are used, no streaming information is *directly* attainable.

Table 8.6a lists ($J_x - J_{av}$) and its significance (value / error) for all available detectors from 1975-78 and Table 8.6b lists the same data for 1982-85. Note that the actual values of ($J_x - J_{av}$) are not comparable between detectors due to incompatible detector efficiencies. However, the significance is directly comparable.

The results shown in Tables 8.6a and 8.6b do not disprove the hypothesis and hence the model predictions that there is a greater intensity of cosmic rays near the neutral sheet. A large fraction of the results however gave a null result to the hypothesis, based on a 'significant' result being that where the error (1σ) is less than the value obtained. Very few results are significant to 3σ . Only four results do not support the hypothesis (labelled 'refute'), however the significance is low in all but one case (sscomb for 1977). All other results (labelled 'support') support the hypothesis to various degrees.

The results of this small test are certainly not conclusive. Reasons for this are probably that the statistics proved to be too poor to determine the difference in the intensity of cosmic rays near the neutral sheet compared with far from it. That is, this difference is too small to be observable in the data. It must be remembered that this is a simplistic test of the hypothesis. No attempt was made to incorporate into the analysis the information of the viewing direction of the detectors or the range of energy of the primary particles which they detect. Detectors sensitive to lower energy cosmic rays should be more sensitive to this test because the region in space where these particles have been last modulated (before being detected on Earth) is on average closer to the Earth. Hence the particle modulation better reflects the *local* interplanetary magnetic field conditions as described by the stream of T/A days.

| year | detector mnemonic | J_{av} | $(J_x - J_{av})$ | significance * |
|------|-------------------|--------------------|------------------|----------------|
| 1975 | mtwiqs | 3542.40 ± 2.95 | -3.80 ± 5.61 | 0.68 |
| 1975 | nmcomb | 596.60 ± 0.51 | 1.05 ± 0.91 | 1.16 (support) |
| 1975 | sncomb | 1671.36 ± 1.79 | -1.92 ± 3.00 | 0.64 |
| 1975 | sscomb | 1717.83 ± 1.61 | -1.80 ± 2.69 | 0.67 |
| 1975 | cammu | 536.15 ± 0.11 | -0.07 ± 0.18 | 0.38 |
| 1975 | cam4n | 552.54 ± 0.10 | 0.09 ± 0.20 | 0.45 |
| 1975 | dpriq | 7014.14 ± 5.20 | 5.06 ± 8.77 | 0.58 |
| 1976 | mtwiqs | 3553.86 ± 1.83 | 10.83 ± 3.09 | 3.51 (support) |
| 1976 | nmcomb | 598.95 ± 0.55 | 0.77 ± 0.82 | 0.94 |
| 1976 | hobnn | 490.48 ± 0.24 | 0.57 ± 0.43 | 1.31 (support) |
| 1976 | sncomb | 1501.52 ± 1.07 | 0.20 ± 1.68 | 0.12 |
| 1976 | sscomb | 1517.27 ± 1.16 | -0.83 ± 1.85 | 0.45 |
| 1976 | cammu | 530.00 ± 0.12 | 0.50 ± 0.19 | 2.69 (support) |
| 1976 | cam4n | 546.08 ± 0.15 | 0.34 ± 0.27 | 1.25 (support) |
| 1976 | dpriq | 7062.16 ± 3.15 | 10.30 ± 5.24 | 1.96 (support) |
| 1977 | mtwiqs | 3546.94 ± 3.31 | 11.40 ± 5.34 | 2.13 (support) |
| 1977 | nmcomb | 604.55 ± 0.52 | 2.18 ± 0.86 | 2.55 (support) |
| 1977 | briiqs | 1108.35 ± 0.66 | 1.86 ± 1.18 | 1.58 (support) |
| 1977 | hobnn | 487.09 ± 0.40 | 2.03 ± 0.72 | 2.82 (support) |
| 1977 | sncomb | 1416.73 ± 1.81 | -3.28 ± 2.62 | 1.25 (refute) |
| 1977 | sscomb | 1434.71 ± 1.71 | -6.53 ± 2.55 | 2.56 (refute) |
| 1977 | dpriq | 7028.48 ± 6.70 | 25.7 ± 11.4 | 2.25 (support) |
| 1978 | mtwiqs | 3450.24 ± 5.37 | 14.64 ± 7.99 | 1.83 (support) |
| 1978 | nmcomb | 595.09 ± 1.02 | 1.19 ± 1.46 | 0.82 |
| 1978 | briiqs | 1096.71 ± 0.96 | 2.98 ± 1.36 | 2.19 (support) |
| 1978 | dariqs | 1648.44 ± 1.08 | 0.79 ± 1.82 | 0.43 |
| 1978 | hobiqs | 1333.66 ± 2.24 | 6.93 ± 3.45 | 2.01 (support) |
| 1978 | sncomb | 1300.07 ± 2.42 | 1.12 ± 4.53 | 0.25 |
| 1978 | sscomb | 1353.61 ± 3.73 | -5.52 ± 6.23 | 0.89 |
| 1978 | dpriq | 6857.30 ± 9.36 | 11.3 ± 15.4 | 0.74 |

Table 8.6a. Values of the difference between the average daily count-rate of the detectors on days where the Earth is crossing the neutral-sheet (J_x) compared with days well within a single sector (J_{av}) for 1975-1978. 'dpriq' is data from the Deep River neutron monitor (source is CD ROM NGDC-05/1, National Geophysical Data Centre, Boulder CO, USA). Errors are 1σ .

* Significance is the value divided by the error of $J_x - J_{av}$.

| year | detector mnemonic | J_{av} | $(J_x - J_{av})$ | significance * |
|------|----------------------|--------------------|------------------|----------------|
| 1982 | mtwiqs | 3080.70 ± 5.40 | -5.43 ± 16.1 | 0.34 |
| 1982 | nmcomb | 530.66 ± 0.82 | -0.88 ± 2.46 | 0.36 |
| 1982 | briiqs | 1040.46 ± 1.07 | 2.40 ± 3.17 | 0.76 |
| 1982 | dariqs | 1621.49 ± 0.93 | 5.41 ± 3.09 | 1.75 (support) |
| 1982 | hobiqs | 1212.96 ± 2.00 | -0.36 ± 5.78 | 0.06 |
| 1982 | sncomb | 1186.32 ± 0.68 | 1.03 ± 1.43 | 0.72 |
| 1982 | sscomb | 1165.26 ± 0.66 | 3.93 ± 1.55 | 2.54 (support) |
| 1982 | dpriq | 6176.08 ± 10.5 | -1.31 ± 35.8 | 0.04 |
| 1983 | mtwiqs | 3158.68 ± 3.19 | -2.18 ± 5.50 | 0.40 |
| 1983 | nmcomb | 542.47 ± 0.52 | -0.04 ± 0.92 | 0.05 |
| 1983 | briiqs | 1056.63 ± 0.70 | -0.96 ± 1.22 | 0.78 |
| 1983 | dariqs | 1638.72 ± 0.74 | -0.13 ± 1.34 | 0.10 |
| 1983 | hobiqs | 1237.47 ± 1.16 | 0.12 ± 1.97 | 0.06 |
| 1983 | sncomb | 1091.11 ± 0.43 | 1.32 ± 0.74 | 1.77 (support) |
| 1983 | sscomb | 1085.60 ± 0.51 | 1.35 ± 0.86 | 1.57 (support) |
| 1983 | uncomb | 962.62 ± 0.17 | 0.12 ± 0.30 | 0.40 |
| 1983 | p6 | 713.24 ± 0.12 | 0.02 ± 0.21 | 0.09 |
| 1983 | dpriq | 6343.98 ± 5.39 | -7.49 ± 9.35 | 0.80 |
| 1984 | mtwiqs | 3215.82 ± 3.59 | 20.1 ± 12.8 | 1.57 (support) |
| 1984 | nmcomb | 550.18 ± 0.58 | 3.12 ± 1.90 | 1.64 (support) |
| 1984 | briiqs | 1061.65 ± 0.68 | 4.60 ± 1.98 | 2.32 (support) |
| 1984 | dariqs | 1635.17 ± 0.63 | 2.63 ± 1.49 | 1.76 (support) |
| 1984 | hobiqs | 1257.19 ± 1.33 | 7.28 ± 4.60 | 1.58 (support) |
| 1984 | sncomb | 1069.45 ± 0.96 | -5.08 ± 2.96 | 1.72 (refute) |
| 1984 | sscomb | 1050.75 ± 0.86 | -3.59 ± 2.69 | 1.33 (refute) |
| 1984 | uscomb | 1201.77 ± 0.16 | 0.23 ± 0.40 | 0.59 |
| 1984 | dpriq | 6425.66 ± 7.01 | 49.1 ± 22.5 | 2.18 (support) |
| 1985 | mtwiqs | 3398.36 ± 4.40 | 6.11 ± 10.6 | 0.58 |
| 1985 | nmcomb | 578.86 ± 0.39 | -0.67 ± 1.16 | 0.58 |
| 1985 | briiqs | 1098.12 ± 0.40 | 2.06 ± 0.90 | 2.29 (support) |
| 1985 | dariqs | 1666.85 ± 0.71 | 3.07 ± 1.64 | 1.87 (support) |
| 1985 | hobiqs | 1324.68 ± 0.70 | 3.44 ± 1.40 | 2.46 (support) |
| 1985 | uncomb | 1270.93 ± 0.20 | 0.20 ± 0.47 | 0.42 |
| 1985 | uscomb | 1186.78 ± 0.16 | -0.03 ± 0.35 | 0.10 |
| 1985 | p6 | 711.76 ± 0.10 | 0.11 ± 0.24 | 0.47 |
| 1985 | dpriq | 6808.34 ± 3.77 | 9.59 ± 6.93 | 1.38 (support) |

Table 8.6b. Values of the difference between the average daily count-rate of the detectors on days where the Earth is crossing the neutral-sheet (J_x) compared with days well within a single sector (J_{av}) for 1982-1985. 'dpriq' is data from the Deep River neutron monitor (source is CD ROM NGDC-05/1, National Geophysical Data Centre, Boulder CO, USA). Errors are 1σ .

* Significance is the value divided by the error of $J_x - J_{av}$.

Conclusion.

The transport equation governing the temporal and spatial evolution of the intensity distribution of galactic cosmic rays in the heliosphere was numerically modelled using two different schemes - ADI and LOD. In particular, investigations concentrated on determining how the radial gradient predicted for the cosmic ray intensity at Earth depended on the parameterization of the modelled inner-heliosphere. Along with this, an analysis determining the relative importance of radially propagating shock regions to the 11-year cycle of intensity was undertaken. As a comparison with the models, the radial gradient at Earth during 1975-78 and 1982-85 was calculated, via a north-south anisotropy analysis, using data collected by the cosmic ray detectors operated by the Hobart Cosmic Ray groups. A requirement for this analysis is that data are free of atmospheric effects and that coupling coefficients are available for each detector used. This is to enable the observed intensity variations to be converted to a free-space anisotropy. Previously undetermined atmospheric correction coefficients and coupling coefficients were therefore calculated for some surface muon telescopes operating at Mawson. In the process, a method to correct for large seasonal intensity variations superimposed on an observed count rate decay produced by Gieger tube efficiency deterioration was also developed.

The results of Section 4.4 and plots in Appendix 10 conclusively show that the LOD integrating scheme is less accurate than the ADI scheme at radii near the inner-boundary of the heliosphere. The only apparent reason for this discrepancy is that the ADI scheme is a higher order numerical difference representation of the transport equation than the LOD scheme. That is, some numerical derivatives in the ADI scheme contain more terms of the Taylor series expansion of the corresponding derivatives in the transport equation. Invariably, LOD produced a radial gradient (g_r) in the intensity of galactic cosmic rays at Earth much higher than is expected from observational evidence. ADI also produced a gradient higher than expected, except for two cases. The gradient produced by ADI was always lower than that produced by LOD under equivalent modelled heliospheric conditions. It is interesting to contemplate whether, under the same inner-boundary conditions and values of diffusion coefficients specified, a higher order, more accurate algorithm than ADI would produce a gradient much lower than those produced by the runs using the ADI algorithm. The problem with using a higher order scheme than ADI is that the matrix which describes the implicit scheme is no longer tri-diagonal. The algorithm for the solution of the implicit scheme, given in Section 2.3, is no longer able to be used. An implicit scheme, describing the solution to the transport equation in the heliosphere for a matrix system which is more complicated than tri-diagonal, becomes prohibitively computationally intensive. Explicit schemes do not suffer from this complexity increase when increasing the order of accuracy of the numerical approximations to the derivatives of the transport equation. Unfortunately, as discussed in Section 4.3, the computing power available did not allow solutions to the transport equation using explicit schemes. When better computing resources become available, it will be interesting to determine whether the large gradients at Earth, produced in all ADI runs except Runs 9 and 11, are only due to the chosen diffusion coefficients or also partially due to the accuracy of this scheme. The value of the radial gradient calculated at Earth was found to be primarily a function of the diffusion coefficients and the integrating algorithm chosen. The actual inner-boundary condition used, the position of the inner-boundary, the size of the grid steps in the radius coordinate and the inclusion of a solar-wind termination shock only had minor effects on the calculated value of g_r at Earth.

The results of Section 4.5 suggest that, at least at energies detected by neutron monitors, the 11-year cycle of cosmic ray intensity at Earth can not be explained purely by diffusion effects, caused by a succession of radially propagating shocks which increase in frequency toward solar maximum. It is noted that the modelling runs were for particle rigidities between 0.5 and 10 GV and that neutron monitors have median energies of response slightly higher than this. However, the modelling runs predict less modulation as energy increases (as observed in the plots in Appendix 10). In contrast, the neutron monitors display a greater difference in intensity between solar minimum and solar maximum than the modelling runs. Increased drift modulation caused by an increase in the warp of the neutral sheet is a modulation mechanism which is possibly *required* to fully describe the 11 year cycle at these energies. The correlation presented in Section 6.5 strongly suggests that the neutral sheet is an important large-scale boundary, even for particles with energies greater than 100 GeV.

The modelling runs which give a low radial gradient at Earth predict that this gradient is not strongly energy dependent. An energy-independent value of g_r would imply that $\gamma = 1$ for the north-south anisotropy. A slight energy dependence (such that the gradient decreases as energy increases) would imply a value of γ slightly less than 1. For high γ values ($\gamma > 0.5$) the derived value of g_r at Earth, from data collected by the neutron monitors and muon telescopes operated by the Hobart Cosmic Ray groups, was consistently small ($< 5\% \text{ AU}^{-1}$ for a 10 GV particle) for all upper-limiting rigidity $P_U > 50 \text{ GV}$ using Method 2 (which was considered more accurate than Method 1). As the value of P_U decreased, the errors on g_r increased - reflecting the fact that the median energy of response for muon telescopes becomes higher than the assumed value of P_U . If indeed the radial gradient is only slightly energy dependent for energies above the threshold energy value for neutron monitors, then the spectral index of the north-south anisotropy may be higher than previous predictions. Yasue (1980), for example, predicted $\gamma = 0.3$. A higher value is not inconsistent with the results presented in that paper. Note that the 1970's results for g_r calculated using the north-south anisotropy analysis were less accurate than the 1980's results. This is mainly due to the use of smaller detectors with lower count rates during this period.

Obvious immediate areas of future investigation arising from the work in this thesis include:

- (i) expanding the analysis presented in Chapter 8 to include years after 1985;
- (ii) investigating the waves, shown in Figure 4.1, to determine whether there is a correlation between these waves and the observed enhanced diurnal variations; and
- (iii) developing more complex time-dependent, 3-space dimensional models.

When undertaking the analysis described in Chapter 8, IMF toward/away data were not available in the required format for years after 1985. As it becomes available, the analysis could easily be extended.

To explore whether the waves shown in Figure 4.1 are correlated with the enhanced diurnal variations, a search could be undertaken to observe in the data not only enhancements, but reductions and phase-shifts in the diurnal variation. All these effects should be present at various times depending on the phase relationship between the ordinary diurnal variation (amplitude maximum at ~ 1800 hours local time) and the waves appearing in the recovery phase of the intensity decrease caused by a radially propagating shock region. The models

need to be further explored to determine whether this modelled wave effect is real or just a numerical stability / accuracy artefact.

As available computer memory size becomes larger and processing speeds become faster, the level of complexity in the models will be able to be increased. An increase in available power (size and speed) by a factor of 100 would have made the explicit scheme described in Section 4.3 practical. A further increase by 100 would allow inclusion of a third space dimension in an explicit scheme without the instability problems of the mixed derivatives discussed in Section 4.6. Such computing power is becoming available on the largest supercomputers (eg: CRAY Y-MP C90) but the economic costs are still prohibitively expensive. As costs decrease and the availability of such computing power increases, more and more of the parameter space discussed in Section 4.1 will be able to be simultaneously modelled. Finally, the development of new numerical techniques may remove some of the difficulties inherent in presently employed schemes.

REFERENCES

- Ahluwalia, H.S. and Riker, J.F. 1987. *Planet Space Science*, Vol 35, #1, p39.
- Arfken, G. 1985. "Mathematical Methods for Physicists", Academic Press Inc.
- Badraddin, R.S. Yadav and N.R. Yadav. 1985. *Planet Space Science*, Vol 33, #2, p191.
- Baker, C.P. 1988. Honours Thesis, University of Tasmania, Australia.
- Behannon, K.W., Burlaga, L.F., Hoeksema, J.T. and Klein, L.W. 1989. *Journal of Geophysical Research*, Vol 94, p1245.
- Bercovitch, M. 1969. *Proceedings of the 11th International Cosmic Ray Conference*, Budapest, Vol. 2, p169.
- Bercovitch, M. 1971. *Proceedings of the 12th International Cosmic Ray Conference*, Hobart, Vol. 7, p2658.
- Berezinskii, V.S., Bulanov, S.V., Dogiel, V.A., Ginzburg, V.L. and Ptuskin, V.S. 1990. "Astrophysics of Cosmic Rays", North-Holland.
- Bieber, J.W. and Burger, R.A. 1990. *Astrophysical Journal*, Vol 348, p597.
- Bieber, J.W. and Pomerantz, M.A. 1986. *Astrophysical Journal*, Vol 303, p843.
- Brandt, J.C. 1970. "Introduction to the Solar Wind", W.H. Freeman & Company.
- Burlaga, L.F., McDonald, F.B., Goldstein, M.L. and Lazarus, A.J. 1985. *Journal of Geophysical Research*, Vol 90, p12027.
- Burlaga, L.F., McDonald, F.B., Ness, N.F. and Lazarus, A.J.. 1991. *Journal of Geophysical Research*, Vol 96, p3789.
- Chen, J., Bieber, J.W. and Pomerantz, M.A. 1991. *Journal of Geophysical Research*, Vol 96, p11569.
- Compton, A.H. and Getting, I.A. 1935. *The Physical Review*, Vol 47, #11, p817.
- Cramp, J.L. 1991. Honours thesis, University of Tasmania.
- Dorman, L.I. 1974. "Cosmic Rays, Variations and Space Explorations", North-Holland Publishing Co., Amsterdam.
- Dorman, L.I. 1987. *Proceedings of the 20th International Cosmic Ray Conference*, Moscow, Vol 8, p186.
- Duggal, S.P. and Pomerantz, M.A. 1977. *Proceedings of the 15th International Cosmic Ray Conference*, Plovdiv, Vol 3, p215.

- Duggal, S.P. and Pomerantz, M.A. 1979. *Journal of Geophysical Research*, Vol 84, p7382.
- Duldig, M.L. 1987. *Proceedings of the 20th International Cosmic Ray Conference*, Moscow, Vol 4, p75.
- Duldig, M.L. 1990. *Proceedings of the 21st International Cosmic Ray Conference*, Adelaide, Vol 7, p288.
- Duldig, M.L. and Humble, J.E. 1990. *Proceedings of the Astronomical Society of Australia*, Vol 8, #3, p268.
- Duldig, M.L., Jacklyn, R.M. and Pomerantz, M.A. 1985. *Proceedings of the 19th International Cosmic Ray Conference*, La Jolla, Vol 5, p5.
- Fenton, A.G., Jacklyn, R.M. and Taylor, R.B. 1961. *Il Nuovo Cimento*, Vol. 22, p285.
- Fillius, W. 1989. *Advances in Space Research*, Vol 9, #4, p209.
- Fluckiger, E.O. 1991. *Proceedings of the 22nd International Cosmic Ray Conference*, Dublin, Vol 5, p273.
- Forman, M.A. 1987. *Proceedings of the 20th International Cosmic Ray Conference*, Moscow, Vol 8, p165.
- Forman, M.A. and Gleeson, L.J. 1975. *Astrophysics and Space Science*, Vol 32, p77.
- Fujimoto, K., Inoue, A., Murakami, K. and Nagashima, K. 1984. Report 9, Cosmic Ray Research Laboratory, Nagoya University, Nagoya, Japan.
- Gleeson, L.J. and Webb, G.M. 1980. *Fundamentals of Cosmic Physics*, Vol 6. p187.
- Gourlay, A.R. and Mitchell, A.R. 1972. *J. Inst. Maths. Applics.*, Vol 9, p80.
- Hoeksema, J.T., Wilcox, J.M. and Scherrer, P.H. 1982 *Journal of Geophysical Research*, Vol 87, p.10331.
- Hoeksema, J.T., Wilcox, J.M. and Scherrer, P.H. 1983 *Journal of Geophysical Research*, Vol 88, p.9910.
- Isenberg, P.A. and Jokipii, J.R. 1979. *Astrophysical Journal*, Vol 234, p746.
- Jacklyn, R.M., Duldig, M.L. and Pomerantz, M.A. 1987. *Journal of Geophysical Research*, Vol 92, p8511.
- Jokipii, J.R. 1971. *Reviews of Geophysics and Space Physics*, Vol 9, #1, p27.
- Jokipii, J.R. 1986. *Journal of Geophysical Research*, Vol 91, p2929.
- Jokipii, J.R. 1989. *Advances in Space Research*, Vol 9, #12, p105.

- Jokipii, J.R. and Kopriva, D.A. 1979. *Astrophysical Journal*, Vol 234, p384.
- Jokipii, J.R. and Kota, J. 1989. *Geophysical Research Letters*, Vol 16, #1, p1.
- Jokipii, J.R., Levy, E.H. and Hubbard, W.B. 1977. *Astrophysical Journal*, Vol 213, p861.
- Jokipii, J.R. and Thomas, B.T. 1981. *Astrophysical Journal*, Vol 243, p1115.
- Kadokura, A. and Nishida, A. 1986. *Journal of Geophysical Research*, Vol 91, p1.
- Kota, J. 1990. "Physics of the Outer Heliosphere", ed. Grzedzielski, S. and Page, D.E. Pergamon Press, p119.
- Kota, J. 1991. *Proceedings of the 22nd International Cosmic Ray Conference*, Dublin, Vol 3, p573.
- Kota, J. and Jokipii, J.R. 1983. *Astrophysical Journal*, Vol 265, p573.
- Kota, J. and Jokipii, J.R. 1991a. *Proceedings of the 22nd International Cosmic Ray Conference*, Dublin, Vol 3, p533.
- Kota, J. and Jokipii, J.R. 1991b. *Geophysical Research Letters*, Vol 18, #10, p1979.
- Lapidus, L. and Pinder, G.F. 1982. "Numerical Solutions of Partial Differential Equations in Science and Engineering", John Wiley & Sons.
- Lopate, C. and Simpson, J.A. 1991. *Journal of Geophysical Research*, Vol. 96, p15877.
- Lyons, P.R.A. 1981. "Atmospheric effects on High Energy Cosmic Rays", PhD Thesis, University of Tasmania, Australia.
- Maeda, K. 1960. *Journal of Atmospheric and Terrestrial Physics*, Vol. 19, p184.
- McDonald, F.B., Moraal, H., Reinecke, J.P.L, Lal, N. and McGuire, R.E. 1992. *Journal of Geophysical Research*, Vol. 97, p1557.
- McKibben, R.B. 1987. *Reviews of Geophysics*, Vol. 25, #3, p711.
- Nagashima, K. 1971. *Report of Ionospheric and Space Research in Japan*, Vol 25, p189.
- Nagashima, K., Tatsuoka, R., Orito, M., Sakakibara, S., Fujimoto, K., Fujii, Z., Satake, H. and Demura, S. 1988. *Report of Cosmic Ray Research Lab. #12 and #13*, Nagoya University, Nagoya, Japan.
- Neher, H.V. and Anderson, H.R. 1964. *Journal of Geophysical Research (Letters)*, Vol. 69, p1911

- Newkirk, G. and Fisk, L.A. 1985. *Journal of Geophysical Research*, Vol 90, p3391.
- O'Brien, G.G, Hyman, M.A. and Kaplan, S. 1950. *Journal of Mathematics and Physics*, Vol 24, p223.
- O'Gallagher, J.J. 1972. *Reviews of Geophysics and Space Physics*, Vol. 10, #3, p821.
- O'Gallagher, J.J. and Simpson, J.A. 1967. *Astrophysics Journal*, Vol. 147, p819.
- Palmer, I.D. 1982. *Reviews of Geophysics and Space Physics*, Vol. 20, p335.
- Parker, E.N. 1958. *Astrophysical Journal*, Vol 128, p664.
- Parker, E.N. 1965. *Planet Space Science*, Vol. 13, p9.
- Parthasarathy, R. and King, J.H. 1991. "Trajectories of Inner and Outer Heliospheric Spacecraft", National Space Science Centre, #WDC-A-R&S 91-08, Goddard Space Flight Centre, Maryland, USA.
- Perko, J.S. and Burlaga, L.F. 1987. *Journal of Geophysical Research*, Vol 92, p6127.
- Perko, J.S. and Burlaga, L.F. 1992. *Journal of Geophysical Research*, Vol 97, p4305.
- Perko, J.S. and Fisk, L.A. 1983. *Journal of Geophysical Research*, Vol 88, p9033.
- Pomerantz, M.A., Duggal, S.P., Owens, A.J., Tolba, M.F. and Tsao, C.H. 1982. *Journal of Geophysical Research*, Vol. 87, p10325.
- Potgieter, M.S. 1984. PhD Thesis, Potchefstroom University, South Africa.
- Potgieter, M.S., Le Roux, J.A. and Burger, R.A. 1987. *Proceedings of the 20th International Cosmic Ray Conference*, Moscow, Vol 3, p287.
- Potgieter, M.S., Le Roux, J.A. and Burger, R.A. 1989. *Journal of Geophysical Research*, Vol 94, p2323.
- Potgieter, M.S. and Moraal, H. 1985. *Astrophysical Journal*, Vol 294, p425.
- Press, W.H., Flannery, B.P., Teukolsky, S.A. and Vetterling, W.T. 1986. "Numerical Recipes", Cambridge University Press.
- Quenby, J.J. 1984. *Space Science Reviews*, Vol 37, p201.
- Sanderson, T.R., Heras, A.M., Marsden, R.G., Wenzel, K.P. and Winterhalter, D. 1991. *Proceedings of the 22nd International Cosmic Ray Conference*, Dublin, Vol. 3, p593.
- Sandstrom, A.E. 1965. "Cosmic Ray Physics", North Holland Publishing Co. Amsterdam.

- Seber, G.A.F. 1977. "Linear Regression Analysis", John Wiley & Sons.
- Sheeley, N.R., Swanson, E.T. and Wang, Y.M. 1991. *Journal of Geophysical Research*, Vol 96, p13861.
- Simpson, J.A. 1989. *Advances in Space Research*, Vol. 9, #4, p5.
- Smith, E.J. 1990. *Journal of Geophysical Research*, Vol. 95, p18731.
- Swinson, D.B. 1969. *Journal of Geophysical Research*, Vol. 74, p5591.
- Swinson, D.B. 1971. *Journal of Geophysical Research*, Vol. 76, p4217.
- Swinson, D.B., Shea, M.A., Smart, D.F. and Humble, J.E. 1990a. *Proceedings of the 21st International Cosmic Ray Conference*, Adelaide, Vol. 6, p75.
- Swinson, D.B., Humble, J.E., Shea, M.A. and Smart, D.F. 1990b. *Proceedings of the 21st International Cosmic Ray Conference*, Adelaide, Vol. 6, p79.
- Swinson, D.B., Humble, J.E., Shea, M.A. and Smart, D.F. 1991. *Journal of Geophysical Research*, Vol. 96, p1757.
- Swinson, D.B. and Yasue, S. 1991(a). *Proceedings of the 22nd International Cosmic Ray Conference*, Dublin, Vol. 3, p481.
- Swinson, D.B. and Yasue, S. 1991(b). *Proceedings of the 22nd International Cosmic Ray Conference*, Dublin, Vol. 3, p485.
- Thomas, B.T. and Gall, R. 1982. *Journal of Geophysical Research*, Vol. 87, p4542.
- Trefall, H. and Nordo J. 1959. *Tellus*, Vol. XI, p467.
- Vrana, A. 1976. MSc Thesis, University of Tasmania, Australia.
- Webber, W.R. and Lockwood, J.A. 1991. *Journal of Geophysical Research*, Vol. 96, p15899.
- Weber, E.J. and Davis Jr. L. 1967. *Astrophysical Journal*, Vol 148, p217.
- Williams, T. and Potgieter, M.S. 1991. *Proceedings of the 22nd International Cosmic Ray Conference*, Dublin, Vol. 3, p545.
- Yasue, S. 1980. *Journal of Geomagnetism and Geoelectricity*, Vol 32, p617.
- Yasue, S., Mori, S., Sakakibara, S. and Nagashima, K. 1982. Report 7, Cosmic Ray Research Laboratory, Nagoya University, Nagoya, Japan.

APPENDIX 1

POWER LAW RELATIONSHIP for INNER-BOUNDARY CONDITION.

Assume the distribution function at the inner and outer boundary is a function only of energy E and follows a power-law in E :

$$f(r = r_{\min}, \theta, E) = f_I E^{-\gamma_1} \quad \text{at the inner - boundary } (\forall \theta)$$

and

$$f(r = r_{\max}, \theta, E) = f_O E^{-\gamma_0} \quad \text{at the outer - boundary } (\forall \theta)$$

where f_I and f_O are constants. Let

$$X(E) = \frac{f(r = r_{\min}, \theta, E)}{f(r = r_{\max}, \theta, E)} \leq 1.0 \quad \forall E$$

be the ratio between the distribution at the inner boundary to that at the outer boundary at the same energy. As $E \rightarrow E_\infty$, $X(E) \rightarrow 1.0$. That is, we define E_∞ to be that energy above which no measurable modulation occurs in the heliomagnetic field and the distribution functions at the inner and outer boundary are identical. Then

$$f(r = r_{\min}, \theta, E) = X(E) \cdot f(r = r_{\max}, \theta, E)$$

where

$$X(E) = \frac{f_I}{f_O} E^{\gamma_0 - \gamma_1}$$

but

$$X(E_\infty) = \frac{f_I}{f_O} E_\infty^{\gamma_0 - \gamma_1} = 1.0$$

therefore

$$X(E) = E_\infty^{\gamma_1 - \gamma_0} \cdot E^{\gamma_0 - \gamma_1}$$

and

$$f(r = r_{\min}, \theta, E) = f(r = r_{\max}, \theta, E) \cdot \left(\frac{E}{E_\infty} \right)^{\gamma_0 - \gamma_1}$$

APPENDIX 2

FOURIER SERIES FOR ERROR TERMS IN von NEUMANN STABILITY ANALYSIS

In chapter 3 it was stated that an initial error $E(0,x)$ in a solution to a finite difference equation could be represented by the sum of terms of the form $e^{j\beta x}$ for arbitrary β . A general function $f(x)$ has a harmonic decomposition, or Fourier series, of the form:-

$$f(x) = \sum_{n=-\infty}^{\infty} C_n e^{jnx}$$

where C_n is complex, n is an integer and $j=\sqrt{-1}$ (eg: see Arfken 1985). O'Brien *et al.* (1950) state in their original paper that we must let β be any real number for the stability analysis to be general. It is not immediately obvious that a sum of terms of the form $e^{j\beta x}$ for *real* β is equivalent to a sum of terms of the form e^{jnx} for *integer* n .

By expanding the coefficients and equating real and imaginary parts, it can be shown that a Fourier series of the form:-

$$f(x) = \sum_{\beta} Z_{\beta} e^{j\beta x} \quad \beta \text{ real}$$

is equivalent to

$$f(x) = \sum_n C_n e^{jnx} \quad n \text{ integer}$$

where the coefficients $Z_{\beta} = (x_{\beta} + j y_{\beta})$ and $C_n = (a_n + j b_n)$, with a, b, x and y real, are related via

$$x_{\beta} = a_n \cos(\beta'x) + b_n \sin(\beta'x)$$

$$y_{\beta} = b_n \cos(\beta'x) - a_n \sin(\beta'x) \quad \text{with } \beta' = \beta - n$$

for a given β and n .

APPENDIX 3

LINE OF BEST FIT THROUGH DATA WITH ANNUAL VARIATION AND EFFICIENCY DECAY

In chapter 7, it was stated that for data which sinusoidally vary over a year and which have a superimposed linear efficiency decay, the line of best fit through the data does not equal the efficiency trend (see Figure 7.2). This is easily proved as follows:

Consider points (y_i, x_i) which define the data set. We wish to fit a straight line $y = mx + c$. The slope m and y-intercept c are determined via the standard least-squares criteria:

$$\frac{\partial \xi}{\partial m} = \frac{\partial \xi}{\partial c} = 0 \quad \xi = \sum_i [y_i - (mx_i + c)]^2$$

Solving these equations for m and c gives the familiar

$$c = \bar{y} - m\bar{x}$$

$$m = \frac{\sum x_i y_i - n \bar{y} \bar{x}}{\sum x_i x_i - n \bar{x} \bar{x}}$$

where the bars above the variables denote averages. Consider now that the data have superimposed on them an arbitrary sine wave, the period being equal to the length of the data span:

$$Y_i = y_i + A \sin \left(2\pi \left(\frac{x_i}{x_n} \right) + \phi \right)$$

The best straight line fit to this data is then given by

$$c = \bar{Y} - m\bar{x}$$

$$m = \frac{\sum x_i Y_i - n \bar{Y} \bar{x}}{\sum x_i x_i - n \bar{x} \bar{x}}$$

Now,

$$\bar{Y} = \frac{1}{n} \sum Y_i = \frac{1}{n} \sum y_i + \frac{1}{n} \sum A \sin \left(2\pi \left(\frac{x_i}{x_n} \right) + \phi \right)$$

$$= \bar{y} + 0 \quad (\text{averaging over one complete cycle})$$

But,

$$\sum x_i Y_i = \sum x_i y_i + \sum x_i A \sin \left(2\pi \left(\frac{x_i}{x_n} \right) + \phi \right) \neq \sum x_i y_i$$

Hence, the slope and intercept will in general be different between the two data sets (intuitively obvious from Figure 7.2). Applying this to muon data spanning a full year, it is therefore clear that, due to the presence of a sinusoidal annual variation in the data caused by atmospheric effects, any linear efficiency decay over that year cannot be removed simply by rotating the data around its straight-line of best fit.

APPENDIX 4

COUPLING COEFFICIENTS for SNCOMB ($\times 10^4$)

| γ | P_U | c_0^0 | c_1^0 | c_1^1 | c_2^0 | c_2^1 | c_2^2 | c_3^0 | c_3^1 | c_3^2 | c_3^3 |
|----------|-------|---------|---------|---------|---------|---------|---------|---------|---------|---------|---------|
| 0.5 | 30. | 337 | -100 | 216 | -109 | -100 | -8 | 103 | -66 | 22 | -149 |
| 0.5 | 50. | 1866 | -92 | 1440 | -833 | -47 | 436 | 89 | -755 | 163 | -330 |
| 0.5 | 100. | 7640 | 527 | 6561 | -3516 | 981 | 3538 | -767 | -3506 | 1214 | 1099 |
| 0.5 | 200. | 17061 | 1579 | 15194 | -7931 | 2697 | 9393 | -2243 | -8231 | 2873 | 4632 |
| 0.5 | 500. | 30297 | 2789 | 27409 | -14248 | 4646 | 17800 | -3965 | -15142 | 4672 | 9815 |
| 0.5 | 1000. | 38504 | 3406 | 34981 | -18204 | 5630 | 22988 | -4848 | -19502 | 5560 | 12974 |
| 0.0 | 30. | 216 | -67 | 138 | -67 | -67 | -6 | 67 | -39 | 14 | -94 |
| 0.0 | 50. | 975 | -66 | 744 | -426 | -44 | 210 | 64 | -379 | 82 | -191 |
| 0.0 | 100. | 3107 | 160 | 2630 | -1417 | 332 | 1345 | -248 | -1394 | 468 | 321 |
| 0.0 | 200. | 5607 | 440 | 4921 | -2588 | 789 | 2896 | -641 | -2646 | 910 | 1255 |
| 0.0 | 500. | 7992 | 660 | 7122 | -3726 | 1143 | 4410 | -954 | -3890 | 1238 | 2189 |
| 0.0 | 1000. | 8980 | 735 | 8033 | -4202 | 1262 | 5035 | -1061 | -4414 | 1345 | 2569 |
| -0.5 | 30. | 140 | -45 | 88 | -41 | -45 | -4 | 44 | -22 | 9 | -60 |
| -0.5 | 50. | 519 | -46 | 390 | -220 | -35 | 101 | 44 | -191 | 42 | -112 |
| -0.5 | 100. | 1314 | 37 | 1092 | -590 | 103 | 520 | -71 | -569 | 185 | 72 |
| -0.5 | 200. | 1983 | 112 | 1705 | -903 | 226 | 935 | -176 | -904 | 304 | 322 |
| -0.5 | 500. | 2421 | 153 | 2109 | -1112 | 292 | 1213 | -234 | -1132 | 365 | 493 |
| -0.5 | 1000. | 2541 | 162 | 2219 | -1170 | 306 | 1289 | -247 | -1196 | 378 | 539 |
| -1.0 | 30. | 92 | -31 | 57 | -25 | -31 | -3 | 29 | -12 | 6 | -39 |
| -1.0 | 50. | 281 | -32 | 208 | -115 | -27 | 49 | 30 | -97 | 22 | -66 |
| -1.0 | 100. | 581 | -1 | 472 | -254 | 25 | 205 | -13 | -239 | 75 | 1 |
| -1.0 | 200. | 762 | 19 | 638 | -339 | 58 | 317 | -41 | -329 | 107 | 68 |
| -1.0 | 500. | 843 | 27 | 713 | -378 | 70 | 369 | -52 | -372 | 119 | 100 |
| -1.0 | 1000. | 858 | 28 | 727 | -385 | 72 | 378 | -54 | -380 | 121 | 105 |
| -1.5 | 30. | 61 | -22 | 38 | -15 | -21 | -2 | 19 | -6 | 3 | -25 |
| -1.5 | 50. | 156 | -23 | 113 | -61 | -20 | 23 | 20 | -49 | 11 | -40 |
| -1.5 | 100. | 270 | -11 | 213 | -113 | -1 | 82 | 4 | -103 | 31 | -15 |
| -1.5 | 200. | 320 | -5 | 259 | -137 | 9 | 113 | -4 | -128 | 40 | 3 |
| -1.5 | 500. | 335 | -4 | 273 | -144 | 11 | 123 | -6 | -136 | 43 | 9 |
| -1.5 | 1000. | 337 | -4 | 275 | -145 | 11 | 124 | -6 | -137 | 43 | 10 |
| -2.0 | 30. | 40 | -15 | 25 | -9 | -15 | -1 | 13 | -3 | 2 | -16 |
| -2.0 | 50. | 89 | -16 | 63 | -32 | -15 | 11 | 14 | -25 | 6 | -24 |
| -2.0 | 100. | 133 | -12 | 102 | -53 | -7 | 34 | 8 | -45 | 14 | -15 |
| -2.0 | 200. | 146 | -10 | 114 | -59 | -5 | 42 | 5 | -52 | 16 | -10 |
| -2.0 | 500. | 149 | -10 | 117 | -60 | -4 | 44 | 5 | -54 | 16 | -9 |
| -2.0 | 1000. | 150 | -10 | 117 | -60 | -4 | 44 | 5 | -54 | 16 | -9 |

| γ | P_U | s_0^0 | s_1^0 | s_1^1 | s_2^0 | s_2^1 | s_2^2 | s_3^0 | s_3^1 | s_3^2 | s_3^3 |
|----------|-------|---------|---------|---------|---------|---------|---------|---------|---------|---------|---------|
| 0.5 | 30. | 0 | 0 | -225 | 0 | 116 | -247 | 0 | 59 | 150 | -138 |
| 0.5 | 50. | 0 | 0 | -1048 | 0 | 166 | -1328 | 0 | 517 | 185 | -1048 |
| 0.5 | 100. | 0 | 0 | -2924 | 0 | 46 | -3966 | 0 | 1606 | -97 | -3597 |
| 0.5 | 200. | 0 | 0 | -4569 | 0 | -8 | -6287 | 0 | 2606 | -210 | -5838 |
| 0.5 | 500. | 0 | 0 | -5652 | 0 | 25 | -7788 | 0 | 3283 | -149 | -7240 |
| 0.5 | 1000. | 0 | 0 | -5948 | 0 | 47 | -8191 | 0 | 3468 | -106 | -7603 |
| | | | | | | | | | | | |
| 0.0 | 30. | 0 | 0 | -144 | 0 | 77 | -157 | 0 | 34 | 98 | -87 |
| 0.0 | 50. | 0 | 0 | -555 | 0 | 104 | -696 | 0 | 263 | 119 | -538 |
| 0.0 | 100. | 0 | 0 | -1260 | 0 | 59 | -1687 | 0 | 672 | 14 | -1493 |
| 0.0 | 200. | 0 | 0 | -1703 | 0 | 44 | -2315 | 0 | 942 | -19 | -2100 |
| 0.0 | 500. | 0 | 0 | -1905 | 0 | 50 | -2597 | 0 | 1068 | -8 | -2361 |
| 0.0 | 1000. | 0 | 0 | -1941 | 0 | 53 | -2646 | 0 | 1091 | -3 | -2406 |
| | | | | | | | | | | | |
| -0.5 | 30. | 0 | 0 | -93 | 0 | 52 | -100 | 0 | 19 | 66 | -55 |
| -0.5 | 50. | 0 | 0 | -300 | 0 | 66 | -371 | 0 | 134 | 78 | -280 |
| -0.5 | 100. | 0 | 0 | -567 | 0 | 49 | -746 | 0 | 289 | 38 | -641 |
| -0.5 | 200. | 0 | 0 | -688 | 0 | 45 | -917 | 0 | 363 | 29 | -807 |
| -0.5 | 500. | 0 | 0 | -726 | 0 | 46 | -971 | 0 | 387 | 31 | -856 |
| -0.5 | 1000. | 0 | 0 | -731 | 0 | 46 | -977 | 0 | 390 | 31 | -862 |
| | | | | | | | | | | | |
| -1.0 | 30. | 0 | 0 | -60 | 0 | 35 | -64 | 0 | 11 | 44 | -35 |
| -1.0 | 50. | 0 | 0 | -165 | 0 | 43 | -201 | 0 | 69 | 52 | -148 |
| -1.0 | 100. | 0 | 0 | -267 | 0 | 36 | -345 | 0 | 128 | 36 | -286 |
| -1.0 | 200. | 0 | 0 | -301 | 0 | 35 | -392 | 0 | 148 | 34 | -332 |
| -1.0 | 500. | 0 | 0 | -308 | 0 | 35 | -402 | 0 | 153 | 34 | -341 |
| -1.0 | 1000. | 0 | 0 | -308 | 0 | 35 | -403 | 0 | 153 | 34 | -342 |
| | | | | | | | | | | | |
| -1.5 | 30. | 0 | 0 | -39 | 0 | 24 | -42 | 0 | 6 | 30 | -22 |
| -1.5 | 50. | 0 | 0 | -92 | 0 | 28 | -111 | 0 | 35 | 34 | -79 |
| -1.5 | 100. | 0 | 0 | -132 | 0 | 26 | -167 | 0 | 58 | 28 | -133 |
| -1.5 | 200. | 0 | 0 | -141 | 0 | 25 | -180 | 0 | 64 | 27 | -145 |
| -1.5 | 500. | 0 | 0 | -143 | 0 | 25 | -182 | 0 | 64 | 28 | -147 |
| -1.5 | 1000. | 0 | 0 | -143 | 0 | 25 | -182 | 0 | 64 | 28 | -147 |
| | | | | | | | | | | | |
| -2.0 | 30. | 0 | 0 | -26 | 0 | 16 | -27 | 0 | 3 | 21 | -15 |
| -2.0 | 50. | 0 | 0 | -53 | 0 | 19 | -63 | 0 | 18 | 23 | -43 |
| -2.0 | 100. | 0 | 0 | -69 | 0 | 18 | -84 | 0 | 27 | 21 | -64 |
| -2.0 | 200. | 0 | 0 | -71 | 0 | 18 | -88 | 0 | 28 | 20 | -68 |
| -2.0 | 500. | 0 | 0 | -71 | 0 | 18 | -88 | 0 | 28 | 20 | -68 |
| -2.0 | 1000. | 0 | 0 | -71 | 0 | 18 | -88 | 0 | 28 | 20 | -68 |

APPENDIX 5

COUPLING COEFFICIENTS for SSCOMB ($\times 10^4$)

| γ | P_U | c_0^0 | c_1^0 | c_1^1 | c_2^0 | c_2^1 | c_2^2 | c_3^0 | c_3^1 | c_3^2 | c_3^3 |
|----------|-------|---------|---------|---------|---------|---------|---------|---------|---------|---------|---------|
| 0.5 | 30. | 337 | -203 | 195 | 27 | -188 | 43 | 86 | 76 | -37 | -26 |
| 0.5 | 50. | 1866 | -1254 | 325 | 418 | -235 | -420 | 189 | -44 | 627 | -252 |
| 0.5 | 100. | 7640 | -5368 | -1584 | 2099 | 2347 | -1283 | 577 | -2444 | 1522 | 252 |
| 0.5 | 200. | 17060 | -11823 | -6698 | 4183 | 8563 | -432 | 2175 | -7135 | -293 | 815 |
| 0.5 | 500. | 30297 | -20419 | -15126 | 6097 | 18117 | 2547 | 5510 | -13203 | -5029 | 572 |
| 0.5 | 1000. | 38504 | -25566 | -20645 | 6923 | 24135 | 4824 | 7900 | -16630 | -8408 | 110 |
| 0.0 | 30. | 216 | -130 | 127 | 17 | -123 | 31 | 56 | 50 | -29 | -13 |
| 0.0 | 50. | 975 | -651 | 199 | 209 | -154 | -196 | 109 | -4 | 299 | -130 |
| 0.0 | 100. | 3107 | -2171 | -485 | 832 | 775 | -533 | 247 | -876 | 658 | 51 |
| 0.0 | 200. | 5607 | -3886 | -1831 | 1391 | 2416 | -320 | 664 | -2121 | 194 | 206 |
| 0.0 | 500. | 7992 | -5438 | -3345 | 1742 | 4134 | 208 | 1259 | -3220 | -649 | 169 |
| 0.0 | 1000. | 8980 | -6058 | -4008 | 1842 | 4858 | 481 | 1546 | -3633 | -1055 | 114 |
| -0.5 | 30. | 140 | -84 | 84 | 11 | -81 | 23 | 37 | 33 | -23 | -6 |
| -0.5 | 50. | 519 | -344 | 123 | 105 | -101 | -90 | 64 | 10 | 140 | -66 |
| -0.5 | 100. | 1314 | -910 | -124 | 339 | 236 | -222 | 114 | -310 | 284 | -1 |
| -0.5 | 200. | 1983 | -1371 | -482 | 490 | 674 | -169 | 223 | -644 | 165 | 42 |
| -0.5 | 500. | 2421 | -1656 | -758 | 555 | 989 | -73 | 331 | -846 | 12 | 36 |
| -0.5 | 1000. | 2541 | -1731 | -839 | 568 | 1077 | -40 | 366 | -896 | -37 | 29 |
| -1.0 | 30. | 92 | -55 | 56 | 7 | -54 | 17 | 25 | 23 | -18 | -2 |
| -1.0 | 50. | 281 | -185 | 78 | 54 | -67 | -39 | 39 | 12 | 63 | -33 |
| -1.0 | 100. | 581 | -398 | -13 | 142 | 57 | -91 | 57 | -106 | 122 | -10 |
| -1.0 | 200. | 762 | -523 | -109 | 183 | 175 | -78 | 86 | -196 | 91 | 2 |
| -1.0 | 500. | 843 | -576 | -160 | 196 | 234 | -61 | 106 | -234 | 63 | 1 |
| -1.0 | 1000. | 858 | -585 | -170 | 197 | 244 | -56 | 110 | -240 | 57 | 1 |
| -1.5 | 30. | 60 | -36 | 38 | 4 | -37 | 12 | 16 | 16 | -13 | 0 |
| -1.5 | 50. | 156 | -102 | 50 | 28 | -44 | -15 | 24 | 11 | 27 | -16 |
| -1.5 | 100. | 270 | -183 | 17 | 61 | 2 | -36 | 30 | -33 | 51 | -8 |
| -1.5 | 200. | 320 | -217 | -10 | 73 | 34 | -33 | 38 | -58 | 43 | -4 |
| -1.5 | 500. | 335 | -227 | -19 | 75 | 45 | -30 | 42 | -65 | 38 | -5 |
| -1.5 | 1000. | 337 | -228 | -21 | 75 | 46 | -29 | 42 | -66 | 37 | -5 |
| -2.0 | 30. | 40 | -24 | 26 | 3 | -25 | 9 | 11 | 11 | -10 | 1 |
| -2.0 | 50. | 89 | -57 | 32 | 15 | -29 | -5 | 15 | 9 | 10 | -8 |
| -2.0 | 100. | 133 | -89 | 20 | 28 | -12 | -13 | 17 | -8 | 20 | -5 |
| -2.0 | 200. | 146 | -98 | 13 | 31 | -4 | -12 | 20 | -14 | 18 | -4 |
| -2.0 | 500. | 149 | -100 | 11 | 31 | -2 | -12 | 20 | -16 | 17 | -4 |
| -2.0 | 1000. | 150 | -100 | 11 | 31 | -1 | -12 | 20 | -16 | 17 | -4 |

| γ | P_U | s_0^0 | s_1^0 | s_1^1 | s_2^0 | s_2^1 | s_2^2 | s_3^0 | s_3^1 | s_3^2 | s_3^3 |
|----------|-------|---------|---------|---------|---------|---------|---------|---------|---------|---------|---------|
| 0.5 | 30. | 0 | 0 | 151 | 0 | -159 | 140 | 0 | 90 | -176 | 83 |
| 0.5 | 50. | 0 | 0 | 1107 | 0 | -1233 | 366 | 0 | 821 | -371 | -105 |
| 0.5 | 100. | 0 | 0 | 3877 | 0 | -4318 | -720 | 0 | 2830 | 1448 | -542 |
| 0.5 | 200. | 0 | 0 | 6580 | 0 | -7151 | -2728 | 0 | 4338 | 4307 | -116 |
| 0.5 | 500. | 0 | 0 | 8451 | 0 | -8984 | -4414 | 0 | 5104 | 6512 | 585 |
| 0.5 | 1000. | 0 | 0 | 8971 | 0 | -9471 | -4919 | 0 | 5273 | 7139 | 836 |
| | | | | | | | | | | | |
| 0.0 | 30. | 0 | 0 | 93 | 0 | -99 | 88 | 0 | 55 | -110 | 53 |
| 0.0 | 50. | 0 | 0 | 568 | 0 | -632 | 207 | 0 | 418 | -217 | -37 |
| 0.0 | 100. | 0 | 0 | 1603 | 0 | -1788 | -183 | 0 | 1174 | 442 | -210 |
| 0.0 | 200. | 0 | 0 | 2335 | 0 | -2552 | -720 | 0 | 1584 | 1209 | -101 |
| 0.0 | 500. | 0 | 0 | 2683 | 0 | -2895 | -1032 | 0 | 1729 | 1618 | 28 |
| 0.0 | 1000. | 0 | 0 | 2748 | 0 | -2955 | -1094 | 0 | 1749 | 1695 | 58 |
| | | | | | | | | | | | |
| -0.5 | 30. | 0 | 0 | 58 | 0 | -61 | 55 | 0 | 34 | -69 | 34 |
| -0.5 | 50. | 0 | 0 | 295 | 0 | -327 | 118 | 0 | 214 | -128 | -9 |
| -0.5 | 100. | 0 | 0 | 686 | 0 | -764 | -23 | 0 | 501 | 113 | -78 |
| -0.5 | 200. | 0 | 0 | 885 | 0 | -972 | -168 | 0 | 614 | 321 | -50 |
| -0.5 | 500. | 0 | 0 | 951 | 0 | -1037 | -227 | 0 | 642 | 398 | -26 |
| -0.5 | 1000. | 0 | 0 | 959 | 0 | -1045 | -234 | 0 | 645 | 408 | -22 |
| | | | | | | | | | | | |
| -1.0 | 30. | 0 | 0 | 36 | 0 | -38 | 35 | 0 | 21 | -44 | 22 |
| -1.0 | 50. | 0 | 0 | 155 | 0 | -171 | 68 | 0 | 111 | -75 | 1 |
| -1.0 | 100. | 0 | 0 | 304 | 0 | -338 | 17 | 0 | 221 | 14 | -26 |
| -1.0 | 200. | 0 | 0 | 359 | 0 | -396 | -23 | 0 | 253 | 70 | -19 |
| -1.0 | 500. | 0 | 0 | 372 | 0 | -408 | -34 | 0 | 258 | 85 | -14 |
| -1.0 | 1000. | 0 | 0 | 373 | 0 | -409 | -35 | 0 | 258 | 86 | -14 |
| | | | | | | | | | | | |
| -1.5 | 30. | 0 | 0 | 23 | 0 | -24 | 22 | 0 | 13 | -27 | 14 |
| -1.5 | 50. | 0 | 0 | 83 | 0 | -91 | 40 | 0 | 58 | -45 | 4 |
| -1.5 | 100. | 0 | 0 | 140 | 0 | -155 | 21 | 0 | 101 | -12 | -7 |
| -1.5 | 200. | 0 | 0 | 155 | 0 | -171 | 10 | 0 | 110 | 4 | -5 |
| -1.5 | 500. | 0 | 0 | 158 | 0 | -174 | 8 | 0 | 111 | 7 | -4 |
| -1.5 | 1000. | 0 | 0 | 158 | 0 | -174 | 8 | 0 | 111 | 7 | -4 |
| | | | | | | | | | | | |
| -2.0 | 30. | 0 | 0 | 14 | 0 | -15 | 14 | 0 | 8 | -17 | 9 |
| -2.0 | 50. | 0 | 0 | 45 | 0 | -49 | 23 | 0 | 31 | -27 | 4 |
| -2.0 | 100. | 0 | 0 | 67 | 0 | -74 | 16 | 0 | 48 | -14 | 0 |
| -2.0 | 200. | 0 | 0 | 71 | 0 | -78 | 13 | 0 | 50 | -10 | 0 |
| -2.0 | 500. | 0 | 0 | 72 | 0 | -79 | 13 | 0 | 50 | -9 | 1 |
| -2.0 | 1000. | 0 | 0 | 72 | 0 | -79 | 13 | 0 | 50 | -9 | 1 |

APPENDIX 6

LEVEL-CHANGE / SPIKE RECOGNITION ALGORITHM.

Data spikes and level-shifts (see Figure A6.1 below) can occur in raw cosmic-ray data. There are many causes of these, including changes to the E.H.T power supply, static discharges and gas leakage in the detectors. In order to ascertain the true temporal variation of cosmic rays incident on the detector due to heliospheric modulation it is necessary to remove such spikes from the data and correct for level-shifts.

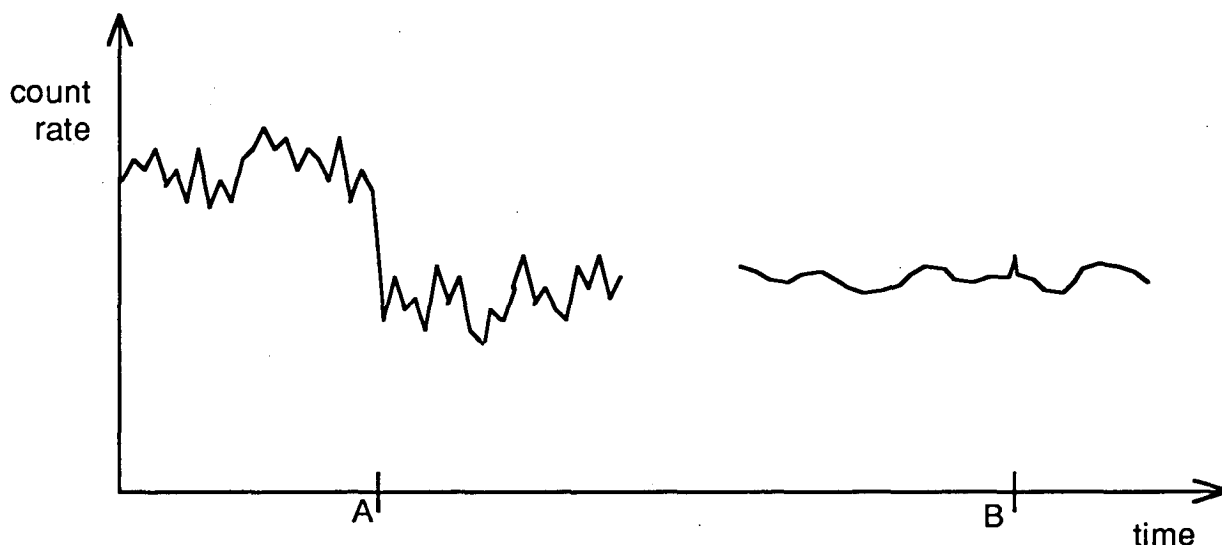


FIGURE A6.1. Two sets of hypothetical cosmic-ray data showing a level-shift at A and a data spike at B. Both these scenarios are common in cosmic-ray data. Note that the noise in the first set of data is larger than in the second set and that the spike in the second set is larger than some noise in the first set.

To find a level-shift or a spike in the data automatically, an algorithm is required to pick out data points which are significantly different from neighbouring points. This is not trivial because measuring whether a point is different from, for example, the mean of neighbouring points, a numerical value of the mean is first required. However, without knowing *a-priori* the location of the data spikes, these spikes cannot be excluded from the 'mean' calculation. Hence the mean will be biased by the data points that are required to be removed.

When visually scanning data for spikes and level-shifts, we tend to look at whether the *difference* between a certain data point and neighbouring points is significantly different, rather than at the absolute values of data points. We can isolate points which may look significantly different to be labelled a data spike and then re-evaluate the shape of the trend in the data with these potential level changes hypothetically removed. In this way we can generally decide unambiguously whether these potential level changes are real or just statistical fluctuations. It is with this in mind that the following algorithm for automatically flagging level-shifts and data spikes for cosmic-ray data was developed.

Input to the routine are n data points x_i ($i=1 \dots n$), tolerance values k_1 and k_2 , and a width parameter w which is the maximum width (in terms of consecutive data points) of an accepted data spike. The routine passes back arrays which contain pointers to areas in the data which are suspected to contain a level-shift or data spike. The routine runs through the data three times. In the first pass, the mean m_1 and standard deviation σ_1 of the difference between neighbouring points for all points, weighted by the inverse of the square root of the data (particle detector count-rates follow poisson statistics), are calculated. That is, the mean and standard deviation of the value

$$\frac{|x_{i+1} - x_i|}{\sqrt{\frac{1}{2}(x_{i+1} + x_i)}} \quad i = 1 \dots n-1$$

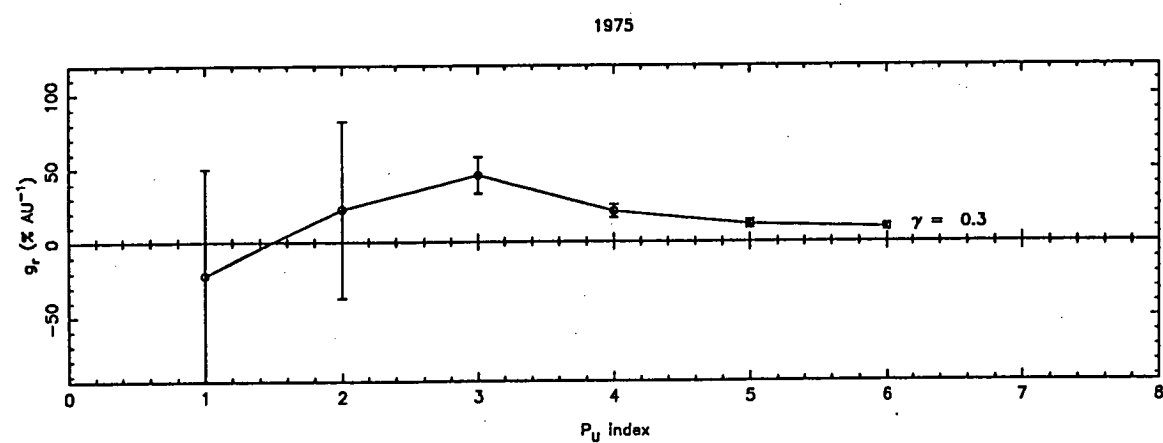
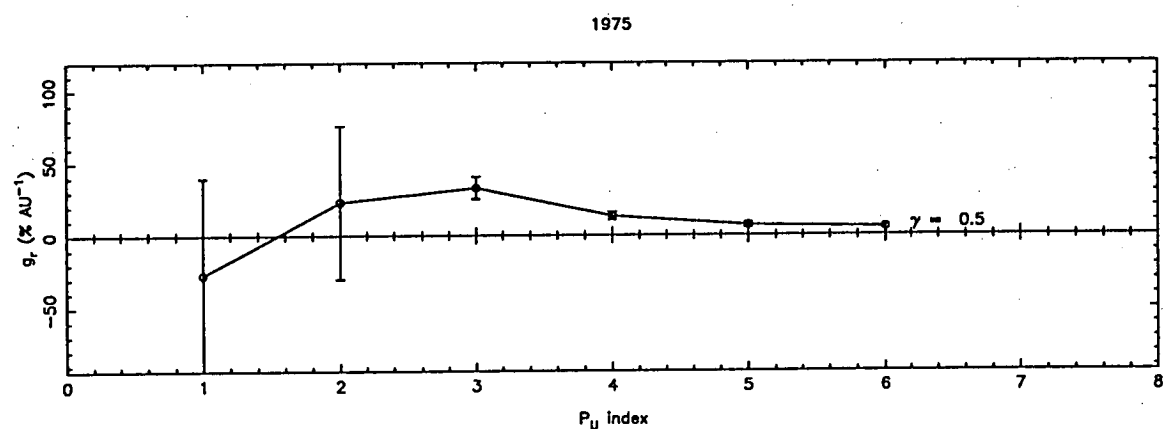
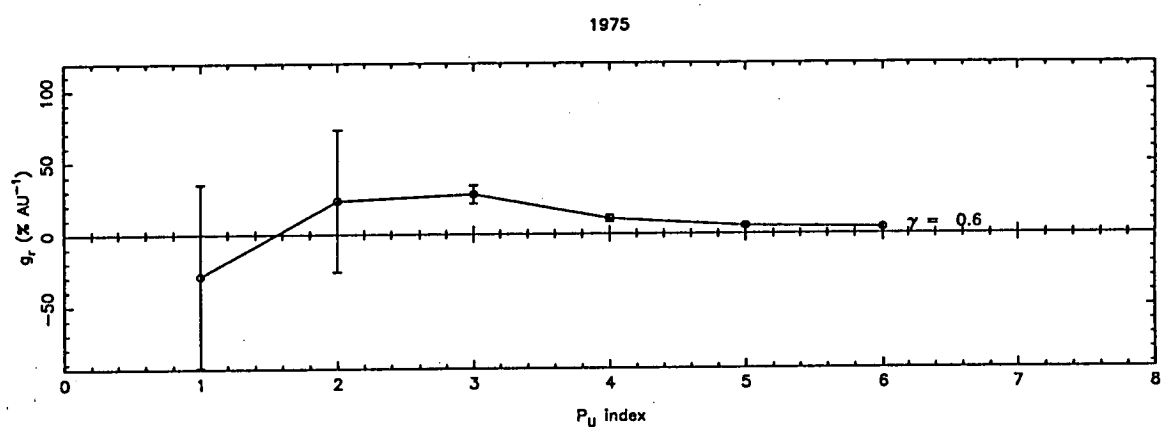
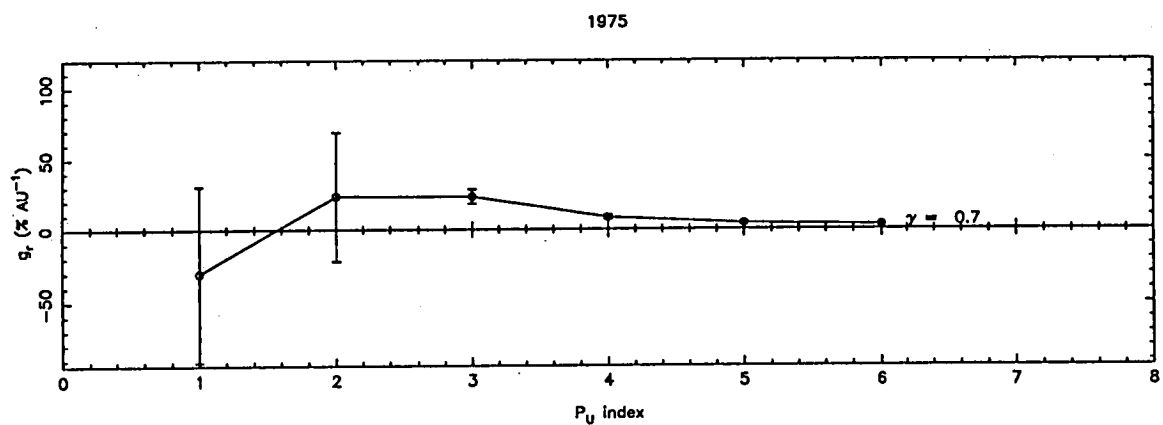
is found. Any difference between two points which is greater than $k_1 \times \sigma_1$ is flagged as a potential level-change in the data. A new mean m_2 and standard deviation σ_2 of the above expression *excluding* those differences flagged as potential level changes is then found. In the second pass, all flagged potential level changes from the first pass are then tested for the condition that the original difference is greater than $k_2 \times \sigma_2$. If so, the level change is accepted as permanent. If not, the difference is rejected as a level change. In the third pass, the routine runs through the data and checks if there are two level changes (of opposite direction) at least as close together as given by the parameter w . If so, then data points between and including the position of the level change are labelled as belonging to a data spike.

Note that the values of k_1 and k_2 need to be *learned*. In other words, their value would be chosen in order to have the best, or most desired, effect on the data. For cosmic ray data, $k_1 \approx 2$ and $k_2 \approx 6$ were used. A decrease in k_1 will result in a decrease in the second calculated standard deviation and hence more level changes will be flagged - which may be undesirable for inherently noisy data. By increasing k_2 , only the larger of the level-changes will be flagged.

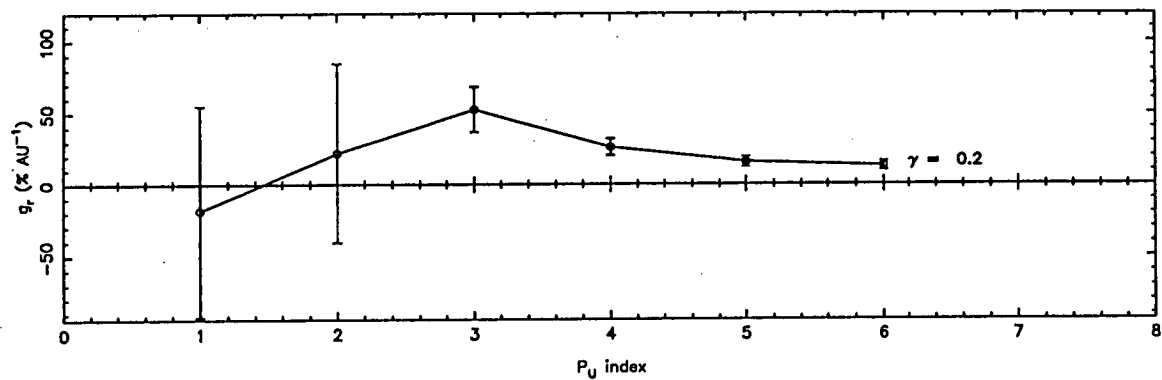
APPENDIX 7

NORTH/SOUTH ANISOTROPY ANALYSIS. RESULTS USING METHOD 1.

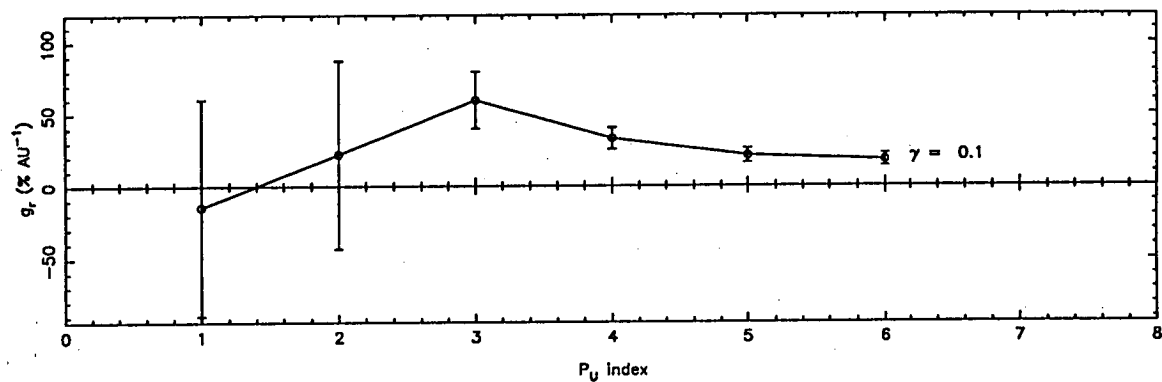
This appendix contains plots of g_r vs P_U index for various γ values, calculated using "method 1" described in Chapter 8. See Table 8.3 for P_U values in GV corresponding to the indices used in these plots. The radial gradient shown is applicable to 10 GV rigidity particles. Values for other rigidities can be found by using the relationship between g_r and rigidity given in equation 8.25b. The plots cover the years 1975-78 and 1982-85. Data have *not* been corrected for any (possible) isotropic intensity wave contamination.



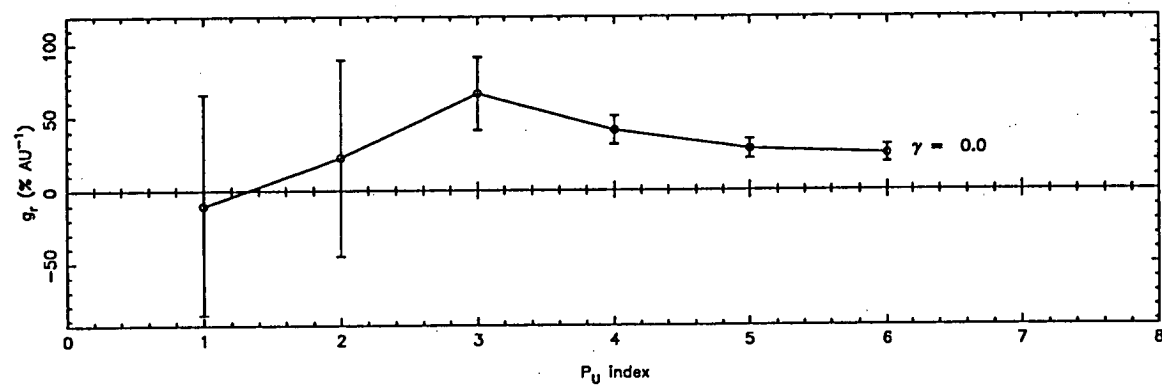
1975



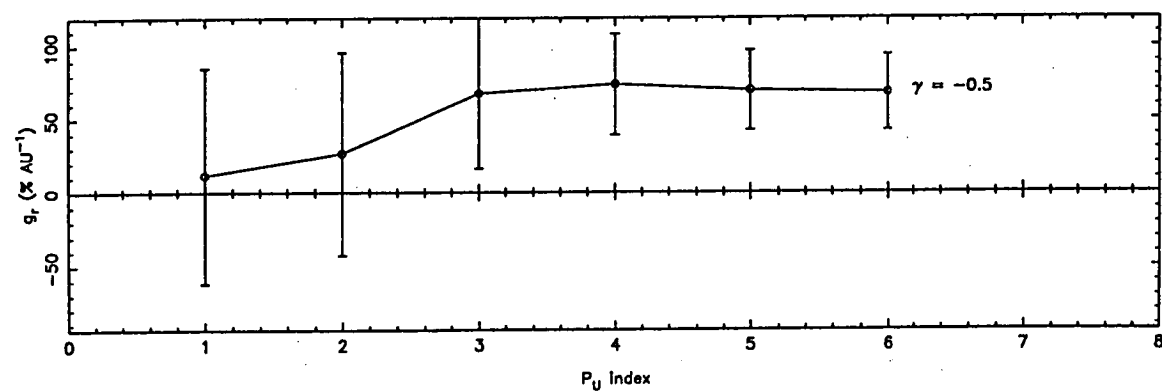
1975

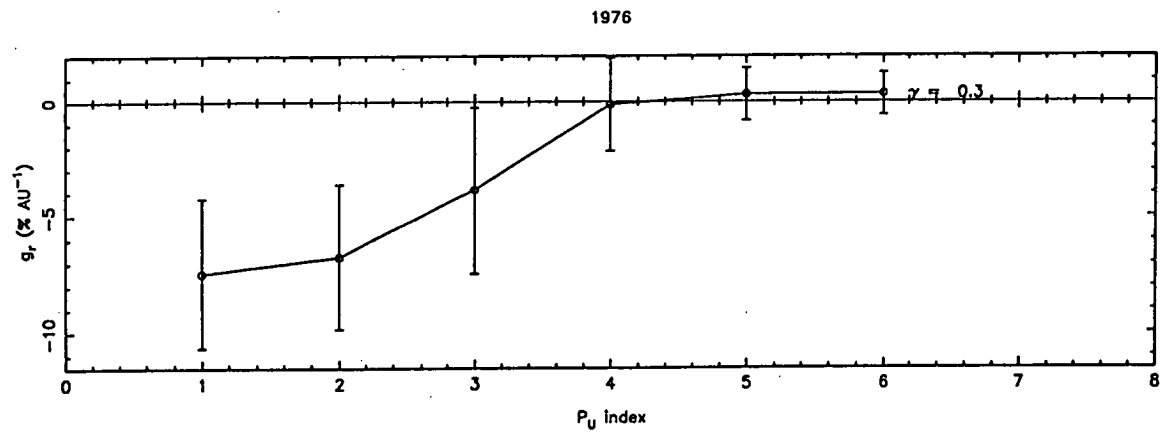
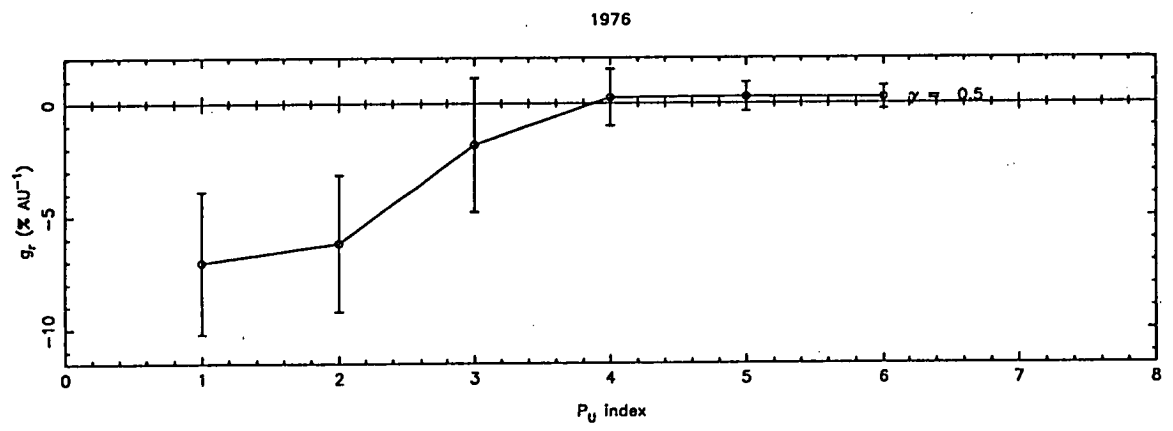
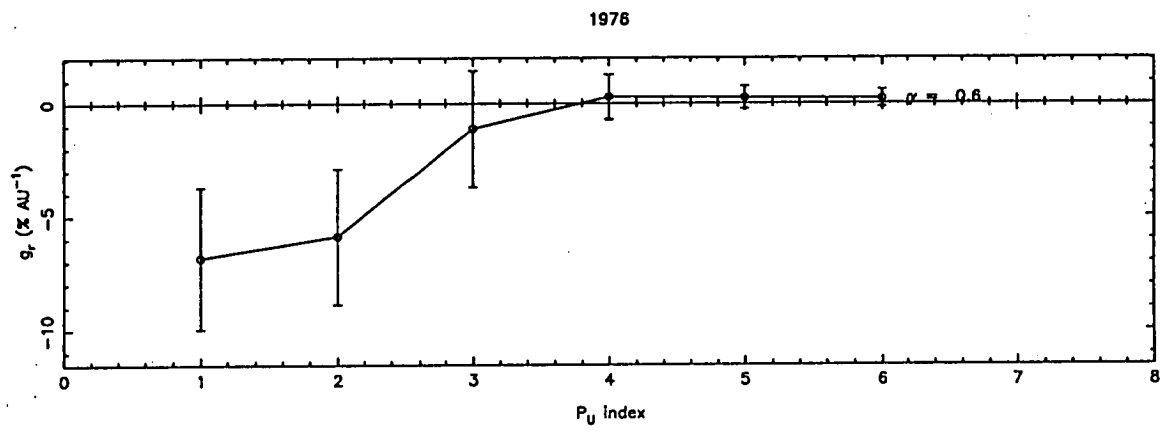
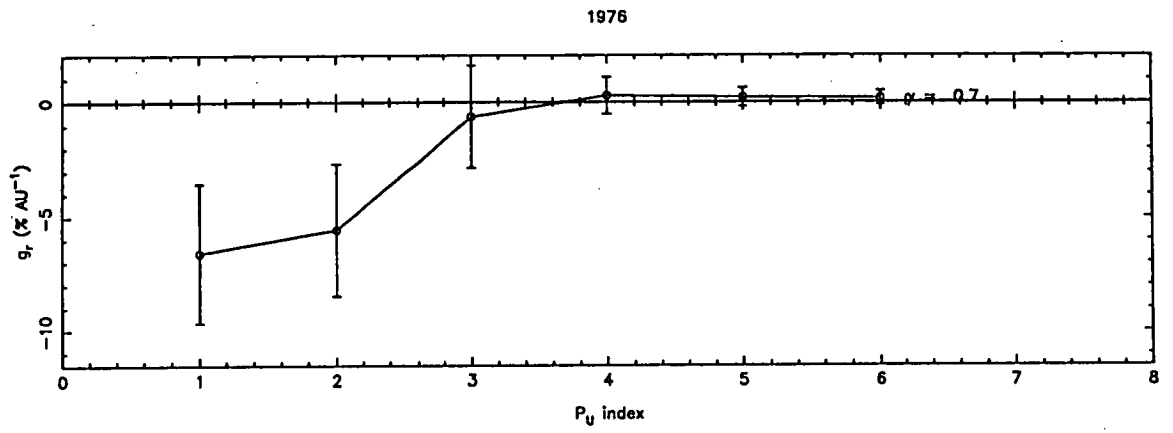


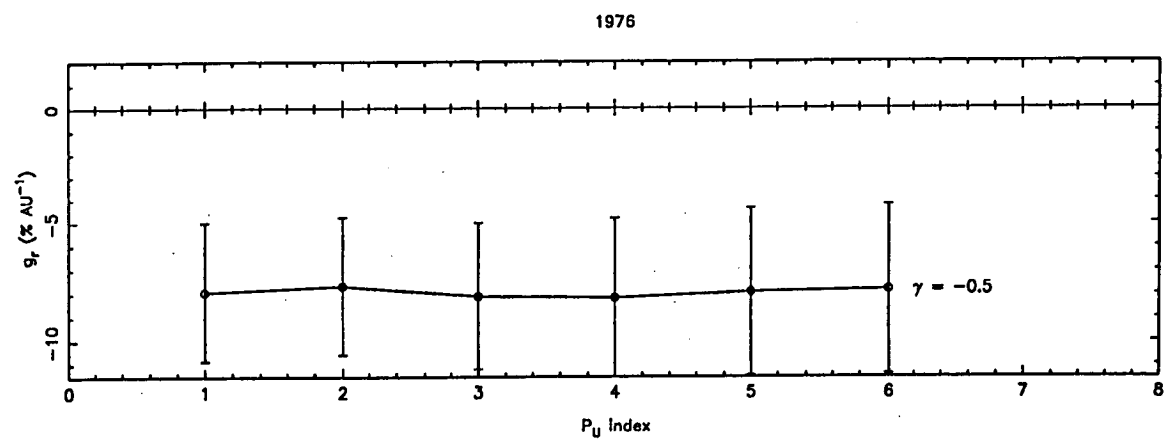
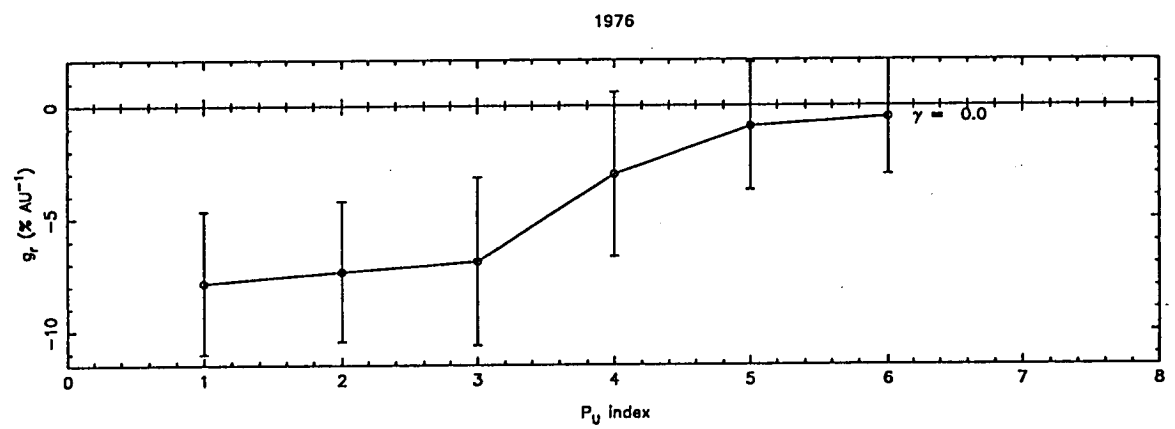
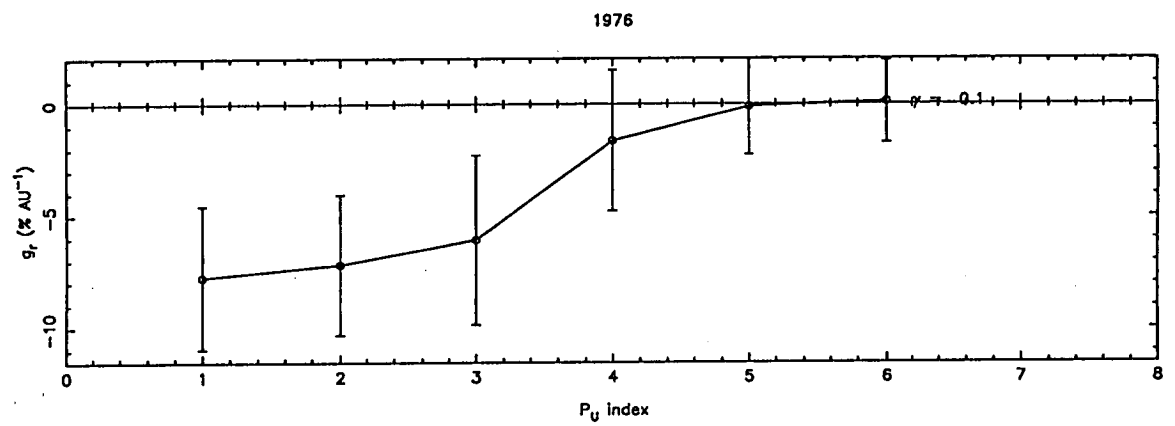
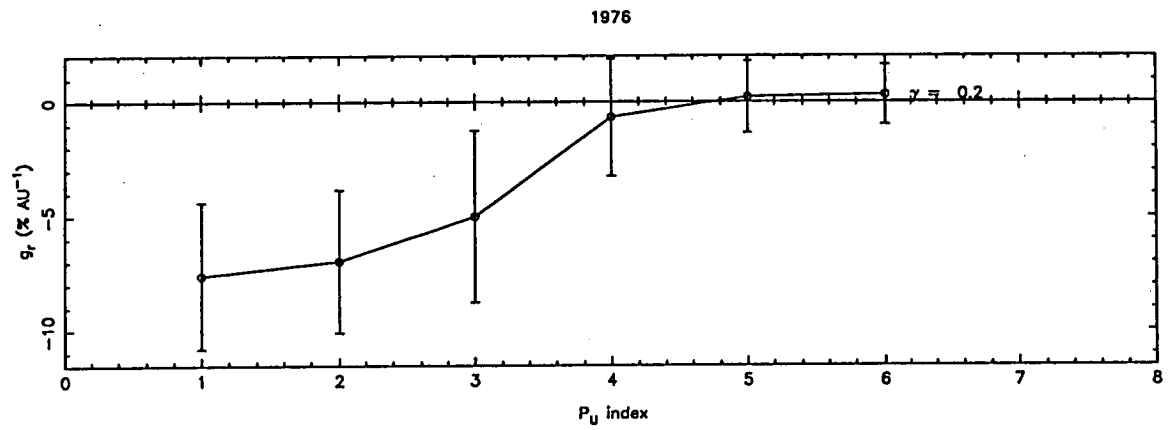
1975



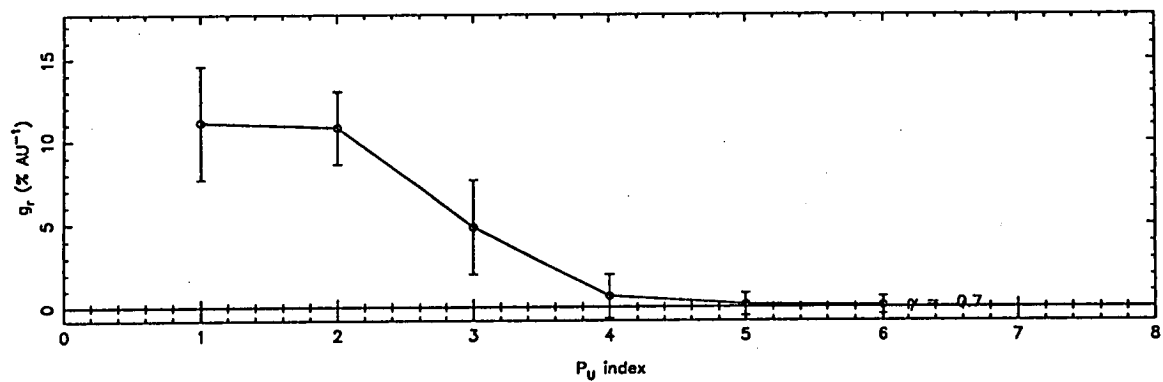
1975



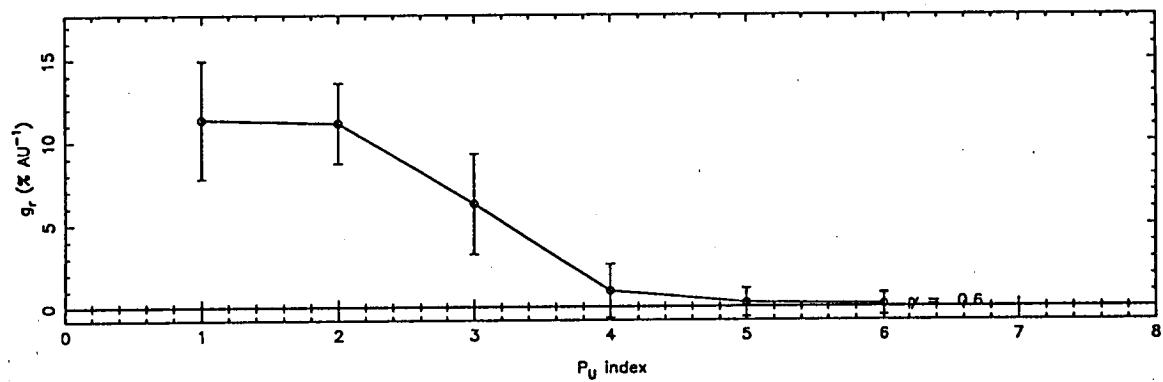




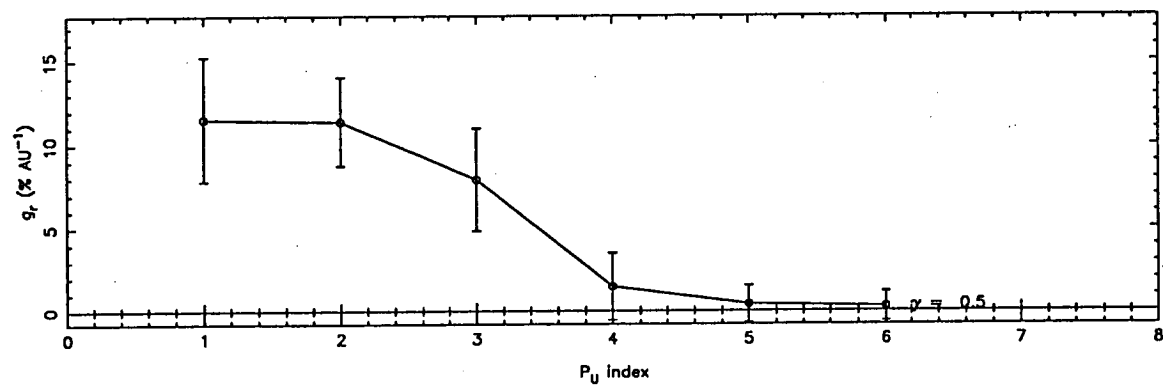
1977



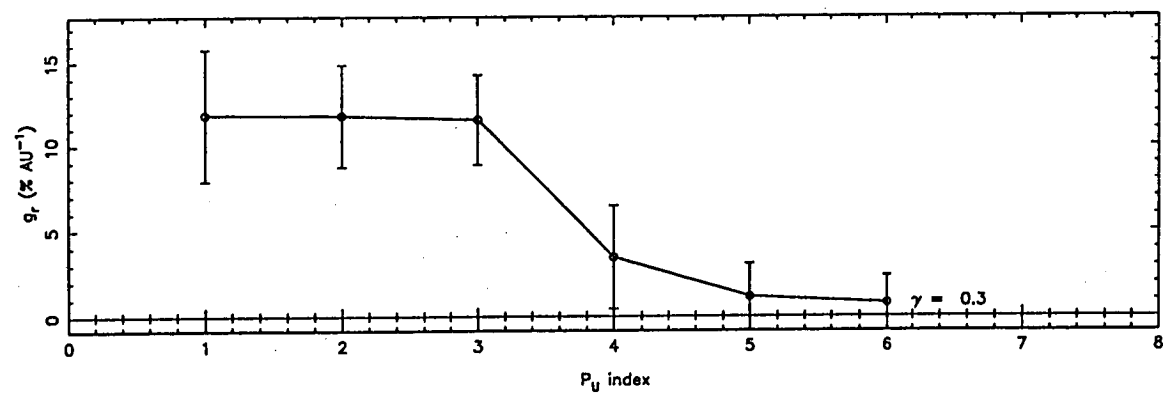
1977

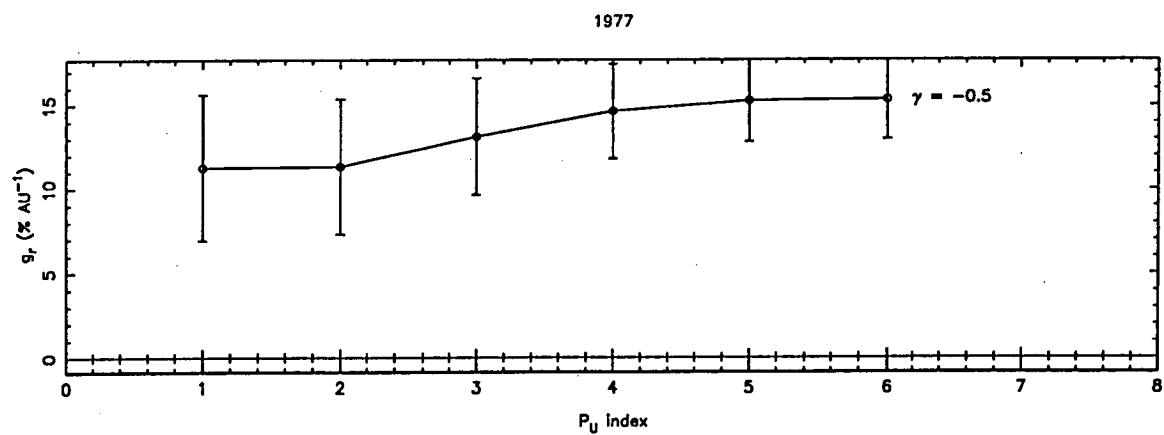
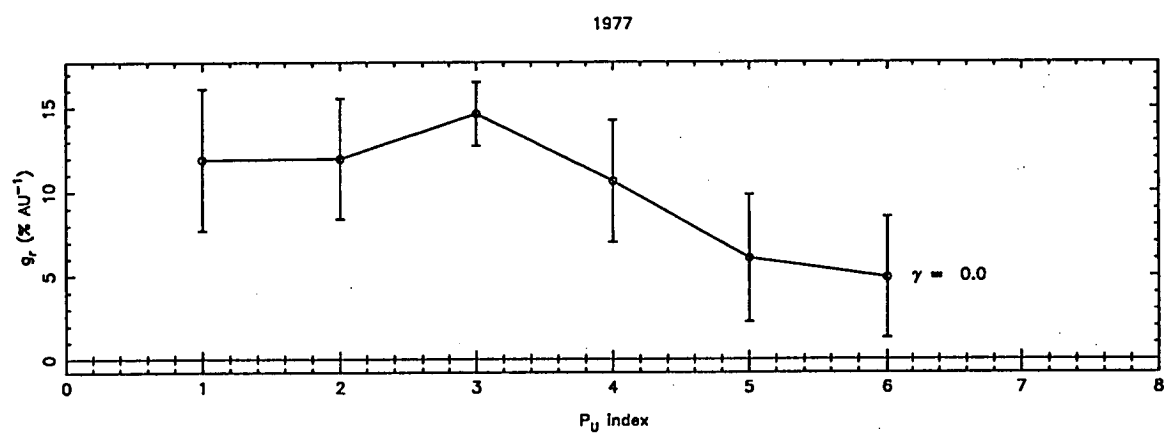
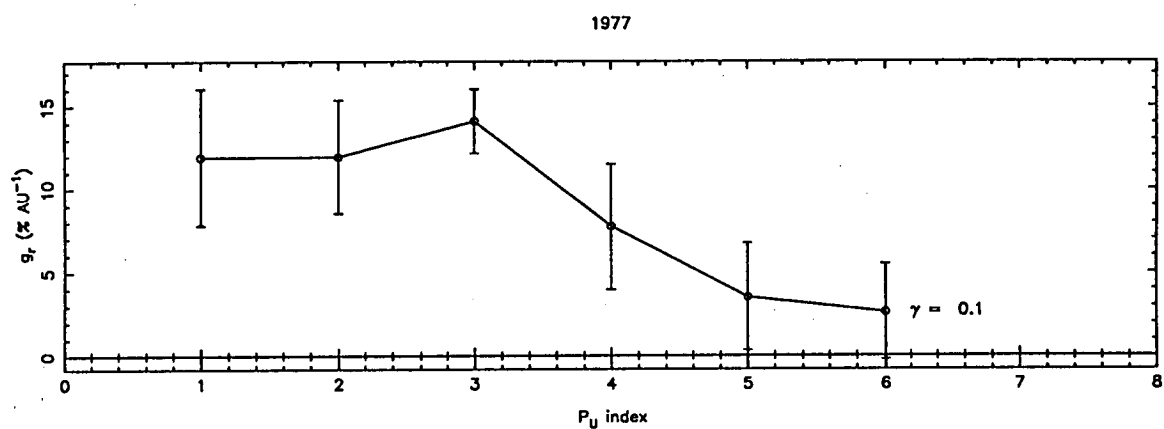
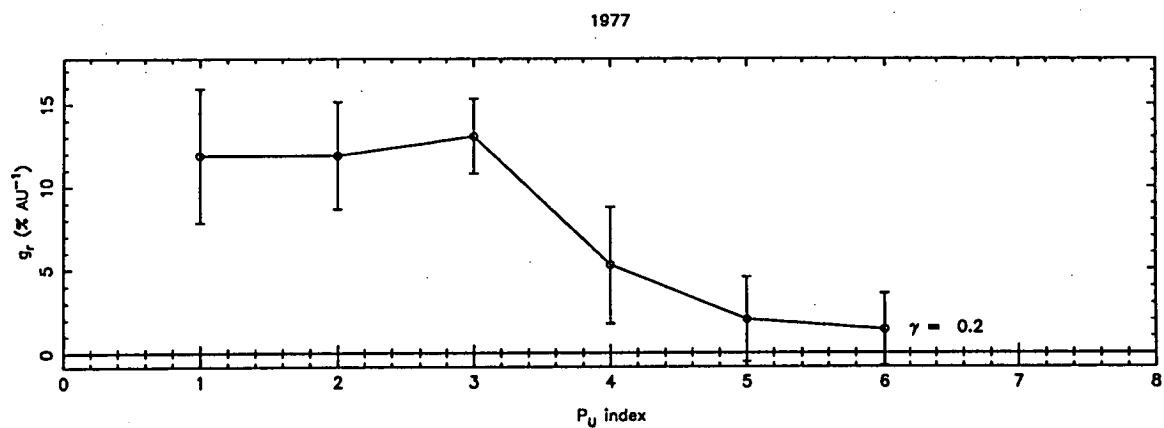


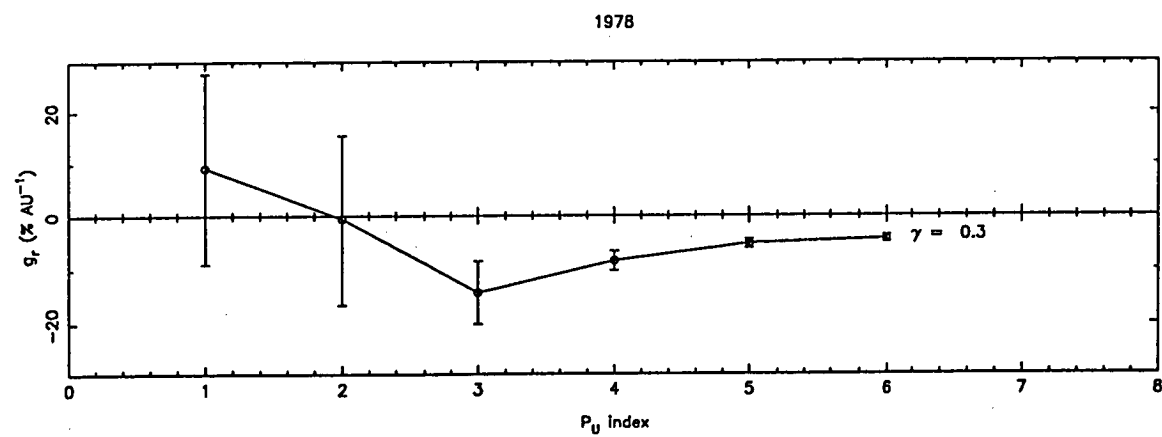
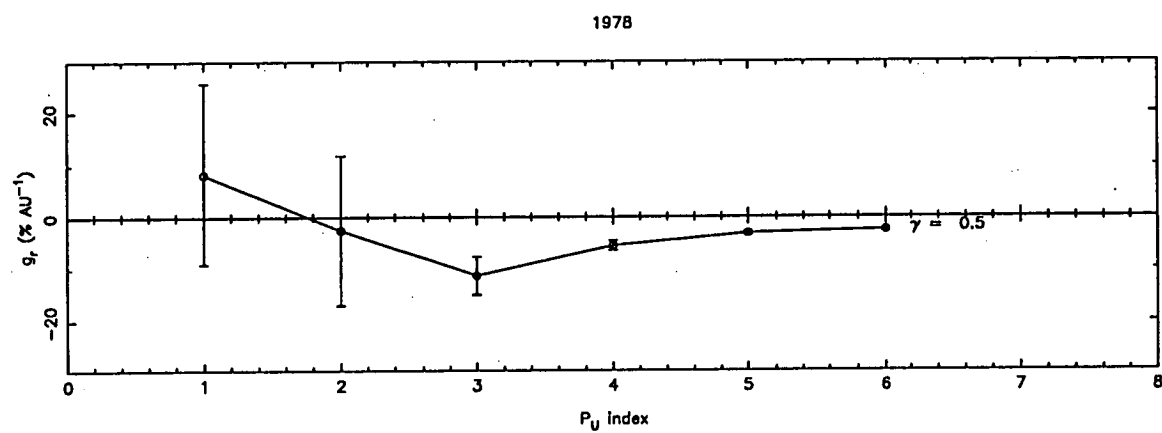
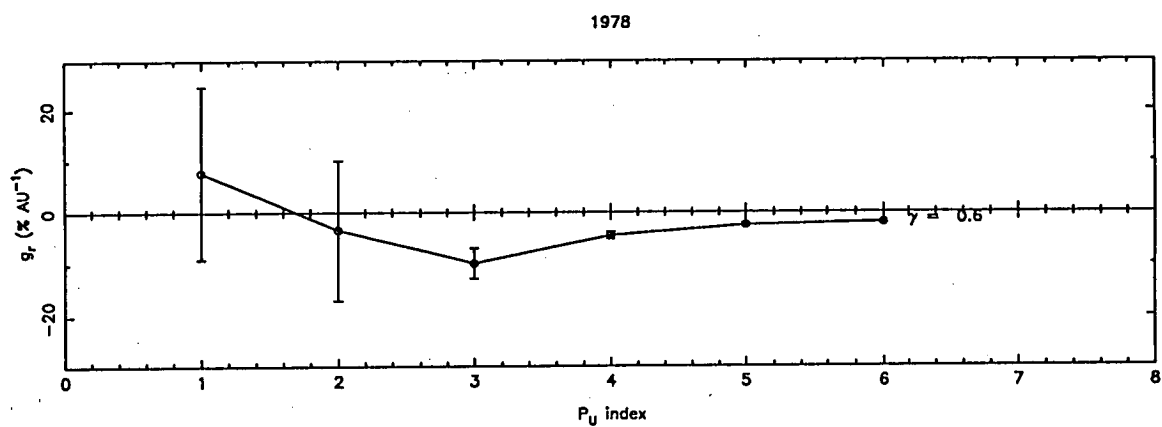
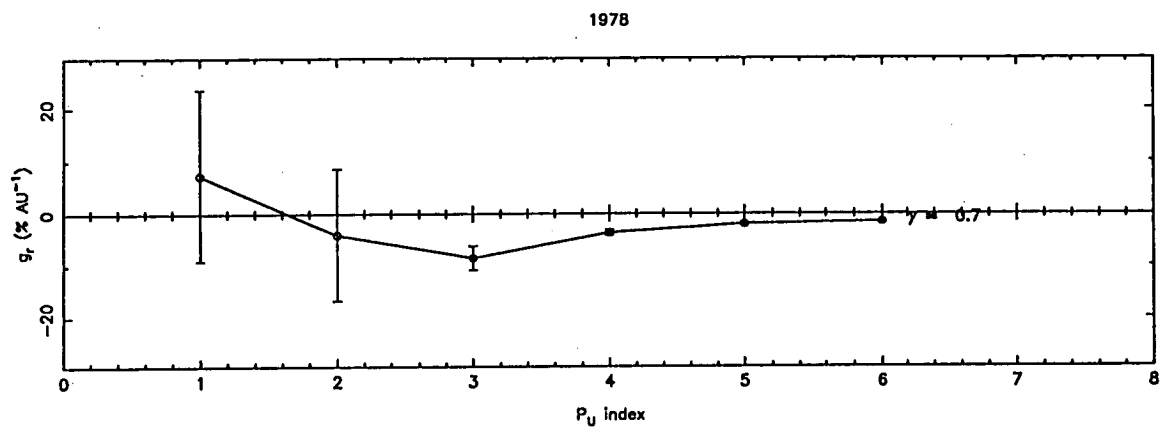
1977



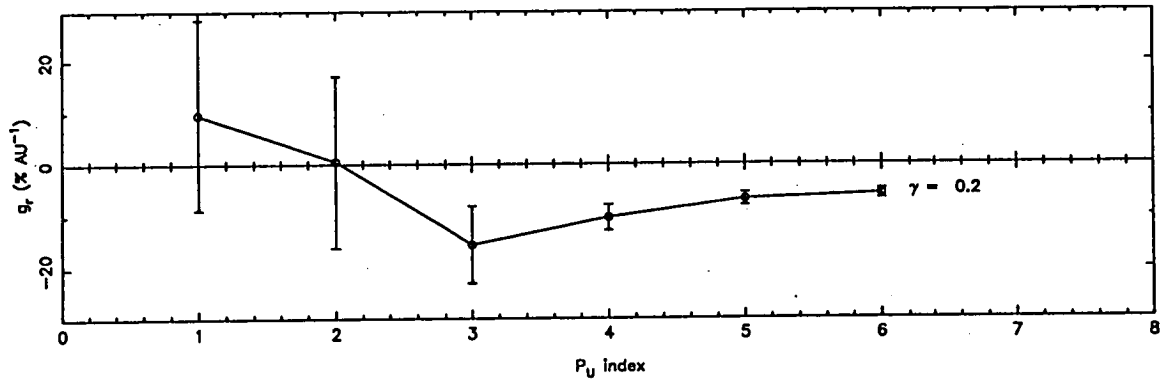
1977



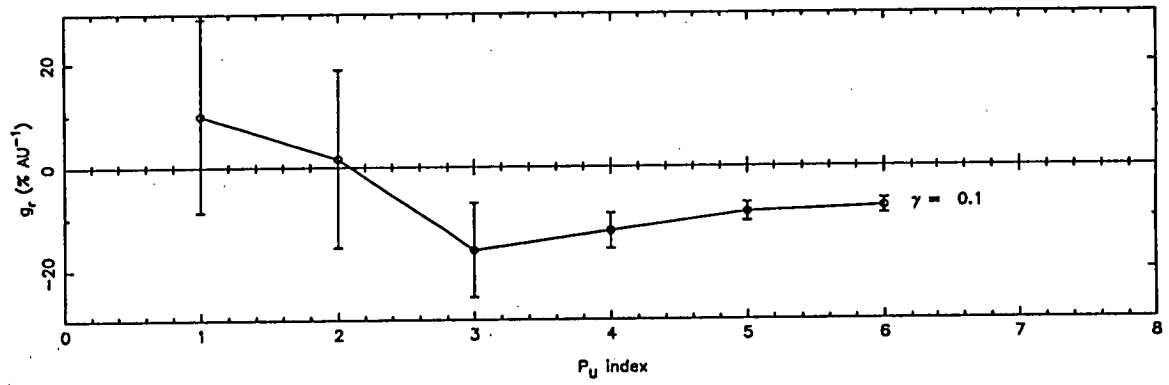




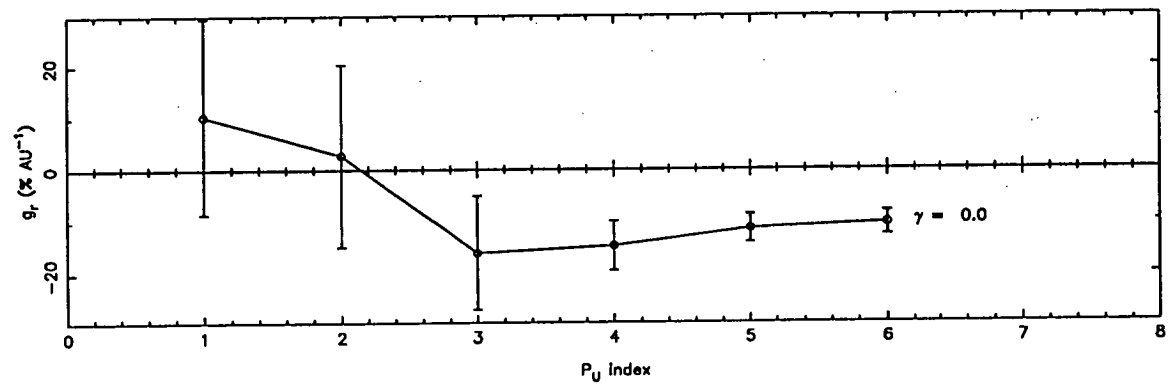
1978



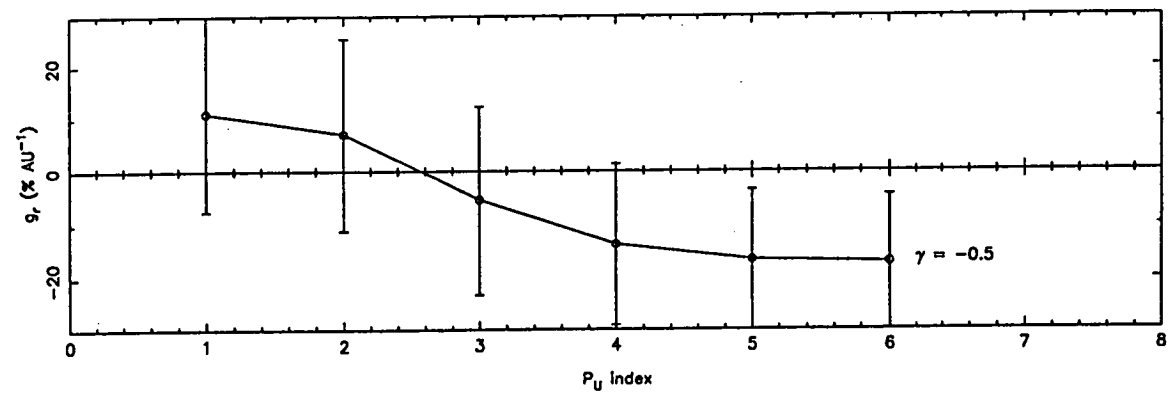
1978

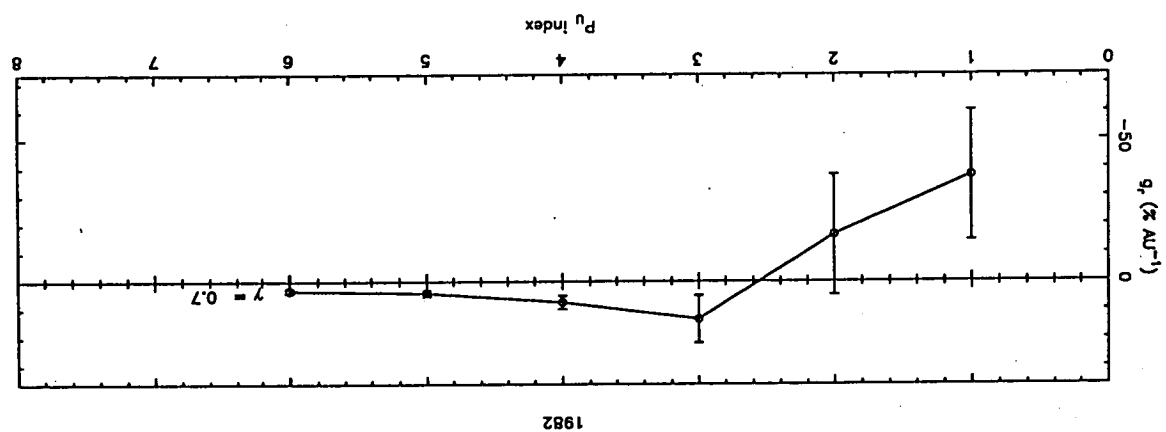
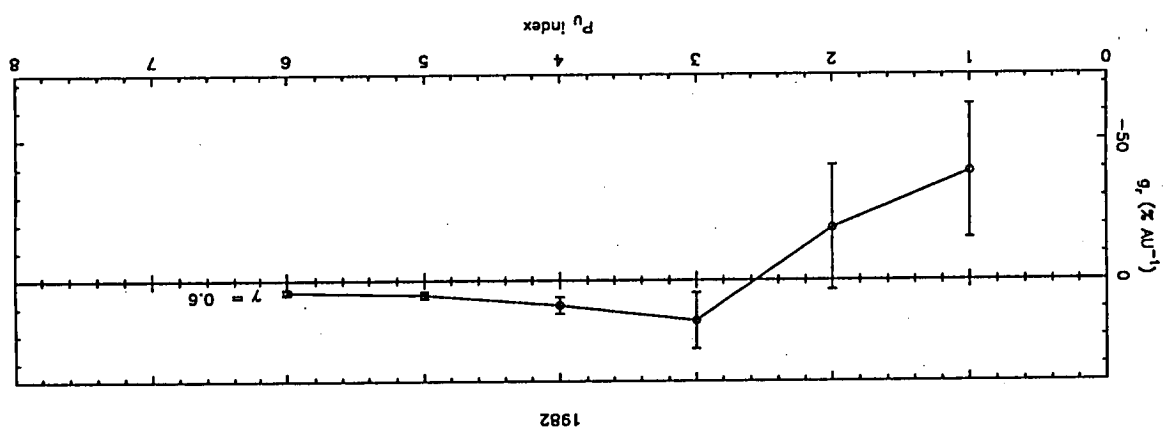
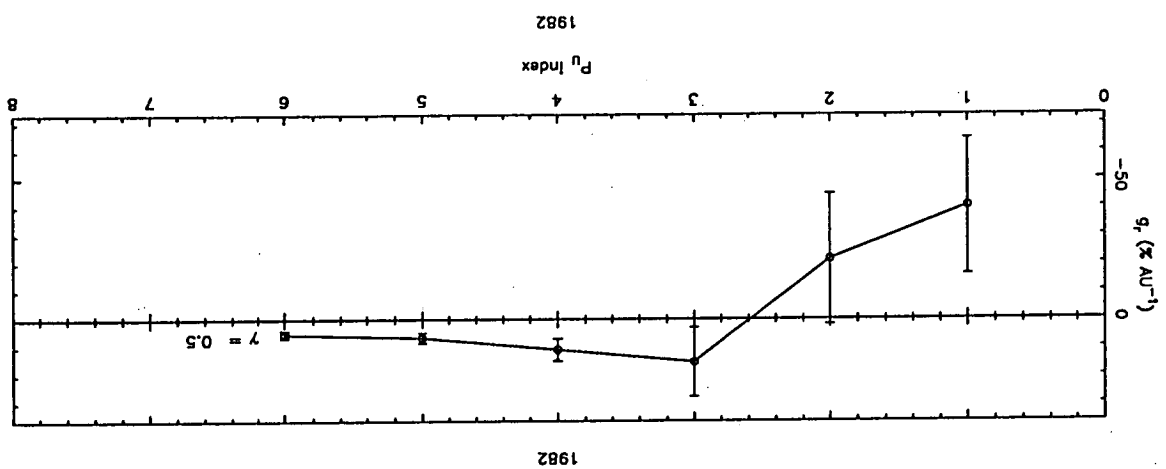
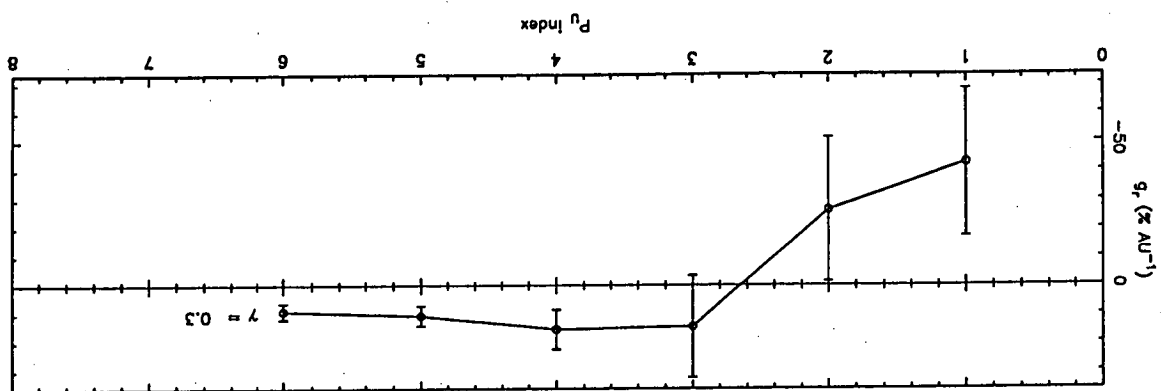


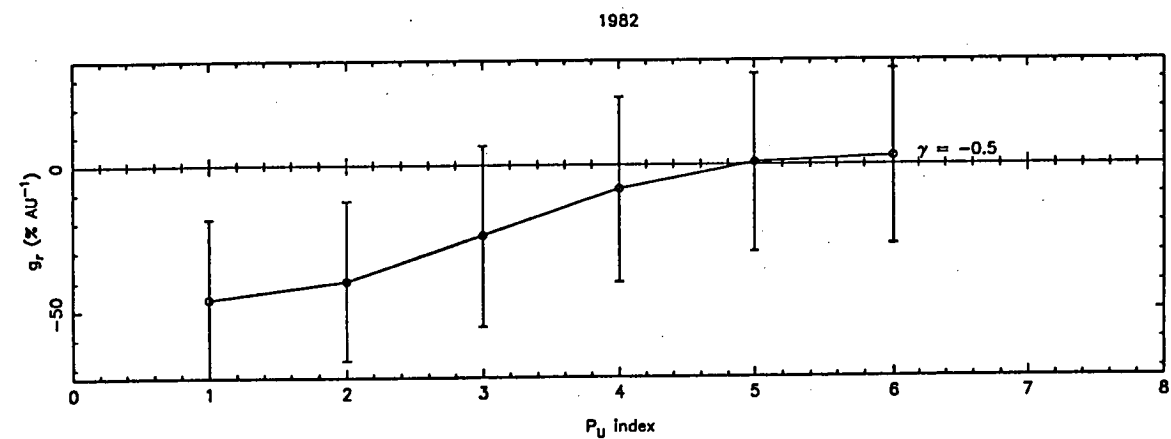
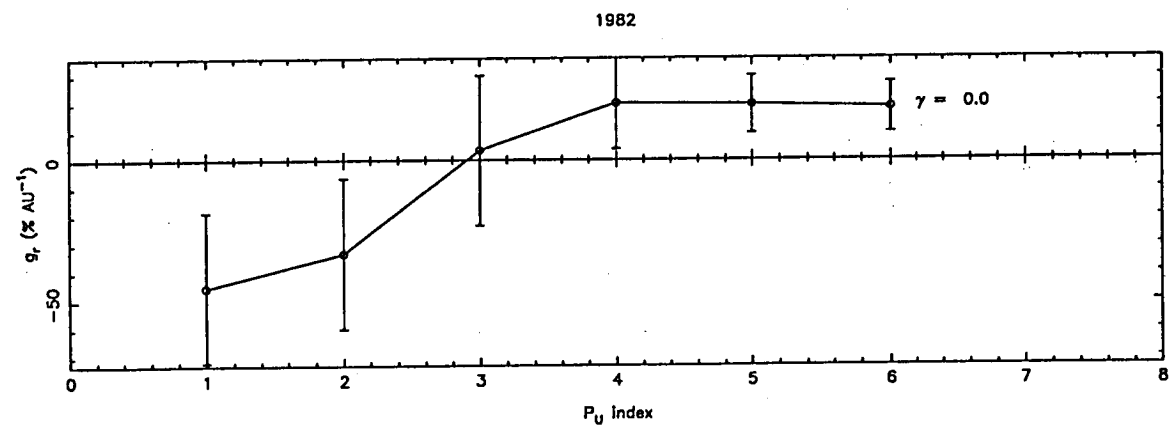
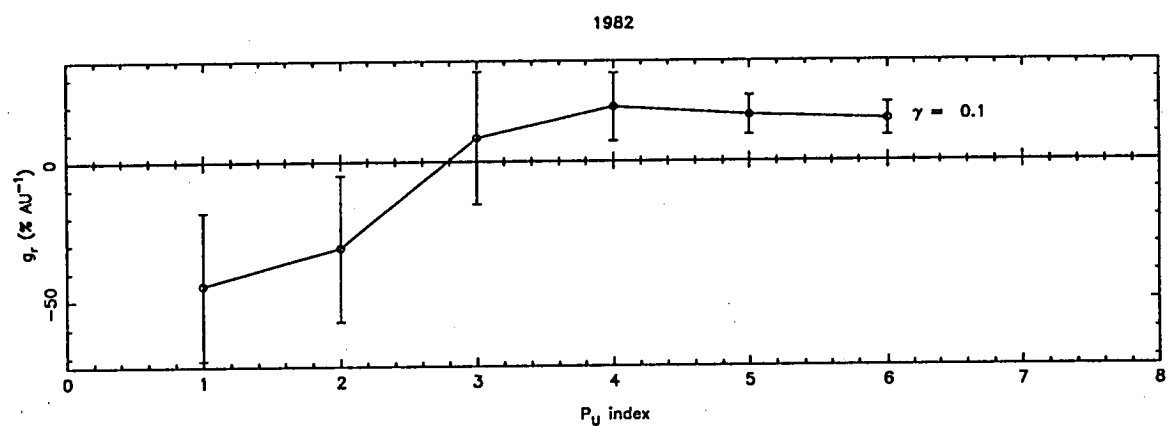
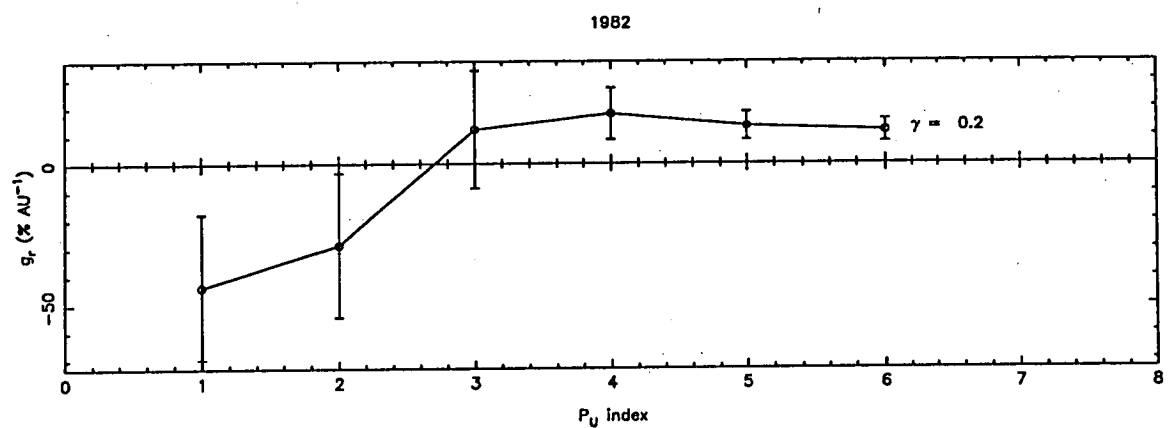
1978

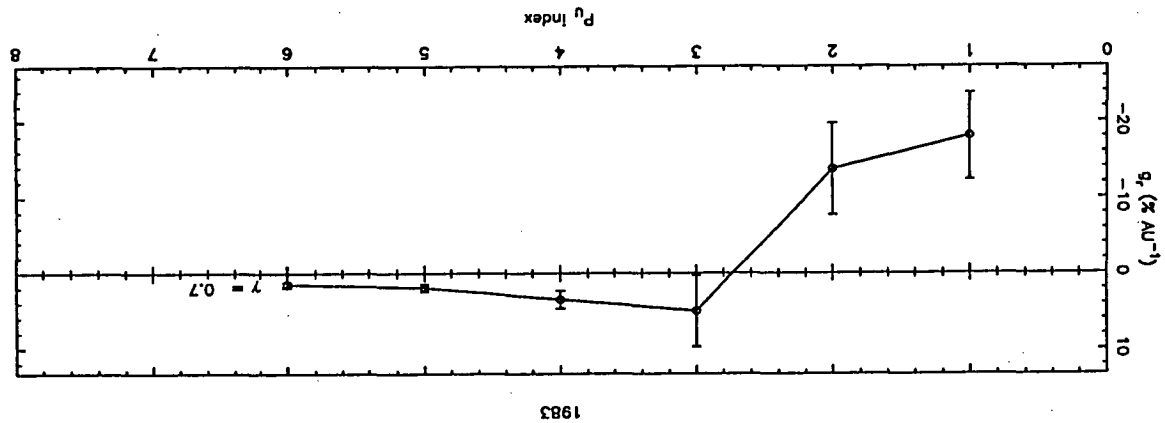
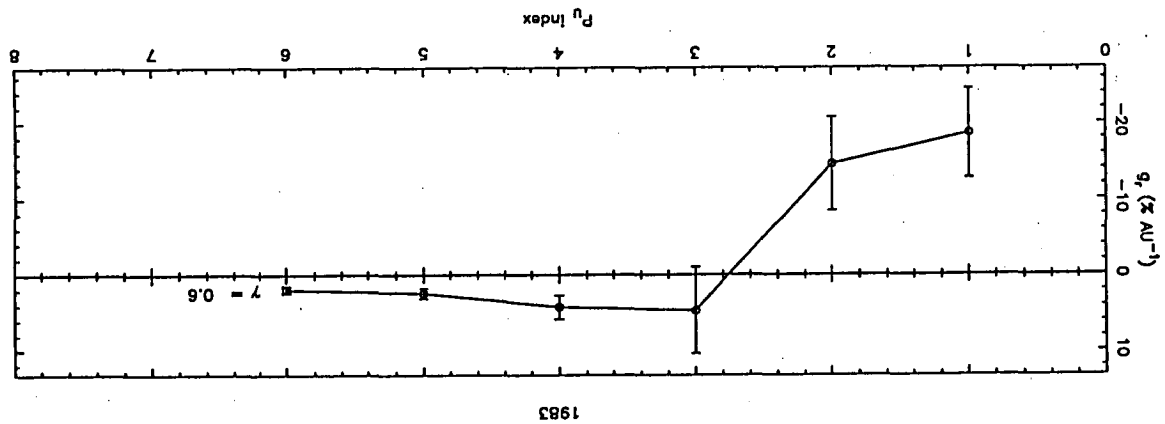
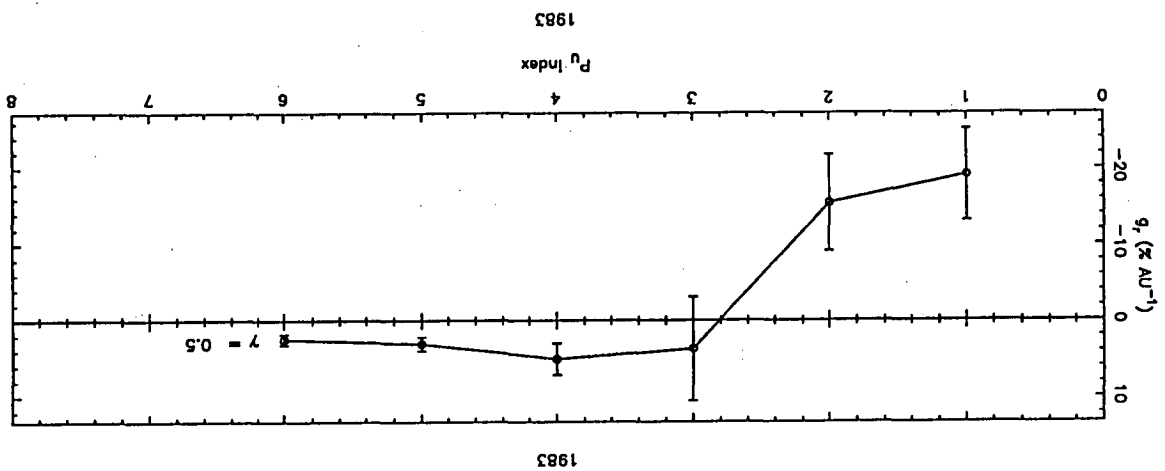
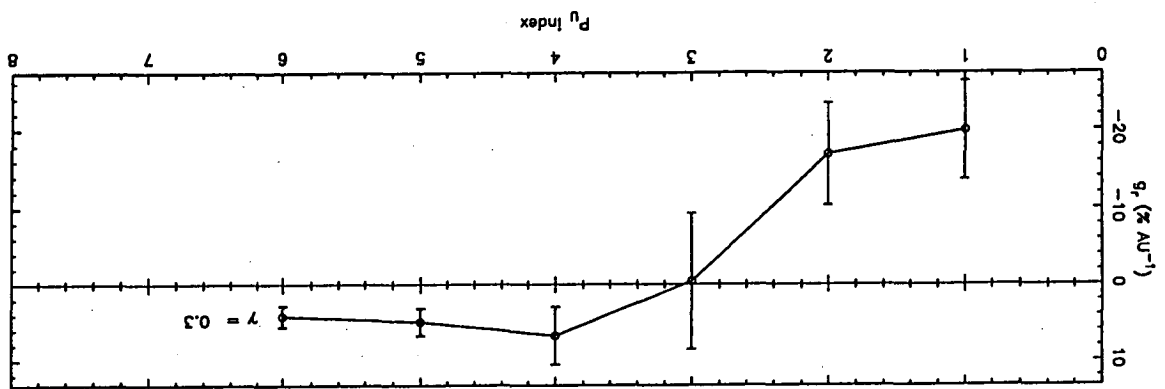


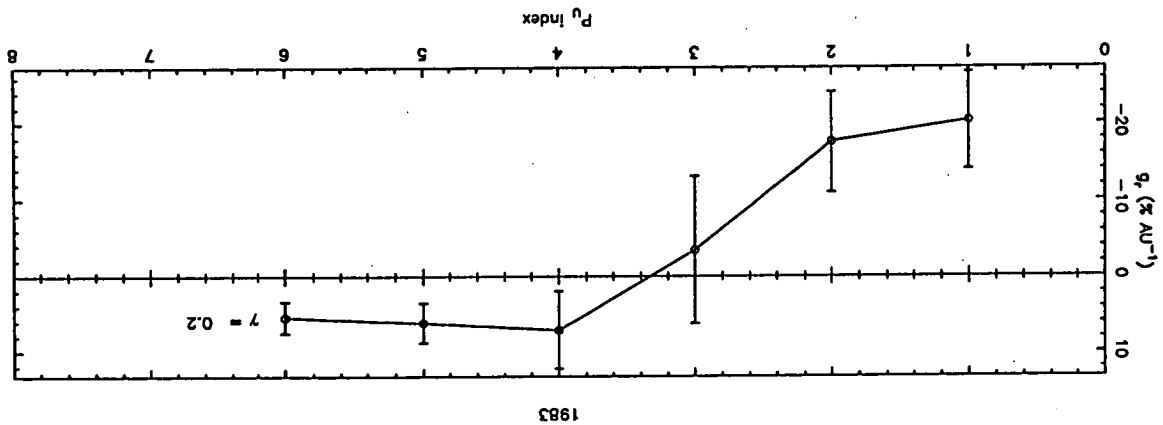
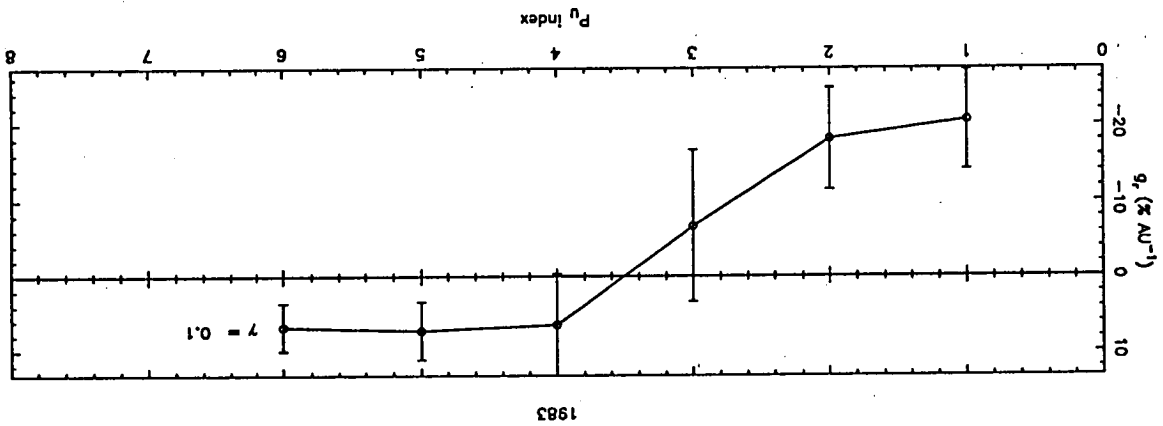
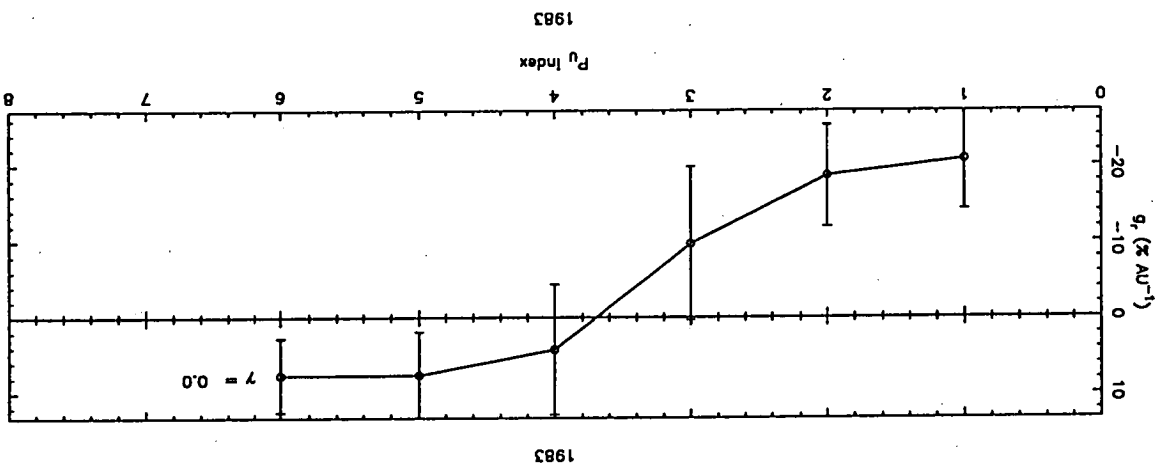
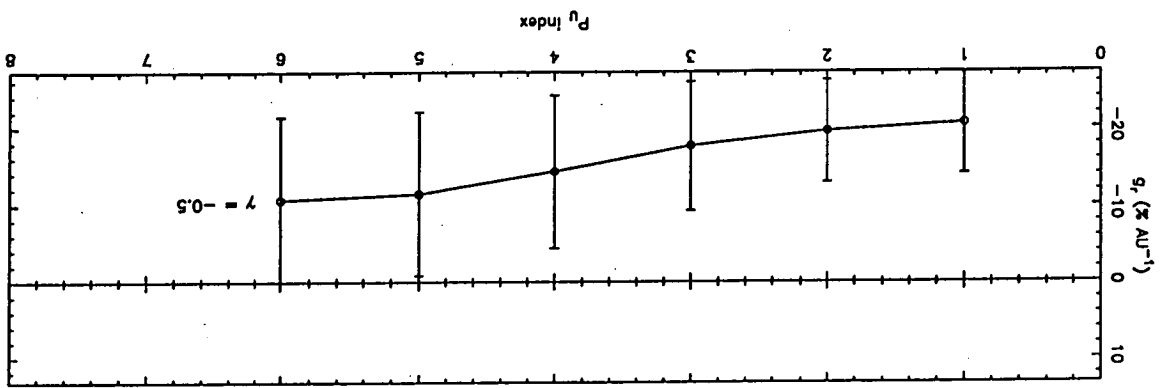
1978



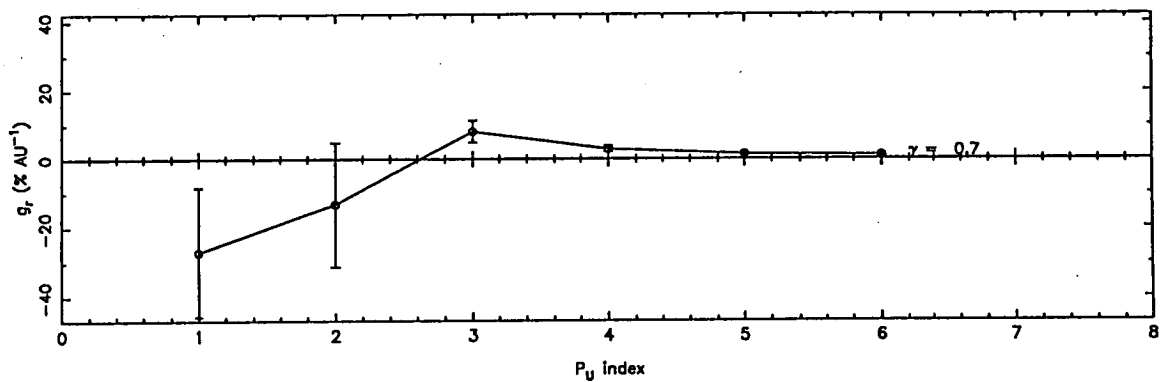




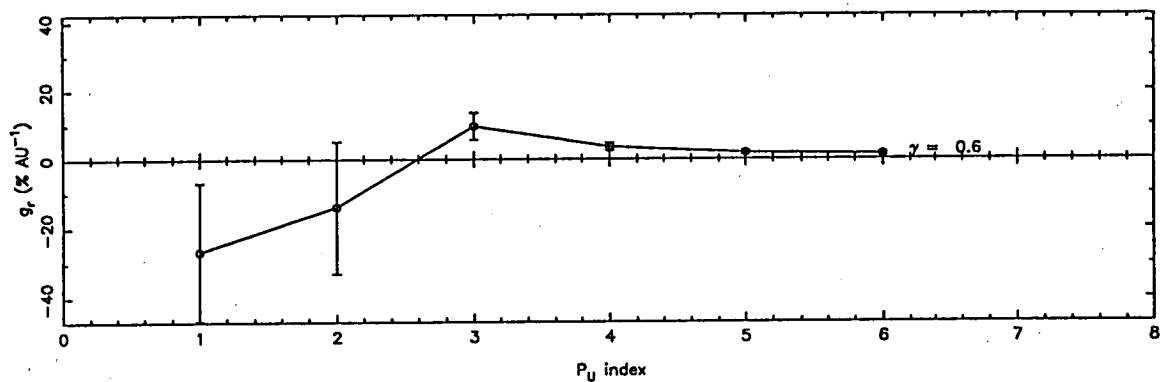




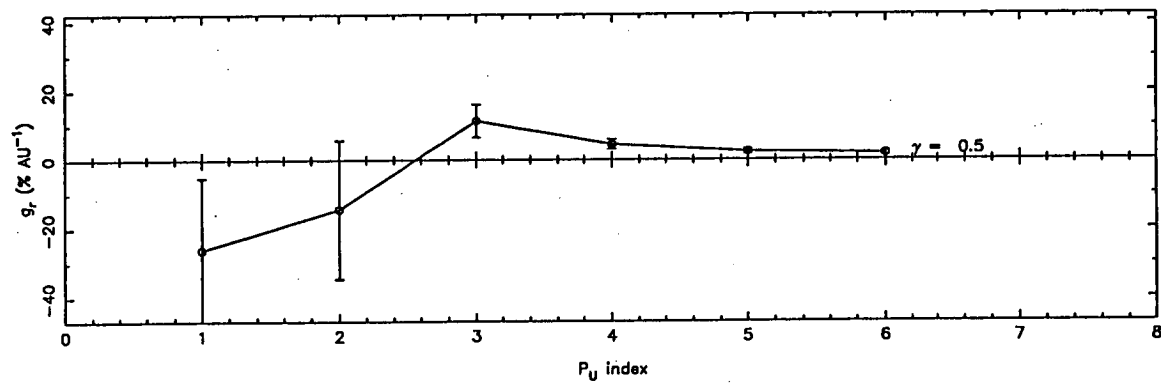
1984



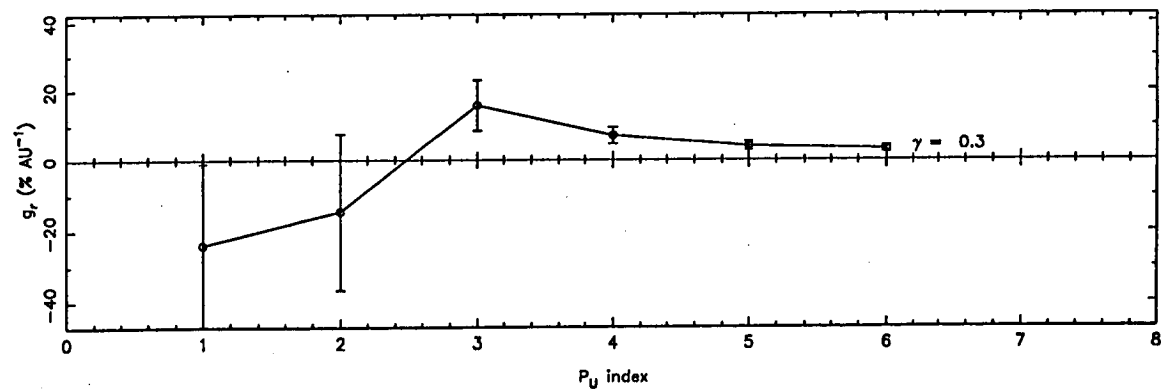
1984

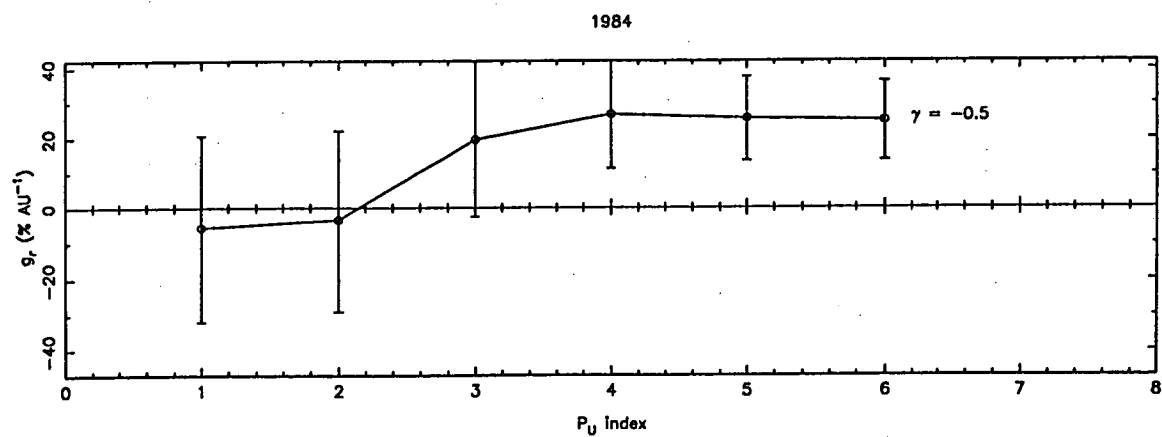
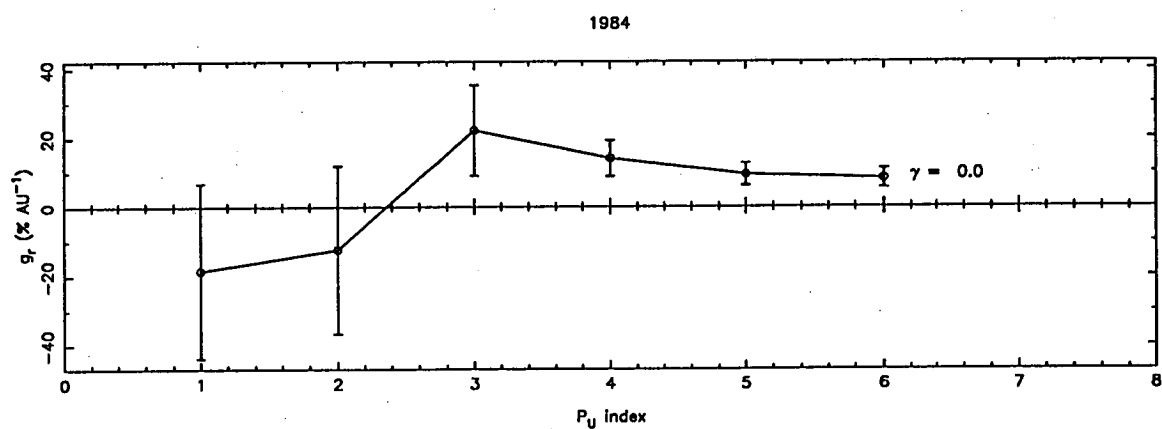
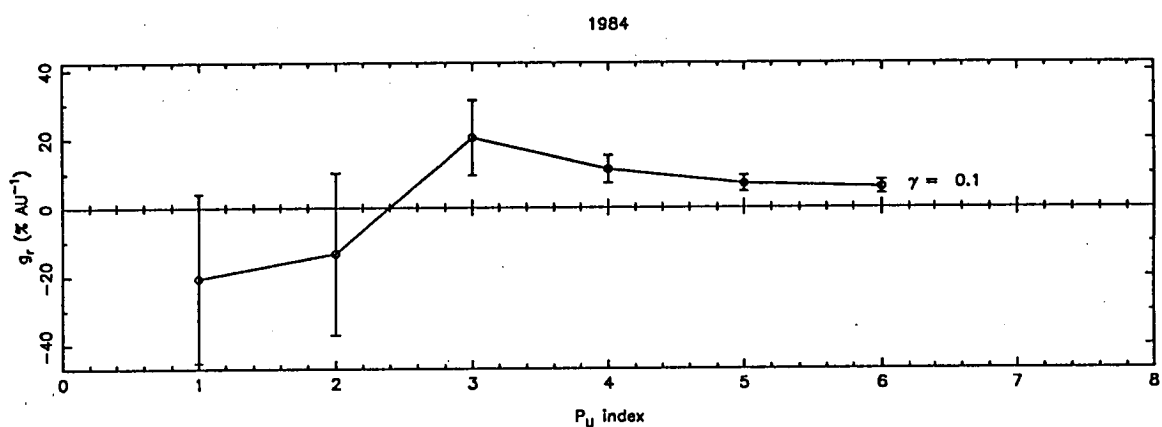
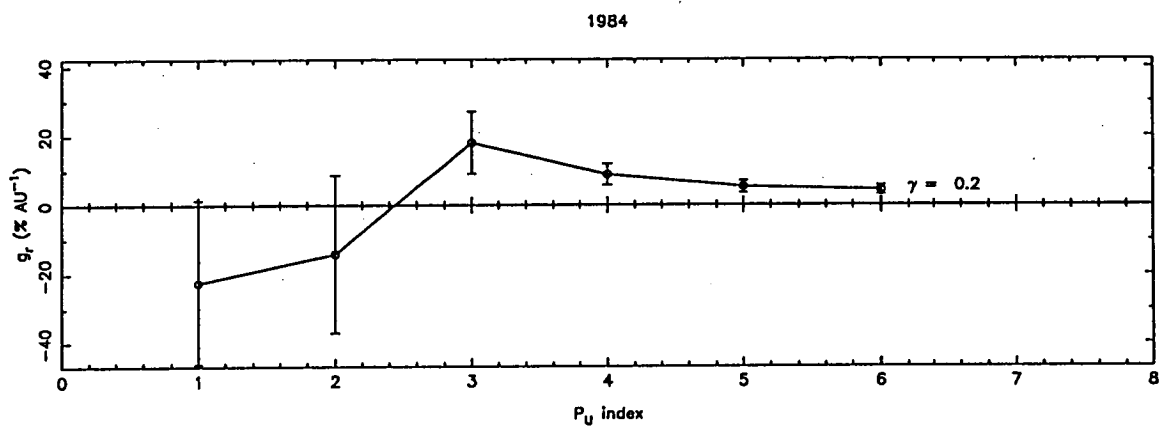


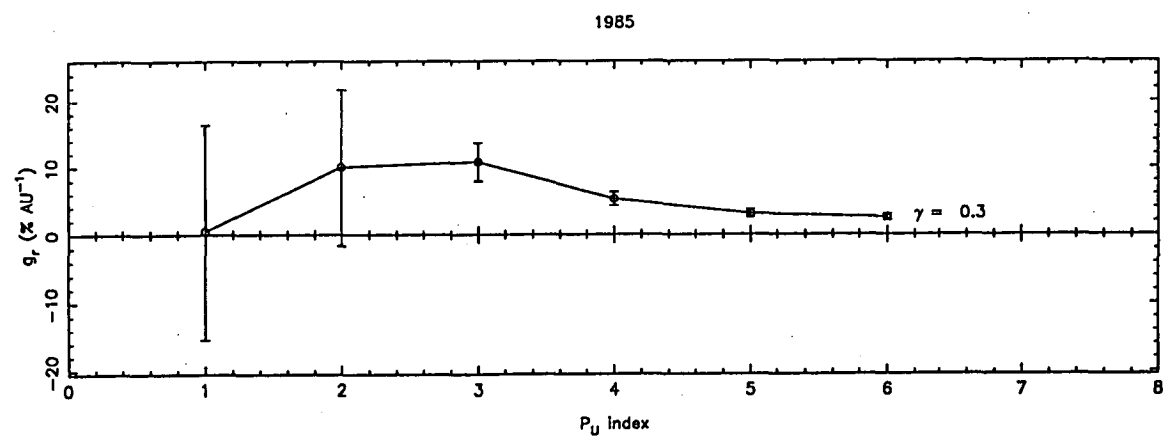
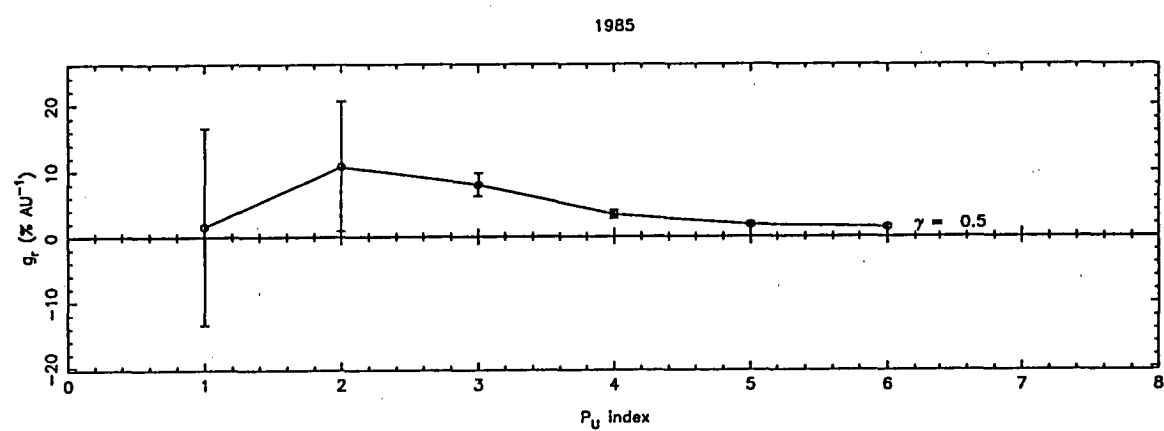
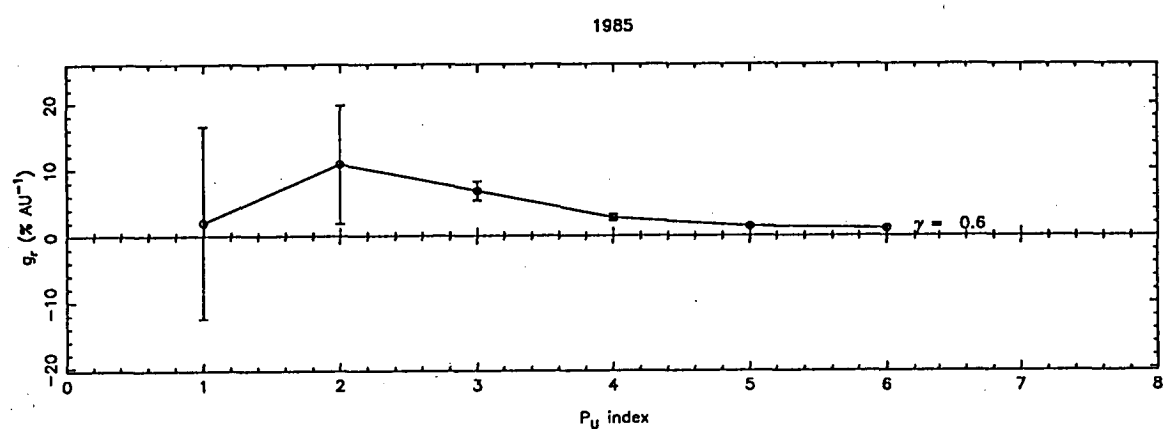
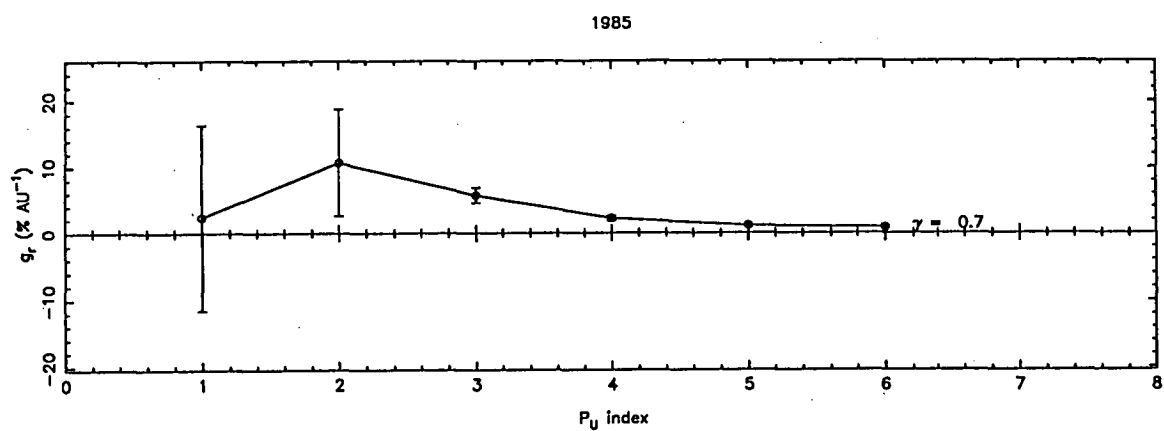
1984

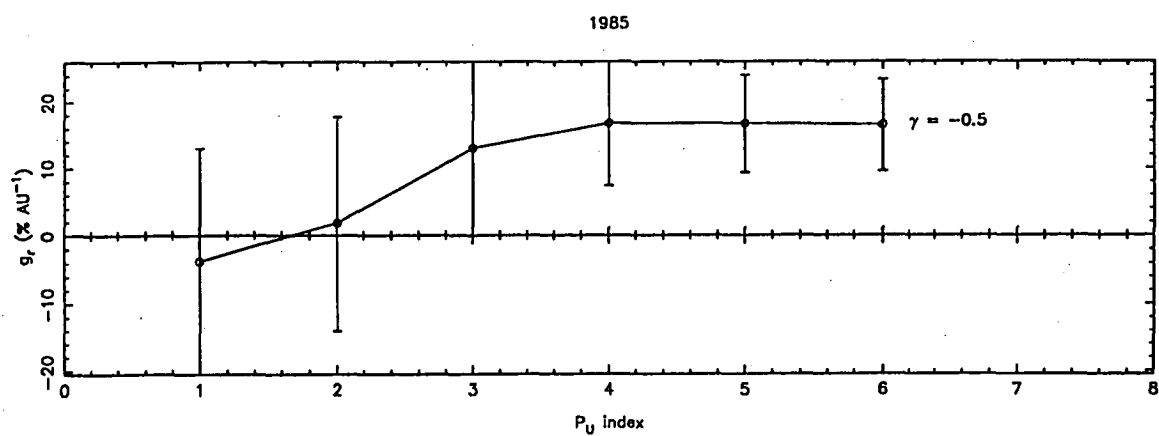
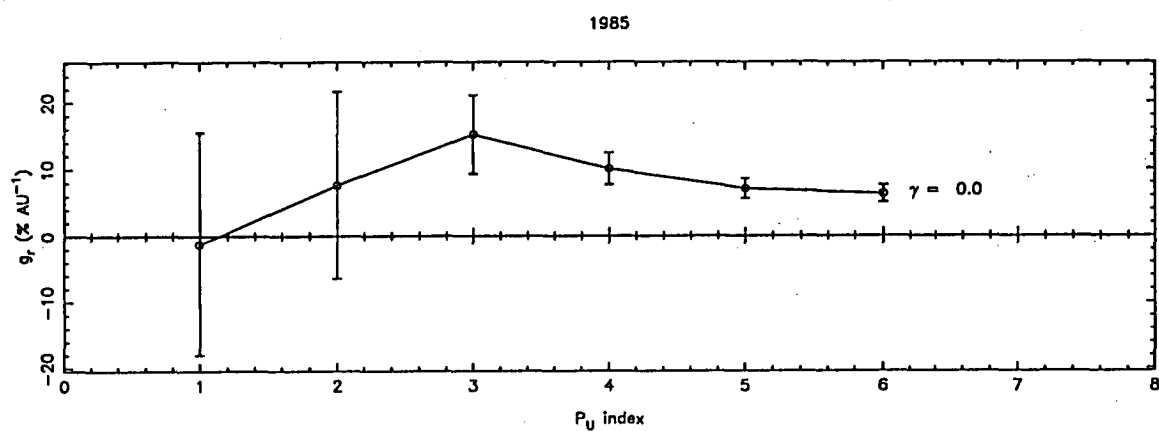
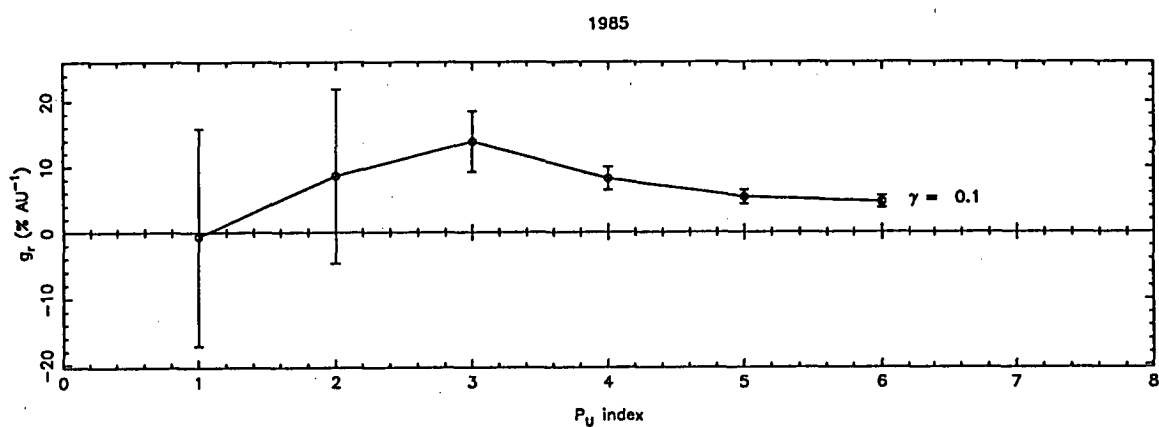
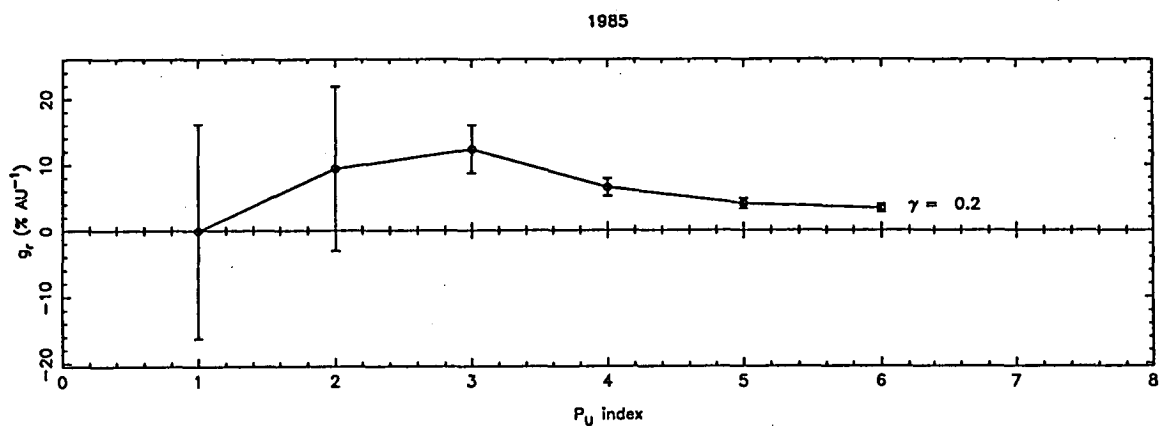


1984





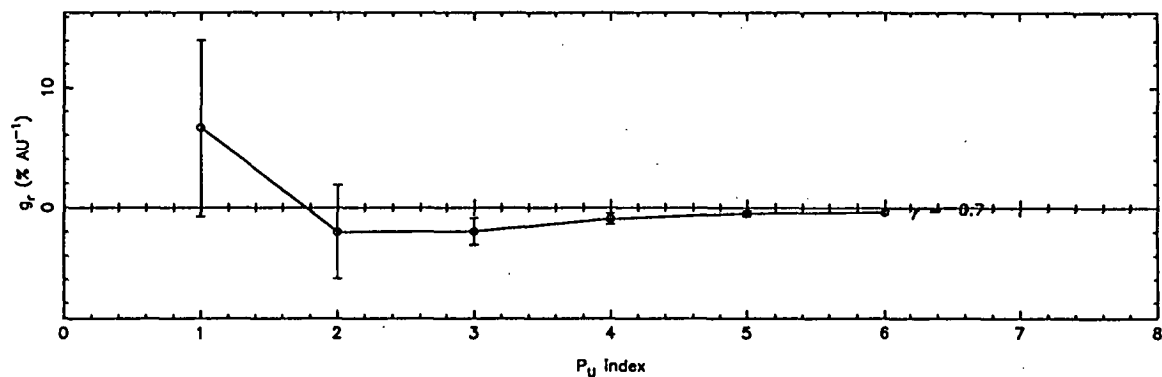
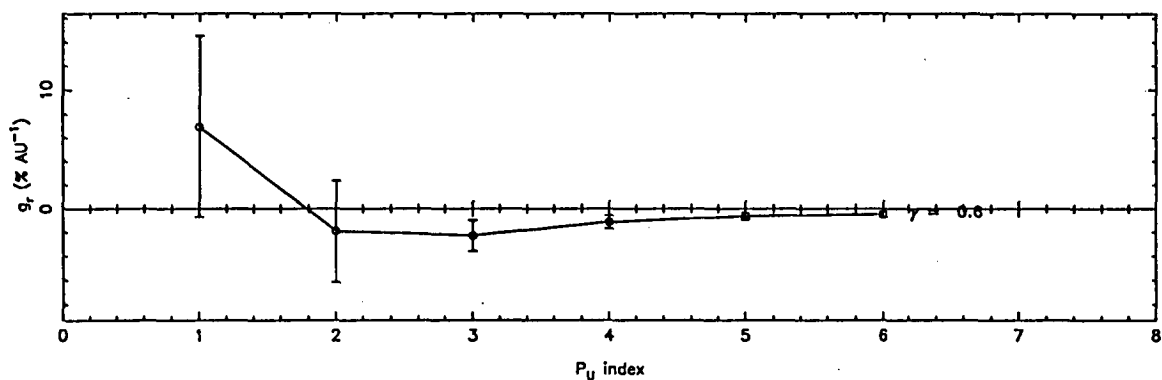
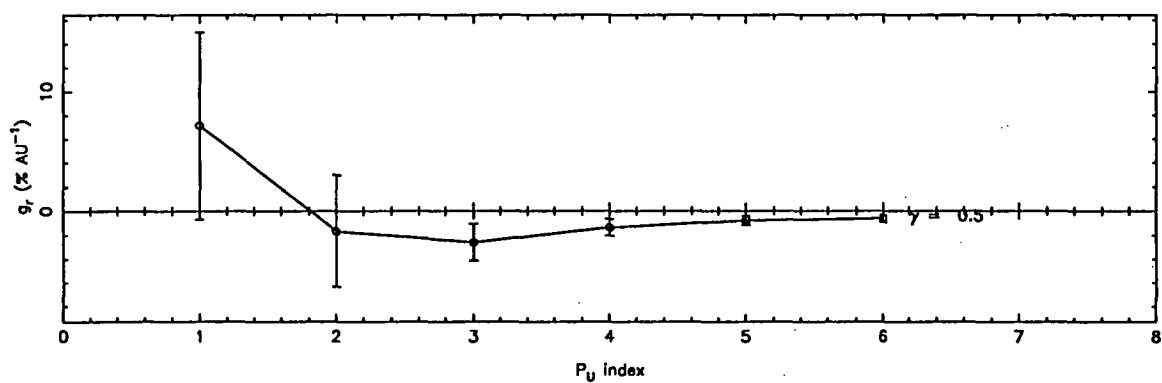
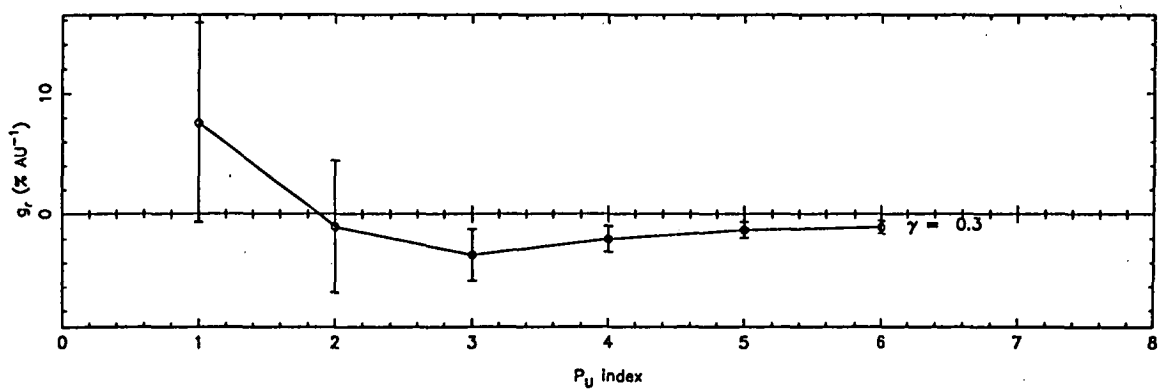


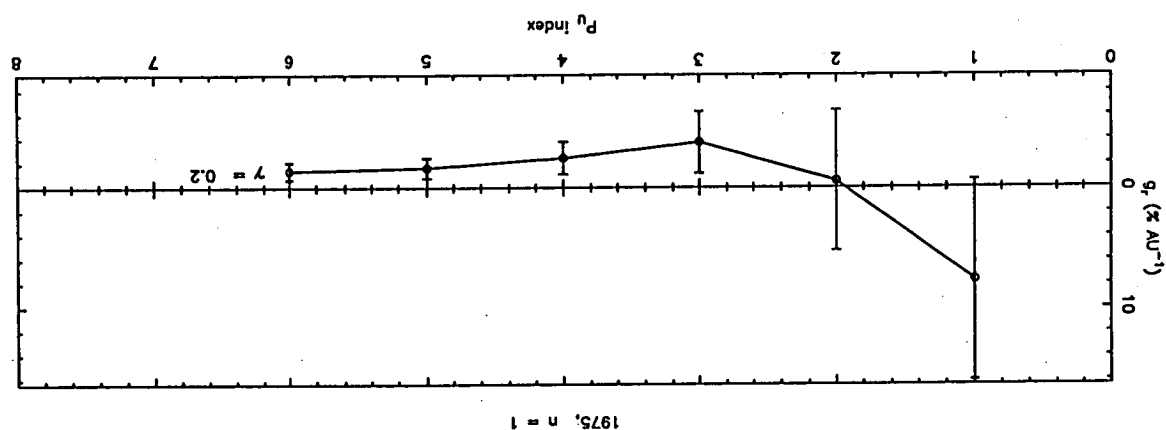
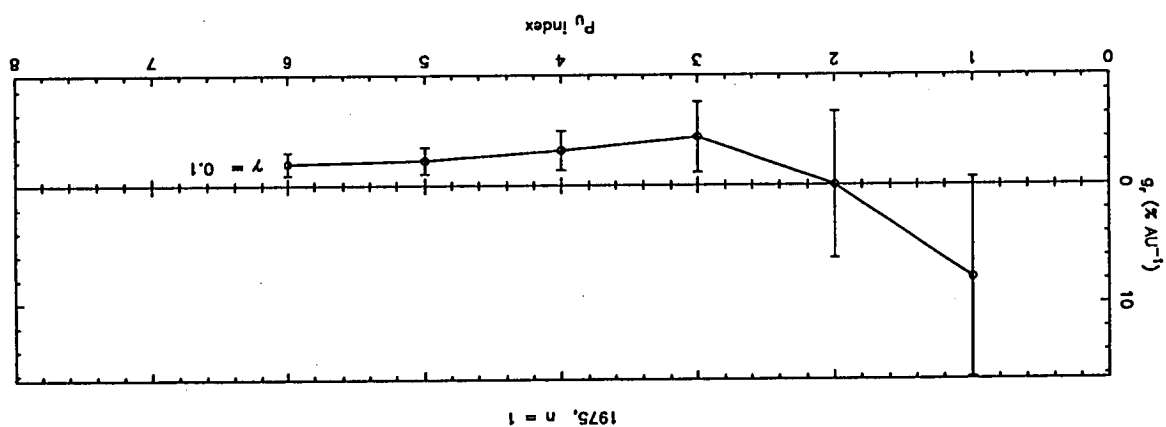
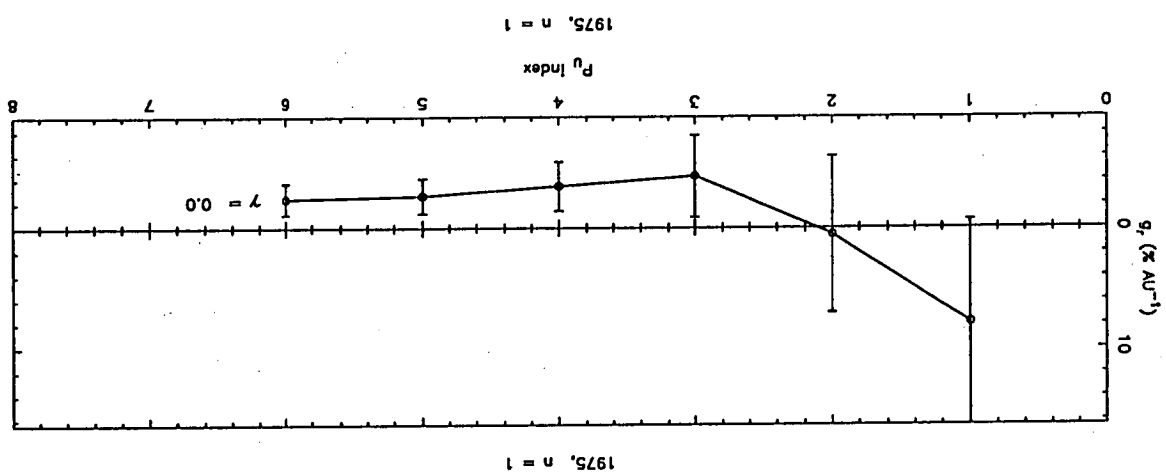
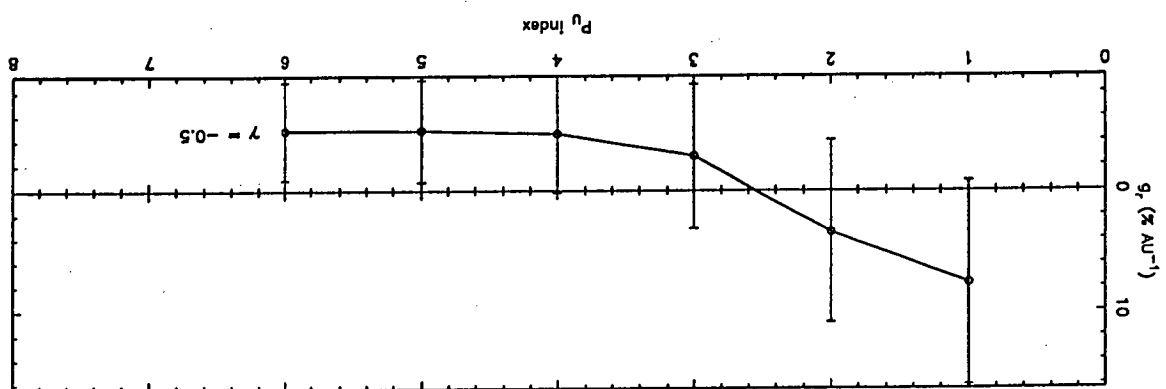


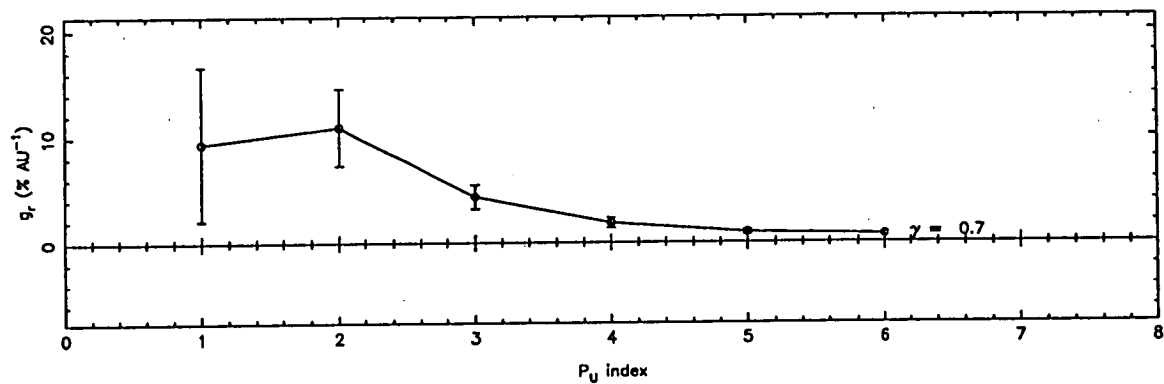
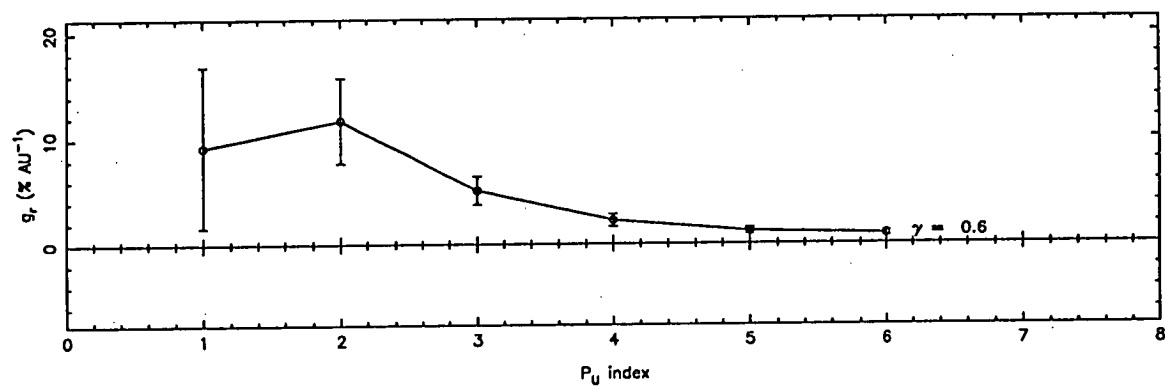
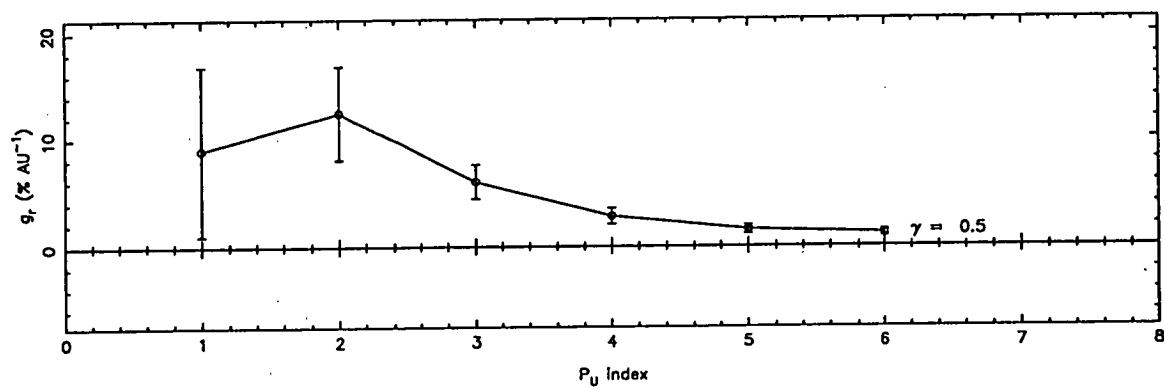
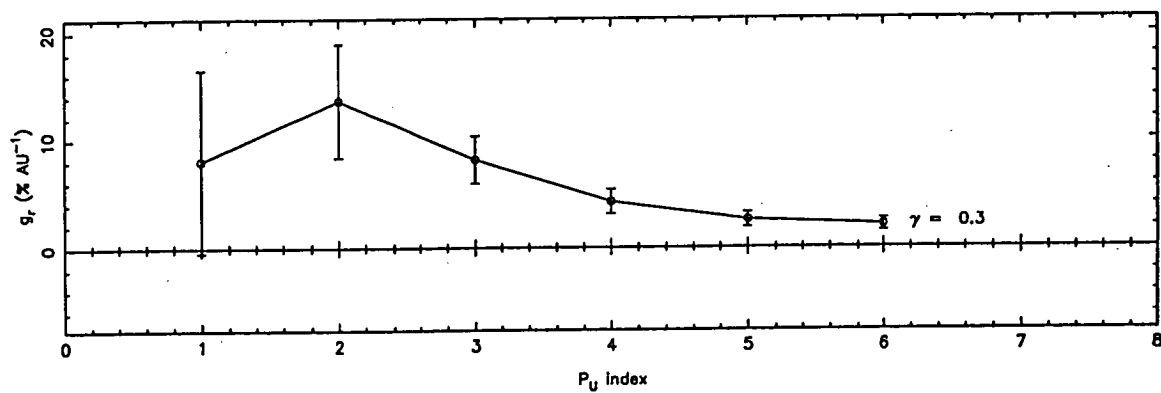
APPENDIX 8

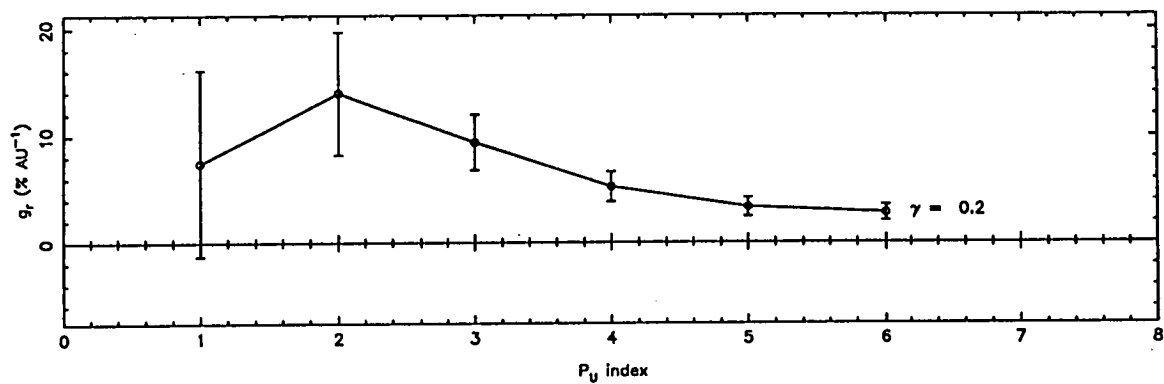
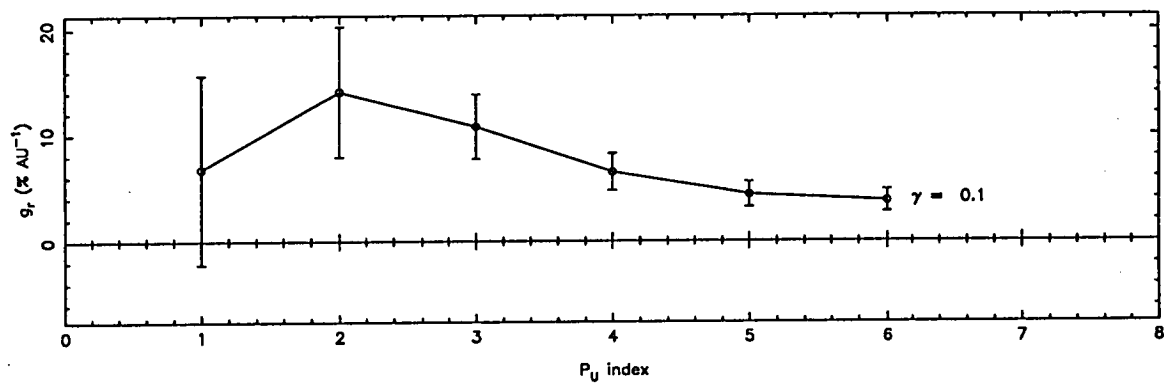
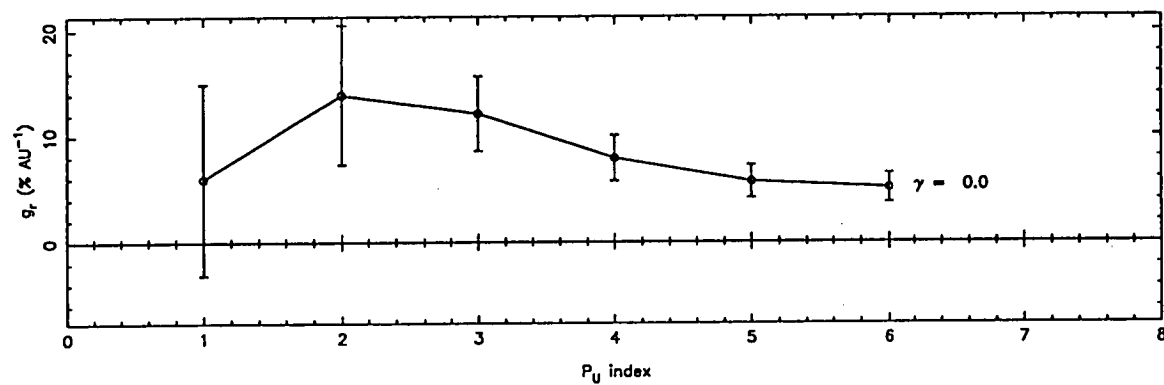
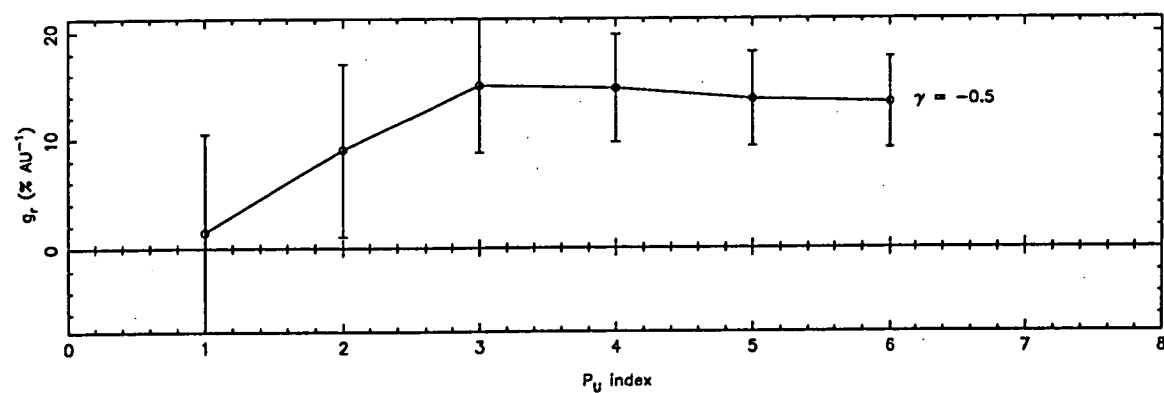
NORTH/SOUTH ANISOTROPY ANALYSIS. RESULTS USING METHOD 2.

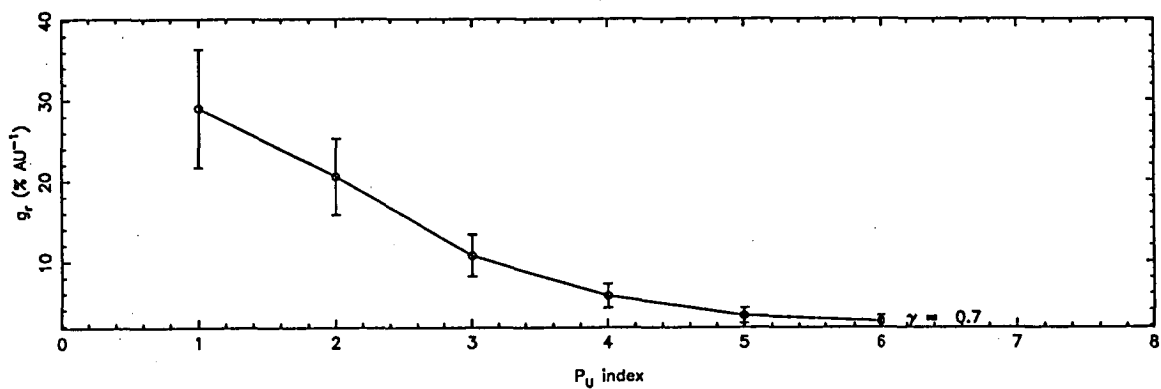
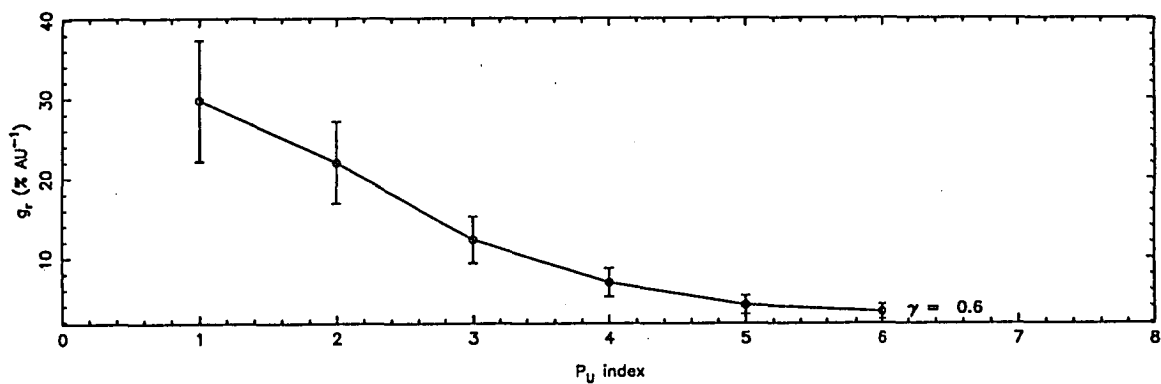
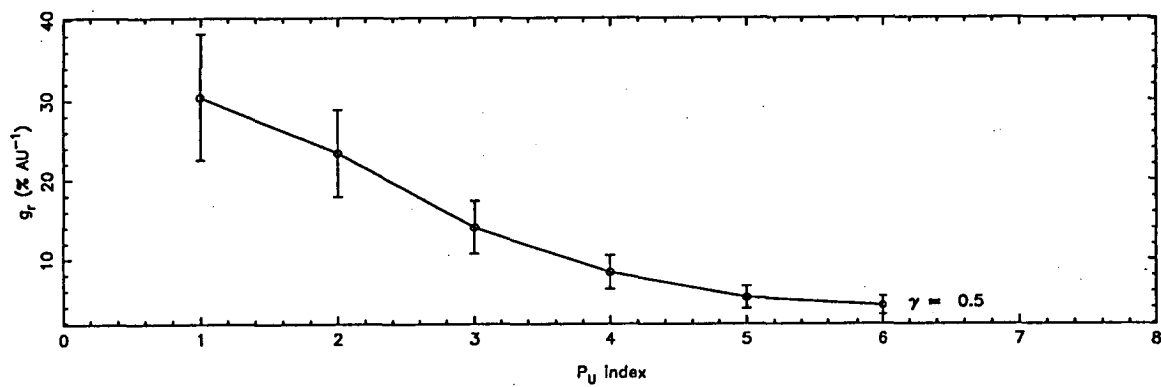
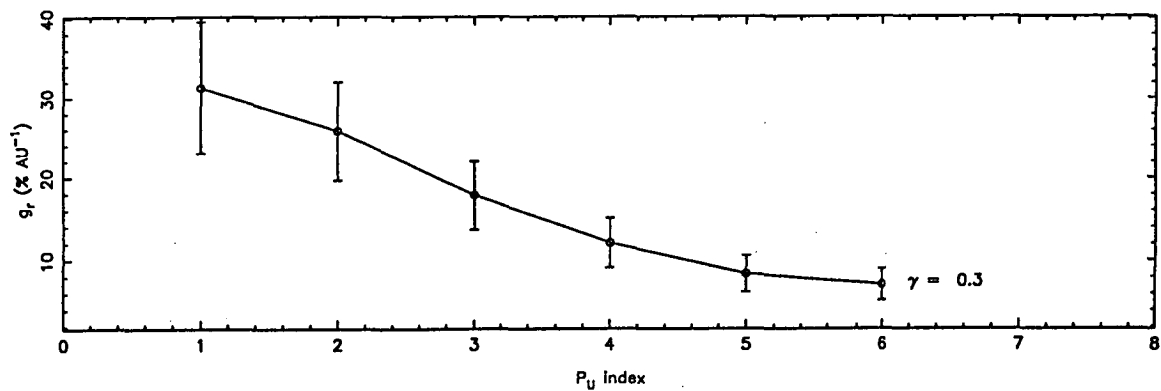
This appendix contains plots of g_r vs P_U index for various γ values, calculated using "method 2" described in Chapter 8. See Table 8.3 for P_U values in GV corresponding to the indices used in these plots. The radial gradient shown is applicable to 10 GV rigidity particles. Values for other rigidities can be found by using the relationship between g_r and rigidity given in equation 8.25b. The plots cover the years 1975-78 and 1982-85. Data have *not* been corrected for any (possible) isotropic intensity wave contamination.

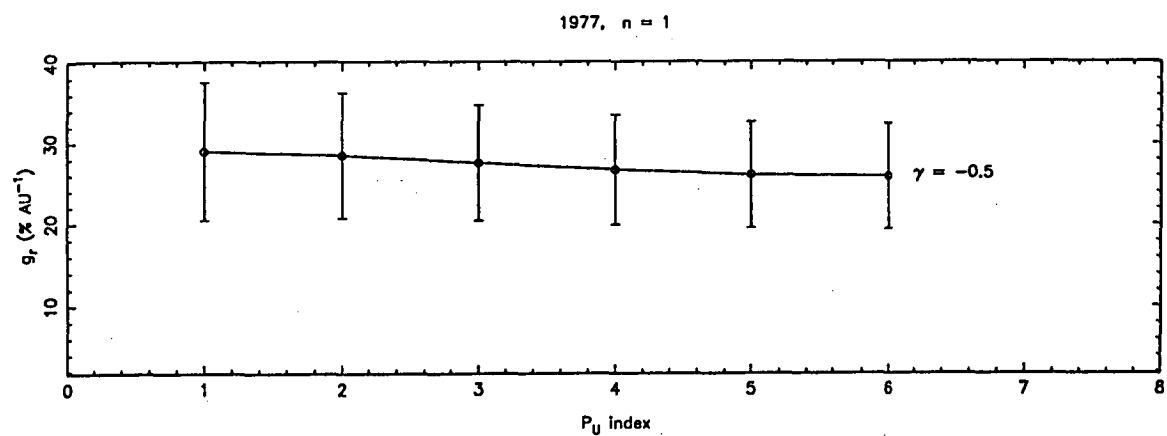
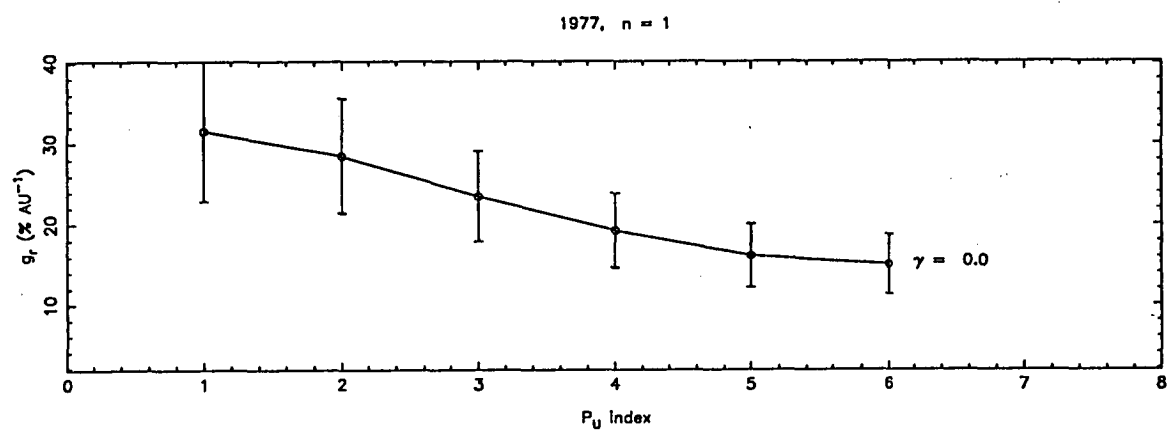
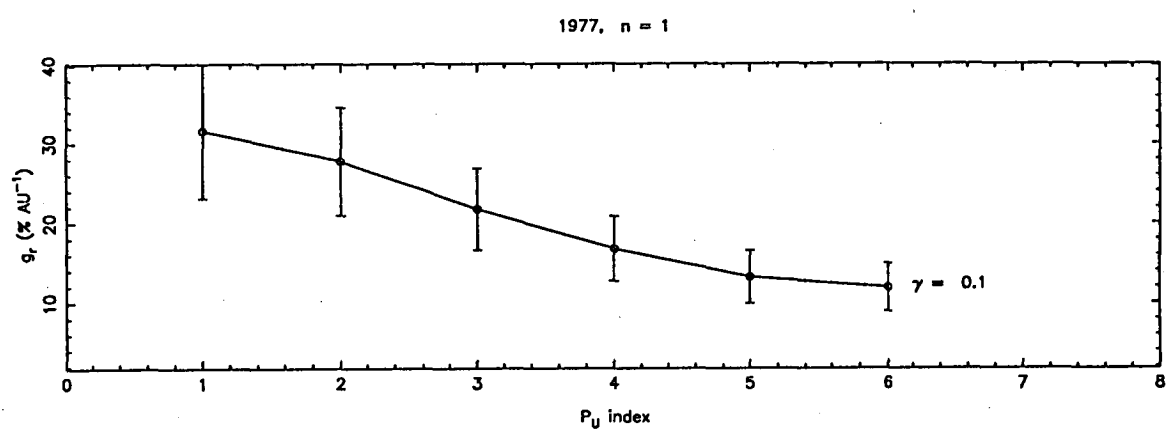
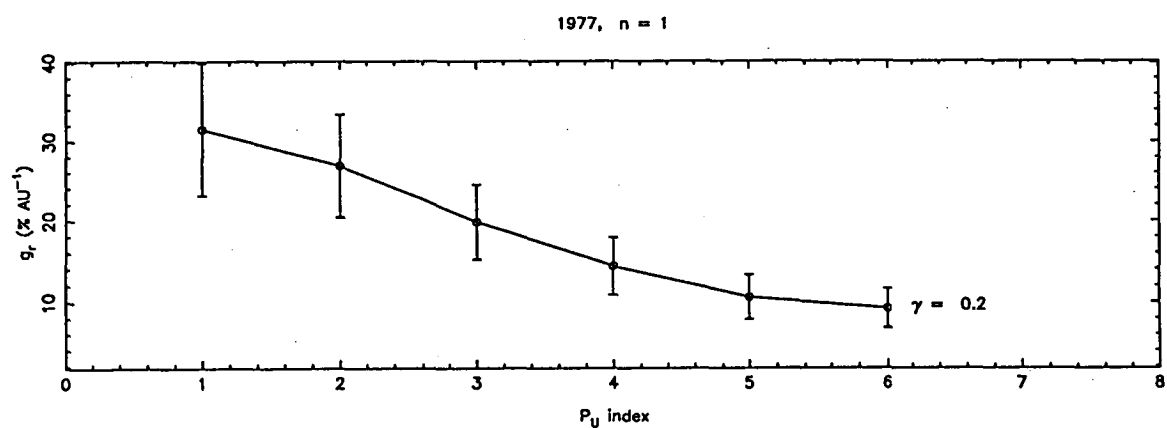
1975, $n = 1$ 1975, $n = 1$ 1975, $n = 1$ 1975, $n = 1$ 

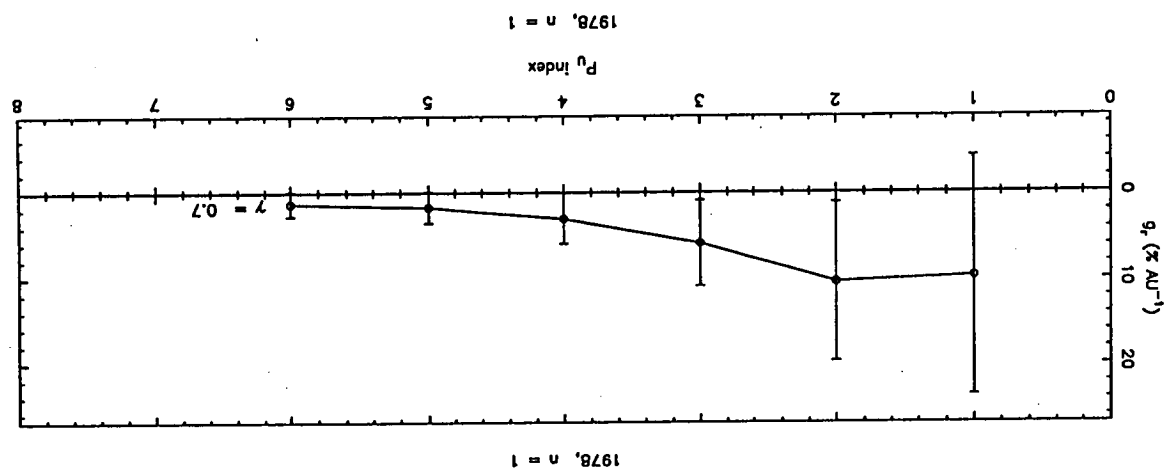
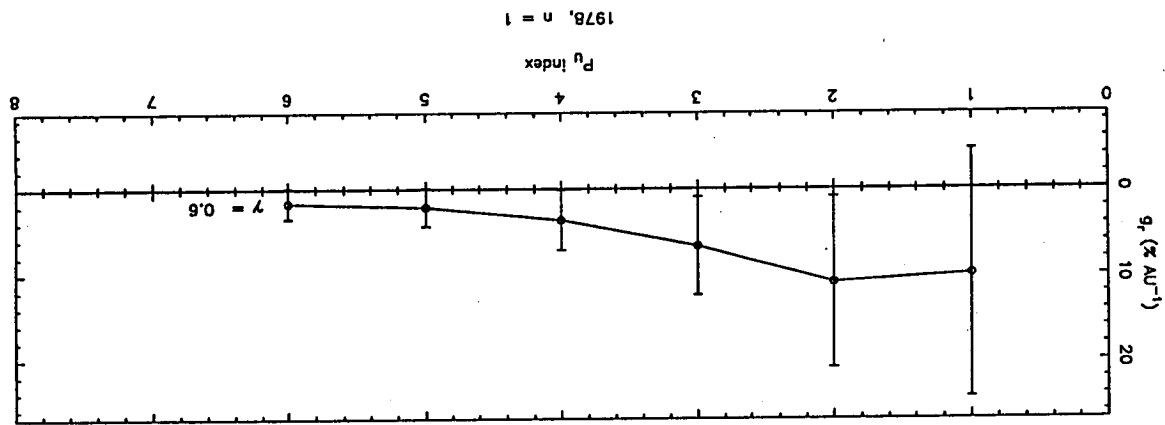
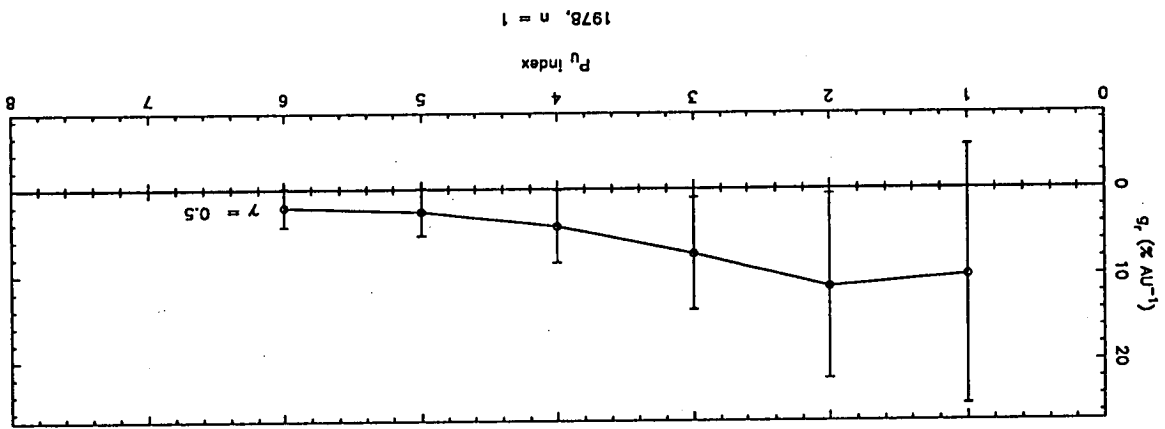
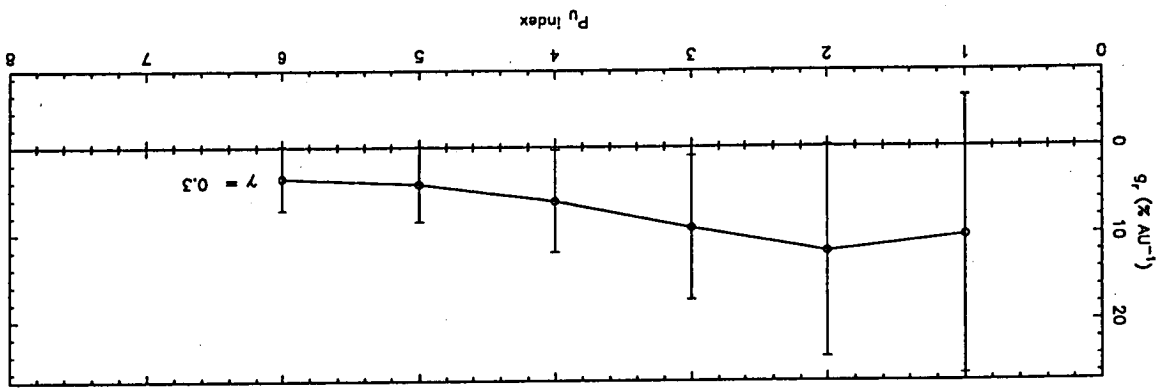


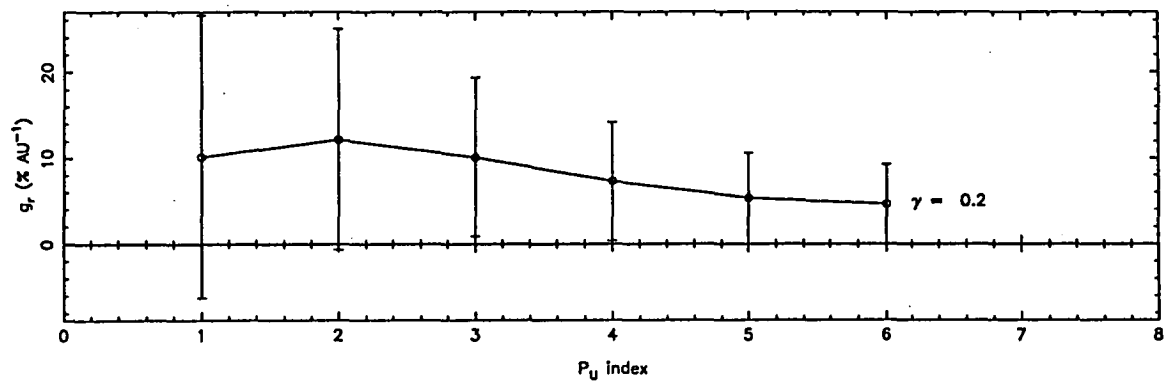
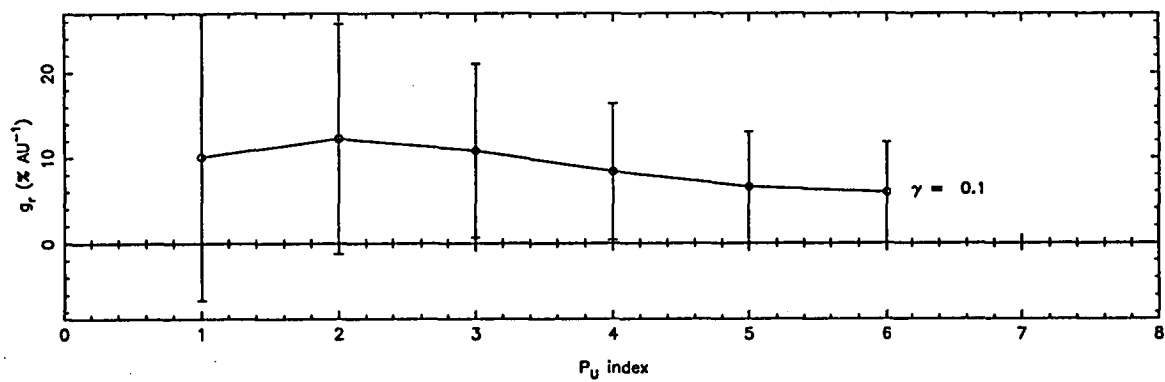
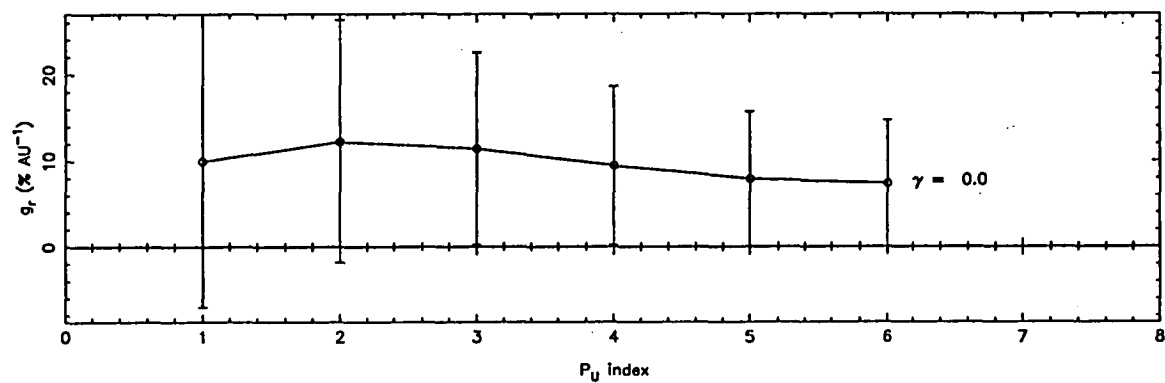
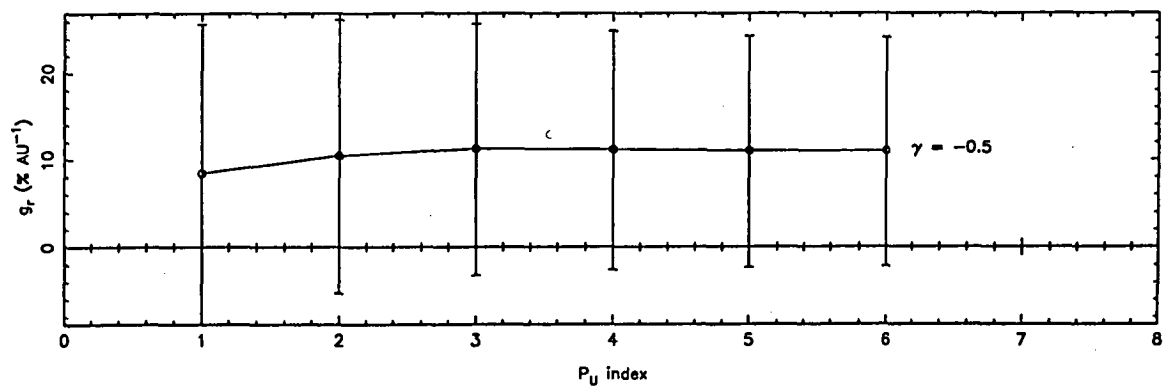
1976, $n = 1$ 1976, $n = 1$ 1976, $n = 1$ 1976, $n = 1$ 

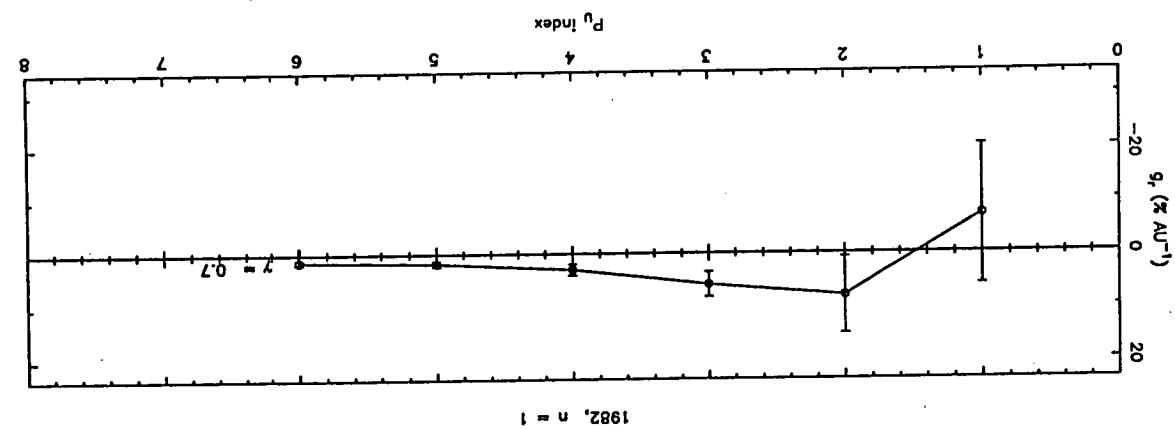
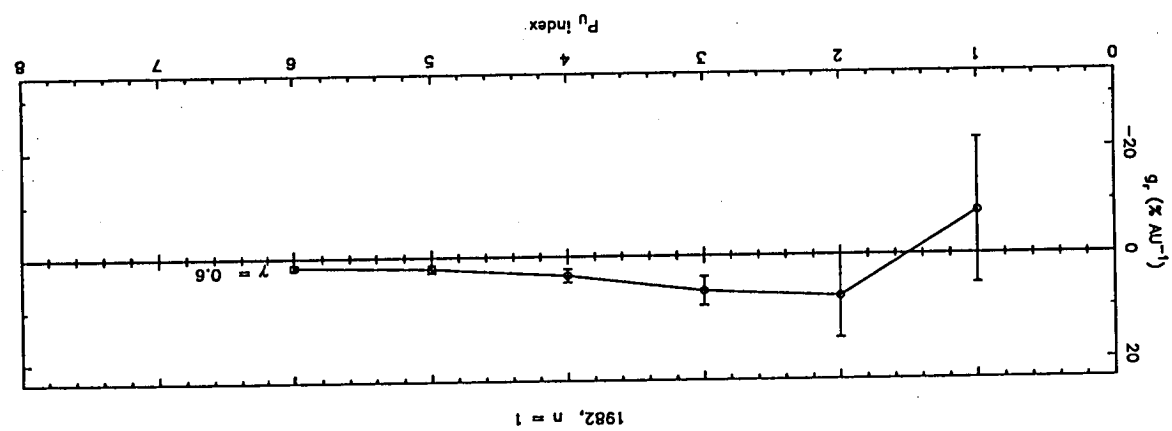
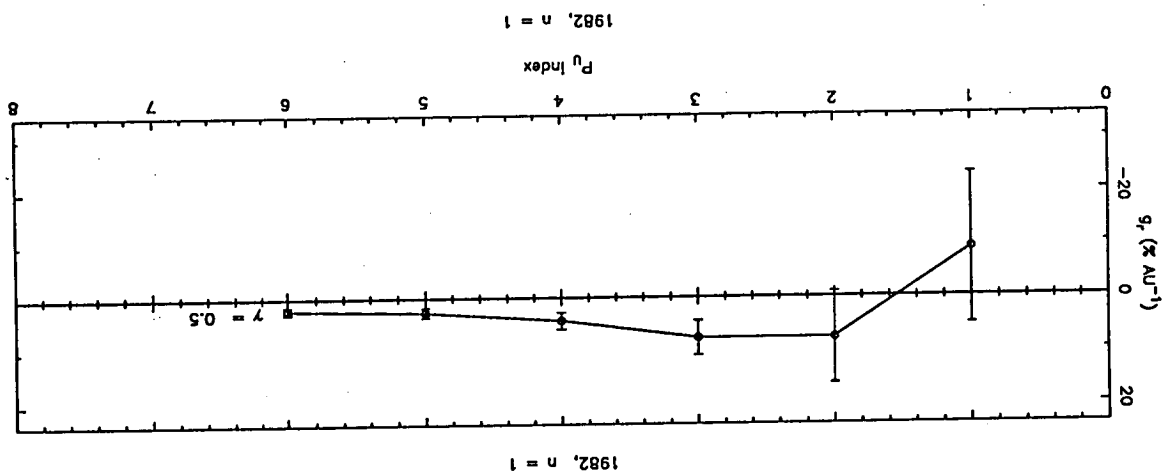
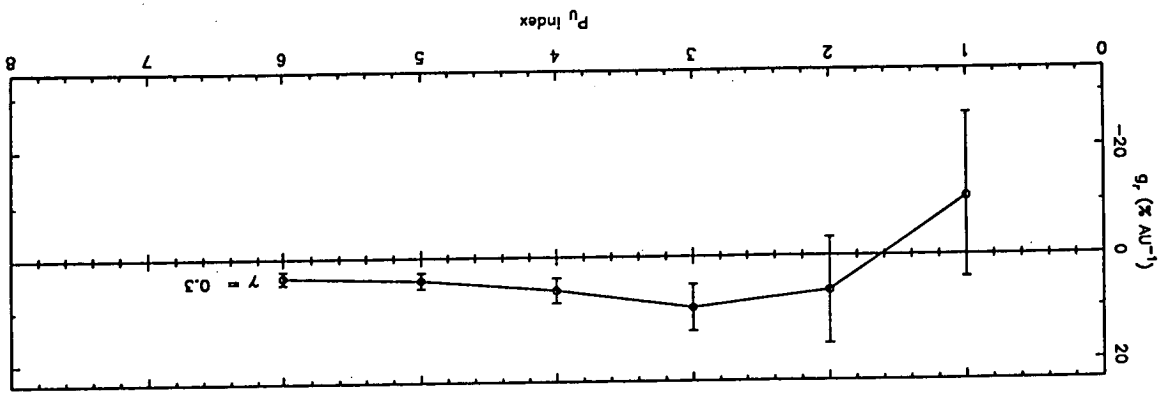
1976, $n = 1$ 1976, $n = 1$ 1976, $n = 1$ 1976, $n = 1$ 

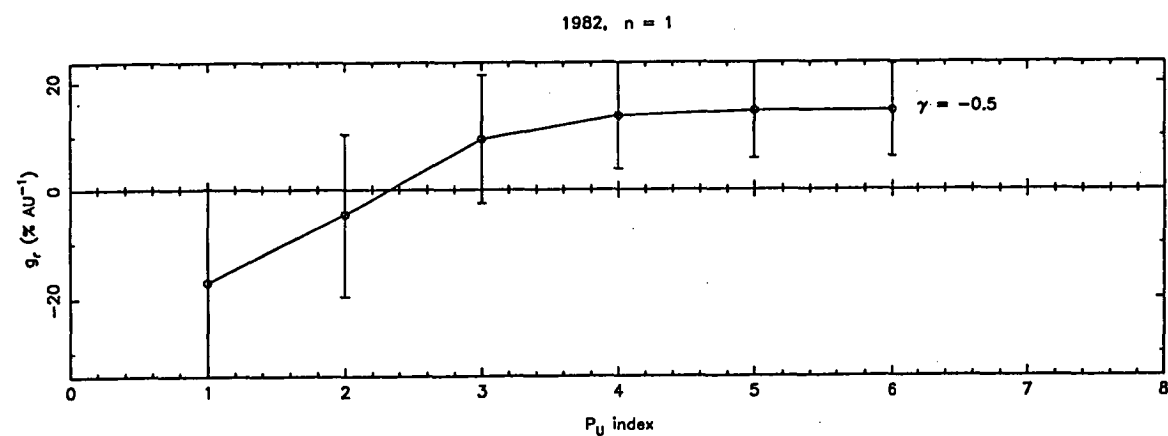
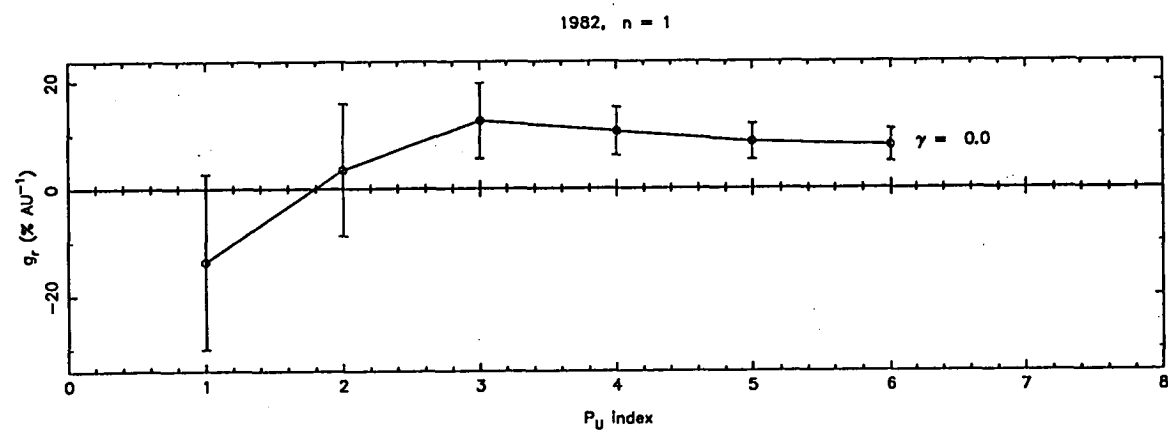
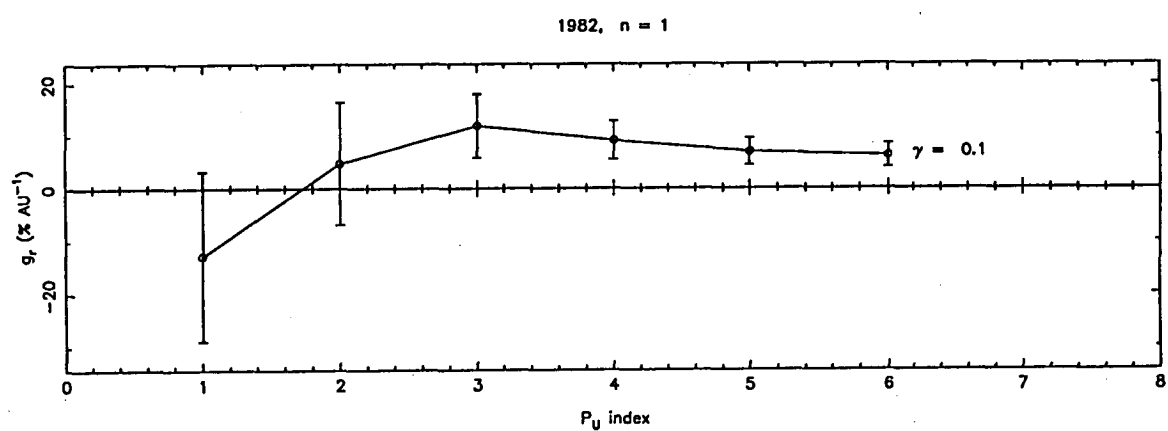
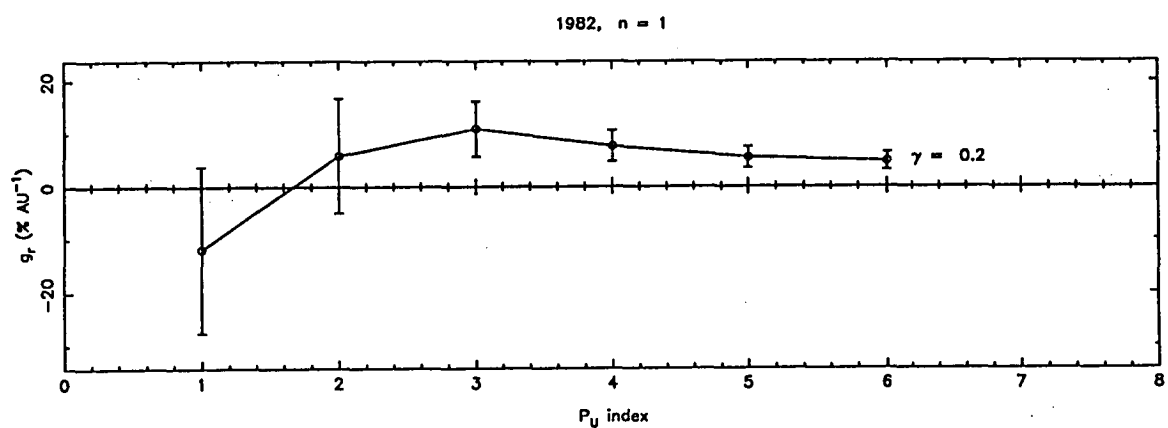
1977, $n = 1$ 1977, $n = 1$ 1977, $n = 1$ 1977, $n = 1$ 

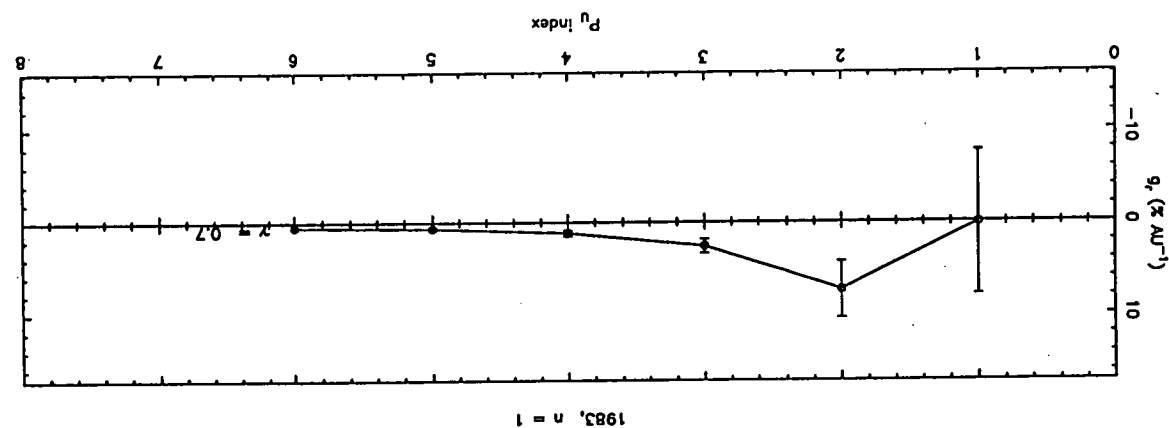
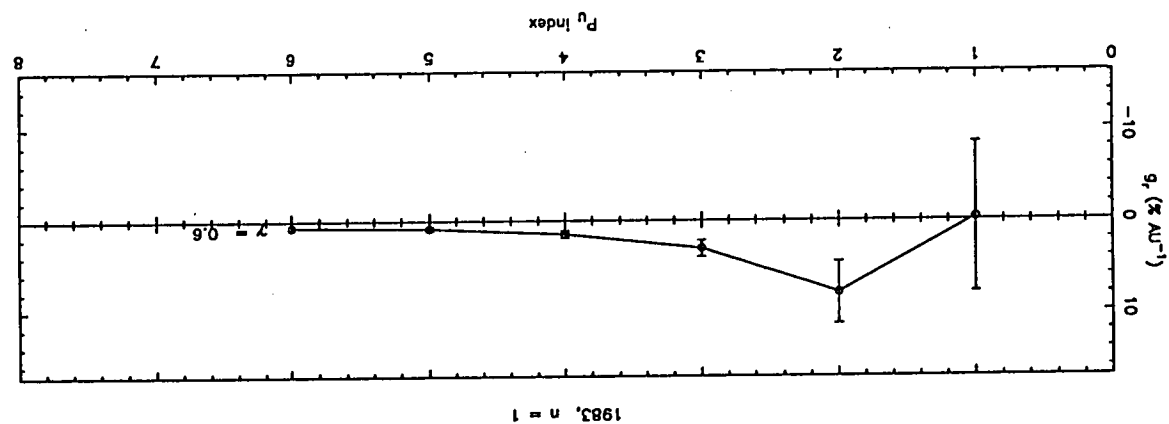
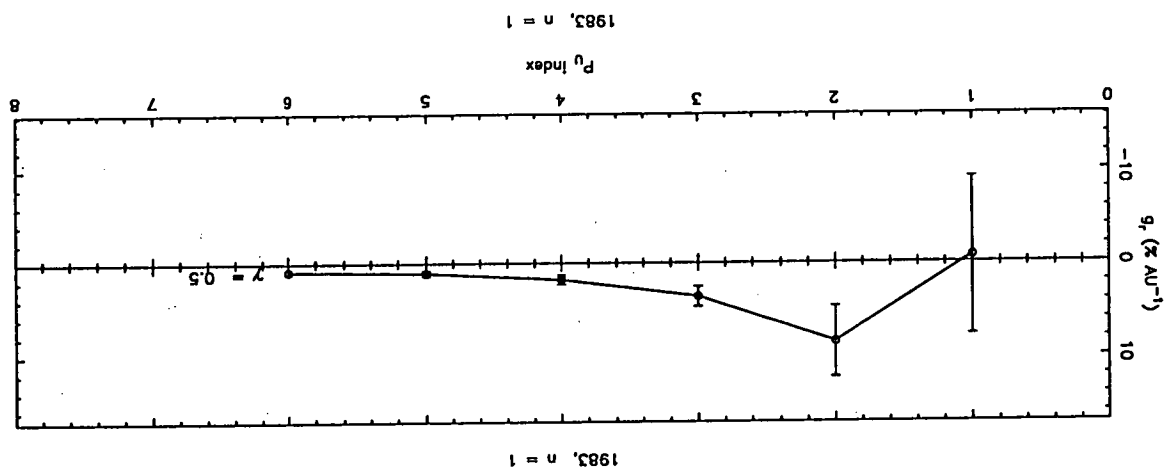
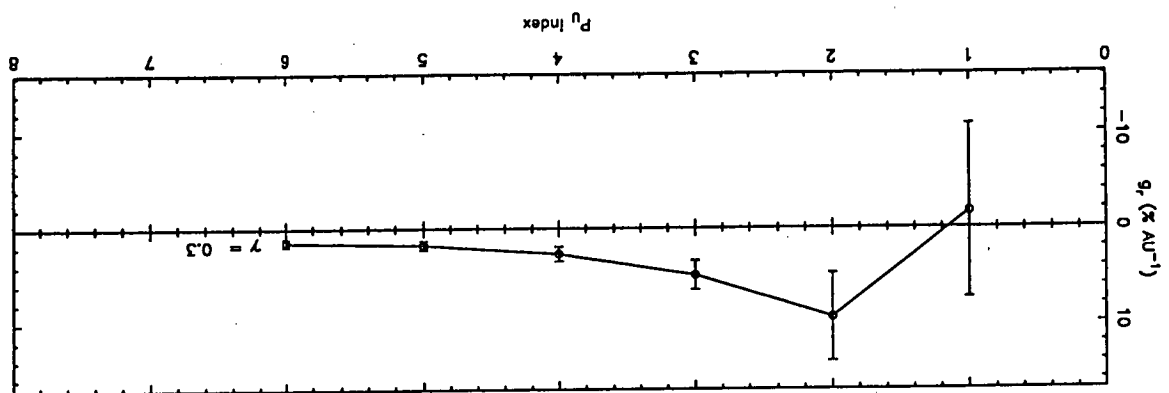


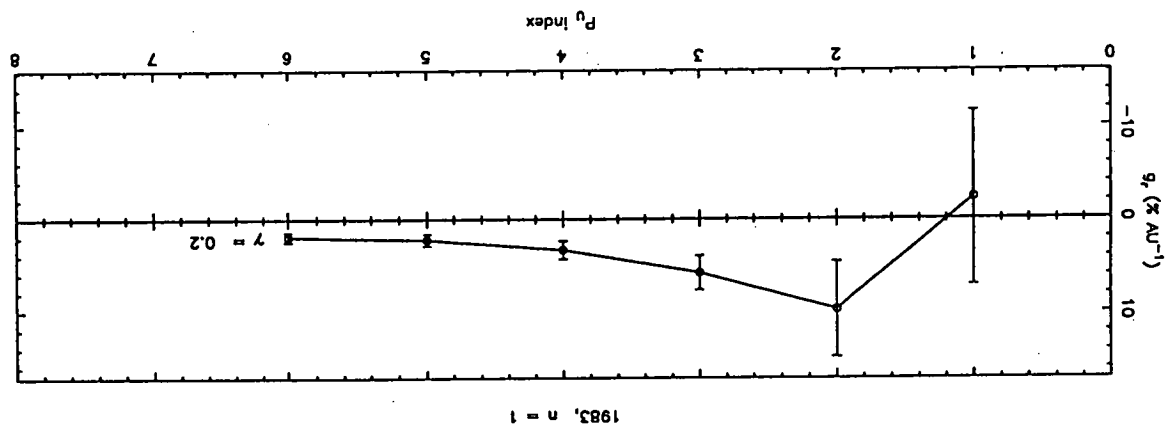
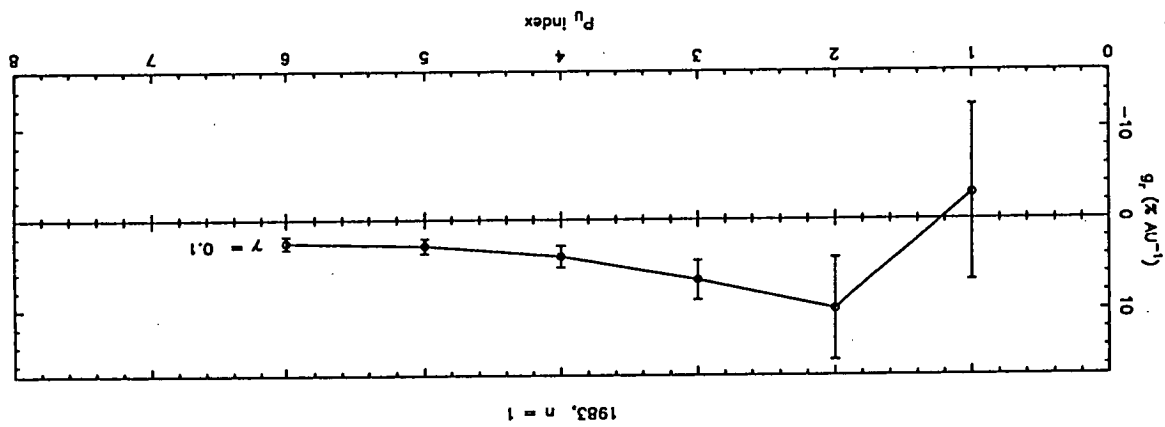
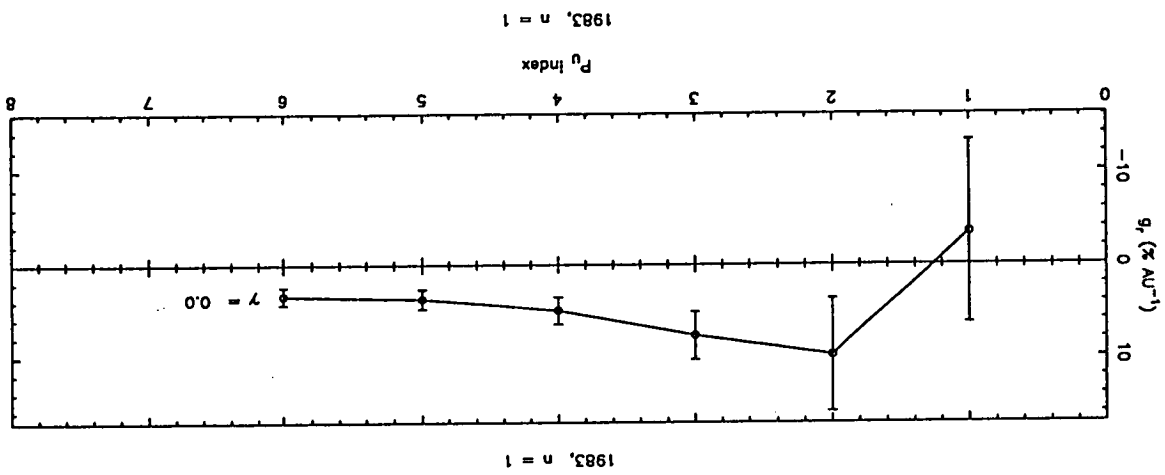
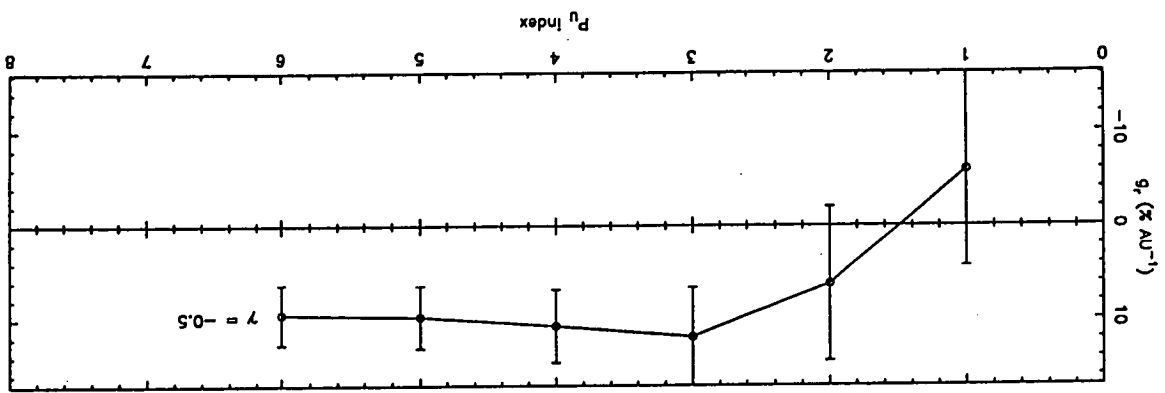


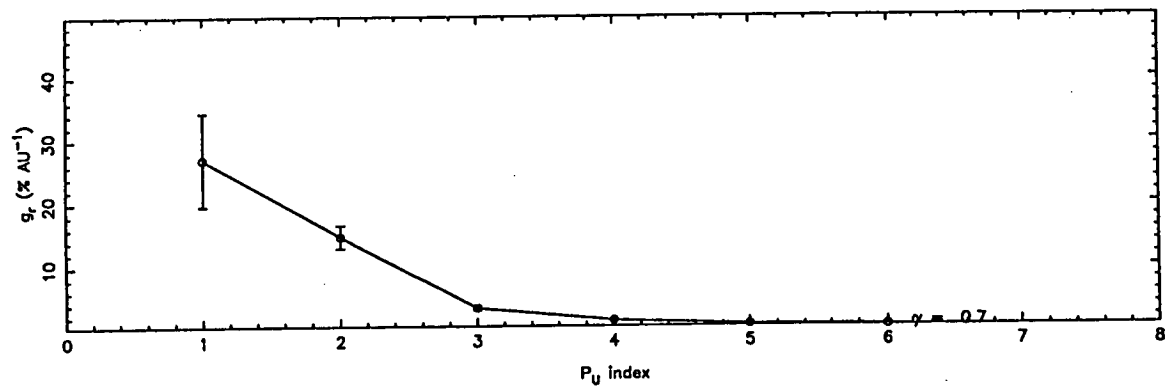
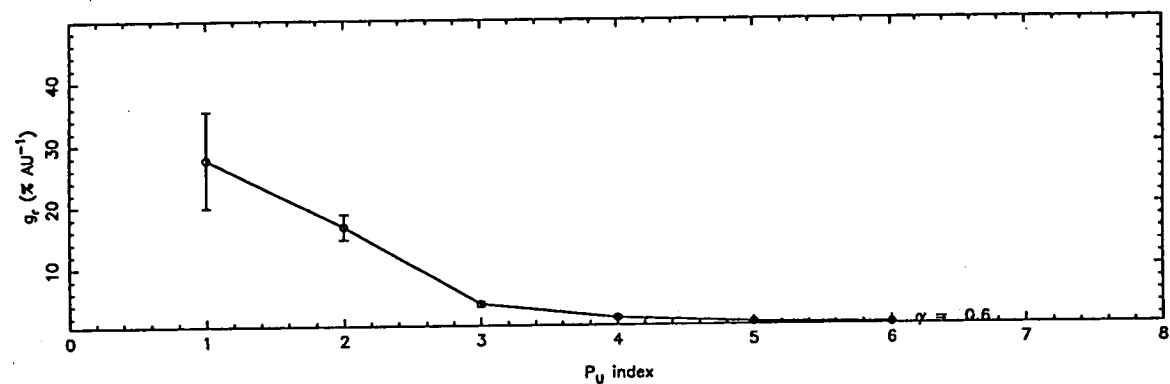
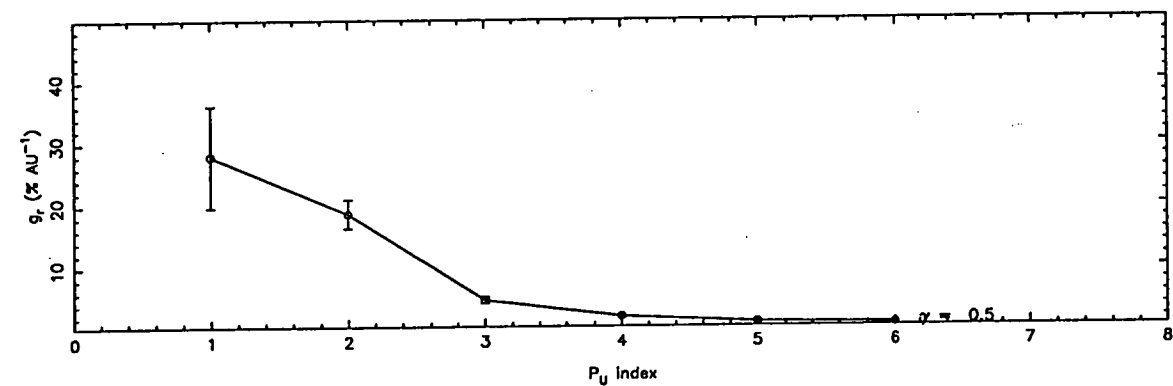
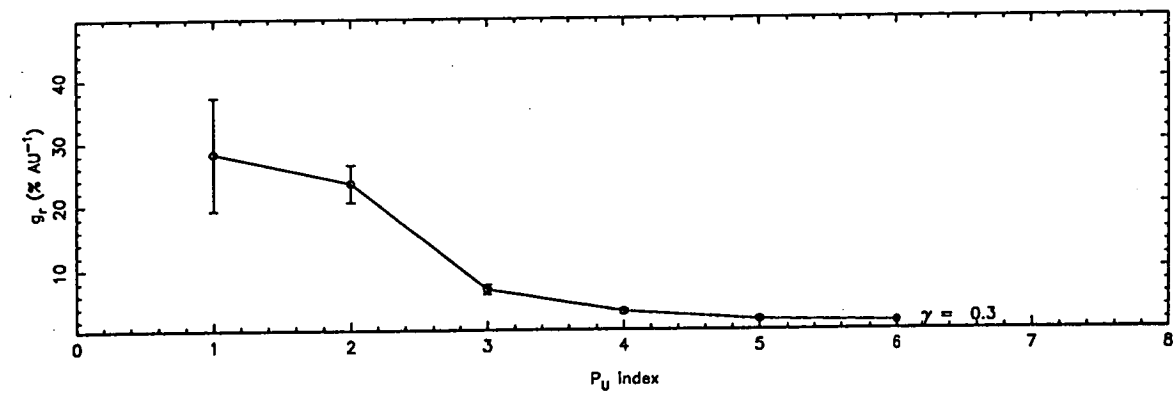
1978, $n = 1$ 1978, $n = 1$ 1978, $n = 1$ 1978, $n = 1$ 

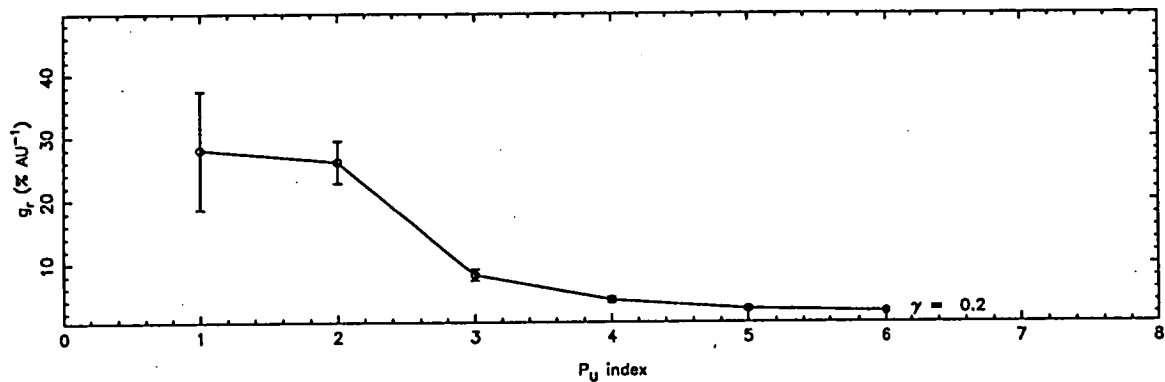
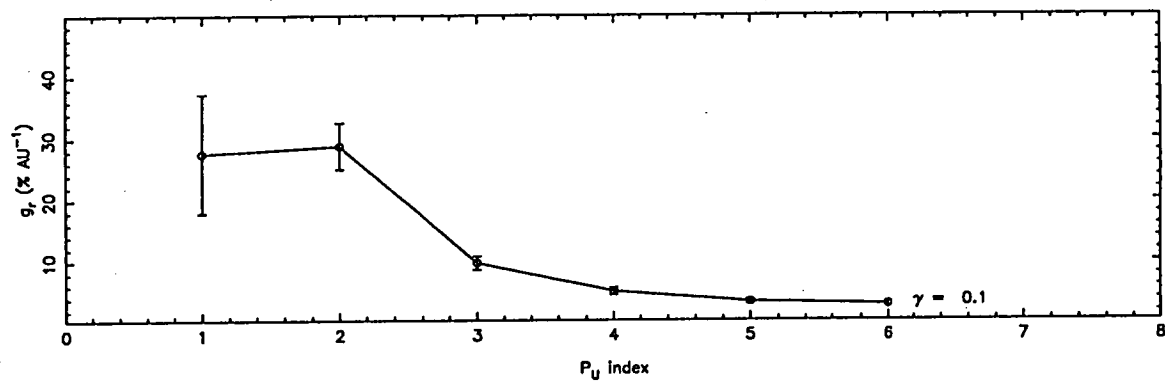
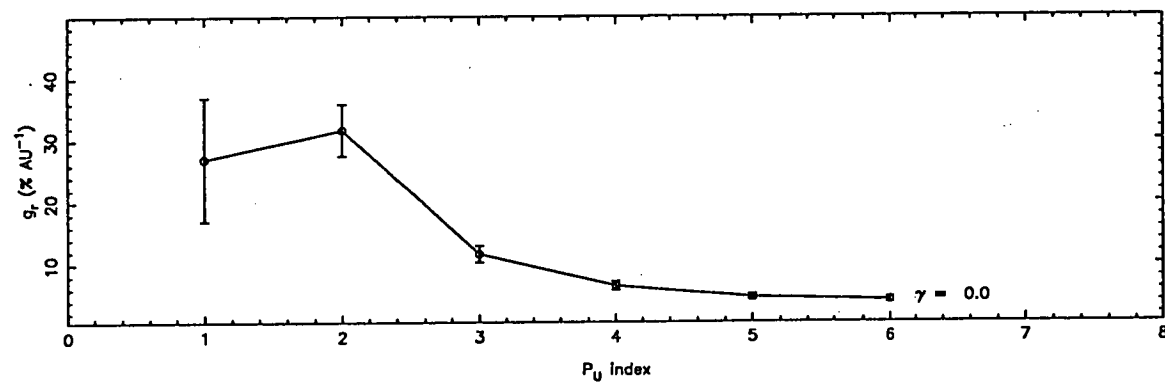
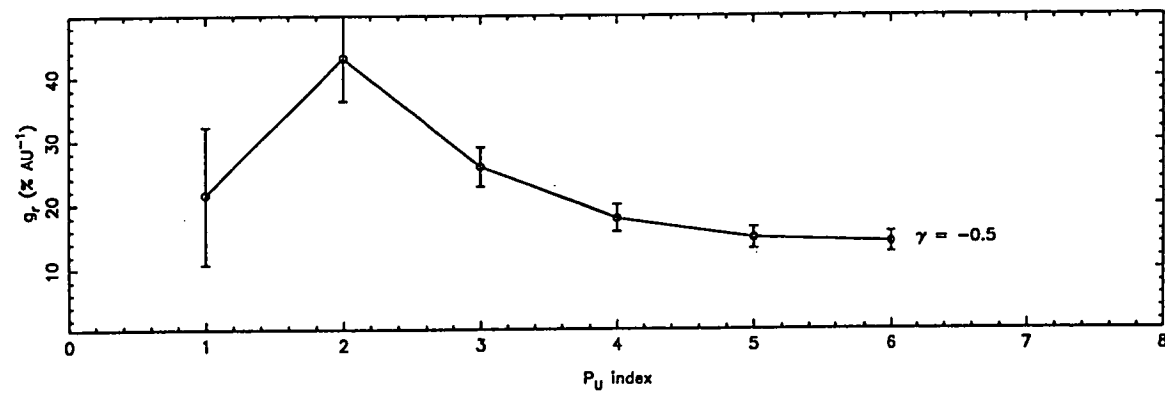


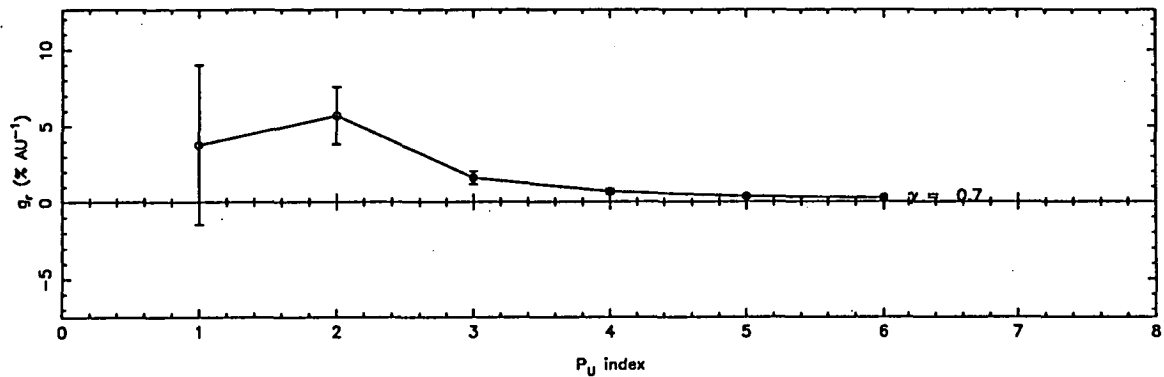
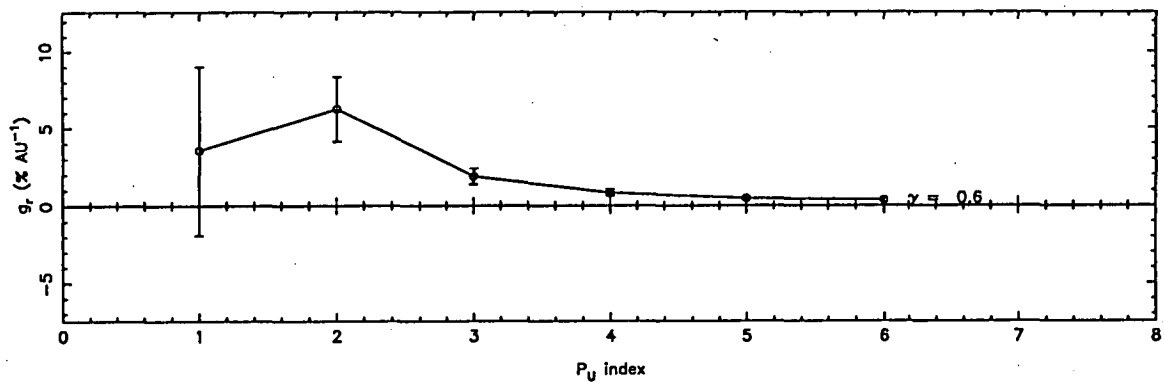
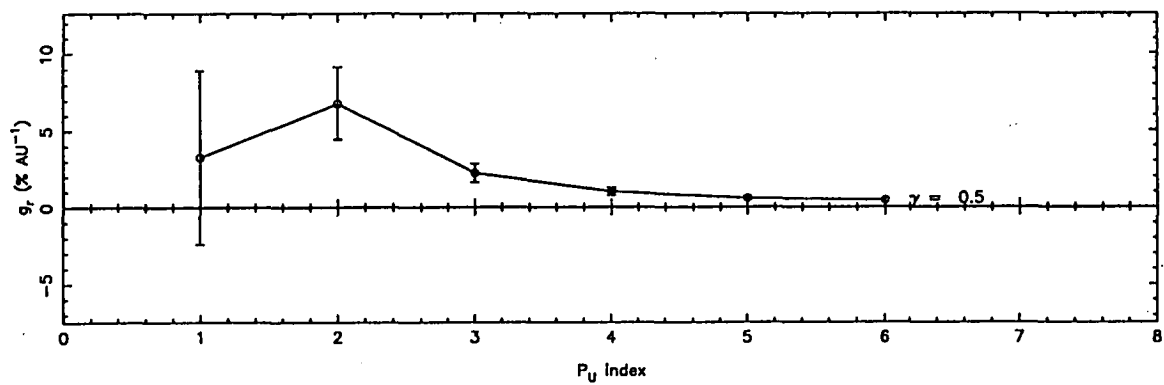
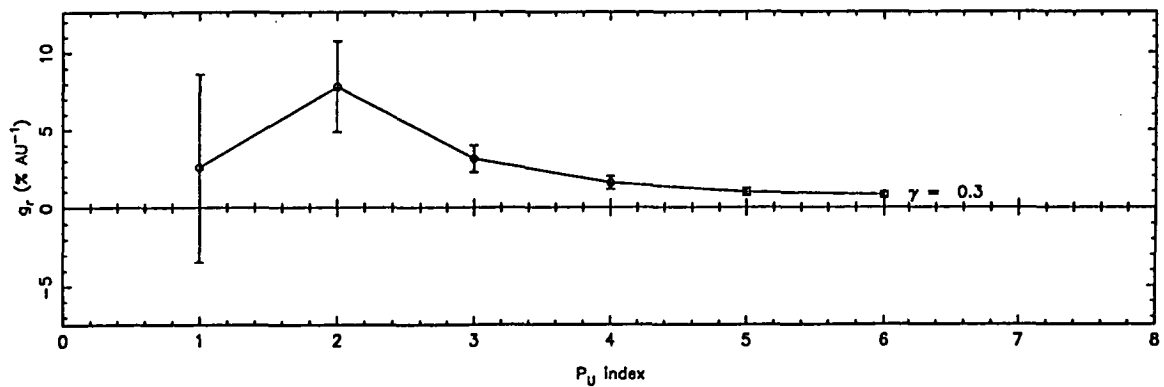


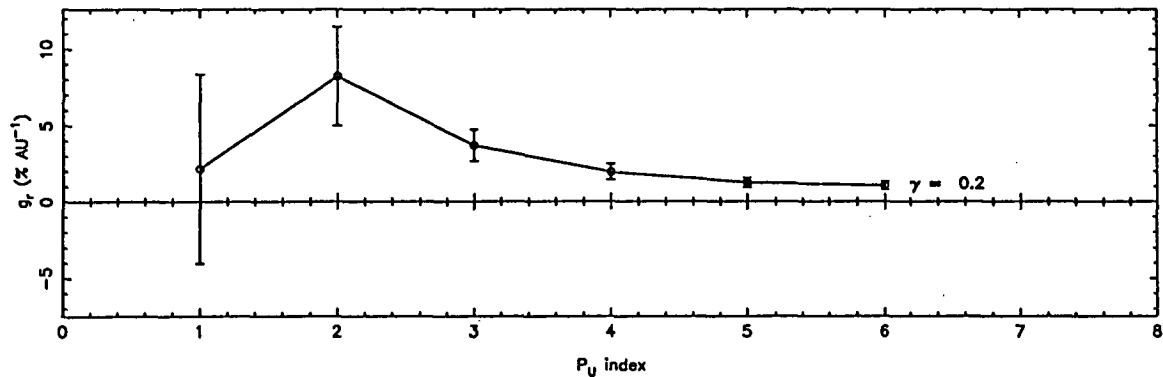
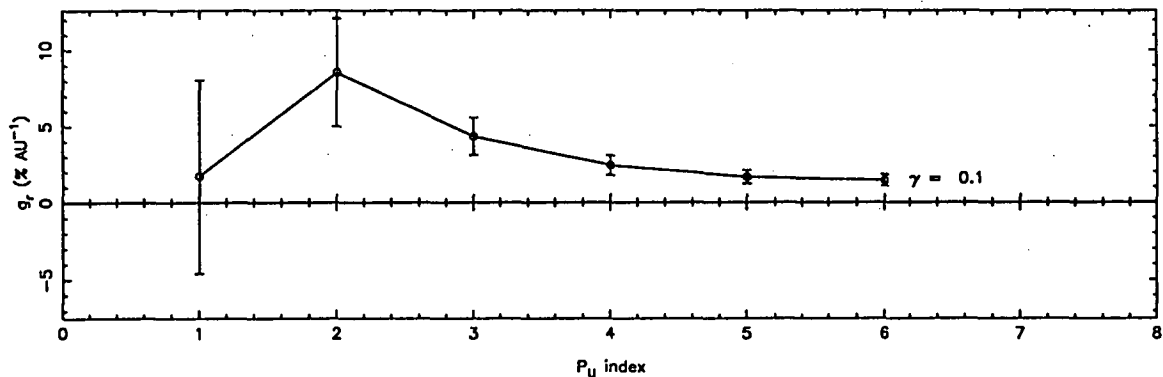
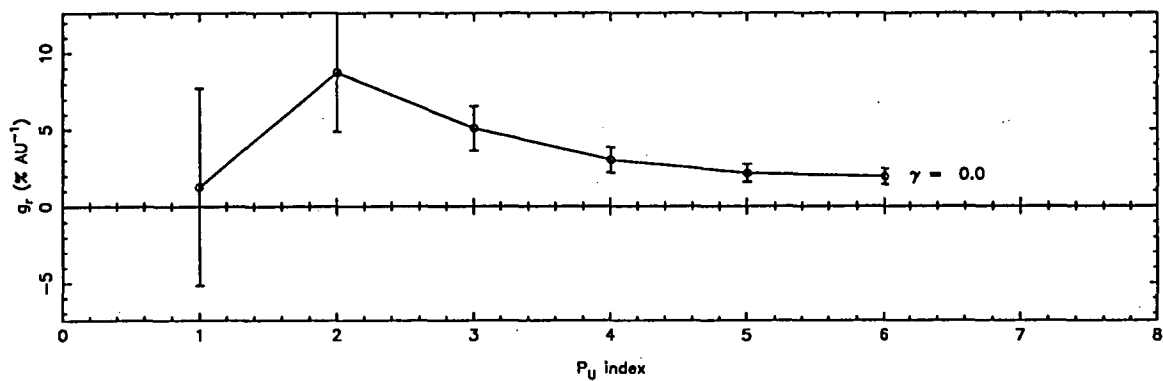
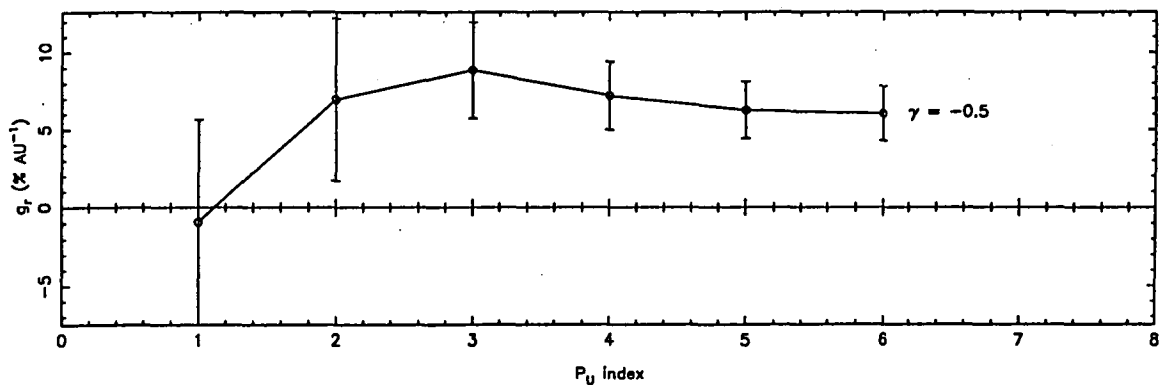




1984, $n = 1$ 1984, $n = 1$ 1984, $n = 1$ 1984, $n = 1$ 

1984, $n = 1$ 1984, $n = 1$ 1984, $n = 1$ 1984, $n = 1$ 

1985, $n = 1$ 1985, $n = 1$ 1985, $n = 1$ 1985, $n = 1$ 

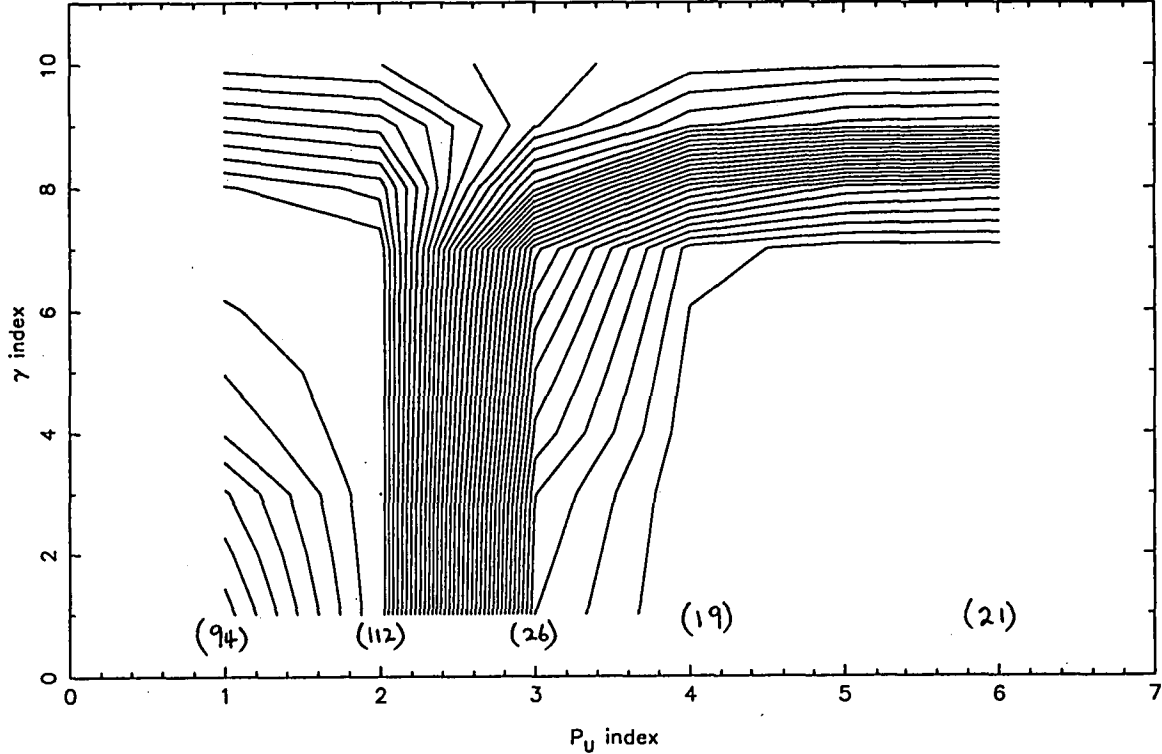
1985, $n = 1$ 1985, $n = 1$ 1985, $n = 1$ 1985, $n = 1$ 

APPENDIX 9

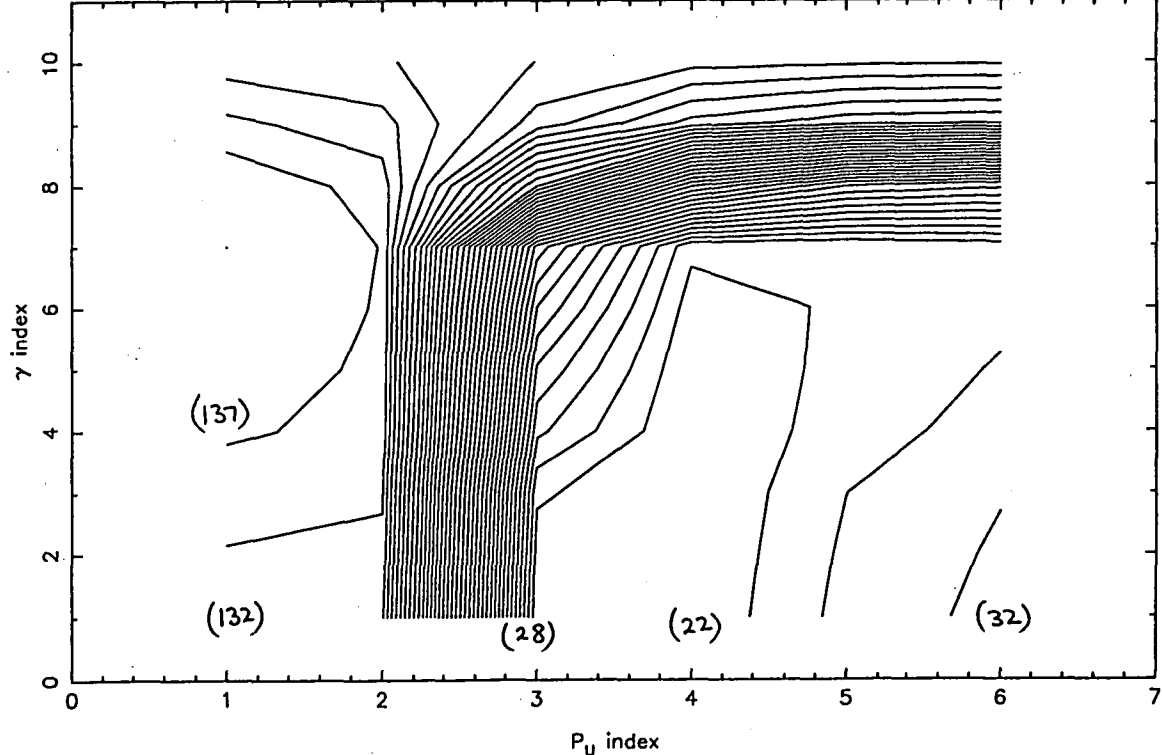
NORTH/SOUTH ANISOTROPY ANALYSIS. CONTOURS OF χ^2 FOR RESULTS USING METHOD 1.

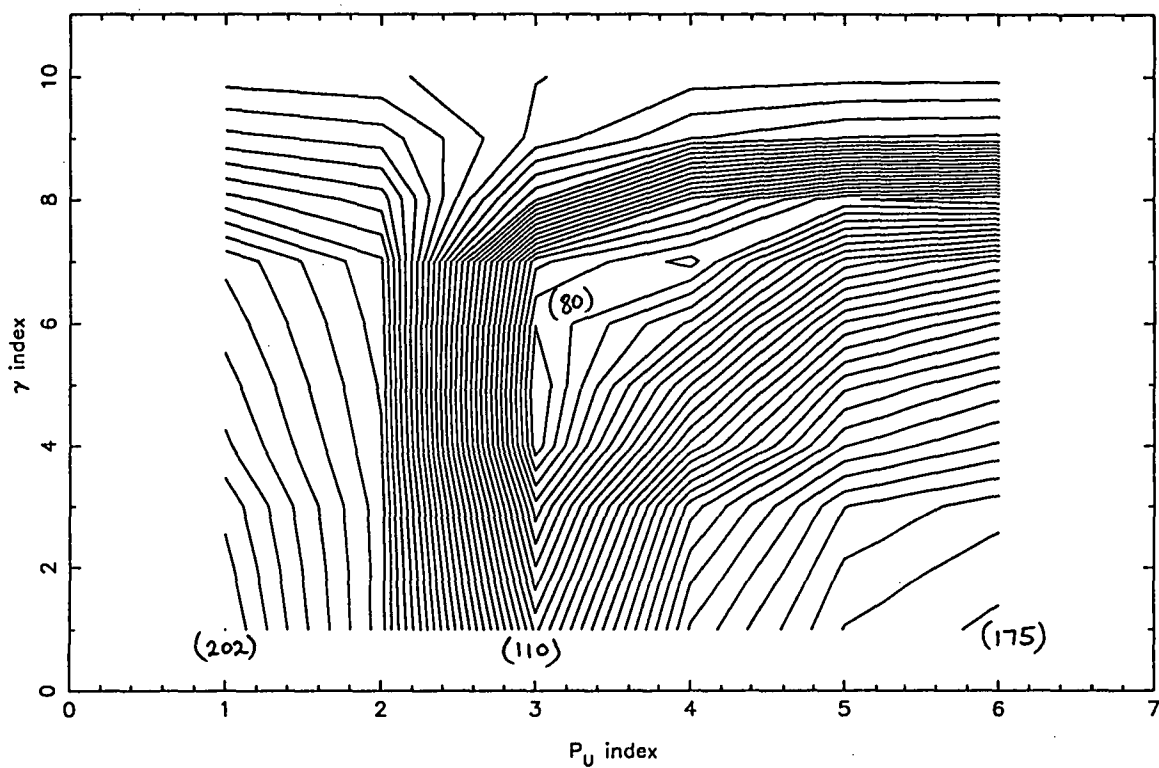
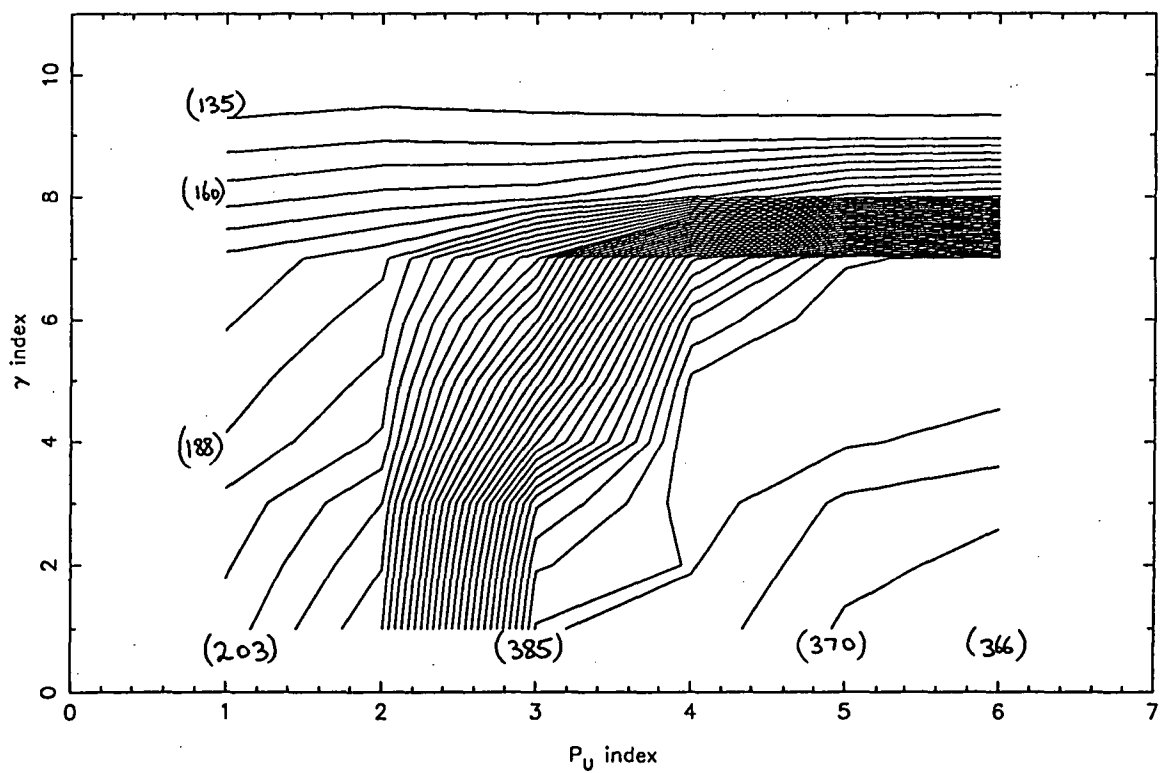
This appendix contains contours of χ^2 over (γ, P_U) index pairs for the results of the fit for g_r using "method 1" described in Chapter 8. See Table 8.3 for P_U values in GV and γ values corresponding to the indices used in these plots. The plots cover the years 1975-78 and 1982-85. Data have *not* been corrected for any (possible) isotropic intensity wave contamination.

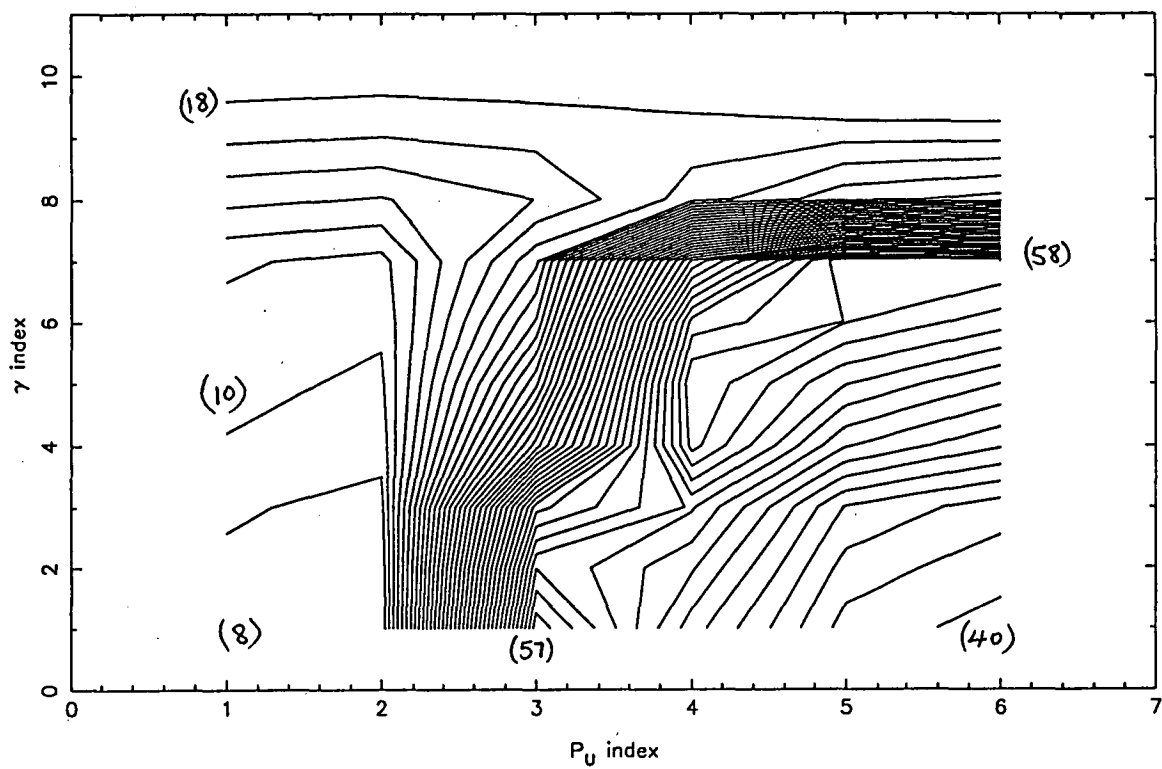
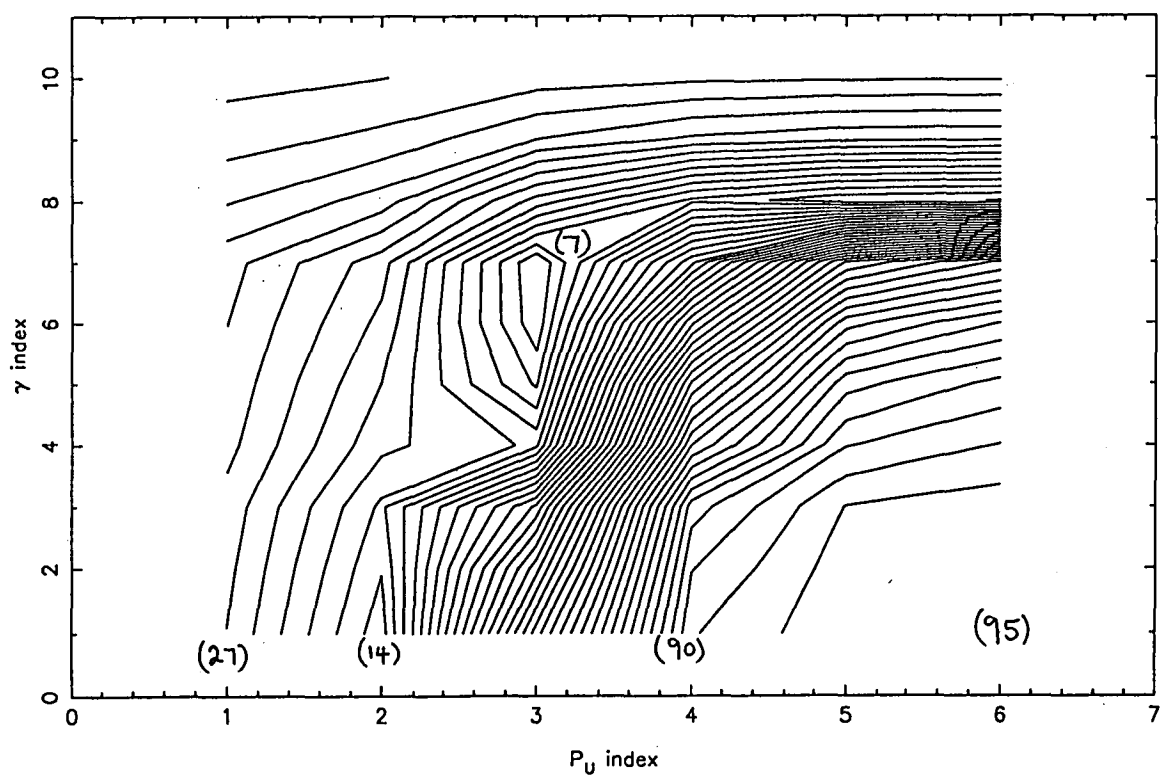
contour of χ^2 (toward sectors) : 1975 n = 2

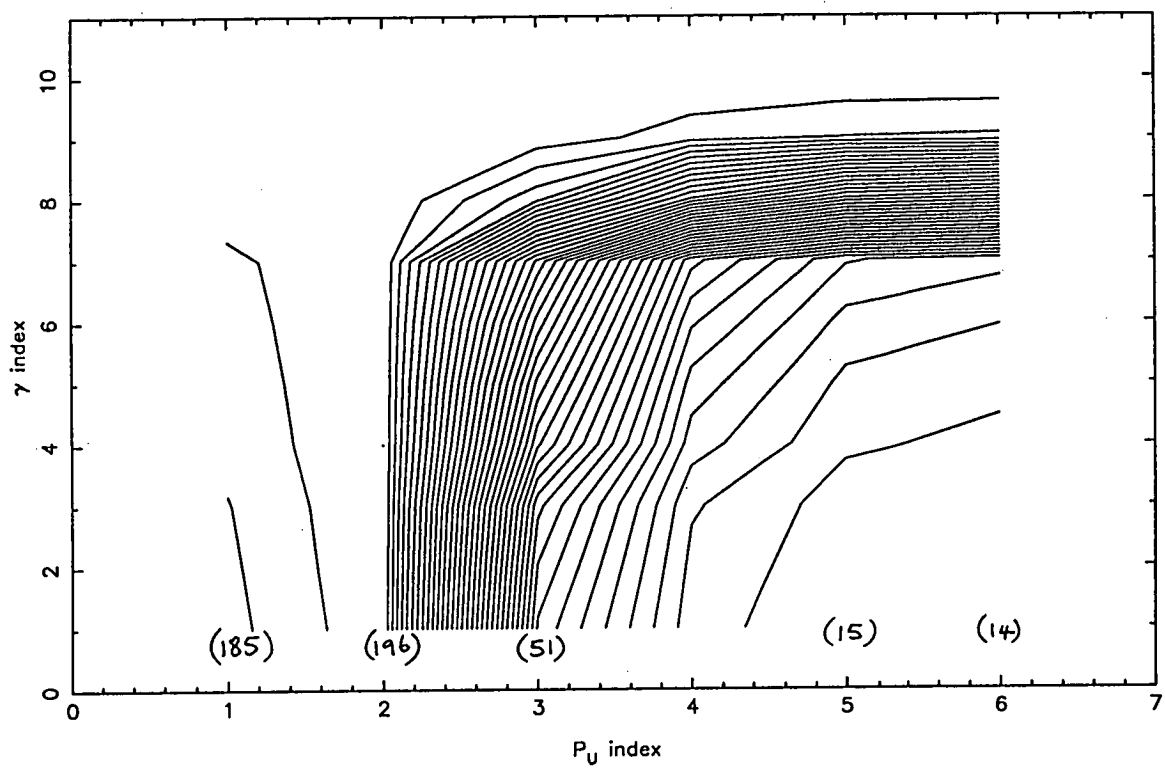
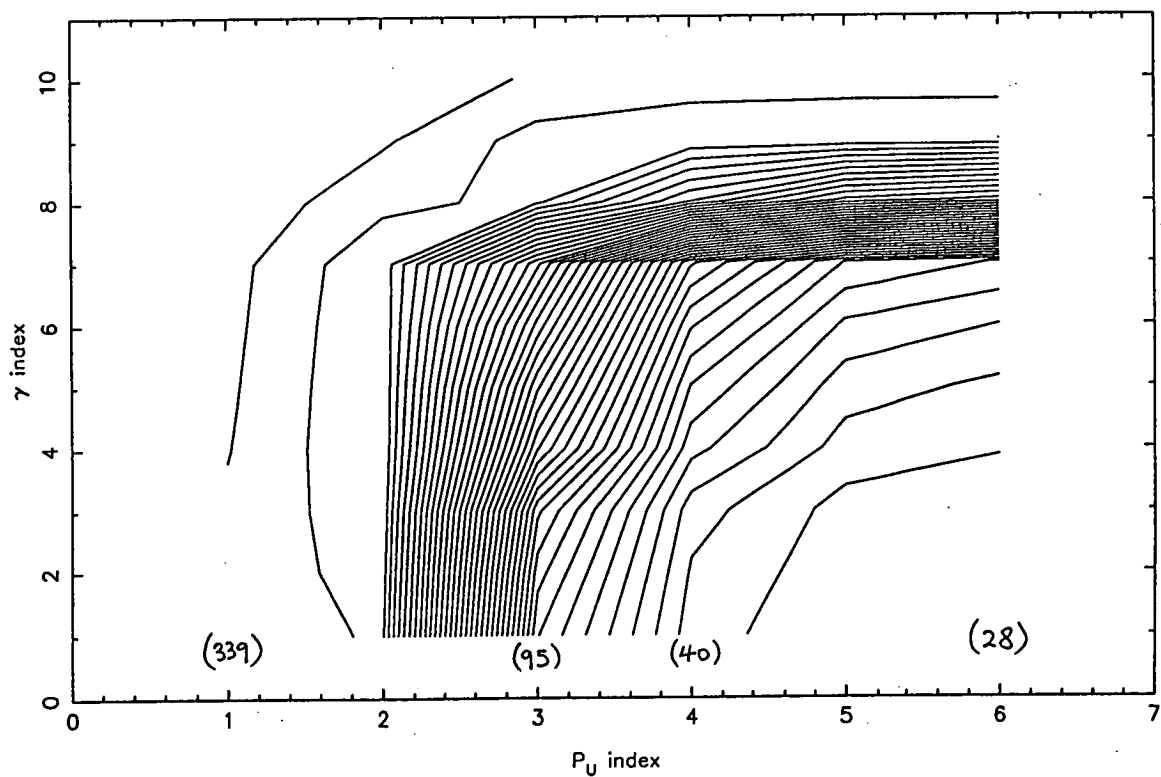


contour of χ^2 (toward sectors) : 1975 n = 1

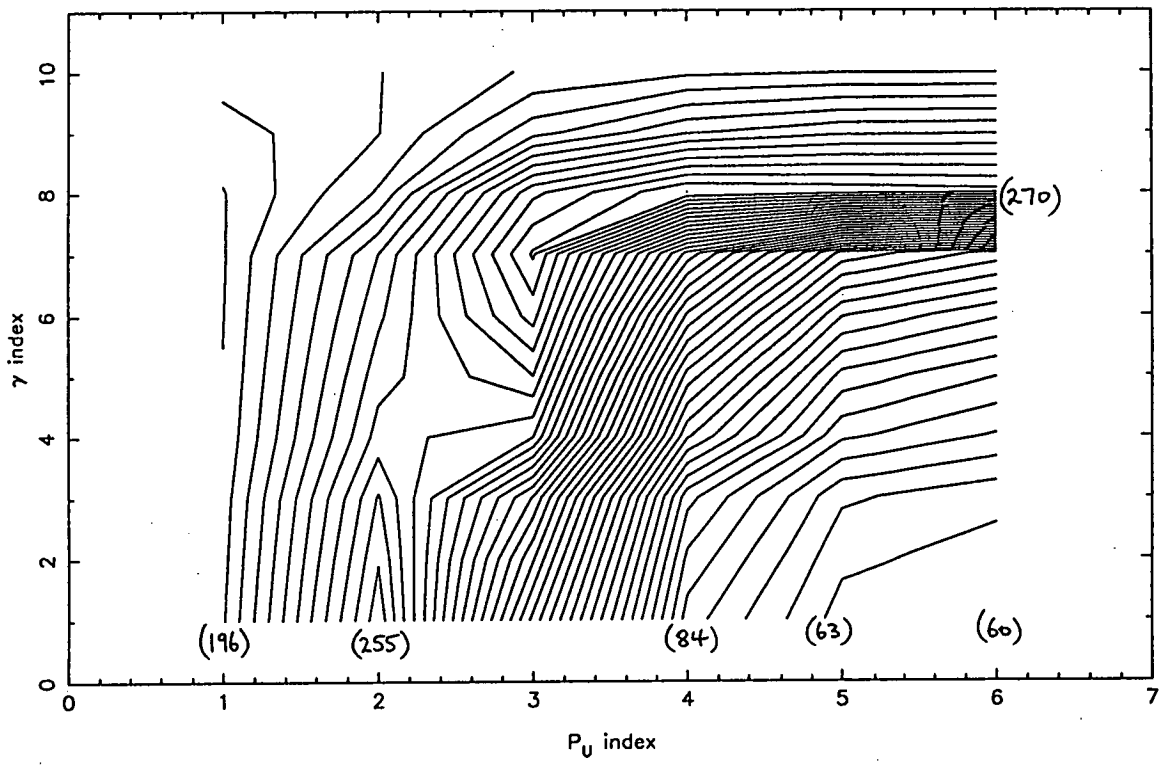


contour of χ^2 (toward sectors) : 1976 $n = 2$ contour of χ^2 (toward sectors) : 1976 $n = 1$ 

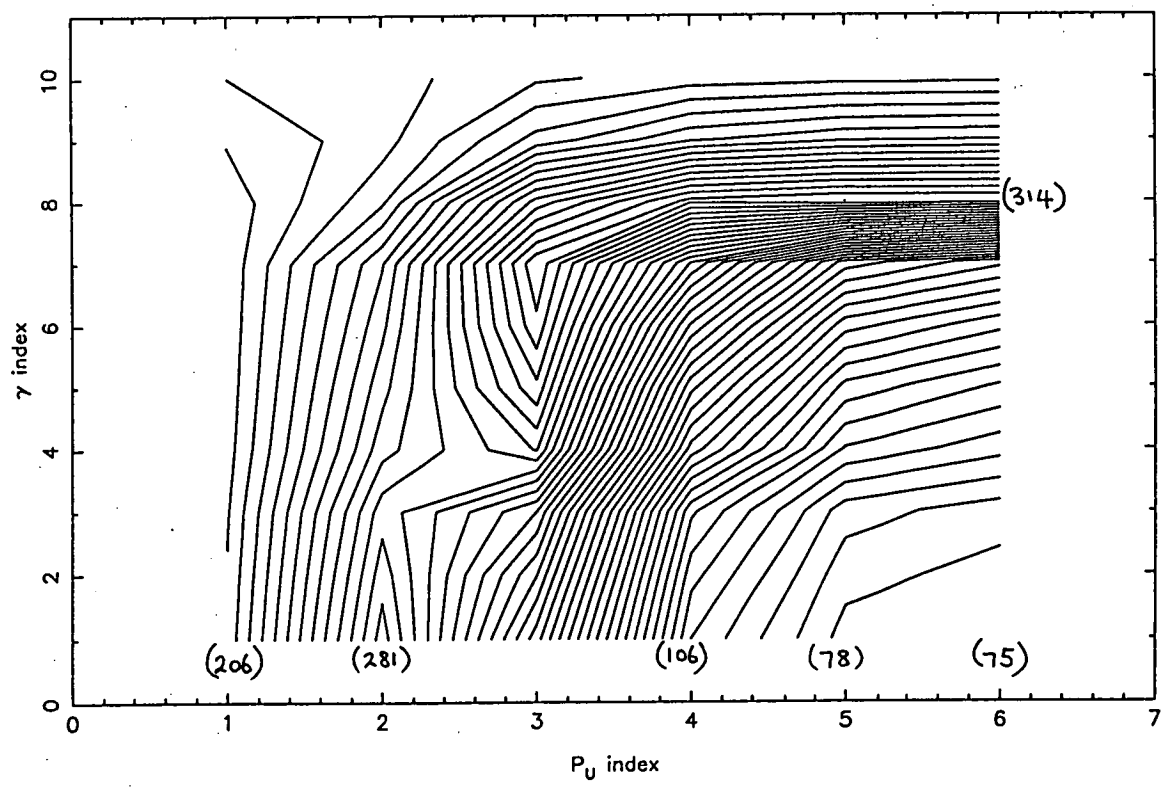
contour of χ^2 (toward sectors) : 1977 n = 2contour of χ^2 (toward sectors) : 1977 n = 1

contour of χ^2 (toward sectors) : 1978 n = 2contour of χ^2 (toward sectors) : 1978 n = 1

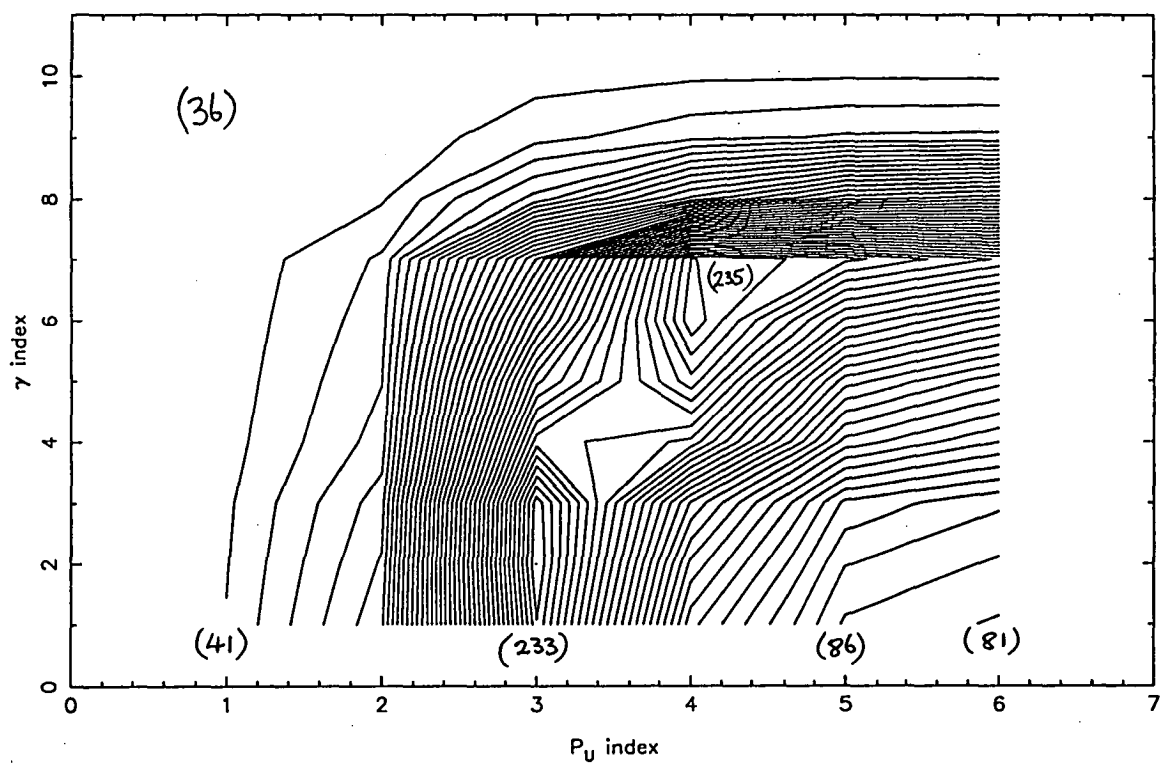
contour of χ^2 (toward sectors) : 1982 n = 2



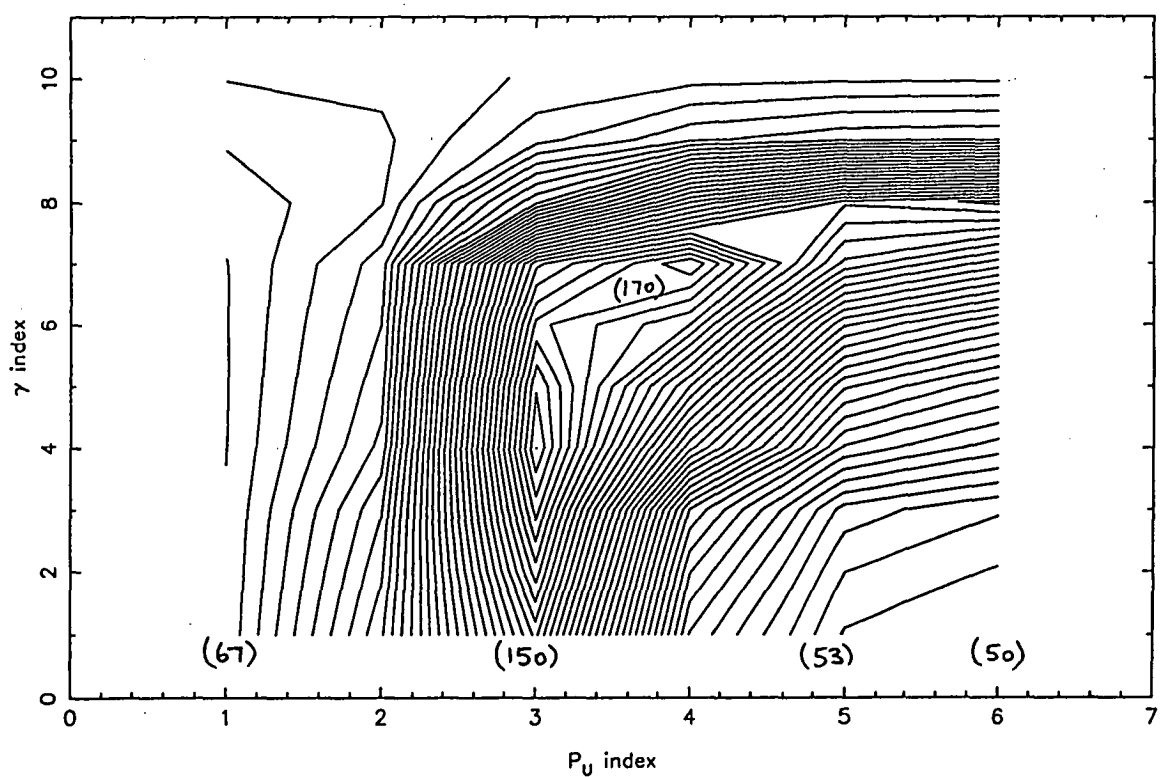
contour of χ^2 (toward sectors) : 1982 n = 1

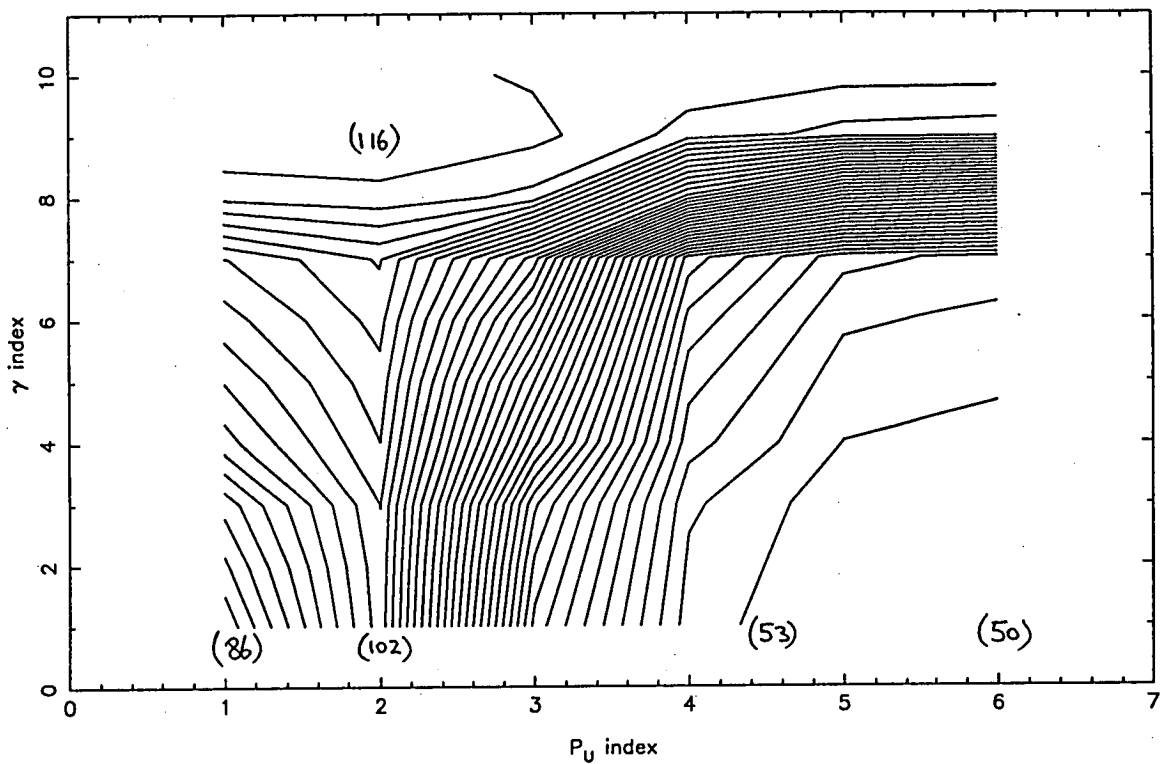
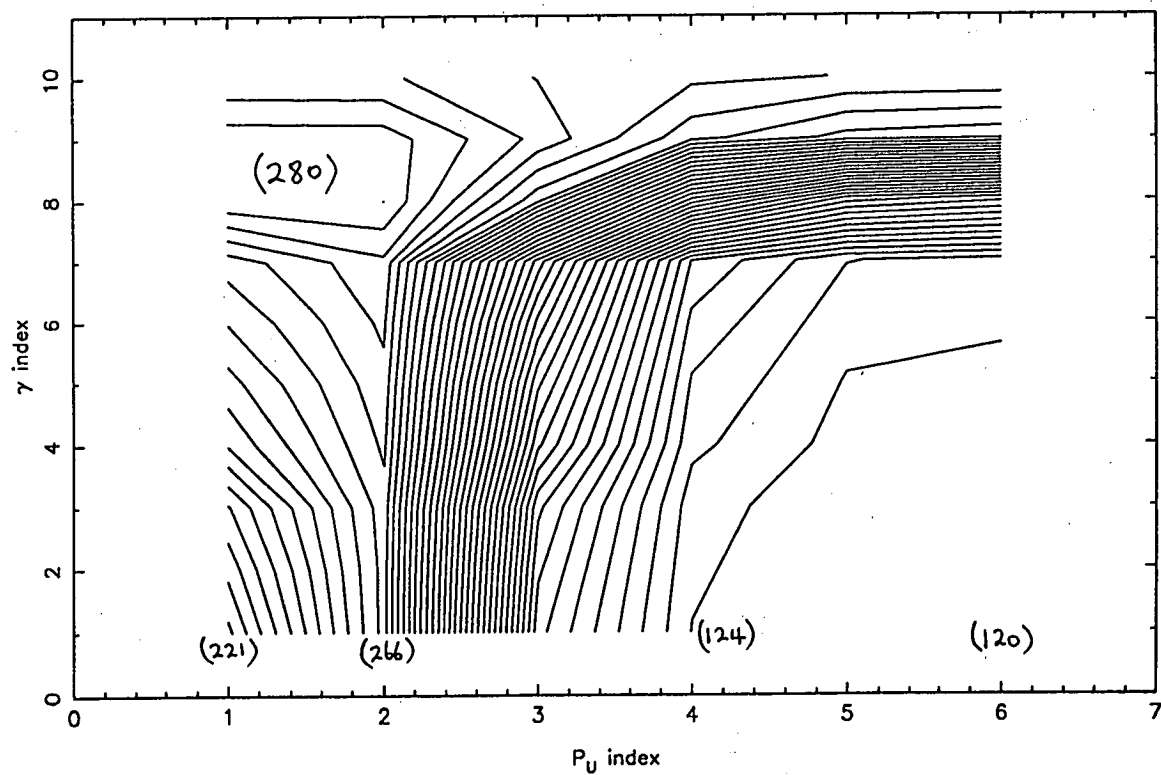


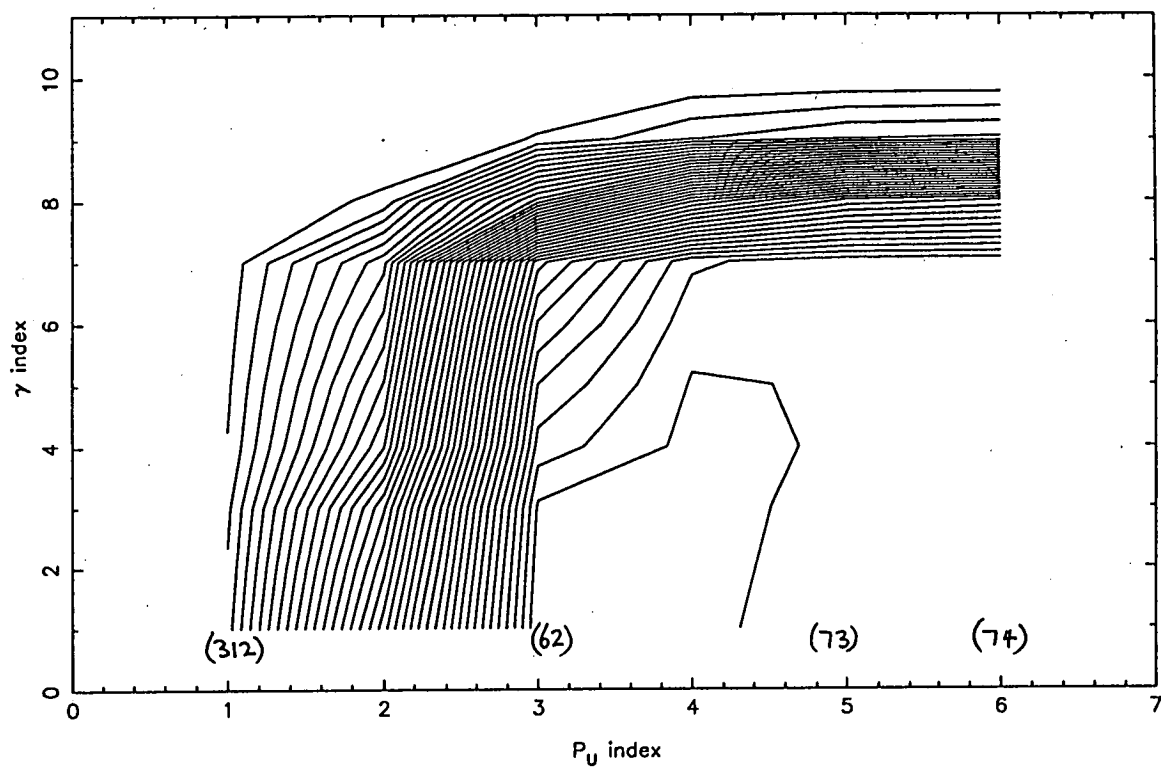
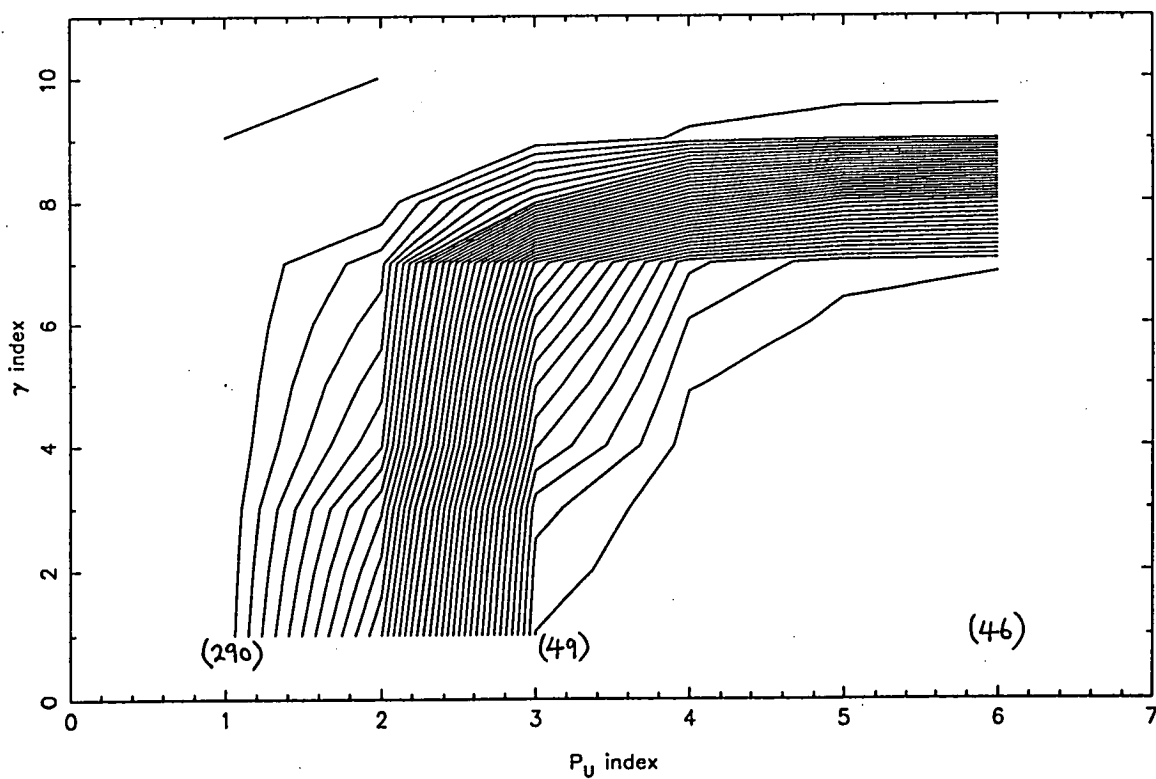
contour of χ^2 (toward sectors) : 1983 n = 2



contour of χ^2 (toward sectors) : 1983 n = 1



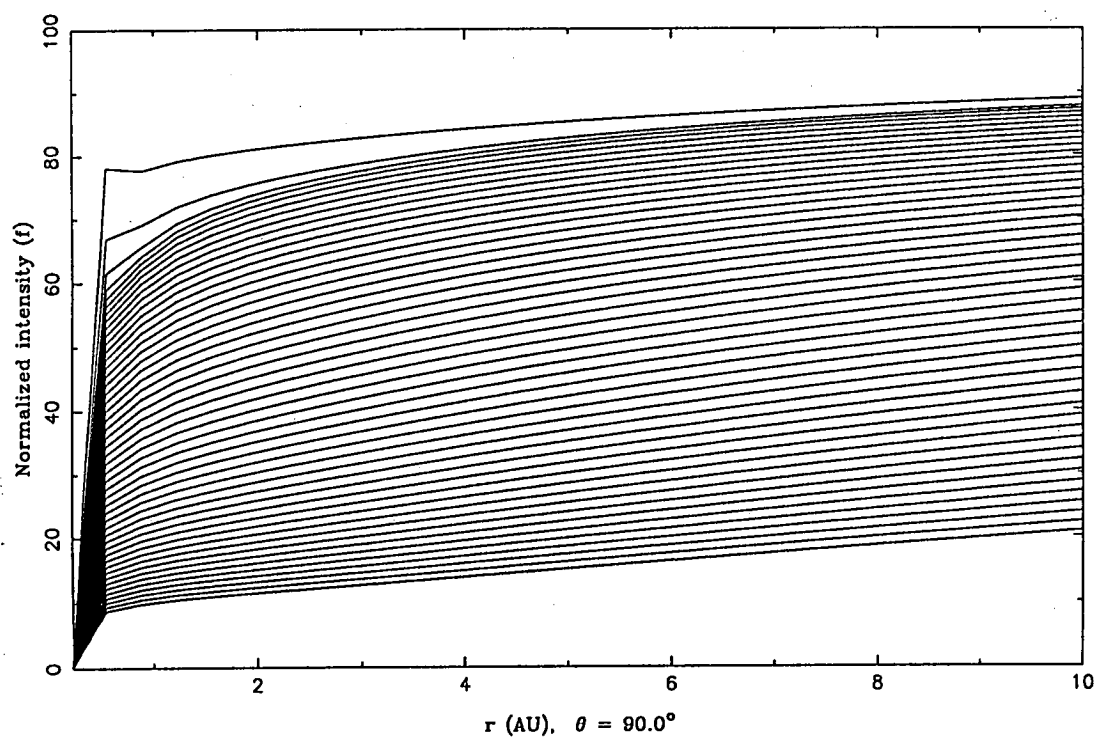
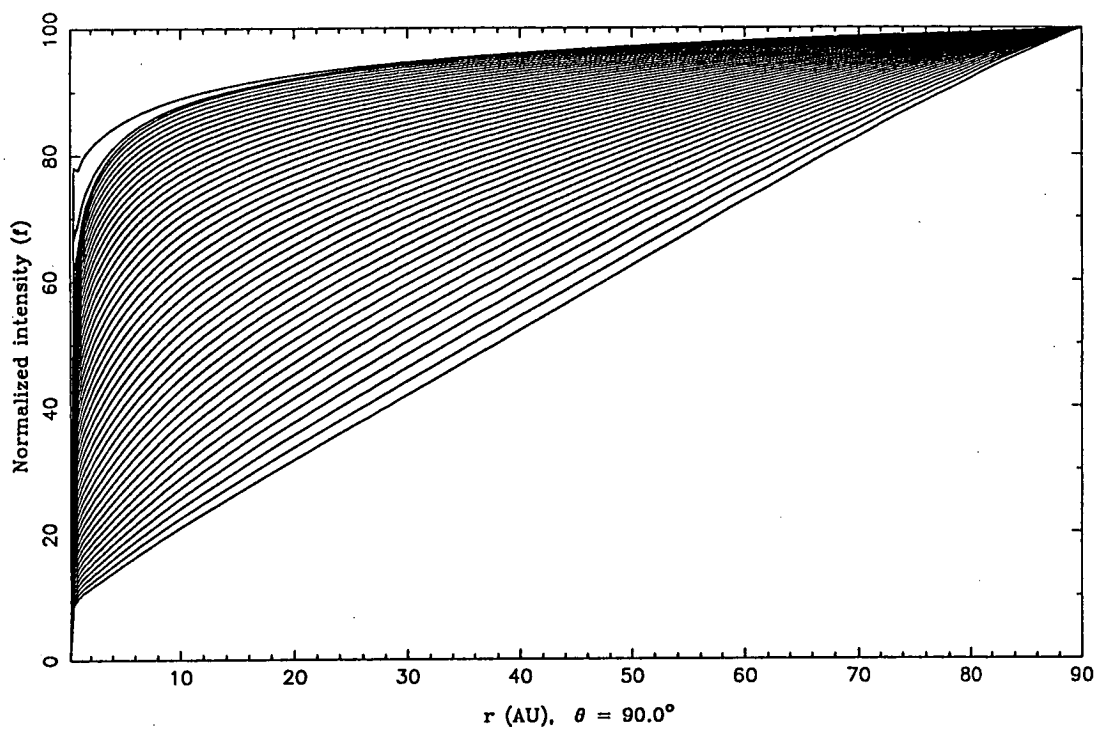
contour of χ^2 (toward sectors) : 1984 n = 2contour of χ^2 (toward sectors) : 1984 n = 1

contour of χ^2 (toward sectors) : 1985 n = 2contour of χ^2 (toward sectors) : 1985 n = 1

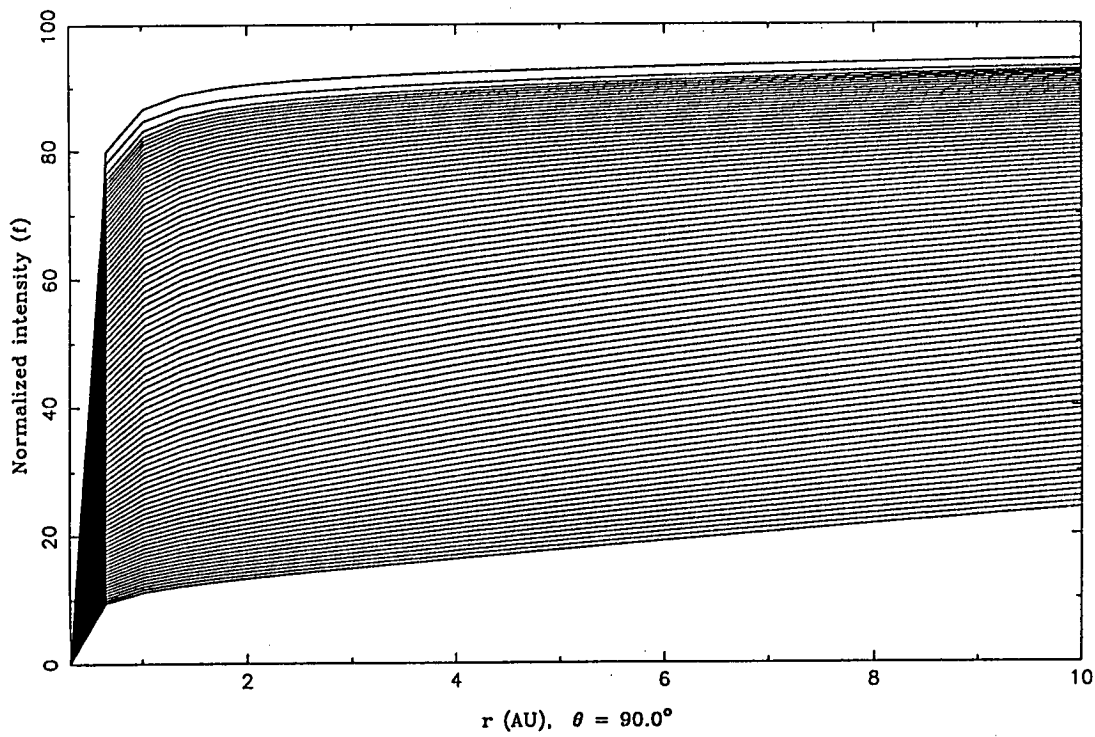
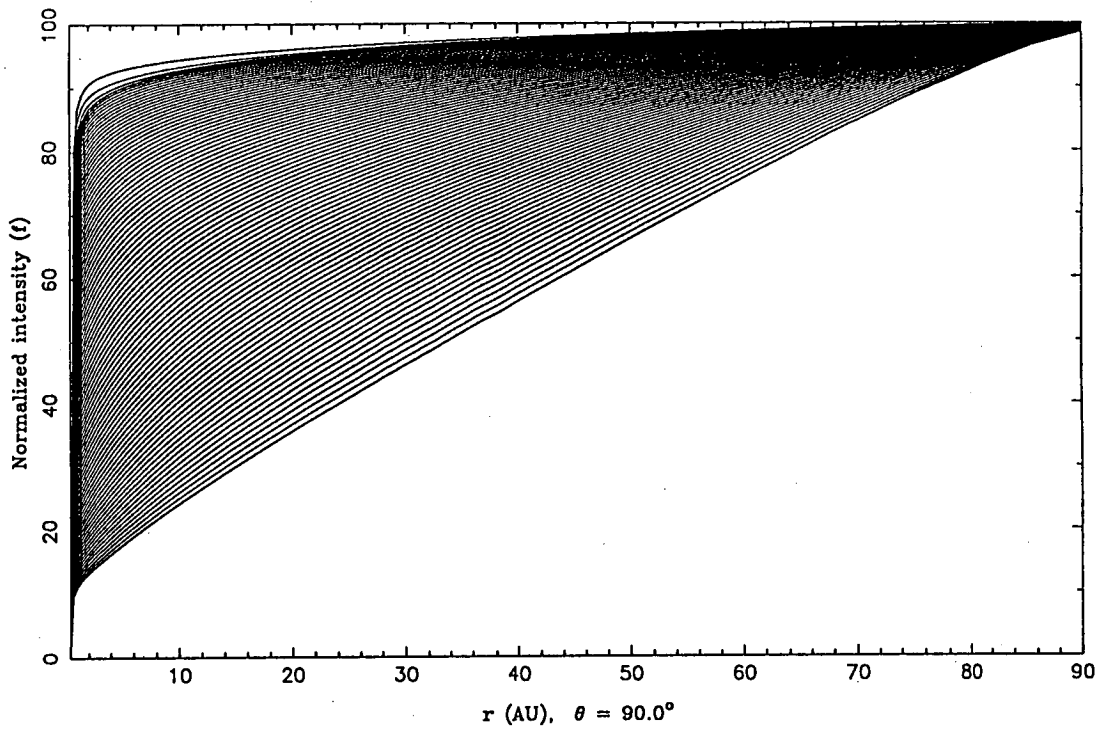
APPENDIX 10

PLOTS OF DISTRIBUTION FUNCTION FOR THE 2-SPACE DIMENSIONAL HELIOSPHERE.

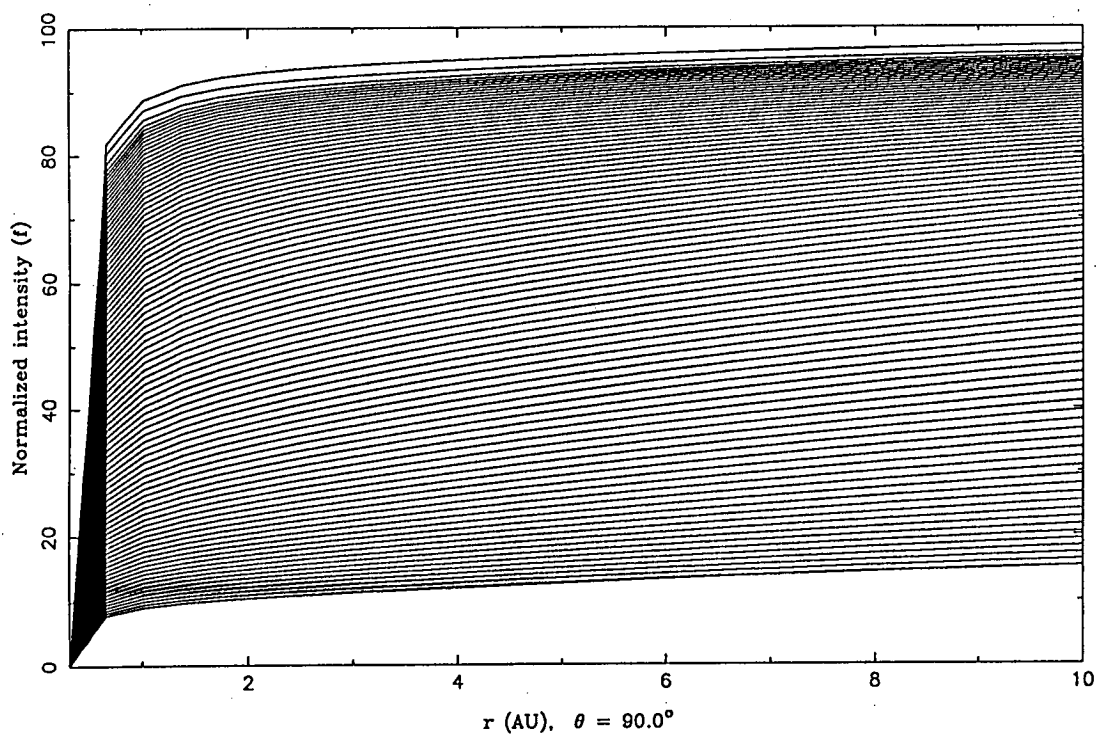
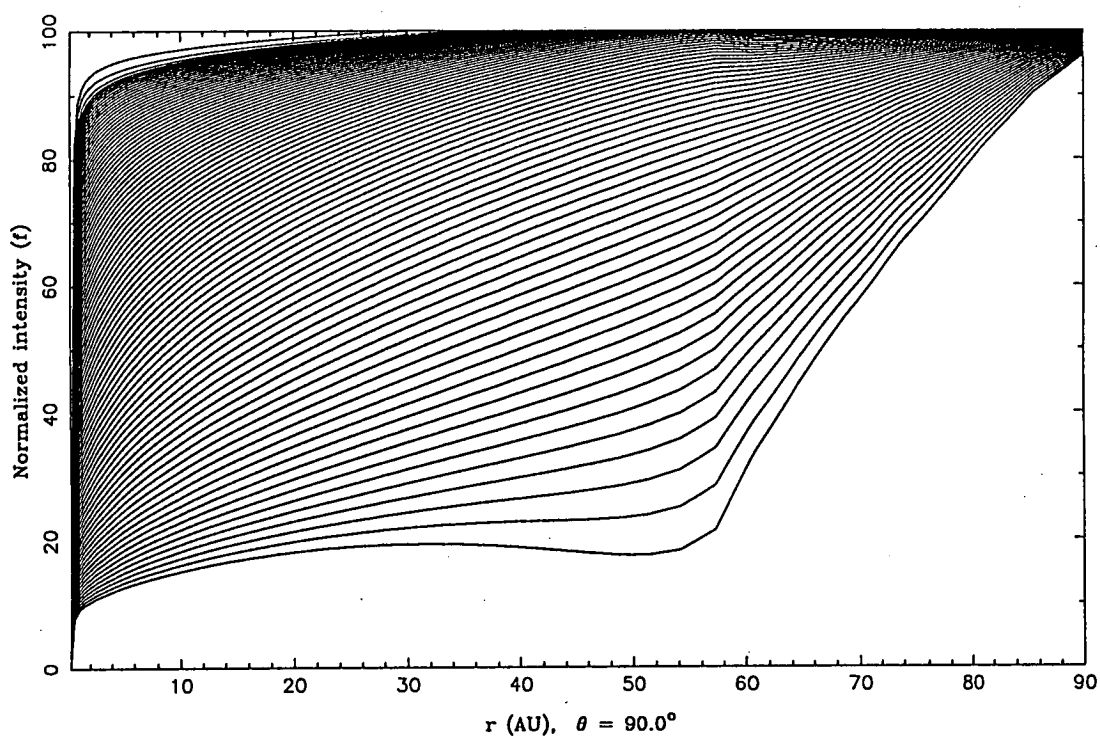
This appendix contains the plots of the distribution function f vs radius coordinate r for a heliographic co-latitude of 90° for the numerical solutions of the two-dimensional transport equation in Chapter 4. In each case, the bottom trace is for rigidity = 0.5 GV and the top trace is for rigidity = 10 GV. Traces in-between correspond to intermediate rigidities at constant logarithmic intervals. Each trace is normalized to the value of the differential intensity at that rigidity at the boundary of the heliosphere. The plots are labelled Run 1 through to Run 13. Runs 1-6 correspond to results from Section 4.2, Run 7 from Section 4.4a, Runs 8-11 from Section 4.4b and Runs 12 and 13 from Section 4.4c.



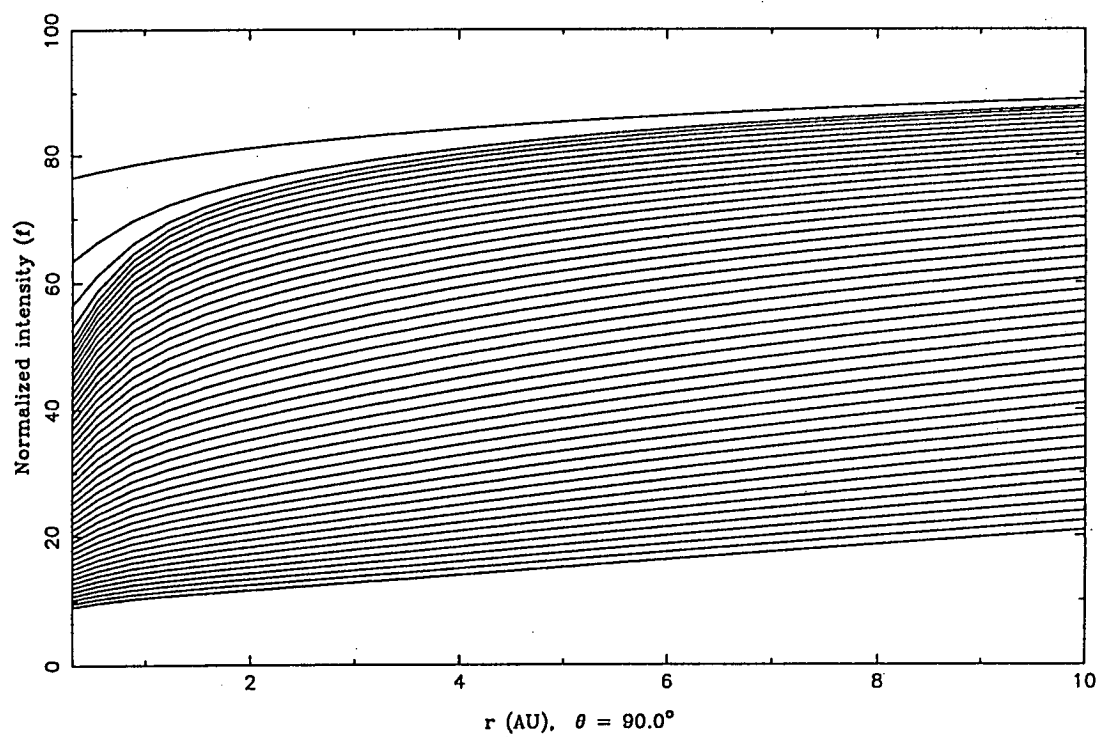
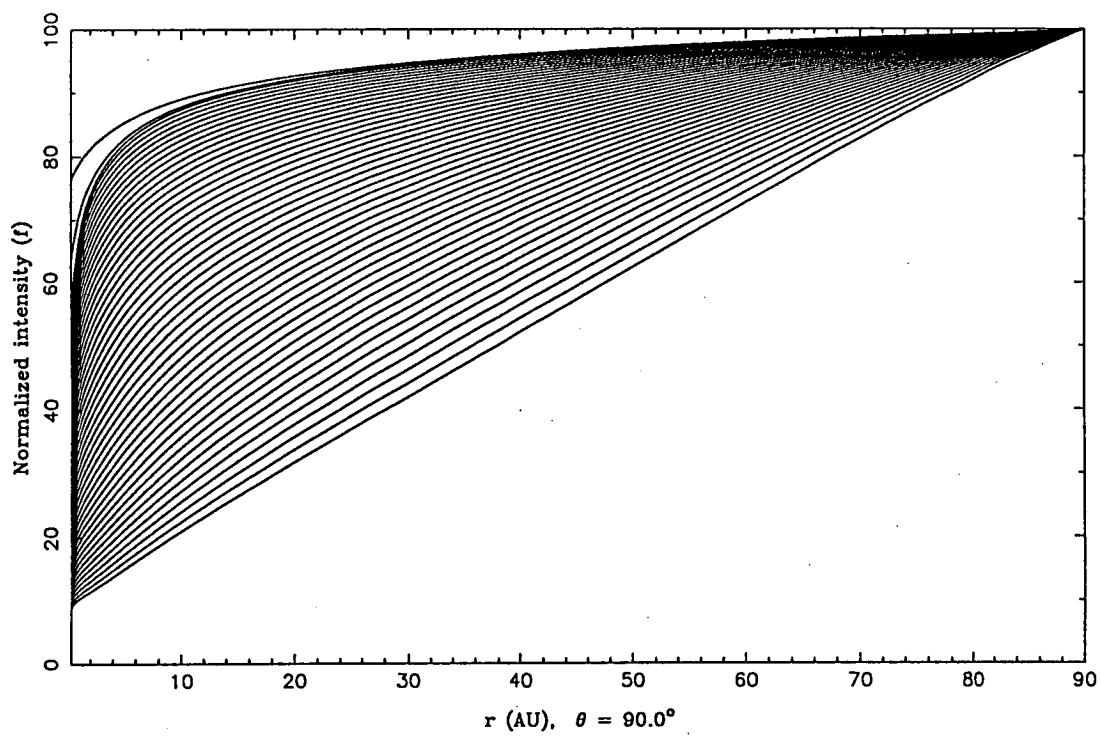
RUN 1: Integrating algorithm is LOD. There is no solar wind termination shock. The inner boundary is fixed at zero. Other parameters are specified in Section 4.2.



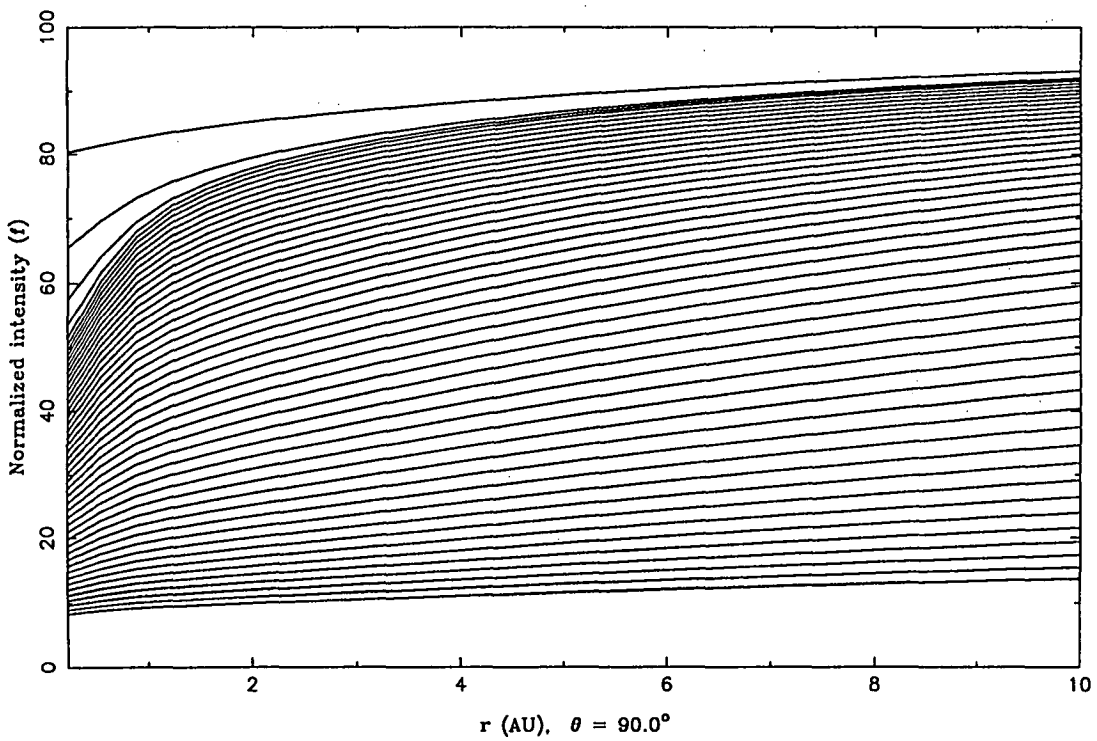
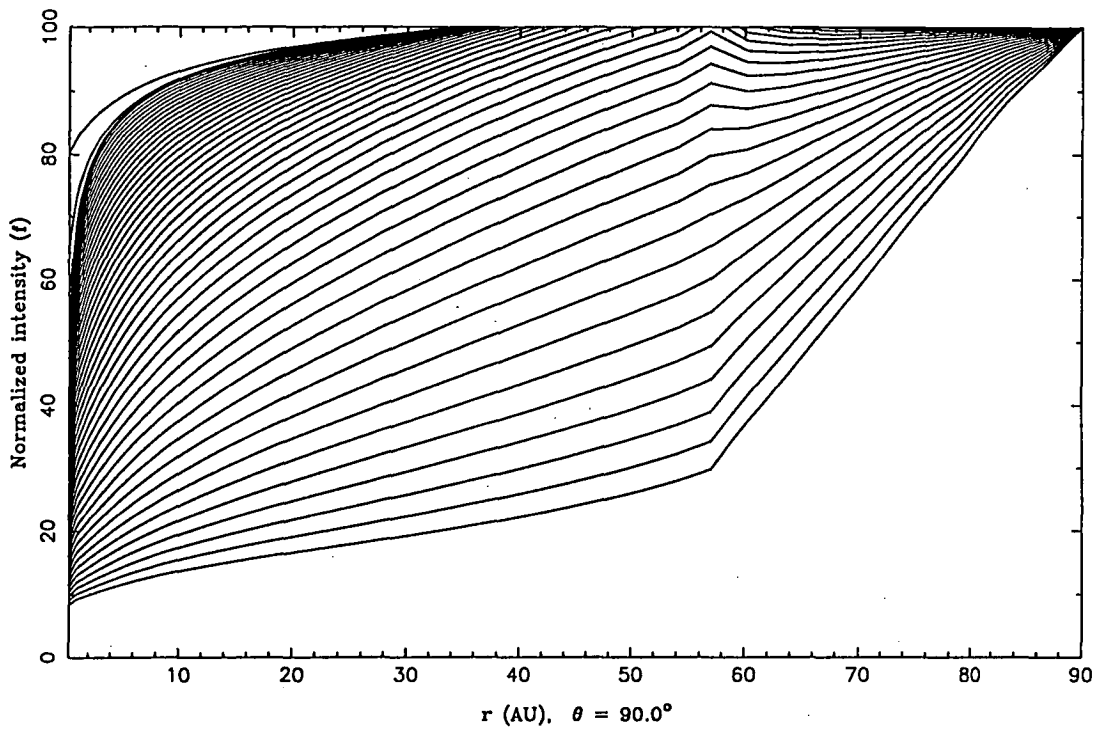
RUN 2: Integrating algorithm is ADI. There is no solar wind termination shock. The inner boundary is fixed at zero. Other parameters are specified in Section 4.2.



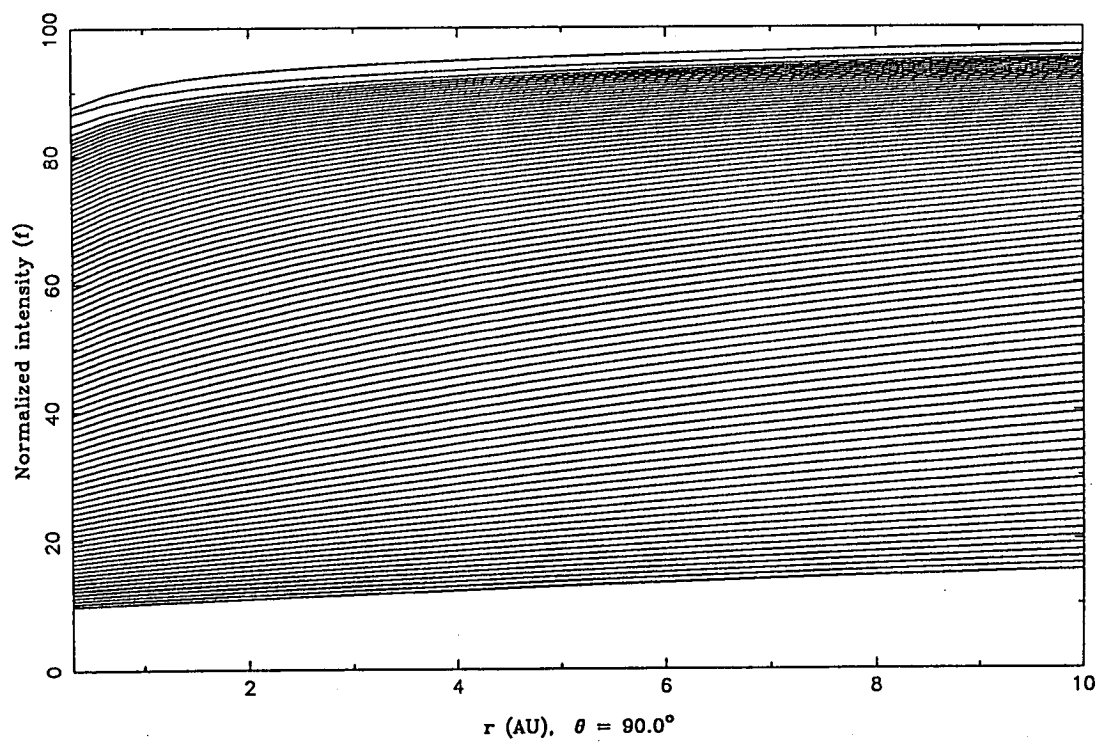
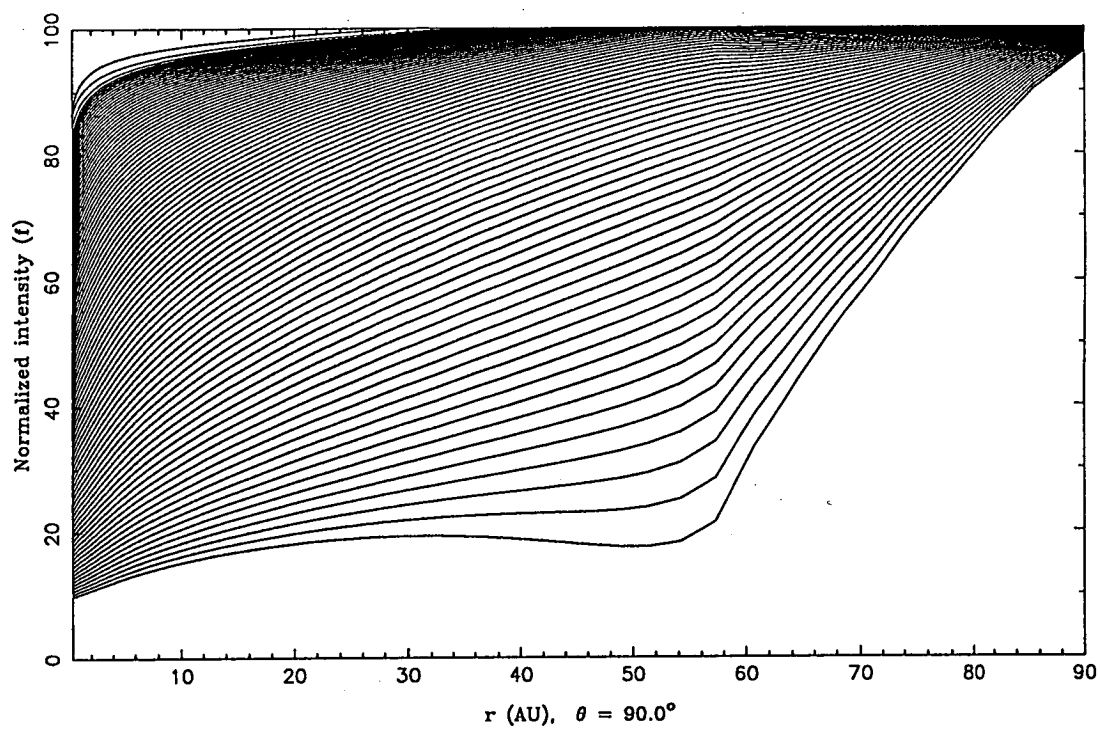
RUN 3: Integrating algorithm is ADI. Solar wind termination shock is at 60 AU. The inner boundary is fixed at zero. Other parameters are specified in Section 4.2.



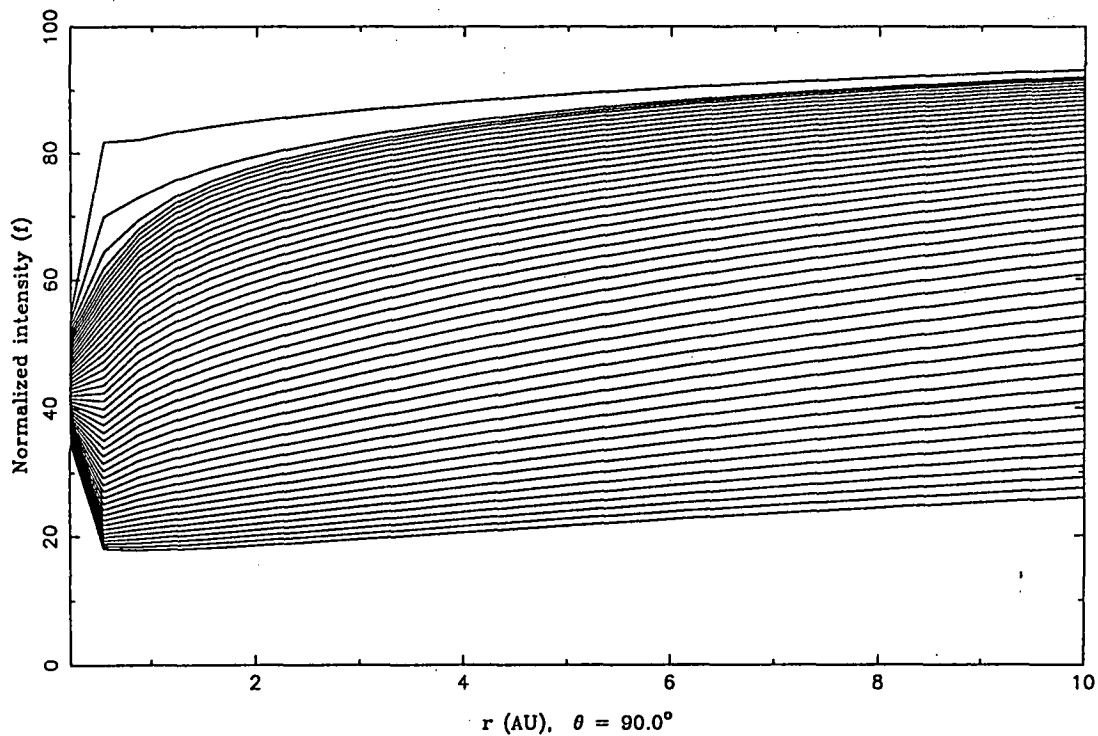
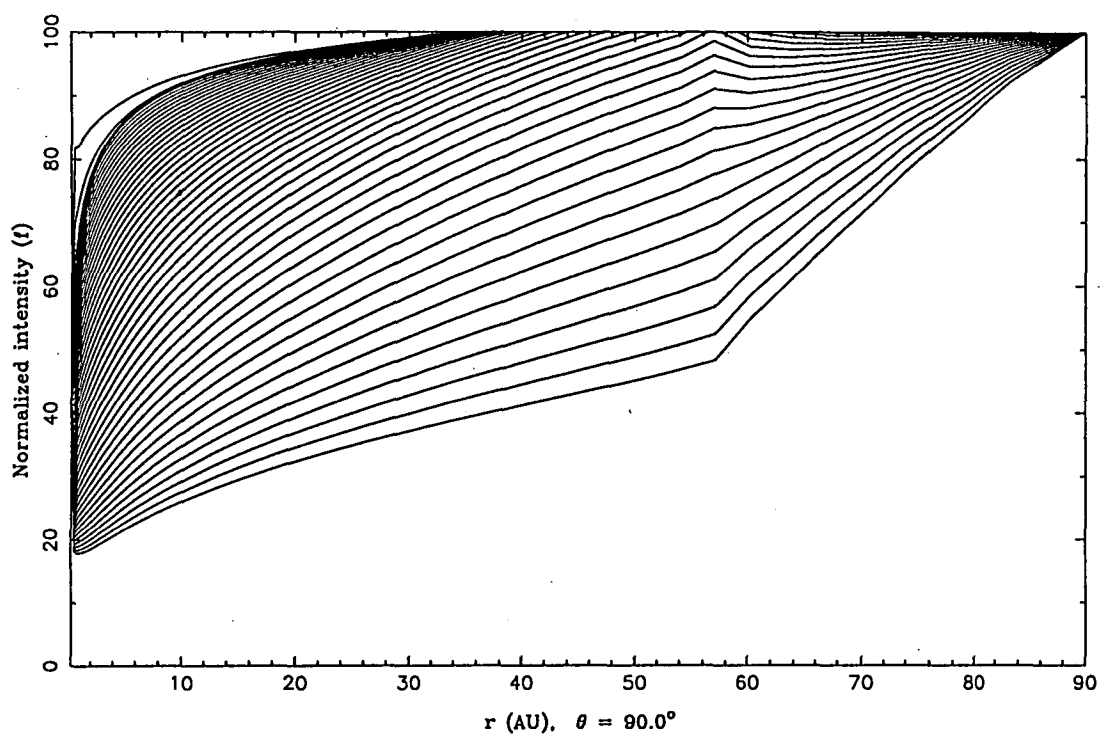
RUN 4: Integrating algorithm is LOD. There is no solar wind termination shock. The inner boundary is floated. Other parameters are specified in Section 4.2.



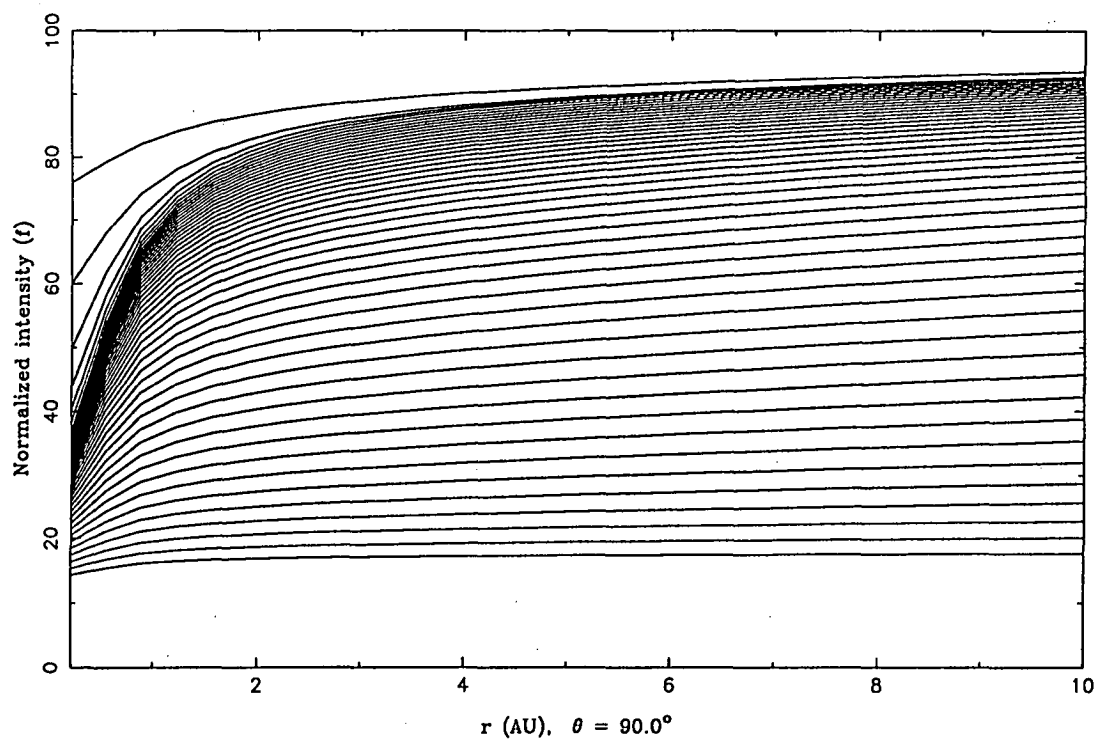
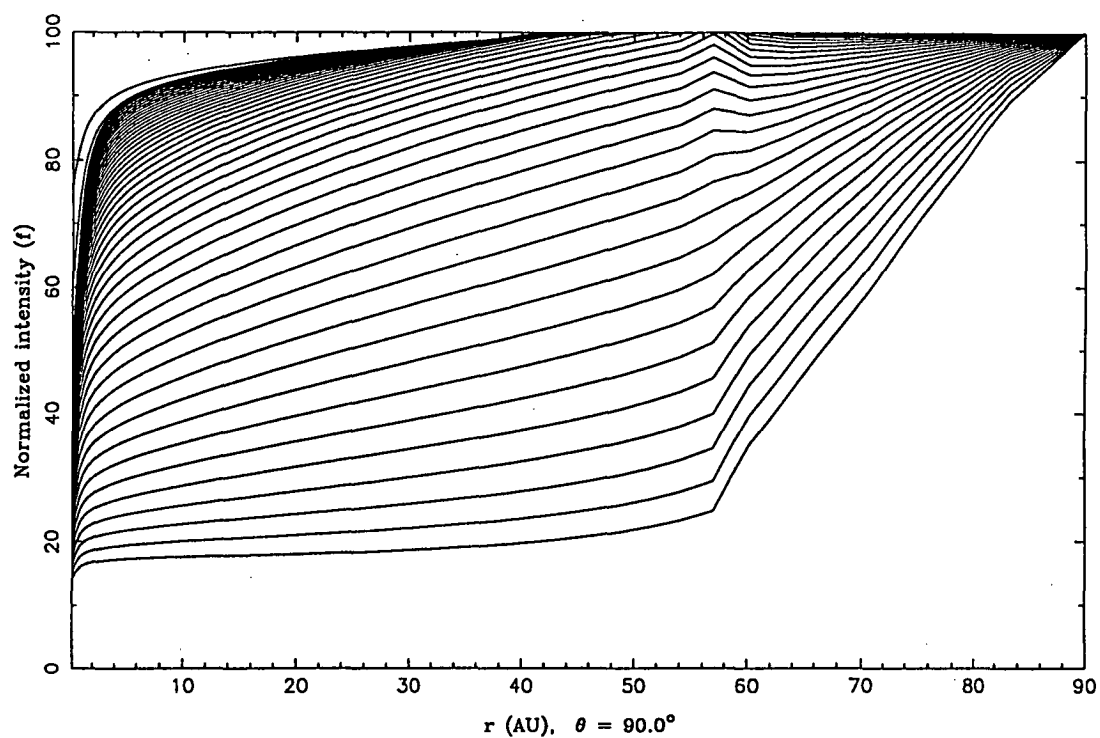
RUN 5: Integrating algorithm is LOD. Solar wind termination shock is at 60 AU. The inner boundary is floated. Other parameters are specified in Section 4.2.



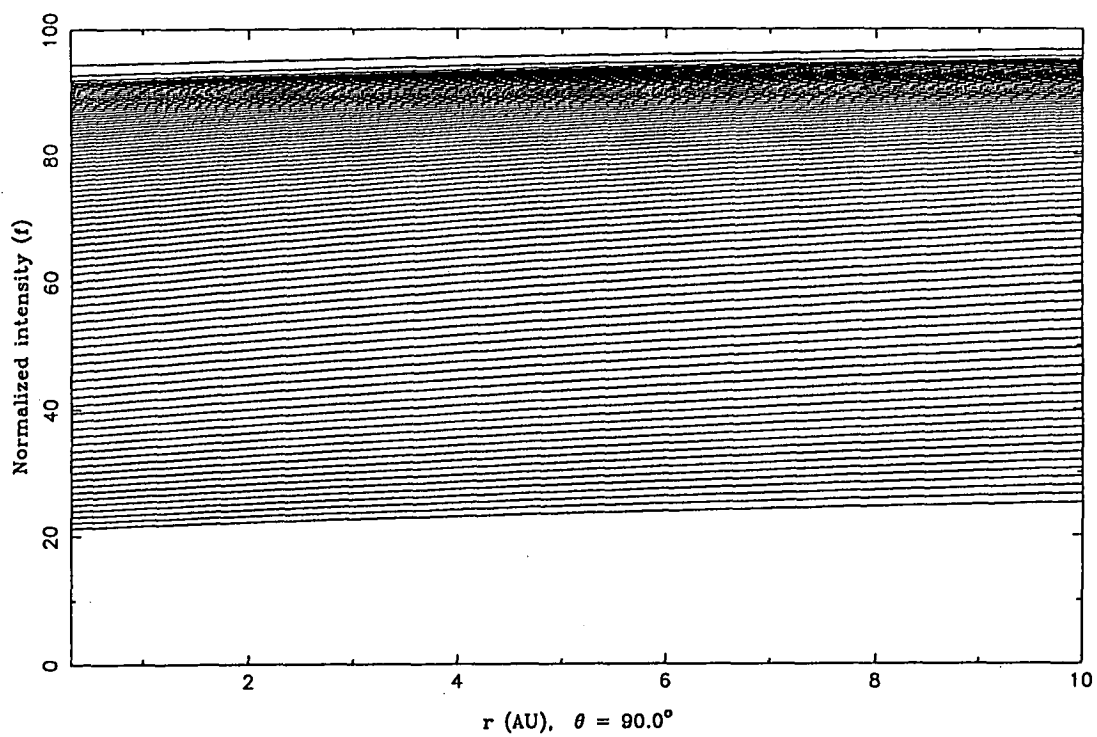
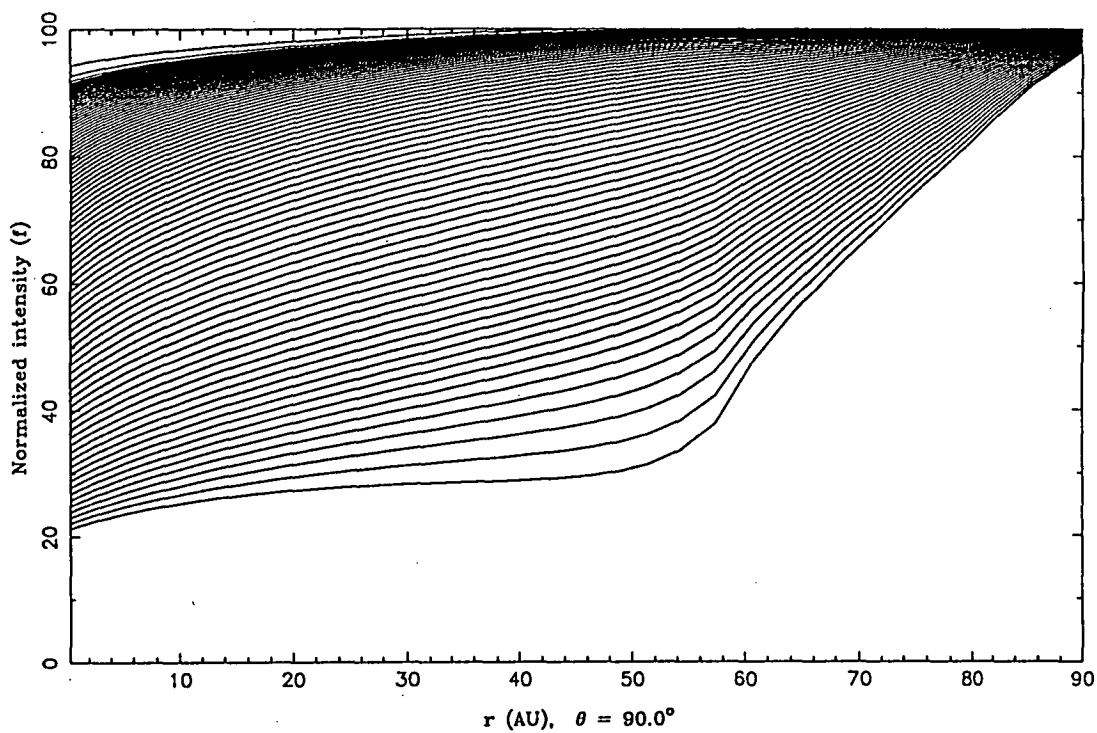
RUN 6: Integrating algorithm is ADI. Solar wind termination shock is at 60 AU. The inner boundary is floated. Other parameters are specified in Section 4.2.



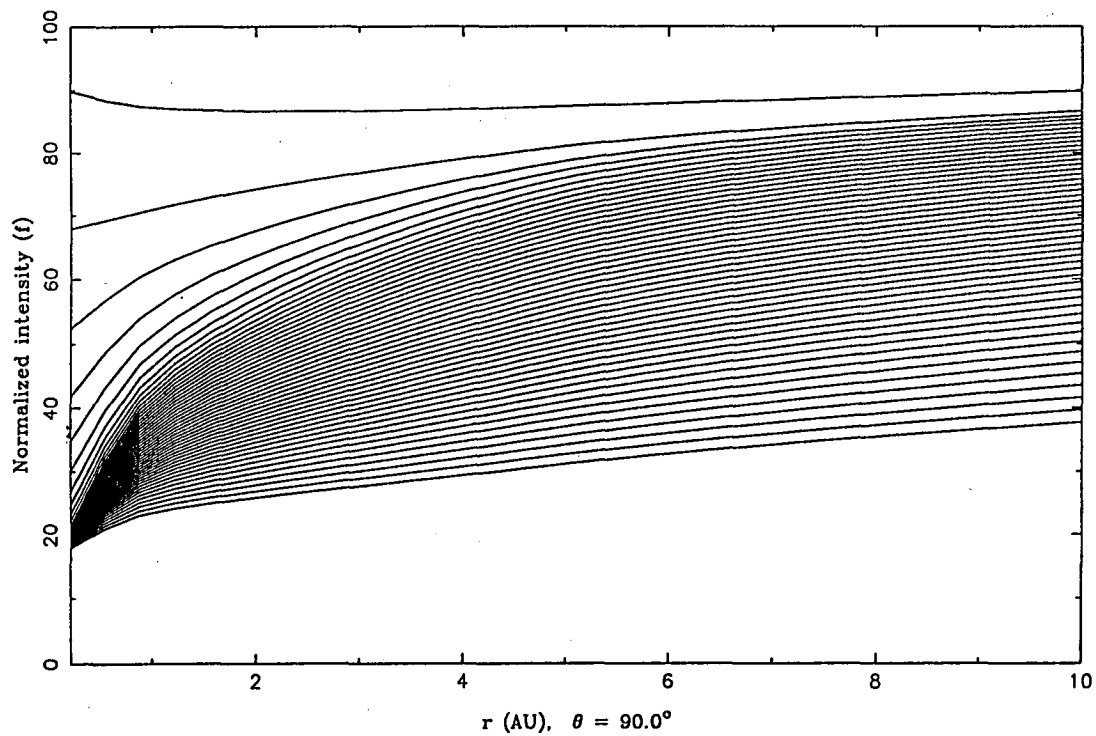
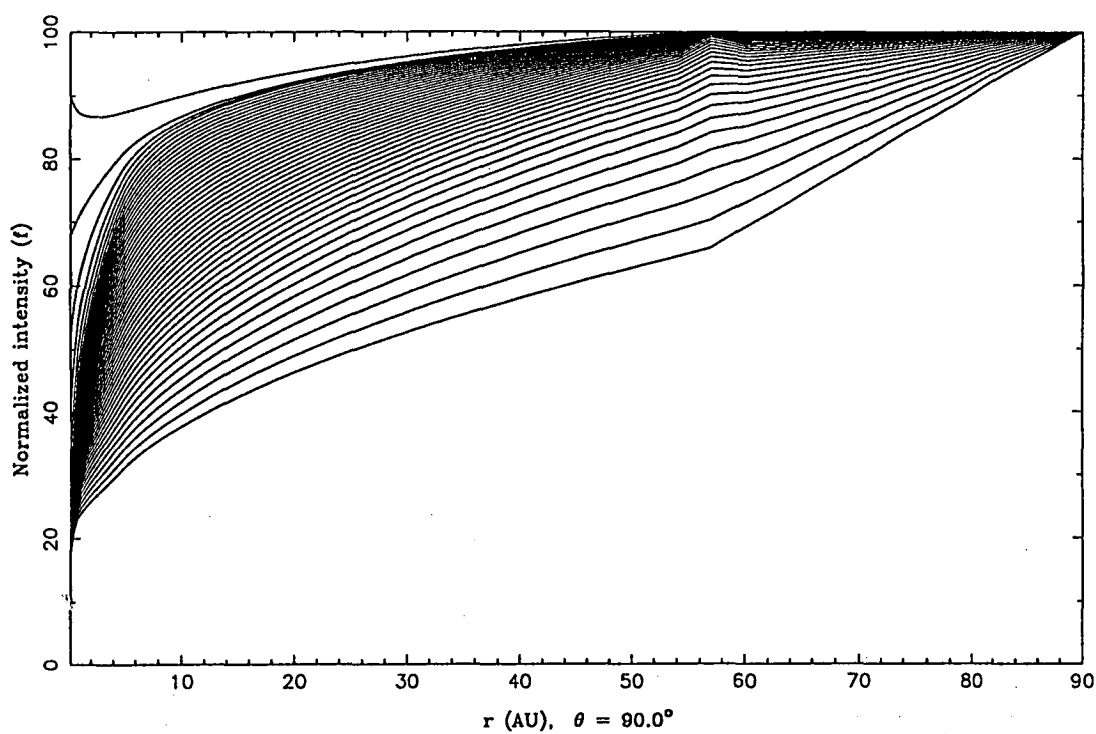
RUN 7: Integrating algorithm is LOD. The inner boundary is specified as a power law spectrum. Parameters are specified in Section 4.4a.



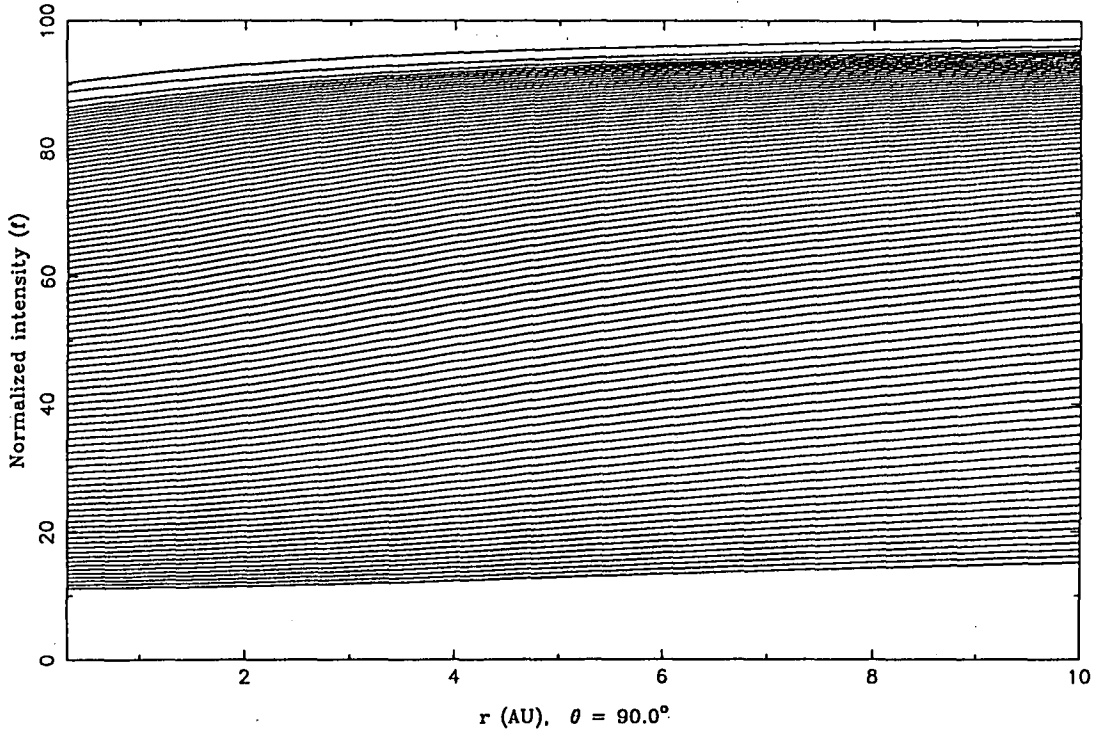
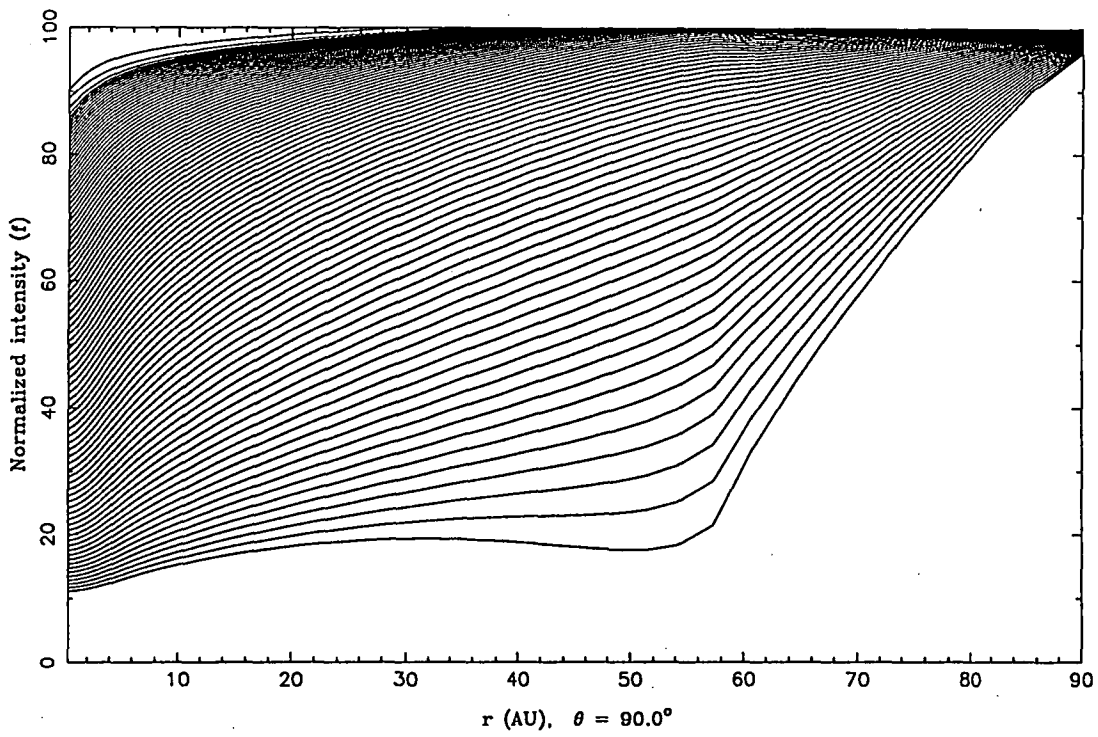
RUN 8: Integrating algorithm is LOD. Solar wind termination shock is at 60 AU. The inner boundary is floated. Diffusion coefficients are specified by SET A in Section 4.4b.



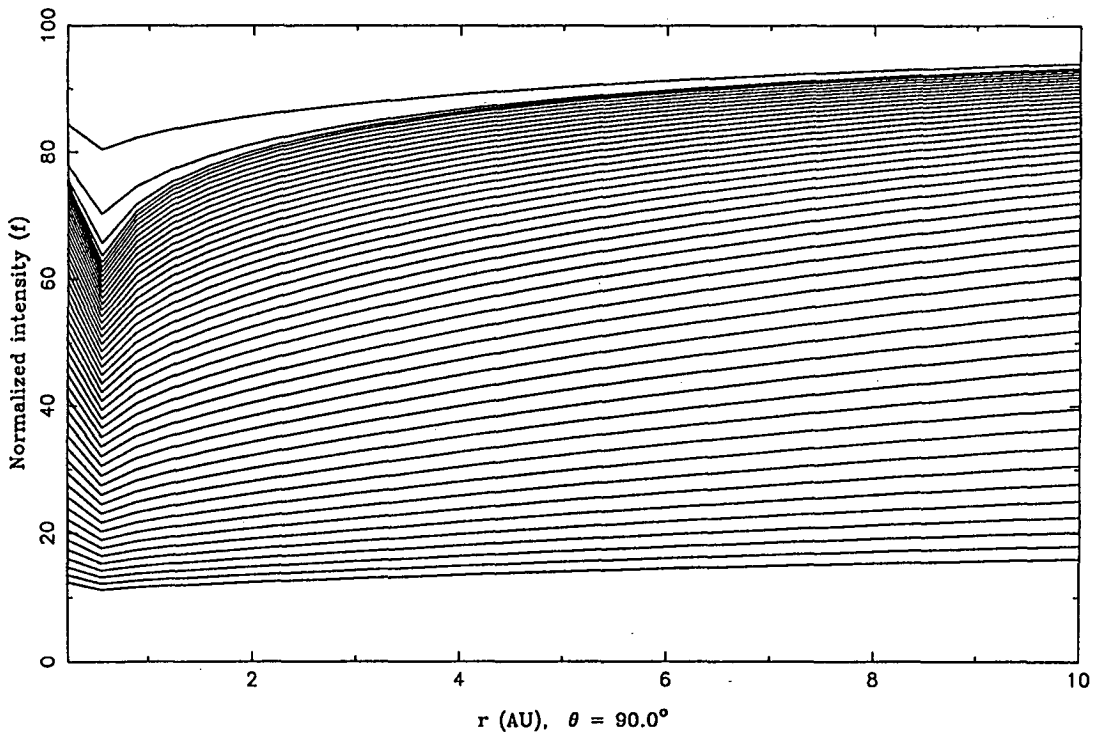
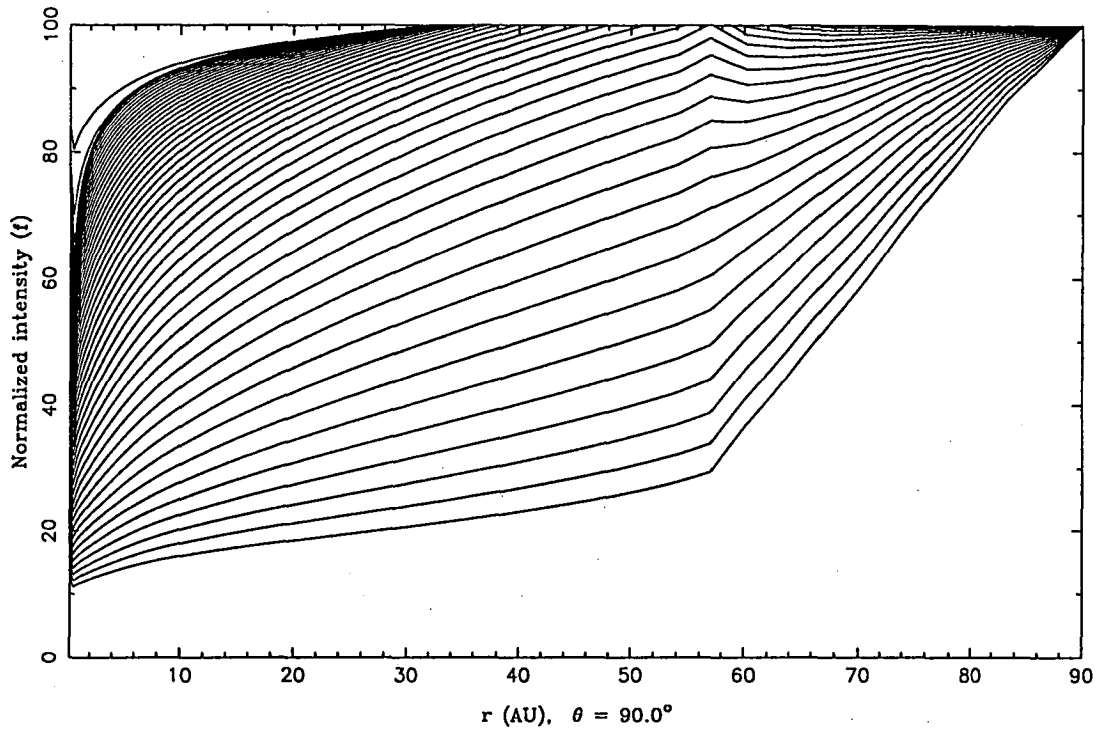
RUN 9: Integrating algorithm is ADI. Solar wind termination shock is at 60 AU. The inner boundary is floated. Diffusion coefficients are specified by SET A in Section 4.4b.



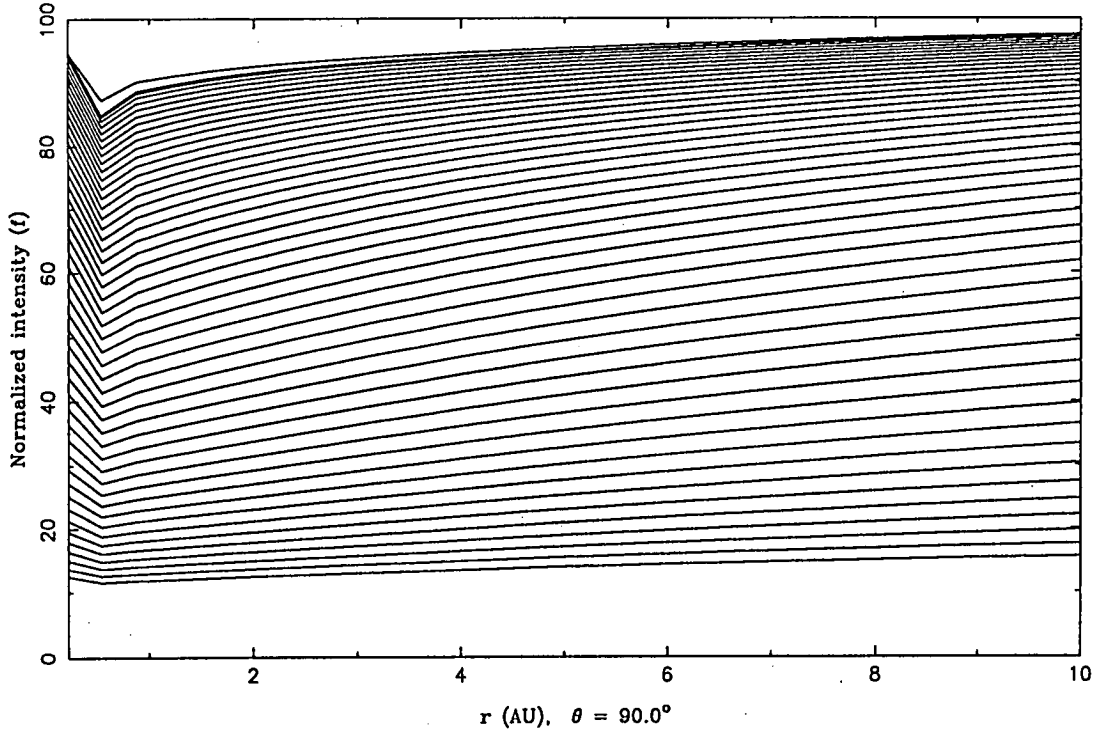
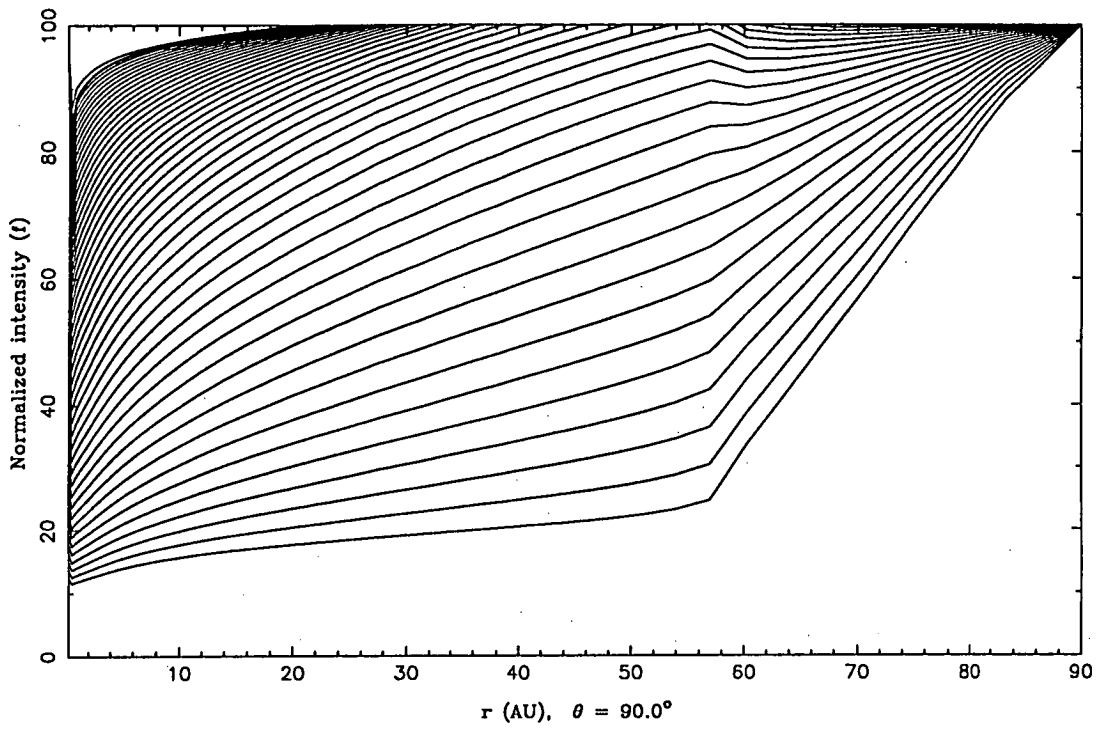
RUN 10: Integrating algorithm is LOD. Solar wind termination shock is at 60 AU. The inner boundary is floated. Diffusion coefficients are specified by SET B in Section 4.4b.



RUN 11: Integrating algorithm is ADI. Solar wind termination shock is at 60 AU. The inner boundary is floated. Diffusion coefficients are specified by SET B in Section 4.4b.



RUN 12: Integrating algorithm is LOD. Solar wind termination shock is at 60 AU. The inner boundary is specified by the condition of zero radial streaming. Other parameters are specified in Section 4.4c.



RUN 13: Integrating algorithm is ADI. Solar wind termination shock is at 60 AU. The inner boundary is specified by the condition of zero radial streaming. Other parameters are specified in Section 4.4c.

APPENDIX 11

PUBLICATIONS.

Publications which arose from research undertaken during the course of this degree are listed below.

Work presented in Sections 6.4 and 6.5 were published in Paper (4). This paper incorrectly reported a *correlation* between the intensity waves and the index k , rather than an *anti-correlation* as presented in the above sections. The hypothesis that there was an excess intensity of galactic cosmic rays in the southern hemisphere, presented in this thesis, was incorrectly reported as an excess in the northern hemisphere in Paper (4).

Work presented in Section 4.5 was published in Paper (5). The integral intensity of galactic cosmic ray particles in a 1 AU region about Earth was found to be depressed, after shock-modulation, by $\sim 8\%$ for the case $\alpha=0.9$. This was incorrectly reported in Paper (5) as $\sim 11\%$.

- 1) CP Baker, ML Duldig and JE Humble, 1989, Extensions to the Coupling Coefficient Calculations for Muon Telescopes. *Proc. Astronomical Soc. Aust.* Vol. 8, #1, 55.
- 2) CP Baker, JE Humble and ML Duldig, 1990, Effect of the Magnetic Field Model on Cosmic Ray Coupling Coefficient Calculations. *J. Geomag. Geoelectr.* Vol. 42, 1137.
- 3) CP Baker, ML Duldig and JE Humble, 1990, Coupling Coefficient Sensitivity and New Calculations for High Zenith Angle Muon Telescopes. *Proc. 21st. Int. Cosmic Ray Conf.* Vol 7, 112.
- 4) ML Duldig, CP Baker and JE Humble, 1990, Intensity Waves and the Neutral Sheet Structure. *Proc. 21st Int. Cosmic Ray Conf.* Vol. 6, 291.
- 5) CP Baker, JE Humble and ML Duldig, 1991, Are Shocks Important in the Modulation of High Energy Cosmic Rays? *Proc. 22nd Int. Cosmic Ray Conf.* Vol. 3, 541.
- 6) JE Humble, CP Baker, ML Duldig, AG Fenton and KB Fenton, 1991, A Southern Survey with a Transportable Neutron Monitor. *Proc. 22nd Int. Cosmic Ray Conf.* Vol. 3, 685.
- 7) CP Baker, JE Humble and ML Duldig, 1993, Heliospheric Modulation Models of High-Energy Cosmic Rays: Theory vs Observation at 1AU. *ANARE Research Notes*, Australian Antarctic Division, Vol. 88, 244
- 8) CP Baker, DL Hall, JE Humble, ML Duldig, 1993, Atmospheric Correction Analysis for the Mawson Muon Telescopes. *Proc. 23rd Int. Cosmic Ray Conf.* IN PRESS.
- 9) CP Baker, DL Hall, JE Humble, ML Duldig, 1993, North-South Anisotropy and the Radial Gradient of Cosmic Rays at 1 AU: 1982-1985. *Proc. 23rd Int. Cosmic Ray Conf.* IN PRESS.